Africa sees promise and peril in Ethiopia's giant dam *p. 904*

Bringing evolution into conservation *p. 922*

Bridging the gap between cell and structural biology *p. 969*

Science

$15
26 FEBRUARY 2016
sciencemag.org
AAAS

Amazon photosynthesis

Young leaves drive seasonal surges *p. 972*

CONTENTS

26 FEBRUARY 2016 • VOLUME 351 • ISSUE 6276

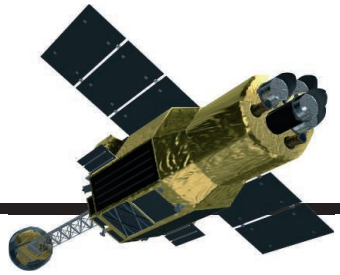

897
Japan launches a new eye on the universe

Nile nations are sparring over the promises and perils of Ethiopia's Grand Renaissance Dam.

NEWS

IN BRIEF

896 News at a glance

IN DEPTH

899 FLAGSHIP ACCELERATORS BID FOR BETTER BEAMS
DOE considers wish list of upgrades to x-ray and neutron sources
By R. F. Service

900 DATA CHECK: FOR INNOVATION, NO MAGIC IN 3% RULE
New studies raise questions about a venerable metric for measuring whether a country is spending enough on scientific research and development
By J. Mervis

901 ARCTIC SHIPWORM DISCOVERY ALARMS ARCHAEOLOGISTS
The discovery of a sunken log full of tunneling mollusks poses mystery, and a possible threat to shipwrecks
By E. Kintisch

902 FIGHT OVER AUTHOR PSEUDONYMS COULD FLARE AGAIN
Editor balks at authors using screen names from RNA folding game
By J. Bohannon

903 WHY DO CELLS' POWER PLANTS HANG ON TO THEIR OWN GENOMES?
Study finds common features in the genes retained since mitochondria evolved from symbiotic microbes *By L. Hamers*

FEATURES

904 POWER PLAY ON THE NILE
Ethiopia stunned neighbors with a colossal dam on the Blue Nile. Could it spread prosperity, not turmoil?
By E. Stokstad

908 NATURE FROM NURTURE
As Japan's rice paddies go fallow, biodiversity suffers—raising questions about rewilding strategies the world over
By D. Normile

INSIGHTS

PERSPECTIVES

912 HOW DO YOU LIKE YOUR TAP WATER?
Safe drinking water may not need to contain a residual disinfectant
By F. Rosario-Ortiz et al.
▸ PODCAST

914 SAVING FRESHWATER FROM SALTS
Ion-specific standards are needed to protect biodiversity
By M. Cañedo-Argüelles et al.

916 BREAKING DNA
A long-sought protein that helps to break DNA is finally discovered
By C. C. Bouuaert and S. Keeney
▸ RESEARCH ARTICLES PP. 939 & 943

918 LEWIS ACIDS TURN UNREACTIVE SUBSTRATES INTO PURE ENANTIOMERS
Chiral organic anion binding to silyl cation provides a new platform for organocatalysis *By A. Dumoulin and G. Masson*
▸ REPORT P. 949

919 MATERNAL T_H17 CELLS TAKE A TOLL ON BABY'S BRAIN
Infection produces an immune molecule that interferes with brain development *By M. L. Estes and A. K. McAllister*
▸ RESEARCH ARTICLE P. 933

920 CRISPR GOES RETRO
RNA contributes directly to the immunological memory recorded in CRISPR sequences *By E. J. Sontheimer and L. A. Marraffini*
▸ RESEARCH ARTICLE P. 932

922 EVOLUTION IN THE ANTHROPOCENE
Taking account of the evolutionary effects of human actions is crucial for humans and nonhumans *By F. Sarrazin and J. Lecomte*

BOOKS *ET AL.*

924 POLITICAL TURBULENCE
By H. Margetts et al.,
reviewed by A. van de Rijt

925 THE ROAD TAKEN
By H. Petroski,
reviewed by L. Vinsel

LETTERS

926 TRADING AWAY ANCIENT AMBER'S SECRETS
By S. Wang et al.

926 MIGRATORY BIRDS NEED COORDINATED PROTECTION
By M. Usman and M. Farooq

927 WALKING THE OPEN SCIENCE WALK
By C. Koch

927 TECHNICAL COMMENT ABSTRACTS

Downloaded from on February 25, 2016

IMAGES: (TOP) JAPAN AEROSPACE EXPLORATION AGENCY; (LEFT) AFP PHOTO/ZACHARIAS ABUBEKER

Published by AAAS

953
A view from a quantum microscope

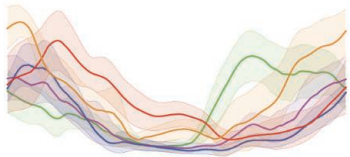

976
A versatile clock

RESEARCH

IN BRIEF

929 From *Science* and other journals

RESEARCH ARTICLES

932 GENE EDITING
Direct CRISPR spacer acquisition from RNA by a natural reverse transcriptase–Cas1 fusion protein *S. Silas* et al.
RESEARCH ARTICLE SUMMARY; FOR FULL TEXT: dx.doi.org/10.1126/science.aad4234
▸ PERSPECTIVE P. 920

933 NEUROIMMUNOLOGY
The maternal interleukin-17a pathway in mice promotes autism-like phenotypes in offspring *G. B. Choi* et al.
▸ PERSPECTIVE P. 919

MEIOSIS
939 A DNA topoisomerase VI–like complex initiates meiotic recombination *N. Vrielynck* et al.
943 The TopoVIB-Like protein family is required for meiotic DNA double-strand break formation *T. Robert* et al.
▸ PERSPECTIVE P. 916

REPORTS

949 ORGANIC LEWIS ACIDS
Asymmetric Lewis acid organocatalysis of the Diels–Alder reaction by a silylated C–H acid *T. Gatzenmeier* et al.
▸ PERSPECTIVE P. 918

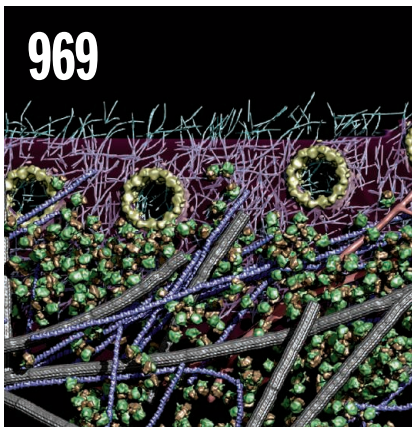

953 QUANTUM SIMULATION
Site-resolved imaging of a fermionic Mott insulator *D. Greif* et al.

957 THIN FILMS
Superlubricity of graphene nanoribbons on gold surfaces *S. Kawai* et al.

961 ORGANIC CHEMISTRY
An aromatic ion platform for enantioselective Brønsted acid catalysis *C. D. Gheewala* et al.

965 CATALYSIS
Palladium-tin catalysts for the direct synthesis of H_2O_2 with high selectivity *S. J. Freakley* et al.

969 CELL NUCLEUS
Visualizing the molecular sociology at the HeLa cell nuclear periphery *J. Mahamid* et al.

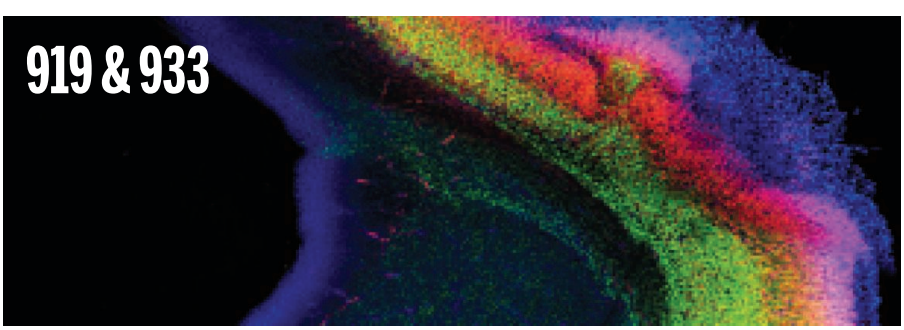

972 FOREST ECOLOGY
Leaf development and demography explain photosynthetic seasonality in Amazon evergreen forests *J. Wu* et al.

976 CIRCADIAN RHYTHMS
Synchronous *Drosophila* circadian pacemakers display nonsynchronous Ca^{2+} rhythms in vivo *X. Liang* et al.

981 SYNAPTIC VESICLES
Single-vesicle imaging reveals different transport mechanisms between glutamatergic and GABAergic vesicles *Z. Farsi* et al.

DEPARTMENTS

895 EDITORIAL
KIST at 50, beyond the miracle
By Byung Gwon Lee

994 WORKING LIFE
Embrace uncertainty
By France A. Córdova

ON THE COVER

Sunrise over a tropical forest in Brazil. The seasonal patterns of leaf development in Amazonian forests, measured using tower-based cameras above the tree crowns, regulate the patterns of carbon dioxide flux in the forest canopy. Photosynthesis tends to be greatest when the crop of young leaves reaches a peak, rather than depending on precipitation in the rainy season. See page 972.
Photo: © Leonide Principe/Alamy

Science Staff 894
AAAS News & Notes 928
New Products 985
Science Careers 986

SCIENCE (ISSN 0036-8075) is published weekly on Friday, except the last week in December, by the American Association for the Advancement of Science, 1200 New York Avenue, NW, Washington, DC 20005. Periodicals mail postage (publication No. 484460) paid at Washington, DC, and additional mailing offices.

Copyright © 2016 by the American Association for the Advancement of Science. The title SCIENCE is a registered trademark of the AAAS.

Domestic individual membership and subscription (51 issues): $165 ($74 allocated to subscription). Domestic institutional subscription (51 issues): $1522; Foreign postage extra: Mexico, Caribbean (surface mail) $55; other countries (air assist delivery) $89. First class, airmail, student, and emeritus rates on request. Canadian rates with GST available upon request, GST #1254 88122. Publications Mail Agreement Number 1069624. **Printed in the U.S.A.**
Change of address: Allow 4 weeks, giving old and new addresses and 8-digit account number. **Postmaster:** Send change of address to AAAS, P.O. Box 96178, Washington, DC 20090–6178. **Single-copy sales:** $15.00 current issue, $20.00 back issue prepaid includes surface postage; bulk rates on request.

Authorization to photocopy material for internal or personal use under circumstances not falling within the fair use provisions of the Copyright Act is granted by AAAS to libraries and other users registered with the Copyright Clearance Center (CCC) Transactional Reporting Service, provided that $35.00 per article is paid directly to CCC, 222 Rosewood Drive, Danvers, MA 01923. The identification code for *Science* is 0036-8075. *Science* is indexed in the *Reader's Guide to Periodical Literature* and in several specialized indexes.

Published by AAAS

Science
AAAS
1200 New York Avenue, NW, Washington, DC 20005
Bateman House, 82-88 Hills Road, Cambridge, UK CB2 1LQ

Editor-in-Chief Marcia McNutt
Executive Editor Monica M. Bradford **News Editor** Tim Appenzeller
Managing Editor, Research Journals Katrina L. Kelner
Deputy Editors Barbara R. Jasny, Andrew M. Sugden(UK), Valda J. Vinson, Jake S. Yeston

Research and Insights

SR. EDITORS Caroline Ash(UK), Gilbert J. Chin, Lisa D. Chong, Julia Fahrenkamp-Uppenbrink(UK), Pamela J. Hines, Stella M. Hurtley(UK), Paula A. Kiberstis, Marc S. Lavine(Canada), Kristen L. Mueller, Ian S. Osborne(UK), Beverly A. Purnell, L. Bryan Ray, Guy Riddihough, H. Jesse Smith, Jelena Stajic, Peter Stern(UK), Phillip D. Szuromi, Sacha Vignieri, Brad Wible, Nicholas S. Wigginton, Laura M. Zahn **ASSOCIATE EDITORS** Brent Grocholski, Keith T. Smith **ASSOCIATE BOOK REVIEW EDITOR** Valerie B. Thompson **ASSOCIATE LETTERS EDITOR** Jennifer Sills **CHIEF CONTENT PRODUCTION EDITOR** Cara Tate **SR. CONTENT PRODUCTION EDITORS** Harry Jach, Lauren Kmec **CONTENT PRODUCTION EDITORS** Jeffrey E. Cook, Chris Filiatreau, Cynthia Howe, Barbara P. Ordway, Catherine Wolner **SR. EDITORIAL COORDINATORS** Carolyn Kyle, Beverly Shields **EDITORIAL COORDINATORS** Joi S. Granger, Lisa Johnson, Anita Wynn **PUBLICATIONS ASSISTANTS** Aneera Dobbins, Jeffrey Hearn, Dona Mathieu, Le-Toya Mayne Flood, Shannon McMahon, Scott Miller, Caitlyn Phillips, Jerry Richardson, Rachel Roberts(UK), Alice Whaley(UK), Brian White **EXECUTIVE ASSISTANT** Anna Bashkirova **ADMINISTRATIVE SUPPORT** Janet Clements(UK), Lizanne Newton(UK), Maryrose Madrid, John Wood(UK)

News

NEWS MANAGING EDITOR John Travis **INTERNATIONAL EDITOR** Richard Stone **DEPUTY NEWS EDITORS** Daniel Clery(UK), Robert Coontz, Elizabeth Culotta, David Grimm, David Malakoff, Leslie Roberts **CONTRIBUING EDITOR** Martin Enserink(Europe) **SR. CORRESPONDENTS** Jeffrey Mervis, Elizabeth Pennisi **NEWS WRITERS** Adrian Cho, Jon Cohen, Jennifer Couzin-Frankel, Carolyn Gramling, Eric Hand, Jocelyn Kaiser, Catherine Matacic, Kelly Servick, Robert F. Service, Erik Stokstad(Cambridge, UK), Emily Underwood **INTERNS** Hanae Armitage, Nala Rogers **CONTRIBUTING CORRESPONDENTS** Michael Balter(Paris), John Bohannon, Ann Gibbons, Mara Hvistendahl, Sam Kean, Eli Kintisch, Kai Kupferschmidt(Berlin), Andrew Lawler, Christina Larson(Beijing), Mitch Leslie, Charles C. Mann, Eliot Marshall, Virginia Morell, Dennis Normile(Shanghai), Heather Pringle, Tania Rabesandratana(London), Gretchen Vogel(Berlin), Lizzie Wade(Mexico City) **CAREERS** Donisha Adams, Rachel Bernstein(Editor) **COPY EDITORS** Julia Cole, Dorie Chevlen, Jennifer Levin (Chief) **ADMINISTRATIVE SUPPORT** Jessica Williams

Executive Publisher Rush D. Holt
Interim Publisher Bill Moran **Chief Digital Media Officer** Rob Covey

BUSINESS OPERATIONS AND PORTFOLIO MANAGEMENT DIRECTOR Sarah Whalen **PRODUCT DEVELOPMENT DIRECTOR** Will Schweitzer **PRODUCT DEVELOPMENT ASSOCIATE** Hal Moore **BUSINESS SYSTEMS AND FINANCIAL ANALYSIS DIRECTOR** Randy Yi **MANAGER OF FULFILLMENT SYSTEMS** Neal Hawkins **SYSTEMS ANALYST** Nicole Mehmedovich **ASSISTANT DIRECTOR, BUSINESS OPERATIONS** Eric Knott **MANAGER, BUSINESS OPERATIONS** Jessica Tierney **BUSINESS ANALYST** Cory Lipman **FINANCIAL ANALYST** Robert Clark **RIGHTS AND PERMISSIONS ASSISTANT DIRECTOR** Emilie David **PERMISSIONS ASSOCIATE** Elizabeth Sandler **RIGHTS, CONTRACTS, AND LICENSING ASSOCIATE** Lili Kiser

MARKETING DIRECTOR Elise Swinehart **ASSOCIATE DIRECTOR OF ACQUISITION AND RETENTION** Julianne Wielga **MARKETING ASSOCIATE** Elizabeth Sattler **SR. MARKETING EXECUTIVE** Jennifer Reeves **ASSOCIATE DIRECTOR, CREATIVE SERVICES** Tzeitel Sorrosa **ART ASSOCIATE** Seil Lee **JR. ART ASSOCIATE** Kim Huynh **ASSISTANT COMMERCIAL EDITOR** Selby Frame **MARKETING PROJECT MANAGER** Angelissa McArthur **PROGRAM DIRECTOR, AAAS MEMBER CENTRAL** Peggy Mihelich **FULFILLMENT SYSTEMS AND OPERATIONS** membership@aaas.org **MANAGER, MEMBER SERVICES** Pat Butler **SPECIALISTS** Terrance Morrison, Latasha Russell **MANAGER, DATA ENTRY** Mickie Napoleoni **DATA ENTRY SPECIALISTS** Brenden Aquilino, Fiona Giblin

INTERIM DIRECTOR, SITE LICENSING Will Schweitzer **PUBLISHER RELATIONS MANAGER** Catherine Holland **PUBLISHER RELATIONS, EASTERN REGION** Keith Layson **PUBLISHER RELATIONS, WESTERN REGION** Ryan Rexroth **SALES RESEARCH COORDINATOR** Aiesha Marshall **MANAGER, SITE LICENSE OPERATIONS** Iquo Edim **SENIOR PRODUCTION SPECIALIST** Robert Koepke **SENIOR OPERATIONS ANALYST** Lana Guz **FULFILLMENT ANALYST** Judy Lillibridge **ASSOCIATE DIRECTOR, MARKETING** Christina Schlecht **MARKETING ASSOCIATES** Thomas Landreth, Isa Sesay-Bah

WEB TECHNOLOGIES SR. DEVELOPER Chris Coleman **DEVELOPERS** Dan Berger, Jimmy Marks, Ryan Jensen **SR. PROJECT MANAGER** Trista Smith **PROJECT MANAGER** Nick Fletcher

DIGITAL MEDIA DIRECTOR OF ANALYTICS Enrique Gonzales **DIGITAL REPORTING ANALYST** Eric Hossinger **SR. WEB PRODUCER** Sarah Crespi **WEB PRODUCER** Alison Crawford **VIDEO PRODUCER** Nguyen Nguyen **SOCIAL MEDIA PRODUCER** Brice Russ

DIRECTOR OF OPERATIONS PRINT AND ONLINE Lizabeth Harman **DIGITAL/PRINT STRATEGY MANAGER** Jason Hillman **QUALITY TECHNICAL MANAGER** Marcus Spiegler **PROJECT ACCOUNT MANAGER** Tara Kelly **DIGITAL PRODUCTION MANAGER** Lisa Stanford **ASSISTANT MANAGER DIGITAL/PRINT** Rebecca Doshi **SENIOR CONTENT SPECIALISTS** Steve Forrester, Antoinette Hodal, Lori Murphy, Anthony Rosen **CONTENT SPECIALISTS** Jacob Hedrick, Kimberley Oster

DESIGN DIRECTOR Beth Rakouskas **DESIGN EDITOR** Marcy Atarod **SENIOR DESIGNER** Garvin Grullón **DESIGNER** Chrystal Smith **GRAPHICS MANAGING EDITOR** Alberto Cuadra **SENIOR SCIENTIFIC ILLUSTRATORS** Chris Bickel, Katharine Sutliff **SCIENTIFIC ILLUSTRATOR** Valerie Altounian **SENIOR ART ASSOCIATES** Holly Bishop, Nathalie Cary, Preston Huey **PHOTOGRAPHY MANAGING EDITOR** William Douthitt **PHOTO EDITORS** Leslie Blizard, Christy Steele

DIRECTOR, GLOBAL COLLABORATION, CUSTOM PUBLICATIONS, ADVERTISING Bill Moran **EDITOR, CUSTOM PUBLISHING** Sean Sanders: 202-326-6430 **ASSISTANT EDITOR, CUSTOM PUBLISHING** Tianna Hicklin: 202-326-6463 **ADVERTISING MARKETING MANAGER** Justin Sawyers: 202-326-7061 science_advertising@aaas.org **ADVERTISING SUPPORT MANAGER** Karen Foote: 202-326-6740 **ADVERTISING PRODUCTION OPERATIONS MANAGER** Deborah Tompkins **SR. PRODUCTION SPECIALIST/GRAPHIC DESIGNER** Amy Hardcastle **SR. TRAFFIC ASSOCIATE** Christine Hall **SALES COORDINATOR** Shirley Young **ASSOCIATE DIRECTOR, COLLABORATION, CUSTOM PUBLICATIONS/CHINA/TAIWAN/KOREA/SINGAPORE** Ruolei Wu: +86-186 0082 9345, rwu@aaas.org **COLLABORATION/CUSTOM PUBLICATIONS/JAPAN** Adarsh Sandhu + 81532-81-5142 asandhu@aaas.org **EAST COAST/E. CANADA** Laurie Faraday: 508-747-9395, FAX 617-507-8189 **WEST COAST/W. CANADA** Lynne Stickrod: 415-931-9782, FAX 415-520-6940 **MIDWEST** Jeffrey Dembski: 847-498-4520 x3005, Steven Loerch: 847-498-4520 x3006 **UK EUROPE/ASIA** Roger Goncalves: TEL/FAX +41 43 243 1358 **JAPAN** Katsuyoshi Fukamizu(Tokyo): +81-3-3219-5777 kfukamizu@aaas.org **CHINA/TAIWAN** Ruolei Wu: +86-186 0082 9345, rwu@aaas.org

WORLDWIDE ASSOCIATE DIRECTOR OF SCIENCE CAREERS Tracy Holmes: +44 (0) 1223 326525, FAX +44 (0) 1223 326532 tholmes@science-int.co.uk **CLASSIFIED** advertise@sciencecareers.org **U.S. SALES** Tina Burks: 202-326-6577, Nancy Toema: 202-326-6578 **EUROPE/ROW SALES** Sarah Lelarge **SALES ASSISTANT** Kelly Grace **JAPAN** Hiroyuki Mashiki(Kyoto): +81-75-823-1109 hmashiki@aaas.org **CHINA/TAIWAN** Ruolei Wu: +86-186 0082 9345 rwu@aaas.org **MARKETING MANAGER** Allison Pritchard **MARKETING ASSOCIATE** Aimee Aponte

AAAS BOARD OF DIRECTORS, CHAIR Geraldine L. Richmond **PRESIDENT** Barbara A. Schaal **PRESIDENT-ELECT** Susan Hockfield **TREASURER** David Evans Shaw **CHIEF EXECUTIVE OFFICER** Rush D. Holt **BOARD** Cynthia M. Beall, May R. Berenbaum, Carlos J. Bustamante, Stephen P.A. Fodor, Claire M. Fraser, Michael S. Gazzaniga, Laura H. Greene, Elizabeth Loftus, Mercedes Pascual

SUBSCRIPTION SERVICES For change of address, missing issues, new orders and renewals, and payment questions: 866-434-AAAS (2227) or 202-326-6417, FAX 202-842-1065. Mailing addresses: AAAS, P.O. Box 96178, Washington, DC 20090-6178 or AAAS Member Services, 1200 New York Avenue, NW, Washington, DC 20005

INSTITUTIONAL SITE LICENSES 202-326-6730 **REPRINTS:** Author Inquiries 800-635-7181 **COMMERCIAL INQUIRIES** 803-359-4578 **PERMISSIONS** 202-326-6765, permissions@aaas.org **AAAS Member Services** 202-326-6417 or http://membercentral.aaas.org/discounts

Science serves as a forum for discussion of important issues related to the advancement of science by publishing material on which a consensus has been reached as well as including the presentation of minority of conflicting points of view. Accordingly, all articles published in *Science*—including editorials, news and comment, and book reviews—are signed and reflect the individual views of the authors and not official points of view adopted by AAAS or the institutions with which the authors are affiliated.

INFORMATION FOR AUTHORS See pages 624 and 625 of the 5 February 2016 issue or access www.sciencemag.org/authors/science-information-authors

SENIOR EDITORIAL BOARD
Gary King, *Harvard University,* **Susan M. Rosenberg,** *Baylor College of Medicine,*
Ali Shilatifard, *Northwestern University Feinberg School of Medicine*

BOARD OF REVIEWING EDITORS (Statistics board members indicated with **(S)**

Adriano Aguzzi, *U. Hospital Zürich*
Takuzo Aida, *U. of Tokyo*
Leslie Aiello, *Wenner-Gren Foundation*
Judith Allen, *U. of Edinburgh*
Sonia Altizer, *U. of Georgia*
Sebastian Amigorena, *Institut Curie*
Kathryn Anderson, *Memorial Sloan-Kettering Cancer Center*
Meinrat O. Andreae, *Max-Planck Inst. Mainz*
Paola Arlotta, *Harvard U.*
Johan Auwerx, *EPFL*
David Awschalom, *U. of Chicago*
Clare Baker, *University of Cambridge*
Jordi Bascompte, *University of Zurich*
Facundo Batista, *London Research Inst.*
Ray H. Baughman, *U. of Texas, Dallas*
David Baum, *U. of Wisconsin*
Carlo Beenakker, *Leiden U.*
Kamran Behnia, *ESPCI-ParisTech*
Yasmine Belkaid, *NIAID, NIH*
Philip Benfey, *Duke U.*
May Berenbaum, *U. of Illinois*
Gabriele Bergers, *U. of California, San Francisco*
Bradley Bernstein, *Massachusettes General Hospital*
Peer Bork, *EMBL*
Bernard Bourdon, *Ecole Normale Supérieure de Lyon*
Chris Bowler, *École Normale Supérieure*
Ian Boyd, *U. of St. Andrews*
Emily Brodsky, *U. of California, Santa Cruz*
Ron Brookmeyer, *U. of California Los Angeles* **(S)**
Christian Büchel, *U. Hamburg-Eppendorf*
Joseph A. Burns, *Cornell U.*
Carter Tribley Butts, *U. of California, Irvine*
Gyorgy Buzsaki, *New York U. School of Medicine*
Blanche Capel, *Duke U.*
Mats Carlsson, *U. of Oslo*
Ib Chorkendorff, *U. of Denmark*
David Clapham, *Children's Hospital Boston*
Joel Cohen, *Rockefeller U., Columbia U.*
James J. Collins, *MIT*
Robert Cook-Deegan, *Duke U.*
Lisa Coussens, *Oregon Health & Science U.*
Alan Cowman, *Walter & Eliza Hall Inst.*
Robert H. Crabtree, *Yale U.*
Roberta Croce, *Vrije Universiteit*
Janet Currie, *Princeton U.*
Jeff L. Dangl, *U. of North Carolina*
Tom Daniel, *U. of Washington*
Frans de Waal, *Emory U.*
Stanislas Dehaene, *Collège de France*
Robert Desimone, *MIT*
Claude Desplan, *New York U.*
Dennis Discher, *U. of Pennsylvania*
Gerald W. Dorn II, *Washington U. School of Medicine*
Jennifer A. Doudna, *U. of California, Berkeley*
Bruce Dunn, *U. of California, Los Angeles*
William Dunphy, *Caltech*
Christopher Dye, *WHO*
Todd Ehlers, *U. of Tuebingen*
David Ehrhardt, *Carnegie Inst. of Washington*
Tim Elston, *U. of North Carolina at Chapel Hill*
Gerhard Ertl, *Fritz-Haber-Institut, Berlin*
Barry Everitt, *U. of Cambridge*
Ernst Fehr, *U. of Zurich*
Anne C. Ferguson-Smith, *U. of Cambridge*
Michael Feuer, *The George Washington U.*
Toren Finkel, *NHLBI, NIH*
Kate Fitzgerald, *U. of Massachusetts*
Peter Fratzl, *Max-Planck Inst.*
Elaine Fuchs, *Rockefeller U.*
Daniel Geschwind, *UCLA*
Karl-Heinz Glassmeier, *TU Braunschweig*
Ramon Gonzalez, *Rice U.*
Julia R. Greer, *Caltech*
Elizabeth Grove, *U. of Chicago*
Nicolas Gruber, *ETH Zurich*
Kip Guy, *St. Jude's Children's Research Hospital*
Taekjip Ha, *U. of Illinois at Urbana-Champaign*
Christian Haass, *Ludwig Maximilians U.*
Michael Hasselmo, *Boston U.*
Martin Heimann, *Max-Planck Inst. Jena*
Yka Helariutta, *U. of Cambridge*
James A. Hendler, *Rensselaer Polytechnic Inst.*
Janet G. Hering, *Swiss Fed. Inst. of Aquatic Science & Technology*
Kai-Uwe Hinrichs, *U. of Bremen*
David Hodell, *U. of Cambridge*
David Holden, *Imperial College*
Lora Hooper, *UT Southwestern Medical Ctr. at Dallas*
Tamas Horvath, *Yale University*
Raymond Huey, *U. of Washington*
Fred Hughson, *Princeton U.*
Auke Ijspeert, *EPFL Lausanne*
Stephen Jackson, *U. of Arizona, USGS*
Steven Jacobsen, *U. of California, Los Angeles*
Stephen Jackson, *U. of Arizona*
Kai Johnsson, *EPFL Lausanne*
Peter Jonas, *Inst. of Science & Technology (IST) Austria*
Matt Kaeberlein, *U. of Washington*
William Kaelin Jr., *Dana-Farber Cancer Inst.*
Daniel Kahne, *Harvard U.*
Daniel Kammen, *U. of California, Berkeley*
Abby Kavner, *U. of California, Los Angeles*
Masashi Kawasaki, *U. of Tokyo*
V. Narry Kim, *Seoul National U.*
Joel Kingsolver, *U. of North Carolina at Chapel Hill*
Robert Kingston, *Harvard Medical School*
Etienne Koechlin, *Ecole Normale Supérieure*
Alexander Kolodkin, *Johns Hopkins U.*
Thomas Langer, *U. of Cologne*
Mitchell A. Lazar, *U. of Pennsylvania*
David Lazer, *Harvard U.*
Thomas Lecuit, *IBDM*
Virginia Lee, *U. of Pennsylvania*
Stanley Lemon, *U. of North Carolina at Chapel Hill*
Ottoline Leyser, *Cambridge U.*
Wendell Lim, *U.C. San Francisco*
Marcia C. Linn, *U. of California, Berkeley*
Jianguo Liu, *Michigan State U.*
Luis Liz-Marzan, *CIC biomaGUNE*
Jonathan Losos, *Harvard U.*
Ke Lu, *Chinese Acad. of Sciences*
Christian Lüscher, *U. of Geneva*
Laura Machesky, *CRUK Beatson Inst. for Cancer Research*
Anne Magurran, *U. of St. Andrews*
Oscar Marin, *CSIC & U. Miguel Hernández*
Charles Marshall, *U. of California, Berkeley*
C. Robertson McClung, *Dartmouth College*
Graham Medley, *U. of Warwick*
Tom Misteli, *NCI*
Yasushi Miyashita, *U. of Tokyo*
Mary Ann Moran, *U. of Georgia*
Richard Morris, *U. of Edinburgh*
Alison Motsinger-Reif, *NC State U.* **(S)**
Thomas Murray, *The Hastings Center*
Daniel Neumark, *U. of California, Berkeley*
Kitty Nijmeijer, *U. of Twente*
Pär Nordlund, *Karolinska Inst.*
Helga Nowotny, *European Research Advisory Board*
Ben Olken, *MIT*
Joe Orenstein, *U. of California Berkeley & Lawrence Berkeley National Lab*
Harry Orr, *U. of Minnesota*
Pilar Ossorio, *U. of Wisconsin*
Andrew Oswald, *U. of Warwick*
Steve Palumbi, *Stanford U.*
Jane Parker, *Max-Planck Inst. of Plant Breeding Research*
Giovanni Parmigiani, *Dana-Farber Cancer Inst.* **(S)**
John H. J. Petrini, *Memorial Sloan-Kettering Cancer Center*
Samuel Pfaff, *Salk Institute for Biological Studies*
Joshua Plotkin, *U. of Pennsylvania*
Albert Polman, *FOM Institute AMOLF*
Philippe Poulin, *CNRS*
Jonathan Pritchard, *Stanford U.*
David Randall, *Colorado State U.*
Felix Rey, *Institut Pasteur*
Trevor Robbins, *U. of Cambridge*
Jim Roberts, *Fred Hutchinson Cancer Research Ctr.*
Barbara A. Romanowicz, *U. of California,Berkeley*
Amy Rosenzweig, *Northwestern University*
Mike Ryan, *U. of Texas, Austin*
Mitinori Saitou, *Kyoto U.*
Shimon Sakaguchi, *Kyoto U.*
Miquel Salmeron, *Lawrence Berkeley National Lab*
Jürgen Sandkühler, *Medical U. of Vienna*
Alexander Schier, *Harvard U.*
Vladimir Shalaev, *Purdue U.*
Robert Siliciano, *Johns Hopkins School of Medicine*
Denis Simon, *Arizona State U.*
Uri Simonsohn, *U. of Pennsylvania*
Alison Smith, *John Innes Centre*
Richard Smith, *U. of North Carolina* **(S)**
John Speakman, *U. of Aberdeen*
Allan C. Spradling, *Carnegie Institution of Washington*
Jonathan Sprent, *Garvan Inst. of Medical Research*
Eric Steig, *U. of Washington*
Paula Stephan, *Georgia State U. and National Bureau of Economic Research*
Molly Stevens, *Imperial College London*
V. S. Subrahmanian, *U. of Maryland*
Ira Tabas, *Columbia U.*
Sarah Teichmann, *Cambridge U.*
John Thomas, *North Carolina State U.*
Shubha Tole, *Tata Institute of Fundamental Research*
Christopher Tyler-Smith, *The Wellcome Trust Sanger Inst.*
Herbert Virgin, *Washington U.*
Bert Vogelstein, *Johns Hopkins U.*
Cynthia Volkert, *U. of Göttingen*
David Wallach, *Weizmann Inst. of Science*
Ian Walmsley, *U. of Oxford*
Jane-Ling Wang, *U. of California, Davis* **(S)**
David A. Wardle, *Swedish U. of Agric. Sciences*
David Waxman, *Fudan U.*
Jonathan Weissman, *U. of California, San Francisco*
Chris Wikle, *U. of Missouri* **(S)**
Ian A. Wilson, *The Scripps Res. Inst.* **(S)**
Timothy D. Wilson, *U. of Virginia*
Rosemary Wyse, *Johns Hopkins U.*
Jan Zaanen, *Leiden U.*
Kenneth Zaret, *U. of Pennsylvania School of Medicine*
Jonathan Zehr, *U. of California, Santa Cruz*
Len Zon, *Children's Hospital Boston*
Maria Zuber, *MIT*

BOOK REVIEW BOARD
David Bloom, *Harvard U.,* **Samuel Bowring,** *MIT,* **Angela Creager,** *Princeton U.,*
Richard Shweder, *U. of Chicago,* **Ed Wasserman,** *DuPont*

EDITORIAL

KIST at 50, beyond the miracle

This month marks the 50th anniversary of the Korea Institute of Science and Technology (KIST). Remarkably, half a century ago, South Korea was one of the poorest countries in the world, recovering from the Korean War and facing serious economic difficulties. Today, it is a member of the G20 major global economies with a market value that ranks 11th in the world. Investment in science and technology as a development strategy is what made South Korea one of the world's fastest-growing economies. Now, as the nation promotes its new Creative Economy plan, KIST moves into its next 50 years, ensuring that science and technology remain the foundation of this new era of innovation.

KIST's establishment in 1966 is widely seen as the birth of Korea's modern science. Fifty years ago, then-president Park Chung-hee recognized the importance of science and technology in the development of a nation and created KIST, the first comprehensive research and development (R&D) institute in Korea. KIST shook up private industry as it developed technologies and transferred them to the industrial sector. Companies began to realize the importance of R&D, and thus began an era of tremendous investment in R&D. The Korean government established 16 R&D spinoff institutes from KIST, and over the past 50 years, government and industry support of science and technology fields has transformed the nation's agriculture-centered economy to a high-tech economy that encompasses the semiconductor, automobile, steel, shipbuilding, electronics, machinery, and petrochemical industries, among others. In 2014, this accounted for 4.29% of the nation's gross domestic product (GDP), and South Korea ranked number one in the world in R&D intensity (R&D expenditure as a percentage of GDP).

The current administration under President Park Geun-hye has been quick to recognize that sustaining the nation's economic growth requires maintaining the competitiveness of Korean companies in an expanding global economy. A reengineering of the government's development strategy produced the Creative Economy initiative, launched in 2013. The new plan leverages South Korea's already strong science and technology capacity to spur innovative technologies and creative businesses as the next economic growth engine. To help facilitate this initiative, KIST is bolstering linkages among industry, academia, and government research institutes, and is providing technical and managerial assistance to startup companies and small and medium-sized enterprises. Although KIST's main focus is on basic and fundamental research, it is actively expanding its responsibilities to revitalize Korea's economy through programs that progress basic research outcomes to a market-ready level.

Armadillo-T, an experimental car made in South Korea

"What South Korea achieved in a half-century is considered nothing short of a miracle."

Importantly, South Korea and KIST continue to help the global community. In 1996, the nation joined the Organization for Economic Cooperation and Development, becoming a strong voice with other governments for improving the economic and social well-being of people around the world. Given that KIST was born out of international development aid, particularly from the United States, the institute strives to serve as a model to help other countries and is currently assisting Vietnam in establishing a research institute, the Vietnam-Korea Institute of Science and Technology.

What South Korea achieved in a half-century is considered nothing short of a miracle. Over the next 50 years, all nations will need to make great advances in meeting the challenges of a growing population, sustainable energy and food resources, health and disease issues, and climate change. KIST hopes not only to serve as a research pioneer and hub for national R&D, but to help South Korea make contributions that will bring a better quality of life to all people.

– Byung Gwon Lee

Byung Gwon Lee is the president of the Korea Institute of Science and Technology, Seoul, Korea. E-mail: bglee@kist.re.kr

10.1126/science.aaf5006

PHOTOS: (INSET) REUTERS/KIM HONG-JI; (TOP) KOREA INSTITUTE OF SCIENCE AND TECHNOLOGY

Downloaded from on February 25, 2016

Published by AAAS

> “Ugh so sick of acting as a gatekeeper and stonewaller and rejector and delayer as an editor for journals. After #ASAPbio, resigning from all”

Neurobiologist Leslie Vosshall (@pollyp1), tweeting last week from the Accelerating Science and Publication in Biology meeting about the future of preprints in the biological sciences.

IN BRIEF

NIH to review all nonhuman primate research in U.S. labs

Macaques used in AIDS research in a U.S. lab.

The National Institutes of Health (NIH) is about to take a closer look at the use of nonhuman primates in all federally funded U.S. research labs. In response to a congressional mandate, the agency will convene a workshop this summer to review the ethical policies and procedures surrounding work on monkeys, baboons, and related animals. The move follows NIH’s decision to end controversial monkey experiments at one of its labs and the termination of its support for invasive research on chimpanzees. In a letter to lawmakers last week, NIH Director Francis Collins emphasized the importance of nonhuman primate research in tackling Ebola, cardiovascular disease, and other afflictions. But he added that “NIH takes animal welfare concerns seriously” and will convene experts in primatology, animal welfare, and ethics this summer “to ensure that NIH has the appropriate policies and procedures in place for conducting research with non-human primates.” The agency tells *Science* that it is still in the early stages of planning the workshop and does not have additional details to share at this time. http://scim.ag/NIHnonhum

AROUND THE WORLD

NASA’s next space telescope

WASHINGTON, D.C. | With NASA’s huge James Webb Space Telescope due for launch in 2018, the agency has announced its next major astrophysics project: another telescope known as the Wide-Field Infrared Survey Telescope (WFIRST). With its wide field of view—100 times that of the Hubble Space Telescope—WFIRST will be able to measure the shapes, positions, and distances of millions of galaxies, so as to better understand the dark matter that holds galaxies together and the dark energy speeding the expansion of the universe. In addition, it will be equipped to directly image planets around other stars. Cost overruns on Webb had delayed WFIRST’s development, but in December 2015, Congress approved a 2016 spending plan that included $90 million for work on WFIRST. NASA’s Program Management Council is now looking to launch the instrument in the mid-2020s. http://scim.ag/_WFIRST

LIGO-India gets green light

NEW DELHI | Less than a week after two U.S.-based detectors made the groundbreaking discovery of gravitational waves (*Science*, 12 February, p. 645), the Indian government has approved a longstanding proposal to build its own Laser Interferometer Gravitational-Wave Observatory (LIGO). On 17 February, the Indian cabinet, chaired by Prime Minister Narendra Modi, gave “in principle” approval to construct a LIGO lab in either Rajasthan or Maharashtra, at a projected cost of $375 million. Adding a third instrument will allow scientists to triangulate and locate the source of observed gravitational waves, says Tarun Souradeep, a spokesperson for the IndIGO Consortium, a group of Indian physicists who have pushed for the project for the last 5 years. The site is planned to be ready by 2022; by then, the consortium will import a $140 million detector—identical to the two U.S. instruments—built by U.S. researchers. “I am delighted with the Indian government’s decision,” says Charles

Downloaded from on February 25, 2016

PHOTO: © DAN LAMONT/CORBIS

Published by AAAS

The Hitomi telescope was launched into orbit last week.

Japan puts x-ray observatory in orbit

The largest and most advanced x-ray astronomy platform put in orbit since 1999 was successfully lifted into space 17 February by Japan's H-IIA rocket. ASTRO-H carries four x-ray telescopes to study soft and hard x-rays and gamma rays; the instruments are expected to reveal details about gases trapped in galaxy clusters and wafting through supernova remnants, as well as the turbulent streams of material spiraling away from black holes. A joint project of the Japan Aerospace Exploration Agency's Institute of Space and Astronautical Science and NASA, the ASTRO-H team brought together 240 scientists from 60 institutions in Japan, North America, and Europe. As is customary after Japanese launches, the spacecraft was given a new name, Hitomi (which means "eye" in Japanese), to replace the ASTRO-H mission designation. Mission managers will verify the functioning of the instruments over the next several months. Full-fledged observations will begin before the end of the year.

Elachi, director of the Jet Propulsion Laboratory in Pasadena, California. "This is a great step forward in humanity's quest to understand how our universe works and evolved, and how we all came about."

Fungal toxins can stunt growth

LYON, FRANCE | Children in Africa and parts of Asia are falling victim to an "invisible" epidemic—fungal toxins in food that can stunt their growth and delay their development, according to a new report from the Lyon-based International Agency for Research on Cancer and funded in part by the Bill & Melinda Gates Foundation. The two main toxins—aflatoxin and fumonisin—are present in dangerously high levels in groundnuts, cassava, and corn, which make up the bulk of children's diets from Benin to Kenya. In the United States and Europe, fields and food are heavily treated for the toxins; that management costs U.S. food producers between $500 million and $1.5 billion each year. The new report brings together six studies that show that children with high levels of toxin biomarkers in their blood are shorter and weigh less than other children their age. They also grow at a slower pace than their peers. **http://scim.ag/fungaltoxins**

FINDINGS

Bees brighten orchid's hues

The Eurasian orchid *Anacamptis morio* comes in a wide variety of colors, from deep purple to white. Like some other flowers, it has markings on its lower petal that guide insects in for a landing. But *A. morio* offers no sweet rewards: Its color and marks are a trick designed to resemble those of nectar-laden species. Researchers thought this orchid's array of colors made it harder for pollinators to recognize it as a deceiver. To test this, plant ecologists Nina Sletvold and Jon Ågren from Uppsala University in Sweden and their team marked more than 300 individual plants in the field and hand-pollinated half of them. By comparing the production of hand-pollinated with naturally pollinated fruit from each orchid color, the researchers confirmed that insect preferences shape how the flowers look, they reported online in *Evolution* last week. The new data also suggest the color variety may be the orchid's way of diversifying so that at least some of its flowers resemble the most attractive flowers in an area.

Pollinators influence petal color in the green-winged orchid, *Anacamptis morio*.

Seas rising fastest in 2000 years

Global sea levels are exquisitely sensitive to changes in temperature and greenhouse gas levels, reports a set of four new studies published online this week in the *Proceedings of the National Academy of Sciences*. The different authors used a variety of techniques to study sea level changes over various timescales, including historical tide gauge records, foraminifera

PHOTOS: (TOP TO BOTTOM) KYODO/REUTERS/NEWSCOM; © VERONICA CARTER/ALAMY STOCK PHOTO

Published by AAAS

species in marsh sediment cores as proxies for salinity over the past 3000 years, and a 1.1-kilometer-long core pulled from an Antarctic seabed that sheds light on the ebb and flow of the continent's ice sheets 14 million to 20 million years ago. "The big takeaway is that the modern rate of sea level rise in the 20th century is faster than anything we've seen in the previous two millennia," says Benjamin Horton, a Rutgers University, New Brunswick, in New Jersey geologist who helped direct one of the studies. "This isn't a model. This is data." http://scim.ag/SLriserate

NEWSMAKERS

Three Q's

Optical physicist **Massimo Inguscio**, previously head of Italy's National Institute of Metrological Research, last week became president of the country's largest research organization, the National Research Council (CNR). *Science* spoke with him about CNR's funding woes and the need for fresh talent. http://scim.ag/Inguscio

Q: Italy spends 1.25% of its gross domestic product on research. Does CNR struggle for funding?
A: Almost all of CNR's budget is used to pay salaries and basic expenses such as electricity, which means there are virtually zero funds for research. Twenty years ago there was money to upgrade existing facilities or to buy new equipment. But now we can't do that.

Q: The 2016 budget contains €100 million for 850 new university researchers. Is that a good sign?
A: It is a welcome, if small, reversal compared to the general trend of decreasing finances. But ... in Italy there is no multiyear strategy. Hirings can be blocked for many years and then unfrozen suddenly. That leads to people being recruited because they are on a temporary contract, not necessarily because they are the best person for the job. The presidents of research institutions are asking the government to start up a process of tenure track, as happens in other countries.

Q: Many Italian scientists work abroad. Is that a problem?
A: It is normal that people go overseas to work. The problem is that researchers don't come to Italy. ... Someone comes not only because there is a place and a wage, but also because they can hire postdocs and get projects up and running. I hope that the government can restart Italian research on the basis of excellence and meritocracy.

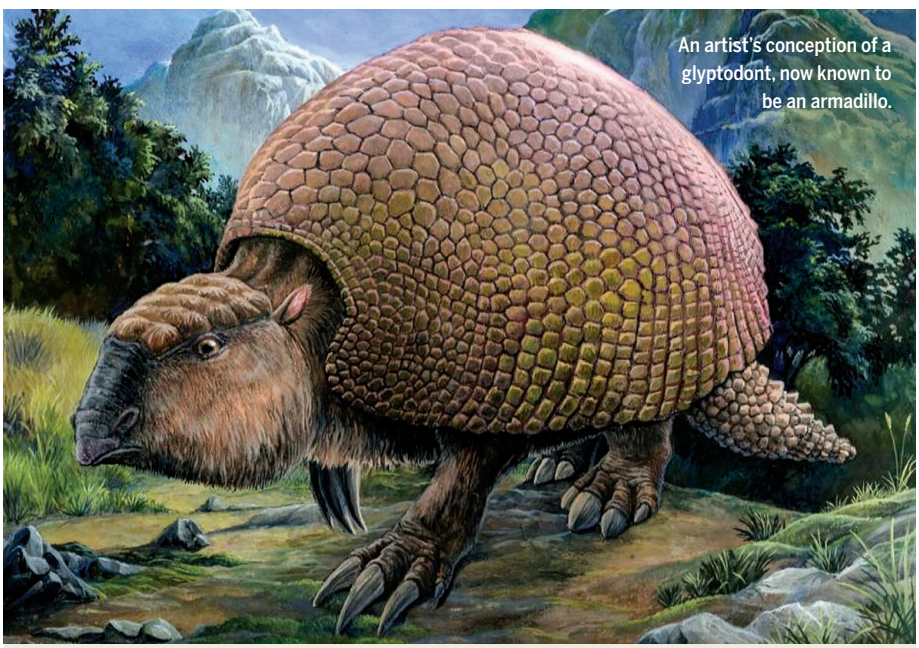

An artist's conception of a glyptodont, now known to be an armadillo.

An armadillo the size of a (Volkswagen) Beetle

During his travels in South America between 1832 and 1833, Charles Darwin collected fossils from a giant, heavily armored mammal later called a glyptodont. Glyptodonts were long suspected to be cousins to modern-day armadillos—but new genetic analyses of a 14,000-year-old fossil from an Argentine museum reveal that the ancient herbivores actually *were* armadillos. The fossil, a shell fragment from a large individual of the genus *Doedicurus*, yielded enough genetic material to completely reconstruct DNA from the creature's mitochondria. When compared to previous genetic analyses from living armadillos, *Doedicurus* landed squarely within the armadillo family tree, the researchers reported online this week in *Current Biology*. The team's analysis suggests that glyptodonts evolved about 35 million years ago. (They went extinct at the end of the last ice age, about 12,000 years ago.) Unlike living armadillos, which can roll into a ball to protect themselves, the largest glyptodonts had fused carapaces and likely depended on their shells and clubbed tails, as well as their immense size, for self-defense.

BY THE NUMBERS

$750 million

Amount that semiconductor-maker Marvell Technology Group will pay to Carnegie Mellon University to end a long-running patent fight, the university announced 17 February.

35

Years left before the depletion of China's phosphate rock reserves at current rates of production. Phosphorus cycling intensified in China in the last 60 years to fertilize crops for food and animal feed (*Proceedings of the National Academy of Sciences*).

29%

Fraction of clinical trials led by researchers at U.S. academic centers that were published within 2 years of study completion (*The BMJ*).

ILLUSTRATION: PAVEL RIHA/WIKIMEDIA COMMONS

Published by AAAS

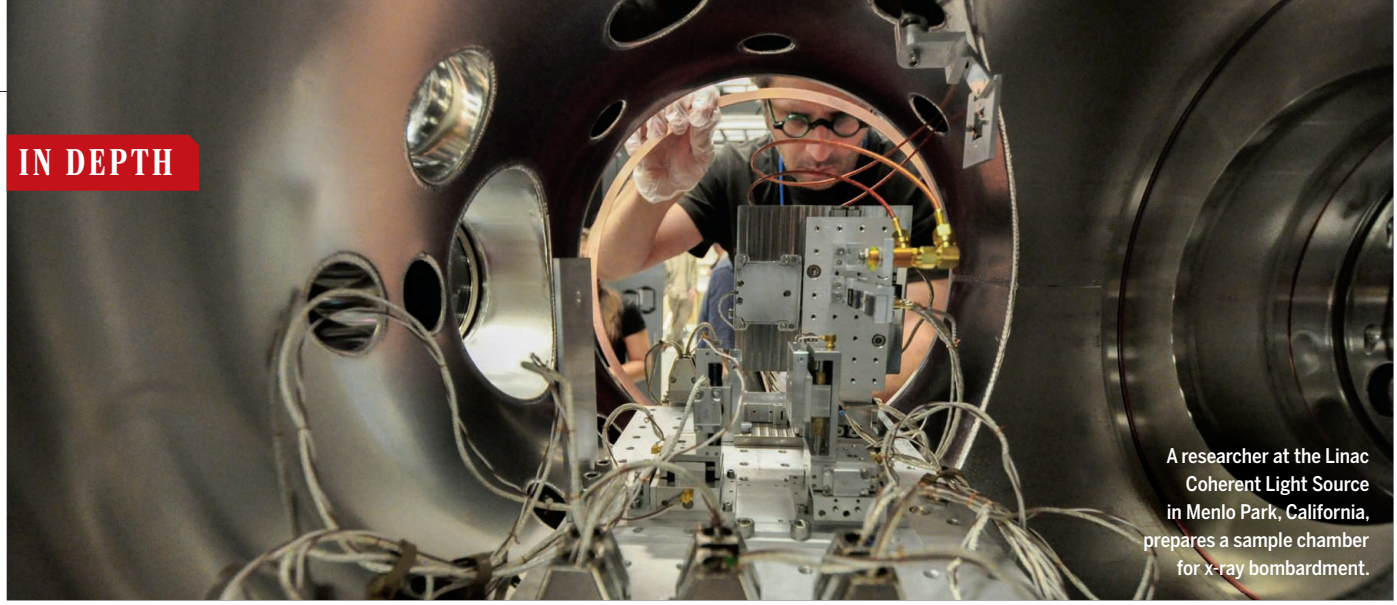

A researcher at the Linac Coherent Light Source in Menlo Park, California, prepares a sample chamber for x-ray bombardment.

PHOTO: DILING ZHU/SLAC

SCIENTIFIC FACILITIES

Flagship accelerators bid for better beams

DOE considers wish list of upgrades to x-ray and neutron sources

By **Robert F. Service**

A scientific advisory panel for the United States Department of Energy (DOE) has begun weighing possible upgrades to four of the nation's top sources of high-energy x-rays and neutron beams. For years, the giant machines—two x-ray synchrotrons, an x-ray free electron laser (FEL), and a neutron accelerator—have given thousands of scientists unparalleled close-up views of the molecules that make up materials and organisms. Recently, however, researchers say the facilities have been losing ground to counterparts in Europe, Asia, and South America.

Now, the United States hopes to turn things around. The advisory panel, known as the Basic Energy Sciences Advisory Committee (BESAC), is expected to issue its priority list in June. If DOE and Congress act on its advice, as they have regularly done in the past, U.S. facilities could regain global preeminence, promoting U.S. leadership in fields including chemistry, alternative energy, materials science, and structural biology for decades. But improving all four facilities within the constraints of a tight budget will require spreading the projects out over time.

Staying ahead of other countries vying to build powerful tools for understanding molecules and materials is growing increasingly difficult. "If you look at facilities worldwide, the U.S. is slipping behind," says DOE's Office of Science director, Cherry Murray, in Washington, D.C. When one of the four U.S. machines, a massive x-ray laser called the Linac Coherent Light Source (LCLS) in Menlo Park, California, was finished in 2009, it relied on technology so cutting-edge that some doubted it would even work. But the LCLS succeeded in turning out ultrashort bursts of coherent x-rays—an advance that has already led to groundbreaking scientific developments in glimpsing the formation of chemical bonds and tracking the movements of electrons in complex materials. That success encouraged the development of more powerful FELs in Europe, Japan, and elsewhere.

DOE is now upgrading the LCLS. LCLS II will produce more x-ray pulses, enabling it to track faster microscopic events. But already x-ray experts are proposing further improvements, known as LCLS II-HE (for "high energy"), to double the power of its x-ray beam.

The two synchrotrons on the list face similar competition. The Advanced Photon Source (APS) in Lemont, Illinois, and the Advanced Light Source (ALS) in Berkeley, California, accelerate electrons in "storage rings" hundreds of meters wide and then steer them through powerful magnets that cause them to shed beams of x-rays that are less intense but have longer pulses than beams from FELs. The APS specializes in producing energetic "hard" x-rays, which are useful for nailing down the positions of individual atoms in samples; the ALS generates less energetic "soft" x-rays, which are better at identifying chemical elements.

Now, Sweden is commissioning its new MAX IV synchrotron, the first to use a novel technology known as multi-bend achromats (MBAs). These devices narrow the synchrotron's x-ray beam, creating a brighter, more powerful, and more coherent x-ray probe to shine on samples. The European Synchrotron Radiation Facility in Grenoble, France, is upgrading its synchrotron with the same technology, which is expected to come online in 2020.

Both the APS and the ALS have proposed MBA upgrades to their machines. If the pro-

Brighter prospects for beamlines

An advisory panel is weighing upgrades to four major U.S. scientific user facilities.

FACILITY	TYPE	COST (EST.)	NEW CAPABILITIES
Linac Coherent Light Source	X-ray FEL	$272 million	Doubles x-ray energy
Advanced Photon Source	Hard x-ray synchrotron	$734 million	Increases brightness 100x to 1000x
Advanced Light Source	Soft x-ray synchrotron	$300 million	Increases brightness 1000x
Spallation Neutron Source	Neutron accelerator		
-Proton power upgrade		$165 million	Doubles beam power
-Second target station		$1.3 billion	Adds new target station

Downloaded from on February 25, 2016

Published by AAAS

posals go forward, officials at both facilities say, the two synchrotrons will again become the brightest x-ray sources at their particular energies—and might well hold the record forever. "It's getting close to the ultimate limit in ring technology," says ALS Director Roger Falcone.

As for neutrons, these chargeless particles are ideal for investigating deep within materials. They also have a property called spin, which makes them good for probing magnetic materials, in which spin plays a key role. Officials at the Spallation Neutron Source (SNS), an accelerator at Oak Ridge National Laboratory in Tennessee, are proposing two upgrades to keep up with the European Spallation Source and other new neutron facilities. The first would double the power of the SNS neutron beam and increase its neutron flux. The second would add a new target station and eight new experimental beamlines. A 2013 BESAC review found that the second upgrade would "present scientific and engineering challenges," but Oak Ridge Director Thom Mason says those concerns have been addressed. "It was a painful process, but we got to the right point," he says.

All of the proposed upgrades would beef up existing equipment without requiring major new construction. Nevertheless, they are estimated to cost $2.8 billion (see table, p. 899). Over the past 17 years, DOE's budget for constructing new scientific user facilities has hovered around $200 million a year. And Murray and others warn that spending much more than that on the upgrades would eat into funds needed to operate the facilities and support research at the sites, which collectively serve roughly 10,000 scientists a year. As a result, Murray says, DOE must prioritize the upgrades and space them out over what's likely to be a 15-year span. "This is very difficult. But it's incredibly important," Murray told BESAC members.

In making those choices, BESAC will consider whether the fixes really would restore each machine to a global leadership position in its field. "What you don't want to do is build something that when you are done is not the best in the world anymore," says John Hemminger, BESAC's chair and a chemist at the University of California, Irvine.

No one knows exactly how BESAC members will vote to prioritize the proposed upgrades, but researchers say the APS upgrade—which DOE has already spent $100 million studying in detail for 5 years—could well top the list. Wayne Hendrickson, an x-ray crystallographer at Columbia University, hopes they will all go forward. With the upgrades "the U.S. will be in a very strong position," Hendrickson says. "But it won't be if it doesn't keep up." ■

DATA CHECK

BEHIND THE NUMBERS

For innovation, no magic in 3% rule

By **Jeffrey Mervis**

Science policy wonks often use the ratio of research spending to overall economic activity to judge whether a country is investing enough in innovation. For decades, 3% has been the magic number, and Israel and South Korea are seen as technological juggernauts because their investment ratio tops 4%.

But two new reports question the 3% target. (The United States stands at roughly 2.8%.) One, from the latest *Science & Engineering Indicators* issued by the National Science Foundation (NSF) in Arlington, Virginia, warns that no single number can capture the key variables in a country's research portfolio. The balance between public and private R&D spending, between military and civilian research, and between basic and applied science is also important, and a government has limited control over the size of its gross domestic product. So "when a government targets a level, achieving it is almost a matter of luck," explains NSF's Beethika Khan, who oversees the biennial report.

46 billion

Additional dollars needed to increase U.S. research intensity from 2.73% to 3% in 2013. The United States spent about $457 billion on research that year within a gross domestic product of $16.75 trillion.

The second salvo comes from the Information Technology and Innovation Foundation, a Washington, D.C., think tank. Research intensity is only a small component of a larger innovation ecosystem shaped by a nation's tax, intellectual property, human capital, and trade policies, it points out. With that in mind, the group scored countries on how they both help and hinder innovation and gives top marks to Finland, Sweden, and the United Kingdom (the last with a R&D intensity ratio of only 1.6%). The United States is ranked 10th.

The 3% target dates back to the 1930s, according to the late Harvey Brooks, a science policy guru and Harvard University physics professor. In a 1995 essay on the evolution of U.S. science policy, Brooks calls the number a "shibboleth [for] technology and competitiveness arguments that persists to this day."

The ratio's endurance comes from its being "far enough away to be a useful aspirational goal, but reachable with a sustained effort," posits Martin Grueber, an Ohio-based economist who studies global research spending. Albert Teich, a veteran science policy analyst at George Washington University in Washington, D.C., cites national pride as another reason. Weeks after taking office, for example, President Barack Obama exhorted members of the U.S. National Academy of Sciences to help him lift the country above 3%, "an amount that exceeds the level achieved at the height of the Space Race."

"The idea was that if we could do it in 1964 [when it stood at 2.88%], we should be able to do it again," Teich says. "But that ignores the fact that the peak was caused by the Apollo project."

There's no evidence that a 3% investment triggers a high level of innovation, or results in a sustained economic payoff. And it would be a heavy lift for most countries. Based on figures for 2013, for example, the United States would have needed to perform an additional $46 billion worth of research that year to reach the 3% target.

Leaving aside whether 3% is attainable, the NSF analysts who work on *Indicators* believe the ratio does have some value. "It's a useful measure of the level of R&D effort by a country," says NSF's Mark Boroush. It's also handy, Khan adds: "If I gave you 50 numbers, it would get very complicated."

Simplicity may indeed be the ratio's biggest virtue. Obama used it in 2009 as shorthand for his administration's commitment to research spending. But the figure was nowhere to be found in this month's budget request to Congress, which included a 4% boost in federal research spending, about one-third of the country's total R&D investment.

That silence may reflect the harsh political realities of a tight budget and a struggling economy. But count presidential science adviser John Holdren among those who believe that 3% should remain a policy goal for the nation.

"It's a plausible number, in the sense that we were there once before," he told an audience at this month's annual meeting of AAAS (publisher of *Science*) in Washington, D.C. "If it were up to me, I'd say 4%." ■

DATA: BASED ON DATA FROM U.S. OFFICE OF MANAGEMENT AND BUDGET

Published by AAAS

When researchers split open the log, they found tiny tunnels full of shipworms.

PHOTOS: GEIR JOHNSON

MARINE RESEARCH

Arctic shipworm discovery alarms archaeologists

Sunken log full of tunneling mollusks poses mystery

By **Eli Kintisch**, *aboard the* RV Helmer Hansson *off Svalbard, Norway*

Marine scientists made a surprise catch last month while trawling for sea creatures in the icy depths of Rijpfjorden, a remote bay in this Arctic archipelago: a log the size of a battering ram. Steel chains hauled the tree trunk up from the sea floor 250 meters below, startling crew and scientists alike. "In 15 years of coming here I've never seen such a big piece of wood from a bottom trawl," said marine biologist Jørgen Berge of the University of Tromsø (UT) in Norway, the cruise leader. Then, an even bigger surprise: The 7-meter log was infested with living shipworms, white and gooey.

The researchers were astonished because shipworms—mollusks adapted to tunnel into and eat wood—had never been documented so far north, just 1100 kilometers from the North Pole, and at such a depth, where the temperature was −1.8°C. Were the borers a southerly species that had moved north with warming seas, or a previously undescribed Arctic native? Either way, "this is a fantastic discovery, something we never would have dreamed of," Berge said.

For another team member, marine archaeologist Øyvind Ødegård of the Norwegian University of Science and Technology, Trondheim, the sight of the 6-centimeter-long creatures was more akin to a nightmare. Historical records suggest more than 1000 shipwrecks dot the coasts around Svalbard, harboring centuries of secrets. Ødegård expected them to be safe from borers. "I believed because of the low temperatures we wouldn't find shipworms," he said. Now, he worries that they could devour the wrecks before scientists find them. Arctic shipworms would be "a disaster" for archaeologists, Berge predicts.

Mariners have cursed species in the genus *Teredo* since wooden ships first set sail. Individuals grow to a meter long, riddling hulls, piers, and other wood structures with undulating tunnels. Shipworms devoured three of Christopher Columbus's ships in 1503, during his fourth voyage to the Americas, marooning the crews. Today, the mollusks cause an estimated $1 billion in damages annually, and have consumed wrecks from the tropics to southern Sweden.

As the oceans have warmed in recent decades, scientists have noticed the borers moving to higher latitudes. A few years ago, they infested a wooden dock at Longyearbyen, Svalbard's biggest town, says UT chemist Bjørn Altermark. To gauge shipworm abundance, in 2014 he placed a sample of spruce on a mooring near shore; a year later it had been attacked by a single borer. Researchers speculated that Atlantic currents might have swept shipworm larvae up from the south, or ships discharging ballast water might have released them.

The burrowing mollusk's heads resemble drillbits.

Intrigued, Ødegård, the archaeologist, ran an experiment to determine their range. Last year, he and Berge placed oak planks in a nearby fjord that also receives Atlantic water, as well as in the distant Rijpfjorden, which is fed by the colder Arctic Ocean to the north. The Rijpfjorden samples were "meant to be a control," Ødegård recalls. He didn't expect to see shipworms in the frigid bay, and hadn't yet retrieved the planks when the log surfaced. "Astonishing," he says.

Scientists are now debating how the Rijpfjord mollusks—not yet definitively identified—could thrive. Studies suggest that the most common shipworm species, *T. navalis*, cannot reproduce at temperatures below 10°C. So one scenario is that the log became infested in warmer waters to the south or east of Svalbard, then recently drifted into the fjord and sank.

But several factors hint at a second possibility: that researchers have discovered a new species or variant able to thrive near the freezing point of saltwater. Ample black sediments inside the log, as well as stringy marine organisms growing on its side, suggest it may have been on the sea floor for a year or more. And when researchers sliced open the wood, they found worms in many stages of development—including young "fresh worms," as Berge calls them—which suggested the community had been around a while. (Svalbard is treeless, but there is plenty of driftwood for shipworms to infest.)

"I'm depressed either way," Ødegård says. He takes some solace, however, from what he saw at a wreck that the *Helmer Hansson* visited just a few days after the log's discovery. The wooden whaler *Figaro* sank near Longyearbyen in 1908. Despite more than a century in the sea, however, digital pictures showed just minor traces of shipworm damage. Still, Ødegård worries that the hulk "is not going to do very well" over the next century if shipworms become more common in the Arctic.

More clues to the origins of the Rijpfjorden shipworms are expected soon. On the last day of the cruise, a researcher used a chainsaw to cut slices from the log. They've been distributed to scientists, including some who are using genetic markers to figure out whether the mollusks are something new to science—or just a familiar face in an unusual place. ■

Downloaded from on February 25, 2016

Published by AAAS

SCIENTIFIC PUBLISHING

Fight over author pseudonyms could flare again

Editor balks at authors using screen names from RNA folding game

By **John Bohannon**

When he heard last week that the *Journal of Molecular Biology* (*JMB*) was postponing publication of a paper he had co-authored because of "ethical" concerns, Rhiju Das was shocked. But then the biophysicist at Stanford University in Palo Alto, California, learned the reason, and he just scratched his head. A *JMB* editor was concerned about some of the co-authors' names. Rather than using their real-world identities, they had given only the screen handles under which they had done the research within *Eterna*, a massive online game that crowdsources RNA folding problems. Listing their screen handles "just seemed intuitive to me," says Das, the co–principal investigator on the *Eterna* project.

The formal scientific authors say they were willing to try another journal, but the three pseudonymous players relented, agreeing to give their full names, and the paper was posted online just hours later than planned. The episode, apparently unprecedented in scientific publishing, has raised questions about the nature of authorship. And given the growth in citizen science efforts, some predict more such standoffs before long—with no guarantee that pseudonymous authors will back down the next time. "In the area of citizen science, there will be many difficult issues of status, ethics, and rewards for good work that we have not yet confronted, let alone solved," says sociologist William Bainbridge. (He co-directs the Cyber-Human Systems program at the National Science Foundation in Arlington, Virginia, but notes that view is personal.)

The paper at issue described a fairly typical study of the "designability" of RNA. The genetic molecule folds itself up into different shapes depending on its sequence. Predicting the stable structure a given sequence forms is hard enough, but the opposite—knowing a desired structure and designing a sequence that will fold into it—is even harder. Such design finesse may be key to realizing custom RNA pharmaceuticals.

Das and his collaborator, Adrien Treuille, a biophysicist at Carnegie Mellon University in Pittsburgh, Pennsylvania, have been tackling RNA folding with the help of a massive community of nonscientists recruited through *Eterna*, which they helped create in 2009. Besides allowing tens of thousands of players to fold RNA on their computer screens, Das and Treuille have hooked up the players' virtual work to an automated lab that tests the players' folding predictions by synthesizing given sequences and seeing what 3D structures the RNA strands actually form. The current paper distills insights from the game and the real-world testing into a set of constraints that make certain RNA structures more or less difficult to achieve. "This paper is a significant contribution," says biophysicist Jane Richardson of Duke University in Durham, North Carolina. "The new design principles seem very understandable."

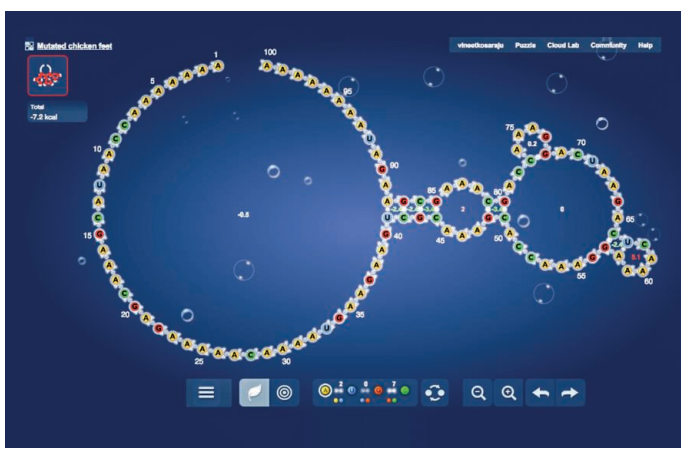

Players of the RNA folding game *Eterna* often don't use their real names.

Several of the leading *Eterna* players conceived the paper, and most of the data came from their work. Whereas earlier papers based on *Eterna* simply credited the game's entire community, this one included individual players as authors. How they should be credited was hashed out in advance on the game's discussion forum. "Many of them felt strongly that real-world names not be required," Treuille says.

But *JMB* editor Peter Wright, a biophysicist at the Scripps Research Institute in San Diego, California, put the paper on hold at the last minute—after an embargoed press release went out—while he consulted with his publisher, Elsevier. "A generally accepted criterion for authorship is that authors must take responsibility for the integrity of the paper," he says. "In my view, identification of an author only by a screen name, which can be changed at an instant, is inappropriate, since that person could not be contacted if issues of accountability arose."

Elsevier doesn't have a blanket pseudonym policy. "Not to say that there won't be exceptions," but it's "rather obvious" that disclosing an author's real-world identity is important, says an Elsevier spokesperson. "I guess it's stretching [journal] boundaries a bit," says player–co-author jandersonlee, also known as Jeffrey Anderson-Lee, a computer systems manager at the University of California (UC), Berkeley. "It's really a bit amusing."

But some observers are less amused. "I see no reason why our 'real' names have to follow us around like shadows," says Bonnie Nardi, an anthropologist at UC Irvine not involved with the study. She notes that pseudonyms may not be permissible in all scholarly contexts, but allowing the gamer-authors to use their online identity is "certainly appropriate in this case." And at least one researcher identification system, ORCID, says it would allow someone using a pseudonym to register.

Others share Wright's position. Marcia McNutt, editor-in-chief of the *Science* journals, notes that pseudonyms prevent the community from recognizing conflicts of interests that authors may have failed to disclose, innocently or otherwise.

"Science is about transparency and replication and accountability. Using a pseudonym flies in the face of that," adds Dmitri Williams, a psychologist at the University of Southern California in Los Angeles. "The only time I think it would be appropriate is if publishing good science were to put the author in some danger," for example if he or she risked persecution. "You want to own the data? Own your identity. Otherwise, you're not an author."

One of the *JMB* article's other player coauthors, matt747—who goes by Mathew Zada in his small south Australian town—might beg to differ. He preferred having his game name on the paper for the sake of privacy. But Zada didn't make a fuss at *JMB*'s demand, he says, because "I'm here for the science." ■

IMAGE: V. KOSARA-JU/*ETERNA*

Downloaded from on February 25, 2016

Published by AAAS

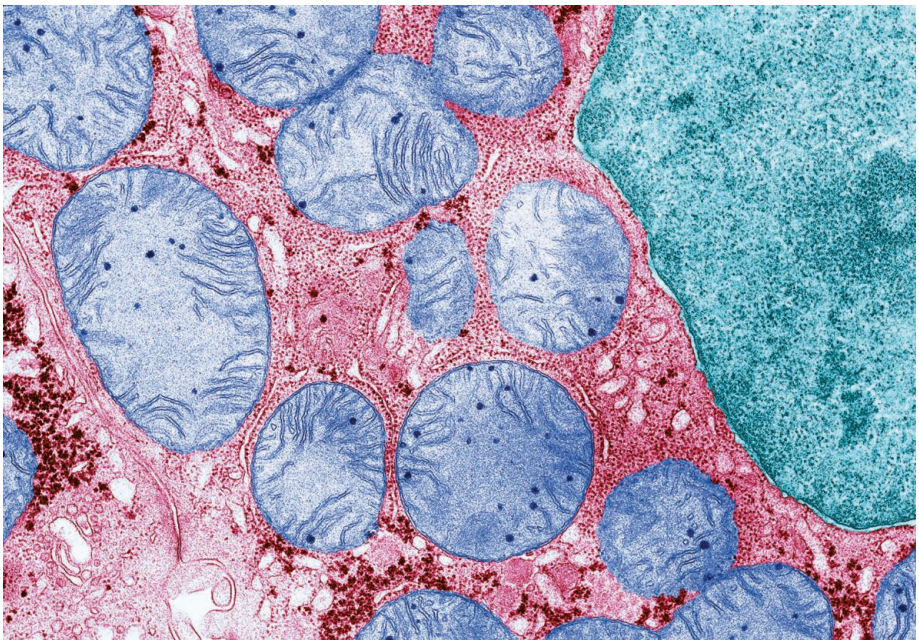

PHOTO: KEITH R. PORTER/SCIENCE SOURCE

Mitochondria—the blue structures in this bat liver cell—evolved from free-living organisms with their own DNA.

EVOLUTION

Why do cells' power plants hang on to their own genomes?

Study finds common features in the genes retained since mitochondria evolved from symbiotic microbes

By **Laurel Hamers**

It's a curious gesture of independence. More than a billion years after once-independent single-celled organisms were swallowed by larger cells to form mitochondria, these organelles—the powerhouses of the cell—still hang on to tiny genomes of their own. A new study suggests why.

Over the years, the mitochondrial genome has shrunk, with many genes migrating to the cell nucleus. The nucleus now harbors the vast majority of the cell's genetic material—even genes that help the mitochondria function. In humans, for instance, the mitochondrial genome contains just 37 genes, compared with the nucleus's 20,000-plus. But that makes it all the more puzzling that mitochondria have retained any genes at all, especially considering that mutations in some of those genes can cause rare but crippling diseases that gradually destroy patients' brains, livers, hearts, and other key organs.

Scientists have tossed around some ideas, but there haven't been hard data to favor one over another. So Iain Johnston, a biologist at the University of Birmingham in the United Kingdom, and biologist Ben Williams of the Whitehead Institute for Biomedical Research in Cambridge, Massachusetts, took a new approach: They modeled the problem mathematically, analyzing more than 2000 different mitochondrial genomes from animals, plants, fungi, and protists (organisms like amoebae). They examined the different combinations of mitochondrial genes present in each species. Then, they created an algorithm that calculated the probabilities that different genes and combinations of genes were lost at particular points along each genome's evolutionary path.

"That's one of the innovative aspects of this work, that it uses modeling which isn't normally included in these sorts of studies," says Keith Adams, a biologist at the University of British Columbia, Vancouver, in Canada, who was not involved in the research. And it revealed some common features in the genes that mitochondria have retained.

Mitochondria make energy through a series of chemical reactions that pass electrons along a membrane. Key to this process is a series of protein complexes—large protein globs embedded in the internal membrane of each mitochondrion. The team found that a gene was more likely to have persisted in the mitochondria if it codes for a protein that is central to one of these complexes. Genes responsible for more peripheral energy-producing functions, meanwhile, were more likely to be outsourced to the nucleus, the group reported last week in *Cell Systems*.

Johnston speculates that having individual mitochondria make their own protein complexes "gives the cell a way to individually control mitochondria." That local control means the cell can more quickly and efficiently regulate energy production moment-to-moment in individual mitochondria, instead of having to make sweeping changes to all of its hundreds or thousands of mitochondria. An out-of-whack mitochondrion can be fixed individually rather than through a blanket, cell-wide response that might then throw something else off balance.

It's like responding to a fire, says John Allen, a biologist at University College London who was not involved in the study. "If a single room in a large building goes up in flames, you don't phone the building manager to ask permission to put it out. You grab a fire extinguisher and aim."

"I think that's a very fundamental feedback mechanism," Allen says. In his own research, he's found evidence suggesting that producing certain mitochondrial proteins right where they're needed helps the cell more precisely regulate individual mitochondria.

Johnston and Williams's model points out other factors that might have shaped which genes stayed in the mitochondria. For instance, mitochondrial proteins that are hydrophobic, or water-repelling, are more likely to be made there than elsewhere in the cell, where they might get stuck during transit through the cell's membranes.

The chemical makeup of the genes themselves can also influence how likely they are to stick around. Genes whose sequence of nucleotides makes them better suited chemically to withstanding the harsh conditions inside the mitochondria instead of being broken down appear more likely to have persisted.

All of which suggests mitochondrial genes aren't just evolutionary oddities. If Johnston and Williams are right, they are survivors, left after mitochondria offloaded every bit of genetic baggage they could. ■

Laurel Hamers is a science journalist based in Santa Cruz, California.

Downloaded from on February 25, 2016

Published by AAAS

FEATURES

POWER PLAY ON THE NILE

Ethiopia stunned neighbors with a colossal dam on the Blue Nile. Could it spread prosperity, not turmoil?

By **Erik Stokstad**

Downloaded from on February 25, 2016

Planned in secrecy, the Grand Ethiopian Renaissance Dam is a massive construction project.

PHOTOS: © ZACHARIAS ABUBEKER/AFP/GETTY IMAGES

Five years ago, as protesters thronged Cairo's Tahrir Square and the Egyptian government teetered, another revolution with high stakes for the region's future ignited far to the south. On 3 February 2011, Ethiopian Prime Minister Meles Zenawi announced that his country would build a massive dam on the Blue Nile, the main tributary of the Nile, the world's longest river. "We not only have a plan, but we also have the capacity to assert our rights," he said that April at the groundbreaking ceremony.

For Egyptians, who view the Nile as their birthright, Zenawi's declaration was an extreme provocation. Egypt depends on the Nile for drinking water and agriculture, and has long claimed rights to 55 billion m^3 of Nile water per year, much more than any other country. Now, a rival state was taking control of the 60% of Nile water that originates from Ethiopia's Blue Nile. The bold move "shocked everyone," says Paul Block, a civil engineer at the University of Wisconsin, Madison, who has studied water issues in the Nile Basin since 2003.

Five years later, the Grand Ethiopian Re-

Published by AAAS

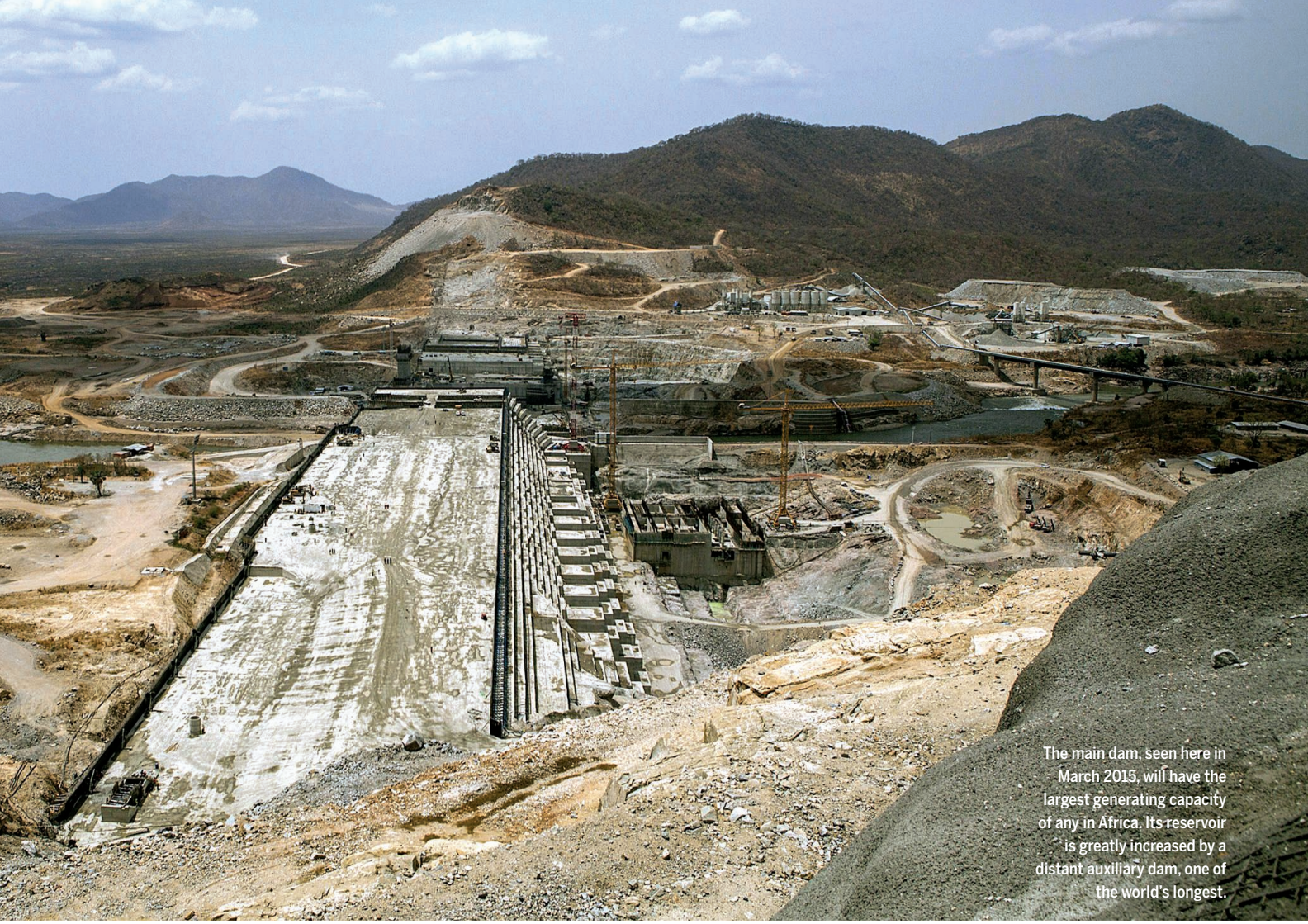

The main dam, seen here in March 2015, will have the largest generating capacity of any in Africa. Its reservoir is greatly increased by a distant auxiliary dam, one of the world's longest.

naissance Dam (GERD) appears to be a fait accompli. Slated for completion next year, GERD will have the greatest hydroelectric capacity of any dam in Africa. The blueprints call for a main dam 175 meters tall and 1800 meters long. Architects vastly enlarged its reservoir with a secondary "saddle" dam—one of the longest ever built—that spans a low spot. When filled completely, the valley will become Ethiopia's largest lake and hold 74 billion m^3 of water, or nearly the annual average flow into Egypt. Construction is proceeding at a breakneck pace.

Supporters say the dam will be a boon for Ethiopia, one of the least developed countries in the world. At peak capacity it will generate 6000 MW of electricity, and even its regular output of 2000 MW could supply 65% of Ethiopia's demand, although some will be sold to Sudan. The dam will also benefit Sudan, the next country downstream, by regulating torrential summer flows and ensuring water supply during the winter dry season. In addition, GERD will trap silt that would otherwise accumulate in downstream reservoirs, including the enormous Lake Nasser behind Egypt's Aswan High Dam, and could reduce water losses from evaporation. In the long term—if all goes well—it could lead to regional cooperation and economic growth in all three countries. "There is a potential triple win," says Pieter van der Zaag, a water resources expert at Delft University of Technology and the United Nations Educational, Scientific and Cultural Organization–IHE Institute for Water Education in the Netherlands.

But the potential for regional benefits has not lessened Egypt's opposition. An immediate concern is that Egypt could face a water shortfall if GERD's reservoir is filled during years of low rainfall, threatening power generation at Aswan and the livelihoods of Egyptian farmers.

The dam has galvanized scientists in Nile countries, particularly in Egypt and Ethiopia, where outspoken academics have rallied to attack or defend the project. Partisan tempers flared when an expert report, leaked in 2014, raised concerns about evaluations of dam safety, how the reservoir will be filled, and possible downstream impacts. The Ethiopian government, which hired the Italian firm Salini Impregilo to build the dam, has kept a tight lid on details of design and construction.

In a sign of progress, last December Ethiopia, Sudan, and Egypt agreed on an approach to evaluating the dam's potential downsides. Negotiators will then face the challenge of agreeing on how to minimize harm. Meanwhile, "I'm sufficiently optimistic that the dam will bring the countries together," says David Grey, a water policy expert at the University of Oxford in the United Kingdom, and former adviser at the World Bank. "But it's a rough road ahead for the next few years."

ETHIOPIA IS RICHLY ENDOWED with wild rivers that plunge through deep canyons. In the 1950s, the Ethiopian government asked the U.S. Bureau of Reclamation to create a master plan for harnessing that energy for hydropower. The bureau proposed four dams on the Blue Nile, which would together hold 73 billion m^3 of water and generate 5570 MW—nearly two-and-a-half times the output of the Hoover Dam. Over the years, Ethiopian experts and consultants refined the plans. By 2001 they had installed 529 MW of hydropower, but even this small start

Published by AAAS

raised the ire of Egyptian leaders. Hoping to forestall conflict, the World Bank and others have spent more than $200 million since 1999 on the Nile Basin Initiative to build technical expertise and launch cooperative water projects among the Nile states.

The pace was too slow for Ethiopia. After Egypt in 2008 nixed plans for a joint 2100-MW dam on the Blue Nile, Zenawi upped the ante with GERD. In the past, Ethiopia would have needed foreign aid to undertake such a gargantuan project. But because the country had been gaining economic strength, Ethiopia decided it could fund the dam itself. The estimated $4.7 billion cost is being paid for in part by selling bonds to government workers and other citizens.

The site is a 17-hour drive northwest of Addis Ababa, Ethiopia's capital, and just 12 kilometers from the border with Sudan, where the Blue Nile flows through an arid valley dotted with scrubby trees. Before construction could begin, Salini Impregilo had to build 120 km of access roads and camps for some 9000 workers, who are working round-the-clock. One of its subcontractors claims to have set a world record for daily cement production: 23,200 m^3, enough to fill nearly 10 Olympic swimming pools. "In all my travels I've never seen anything like it," says Harry Verhoeven, a political scientist at Georgetown University School of Foreign Service in Qatar in Doha, who studies water issues. "You feel that this is a national project and that it has to work."

> ***"In all my travels I've never seen anything like it."***
>
> **Harry Verhoeven**, Georgetown University School of Foreign Service in Qatar

Sparks flew in early 2014 after a confidential report on the dam's design and possible impacts was leaked to the nonprofit advocacy group International Rivers. The study had been completed in 2013 by an expert panel consisting of two representatives each from Ethiopia, Sudan, and Egypt and four outside experts. They urged Ethiopia to better analyze the dam's impact on water supplies in Sudan and Egypt and geotechnical risks such as dam failure. The experts also recommended further studies of its effects on water quality and other issues. To International Rivers, the dam-planning process seemed "chaotic and incomplete," with "precious little oversight." In its official response to the report, the Ethiopian government accepted the report's recommendations but maintained that it showed the "GERD project was being undertaken in line with international design criteria and standards."

Compared with other megadams, GERD will be less disruptive to ecosystems, experts agree. The biological diversity of the reservoir site and the Blue Nile downstream is fairly low, says limnologist Henri Dumont of Ghent University in Belgium, who has studied the areas.

The dam's impact on local communities is cloudier. The Ethiopian government has said that just 3000 people are being relocated from the reservoir site. River geographer Jennifer Veilleux, a postdoc at Florida International University in Miami, visited and studied the GERD site in 2013 and estimated the number to be relocated at 20,000, primarily the ethnic minority Gumuz people. "This could completely eliminate these communities and their culture forever." Still, other experts say overall social harm will be negligible.

Most of the rancor focuses on the plans for filling the reservoir—and the reduced downstream flow that will mean. Impoundment is expected to take place over 5 to 7 years. At first, 10% of the river's base flow will be retained in the reservoir each year, then the fraction will increase. A study by Block and colleagues, published in 2014 in the *Journal of Water Resources Planning and Management*, found that a 10% reduction would mean 5% less water reaching Lake Nasser, assuming the White Nile and other tributaries flow normally. This could result in less hydropower from Aswan High Dam and possibly less water released for irrigation.

A lot hinges on the climate. If the reservoir is filled during normal or wetter-than-average years, Egyptian farmers might feel no impact. A stretch of dry years, on the other hand, would mean greater hardships downstream or a longer timetable for impoundment. "We understand that it is a very sensitive issue downstream," says Yilma Seleshi, a water resources expert at Addis Ababa University. But he says Ethiopia can't afford to wait to generate hydropower, and he hopes downstream countries will accommodate that in the negotiations. "If they don't agree, we will continue to fill it using our own share of water." (Ethiopia and five other Nile states reject a 1959 treaty between Egypt and Sudan, and have signed their own accord.)

Once the reservoir is full, the benefits begin to flow. By trapping all the sand and 80% of the silt in the Blue Nile, GERD will preserve the storage capacity of dams in Sudan and Egypt, prolonging their lifetimes. Agriculture in Ethiopia may benefit indirectly, as the government will have a financial incentive to fight soil erosion; this will reduce the amount of silt that settles in GERD's reservoir and keep the dam's turbines spinning as long as possible.

Other wins come from taming the Blue Nile. For more than half the typical year, the river discharges just 300 m^3 per second. The flow usually rises in July and peaks in September, reaching nearly 4000 m^3 per second. GERD will even out the flow, allowing Sudanese dams to operate in dry months and generate an extra 1000 gigawatt hours or so of electricity per year, a 20% increase. "Now, Sudan is thinking about upgrading the turbines to tap the potential," says Yasir Mohamed, the director of the Sudan government's Hydraulics Research Centre in Wad Medani. Preventing extreme floods will also be a relief for Sudan, where a deluge in 2013 destroyed about 27,000 houses.

Larger farms in Sudan should prosper. Regulated flow will increase the number of months they can pump or divert water from the Blue Nile into irrigation canals. This will be good for the Gezira Scheme, one of the largest irrigation projects in the world, which distributes water stored behind the Roseires Dam to 880,000 hectares of farmland. But steady, lower flows could hurt subsistence farmers who tend small fields in Nile floodplains and depend on the annual flooding to renew their soil, Mohamed says.

Egypt has less to gain than Sudan, because the Aswan High Dam already provides flood control and irrigation. The biggest fear is that if an epic drought sets in, Ethiopia will hoard water and the level of Lake Nasser will drop. This worst case scenario "will result in abandoning huge areas of agricultural lands and scattering millions of families," the Group of Nile Basin, a dozen academics at Cairo University, asserted in a public statement in 2013. Even a smaller reduction in flow could affect the Nile's ability to flush salts from the soil or keep Mediterranean Sea water from intruding aquifers.

Outside experts say that if GERD is operated in coordination with the Aswan High Dam, the direct impacts on Egypt's water supply will be minimal. "They're not going to lose, that's for sure," says Amaury Tilmant, a civil engineer at Laval University in Quebec, Canada, who has modeled Nile water supply. In fact, there could be net gains. Ideally, less water would be stored in hot, low-lying Lake Nasser, which loses roughly 10 billion m^3 each year from evaporation, and more would be stored behind GERD, which is higher and cooler. Ethiopia would release regular supplies, and Egypt would benefit from the increase in storage capacity, providing extra insurance during droughts. But Mohamed Allam of Cairo University, a former water minister, remains wary of Ethiopia's intentions and thinks GERD was deliberately oversized. "They will continue to build dams in order to control every water drop for political reasons."

The greater strategic concern, Tilmant and observers say, ought to be Sudan. Once

Published by AAAS

Ancient rivals vie for upper hand in the Nile Basin

Long North Africa's hegemon, Egypt in 1970 harnessed the Nile with the Aswan High Dam (see left) to expand irrigation and generate 2100 MW of hydropower, then half the country's electricity. But others are now reaping benefits from the river. Sudan is poised to expand its irrigation, and since 2009 it has tripled its hydropower to 3000 MW (see right). The true powerhouse is Ethiopia with its high-elevation tributaries: It has built six major dams over the past 15 years that can generate 3500 MW, a sevenfold boost. The Grand Ethiopian Renaissance Dam (GERD) will give the country potential for nearly 10,000 MW in all—and control over much of the Nile's flow, sparking fear and anger in Egypt.

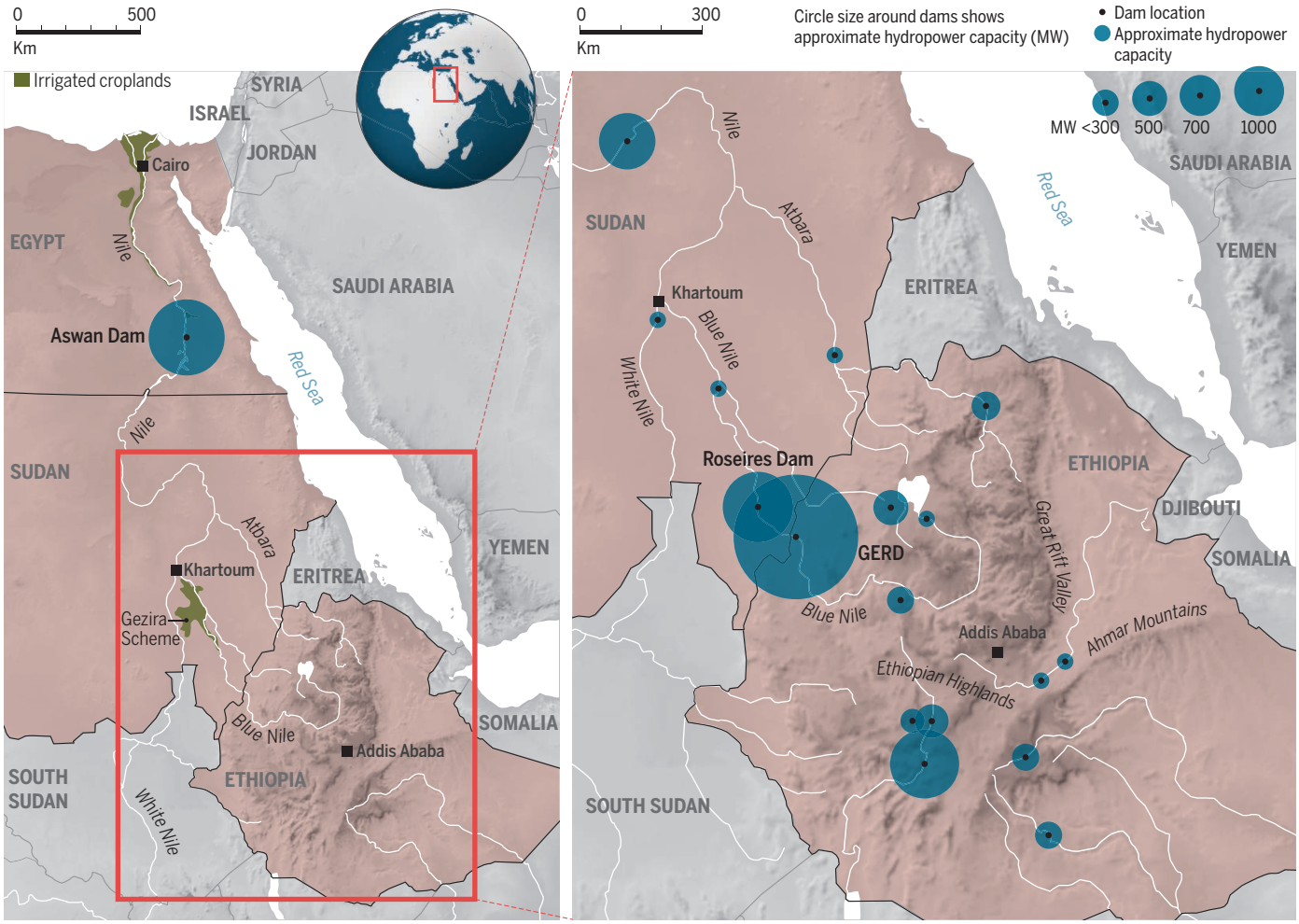

GERD has smoothed out the Blue Nile's flow, Sudanese farmers are likely to take more water to intensify production and expand croplands. Egypt, where population is growing explosively, can ill afford to lose any water. "Already we have some deficit in our water resources," says Alaa Yassin, professor of hydraulics at Alexandria University and adviser to the Ministry of Water Resources and Irrigation in Cairo.

Of all the possible hazards, the most terrifying is posed by GERD's saddle dam. It will stretch for 5 km between two hills to the south of the main dam and increase reservoir capacity fourfold. If it were to fail, a catastrophic flood would be unleashed, threatening millions of people. The 2013 expert review said it lacked adequate documentation to verify that the saddle dam's design is robust. Panelists worried that the structure, which is made of crushed rock, might slide under the weight of the water. And because the saddle dam is built on weathered rock, rather than solid bedrock, water might seep underneath and weaken the structure.

An expert group convened by Massachusetts Institute of Technology (MIT) in Cambridge in 2014 reiterated those concerns. "This is going to be one of the biggest saddle dams in the world," says Dale Whittington, a water resources expert at the University of North Carolina, Chapel Hill, and a member of the group. "It should be looked at very carefully." In a response to the MIT report, Ethiopian scientists noted that Salini Impregilo will use concrete to seal both the saddle dam and fractures in underlying rock. "It's solid," Seleshi says. The Egyptian view: "I can't say I'm confident," Yassin says.

AT THE DISPUTE'S NADIR in June 2013, Egyptian politicians were caught live on TV floating the option of sabotaging the dam. But in March 2015, heads of the foreign ministries and water agencies of the three countries pledged to agree on the reservoir's filling and subsequent operations. Egypt and Sudan praised Ethiopia for continued work to guarantee dam safety. "My view is that they're not far away from a deal," Grey says.

After years of acrimony, no one expects a deal that ensures full cooperation and maximal benefits. "We need to be realistic about what's possible," says Kaveh Madani, an environmental policy analyst at Imperial College London. But over the next 3 decades, the region's population will double, adding nearly 200 million people who will need food and electricity. If trust can be created and GERD proves to be a smarter approach to tapping the Nile, that would be a revolution in its own right. ■

GRAPHIC: P. HUEY/*SCIENCE*

Published by AAAS

Downloaded from on February 25, 2016

NATURE FROM NURTURE

As Japan's rice paddies go fallow, biodiversity suffers—raising questions about rewilding strategies the world over

By **Dennis Normile**, *in Kobe, Japan*

Grasshoppers and dragonflies scatter as Atushi Ushimaru steps gingerly along the banks of a terraced rice paddy. The paddy margins are a tapestry of plants, among them dozens of vulnerable and near-threatened grassland species. The ecologist with Kobe University points out one showy example: an endangered relative of the sunflower found only in this part of central Japan and on Shikoku Island, a couple hundred kilometers away. The major threat it faces: In Japan, small, traditionally managed rice paddies like these are themselves endangered.

In this tiny valley, about half the farmland is abandoned, the once-meticulously manicured paddies turning into unkempt terraces overrun by vegetation. As Japan's population shrinks and dietary preferences shift, demand for rice is dropping. Nationwide, the area planted with rice has declined by half since the early 1960s, with many remote, difficult-to-farm paddies going to seed as elderly farmers retire and part-timers simply give up.

One might assume that fewer humans would mean more nature. But Ushimaru has documented how these isolated rice terraces are unexpected hot spots of biodiversity. As more such paddies across Japan are abandoned, he says, many rare plants and insects that have coexisted with Japanese farming for millennia, including the sunflower relative (the *yaburegasamodoki*), are likely to follow traditional farmers into extinction.

PHOTO: © AMANAIMAGES/CORBIS

Published by AAAS

For millennia, Japan's farmers have encouraged vegetation to grow on terraced rice paddy banks to stabilize the soil. Many of the plant species are now found nowhere else.

Japan is embarking on an unprecedented experiment as the human footprint on its territory shrinks. Its population could drop from a 2008 peak of 128 million to 86 million by 2060, according to one government projection. And that population is increasingly concentrated in cities. In some rural prefectures, one in 10 houses is empty, and local governments are demolishing thousands of derelict schools and other municipal buildings.

Much of the country's former farmland has been consumed by suburban development, but since 1961, 276,000 hectares have simply been allowed to revert to nature. The Ministry of Agriculture, Forestry and Fisheries forecasts that another 120,000 hectares will be taken out of production in the next decade. What happens in Japan "is very important and instructive for many areas of the world, even those countries that are not shrinking at the national scale but may be experiencing regional shrinkage," says Peter Matanle, a sociologist at University of Sheffield in the United Kingdom who studies Japan's population decline.

Japan offers a vivid case study in an ongoing debate: whether allowing farmland to revert to nature is a boon to biodiversity or actually harms it. "Farmland abandonment is changing rural landscapes worldwide, but its impacts on biodiversity are still being debated in the scientific literature," Cibele Queiroz, an ecologist at Stockholm University and colleagues noted in *Frontiers in Ecology and the Environment* in July 2014 after reviewing 276 papers on the topic. In Europe and North America the picture is mixed. But in Japan, Ushimaru and others are finding that as farmland abandonment continues and the human touch recedes from rural landscapes, species will suffer.

Abandoned rice terraces in Japan are soon overrun by vines and other invaders that crowd out grasses and weeds adapted to the paddy environment.

PHOTO: © DENNIS NORMILE

MANY CULTURES nurture romantic visions of an idyllic pastoral past, when farms coexisted peacefully with nature. In Japan, this notion is captured in the *satoyama*, or "mountain village." The archetype is a clutch of traditional wooden buildings nestled in a forested valley surrounded by rice paddies, vegetable plots, orchards, and pasture.

But at an accelerating pace since the 1960s, traditional farming has come under pressure. Paddies have been consolidated and farmed more intensively. And now, demographic and dietary shifts are picking up steam: In 2011, for the first time, Japanese households on average spent more on wheat products—bread and pasta—than on rice. Rice consumption has fallen from 118 kilograms per person per year in the early 1960s to 58 kg in 2013, and the population itself is now shrinking. (Wheat fields are not replacing the dwindling paddies, because most wheat is imported.) The decline in rice cultivation may accelerate because of the Trans-Pacific Partnership trade deal, expected to be ratified within a couple years, which would gradually open Japan's protected rice market to imports.

Researchers and farmers have long lamented the decline of *satoyama*. But in the past 15 years, Ushimaru says, a new generation of researchers has begun documenting the impact on biodiversity. With few exceptions, the studies point in one direction. Writing in the *Journal of Insect Conservation* in 2011, Yasuhiro Nakamura, executive director of the Japan Butterfly Conservation Society in Tokyo, called the loss of *satoyama* ecosystems the "main cause" of steep declines in butterfly populations over 40 years. In another example, Kazuhiro Katoh, a landscape ecologist at the Open University of Japan in Chiba, and colleagues reported in *Biological Conservation* in 2009 that the gray-faced buzzard—"vulnerable" on Japan's Red List of Threatened Species—nests in forests in close proximity to paddies and grasslands, where it preys on frogs, insects, and rodents. Degradation of any of those key ecosystem components hurts the buzzard. And in more than two dozen reports since 2000, Susumu Yamada of the University of Tokyo has concluded that "paddy weed communities are declining with intensification and abandonment of agricultural activities."

Ushimaru has set out to unravel why traditionally managed paddies create habitat for so many species. Paddies are rimmed by banks so that they can be flooded and drained. Since time immemorial, farmers have encouraged wild grassland plants to grow on the banks because the roots stabilize the soil. They mow the banks two or three times a year to keep the vegetation in check. Mowing ceases when farms are abandoned, and is scaled back when smaller plots are merged into large fields. Ushimaru's team compared insect species richness in abandoned, traditional, and large paddies and concluded that the periodic mowing encourages diversity in the grassland plants that, in turn, support an array of butterflies, dragonflies, and grasshoppers, the group reported in *Ecological Monographs* in 2014.

Ushimaru believes this grassland diversity is rooted in history. In the 2012 book *Grasslands and the Japanese*, Ushimaru and two colleagues noted that early Japanese, like many primitive peoples, periodically set fires to create and maintain grasslands that first made hunting easier and later provided fodder for livestock. The scorched landscape paved the way for colonizing plants. Later, as rice cultivation displaced the seminatural grasslands, those plants and their dependent insects and birds adapted to thrive in the paddy environment.

The terraced paddies that march up hillsides provide especially rich habitat. Reaching the terraces here near Kobe takes a 30-minute hike up a narrow road that winds through dense forest—a reminder that feudal-era villagers tried to hide paddies from tax collectors, who took a share of the rice crop. These high terraces are often nutrient-poor, because fertilizer washes downhill—a condition that favors some wild plant species. Ushimaru has found that rare plants are more common in the upper reaches of terraced paddies than in consolidated or abandoned fields.

Published by AAAS

Japan's gray-faced buzzard, listed as vulnerable to extinction, preys on creatures that thrive near traditionally farmed paddies, including rodents and the Japanese brown frog.

Paddies also provide wetland habitat that has disappeared elsewhere, Ushimaru says; Japan has filled in many of its natural wetlands and confined streams to rock-lined channels. Studies of birds highlight the importance of these artificial wetlands. A team led by Naoki Katayama, an ecologist at the National Institute for Agro-Environmental Sciences in Tsukuba, has found that abandoned farmland is a boon to grassland birds, with larger numbers and a greater variety of warblers and other species. But wetland birds—the most threatened group in Japan—are losing out. The researchers found fewer egrets, herons, and other wetland species in abandoned and consolidated fields than in traditional paddies, particularly during the summer breeding season.

The lack of diverse, undisturbed ecosystems near the abandoned paddies means that they are slow to revert to historically natural conditions, Ushimaru and others say. Neglected paddies are initially colonized by a few hardy species such as the aggressive kudzu vine and an invasive goldenrod from North America. "The low level of biodiversity may persist for decades," Katayama says. And the surrounding forests, home to other species that could succeed the first invaders, are a shadow of their old selves. Once a diverse mix of trees and shrubs, these forests are now mostly cedar, which leaves little sunlight for understory plants, Matanle says. And they are now choked by an invasive bamboo from China.

Japan's rewilding experience may foretell what's coming elsewhere. "Japan is a pioneer for a more generalized Asian experience," Matanle says. China and South Korea are both undergoing demographic shifts, changes in diets, and farmland intensification. Terraced rice paddies in China's rural hillsides "are being abandoned as young people leave for the cities," says Yu Ping, a photographer who is documenting the impact of depopulation on China's villages. Some researchers are predicting impacts on biodiversity similar to those seen in Japan, though there is little relevant research yet. In Europe, too, many ecologists believe that traditional agricultural practices coevolved with flora and fauna over millennia; the loss of small farms, they say, imperils this biodiversity.

By contrast, in the Americas and Oceania the arrival of European agricultural practices over the last several hundred years is seen as "very harmful to local biodiversity," Queiroz says. There, many researchers believe, abandoned farmlands will revert to pre-European pristine conditions and allow biodiversity to thrive. "In these places, agricultural abandonment provides an opportunity for the native landscapes to recover," Queiroz says.

Henrique Pereira, a biodiversity expert at the German Centre for Integrative Biodiversity Research in Leipzig and an editor of the 2015 book *Rewilding Abandoned Landscapes in Europe*, argues that the prevailing view of traditional agriculture underestimates the damage it did to biodiversity and the environment. In some instances, he concedes, it might be desirable to maintain an agricultural landscape to preserve particular species. However, "at global scales, this is rarely needed," he argues. "Rewilding is a management strategy that should be considered in any situation of large-scale abandonment."

Japanese researchers disagree. Turning paddies back into forests would have little payoff, they say, because Japan already has plenty of forested habitat, while many species on paddy edges are threatened by habitat loss. "I am fearful that rewilding will increase the extinction probability of many farmland species in Japan," Katayama says. Pereira concedes that "any strategy for large-scale rewilding of rice paddies should involve the restoration of wetlands." This would be difficult, Japanese researchers say, because development has wiped out so many of the country's wetlands.

Meanwhile, demography is steadily working against the *satoyama* and the species they host. At the hidden terraces near Kobe, Ushimaru says, the youngest farmer working the paddies is about 60. None of their children or grandchildren is interested in the laborious occupation. "I don't see a solution to this problem," Ushimaru says sadly. ■

Fewer paddies, fewer mouths

Declining rice consumption and an aging, shrinking population are together whittling down the area of active farmland in Japan, from a peak of 6.1 million hectares in 1961 to 4.5 million hectares in 2015. The Ministry of Agriculture estimates that an additional 120,000 hectares could be taken out of production in the next decade.

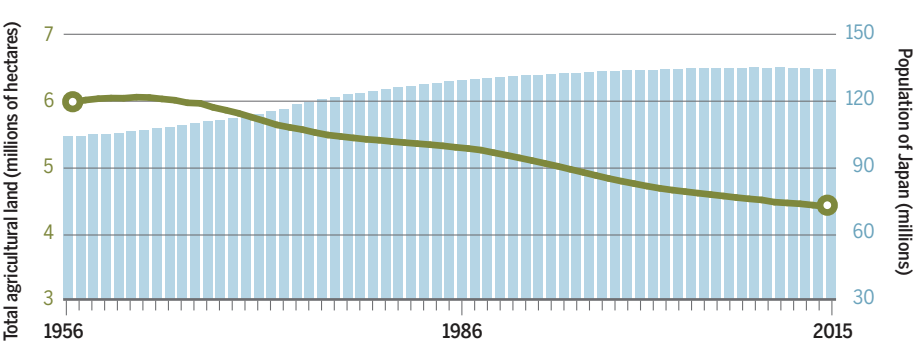

CREDITS: (PHOTOS, LEFT TO RIGHT) © AKIRA SATO/MINDEN PICTURES; © YASUNORI KOIDE/CREATIVE COMMONS; (DATA) JAPAN'S NATIONAL INSTITUTE OF POPULATION AND SOCIAL SECURITY RESEARCH

Published by AAAS

INSIGHTS

Chiral catalysis with ion pairs *p. 918*

Maternal infection and brain development *p. 919* ▸

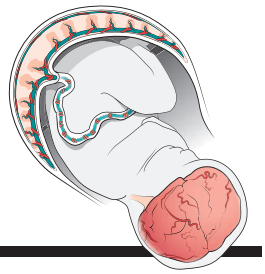

PERSPECTIVES

Getting a drink. Countries around the world differ in their approach to delivering safe drinking water to their citizens. The photo shows a young boy drinking from a waterfront tap in Guam, USA.

Downloaded from on February 25, 2016

WATER INFRASTRUCTURE

How do you like your tap water?

Safe drinking water may not need to contain a residual disinfectant

By **Fernando Rosario-Ortiz,[1,2] Joan Rose,[3] Vanessa Speight,[4] Urs von Gunten,[2,5] Jerald Schnoor[2,6]**

The expectation that tap water is safe has been sorely tested by the recent events in Flint, Michigan, where lead contamination has caused a public health emergency (*1*). Apart from contamination with heavy metals and other harmful substances, a key concern is the control of microbial contamination. To prevent microbial growth and protect consumers from pathogens from other sources, some countries, such as the United States, require the presence of residual disinfectant in drinking water. However, the presence of a disinfectant can lead to the formation of potentially carcinogenic disinfection byproducts, issues with corrosion, and complaints based on the fact that people dislike the taste of disinfectants in their water (*2*). The experience of several European countries shows that such residual disinfectants are not necessary as long as other appropriate safeguards are in place.

From the early 1900s, the control of microbial waterborne pathogens, including *Salmonella typhi* and *Vibrio cholera,* led to a major reduction of waterborne diseases in the industrialized world. Filtration and chlorine disinfection reduced mortality in the United States substantially. But in 1974, chloroform, a probable human carcinogen formed by the reaction of chlorine with naturally occurring organic matter, was discovered in chlorinated drinking water. This discovery led to a debate about microbiological safety versus exposure to harm-

PHOTO: © ANTHONY ASAEL/ART IN ALL OF US/CORBIS

Published by AAAS

ful substances, and the overall effectiveness of disinfectants in the distribution system (*3*, *4*). Furthermore, disinfectants can contribute to the leaching of lead from pipes in older distribution systems (*5*).

In some European countries (including the Netherlands, Switzerland, Austria, and Germany), drinking water can be delivered to consumers without a residual disinfectant as long as there is adequate source protection, treatment, and maintenance of the distribution system to prevent growth of pathogenic bacteria and additional contamination events (see the figure). If one of these elements is missing or improperly managed, disinfectants are added to the distribution system to maintain a residual and a margin of safety.

In the United States, unprotected surface waters often serve as source water. Treatment includes coagulation, sedimentation, filtration, and disinfection with specific contract times. The water is then distributed to the consumer with a residual chemical disinfectant (chlorine, chlorine dioxide, or chloramines) as a last barrier against contamination.

The choice between the two approaches is based on balancing the risk of microbial contamination, exposure to disinfection byproducts and the taste and odor of chlorine. In western Europe, eliminating the use of disinfectant during distribution certainly limits the formation of disinfection byproducts, but does it result in increased incidence of disease? And in the United States, how effective is maintaining a disinfectant residual in reducing the frequency of disease outbreaks? Also, what level of investment is needed to limit problems associated with old infrastructure, such as in the case of Flint? Estimates have ranged from tens of millions to $1.5 billion USD for Flint alone, and many other cities have similar infrastructure problems.

There is little direct evidence that disinfectant residuals have prevented drinking water–related disease outbreaks (including aerosol-associated cases of *Legionella*). A comparison of waterborne disease outbreak data from the Netherlands, United Kingdom, and United States shows that the Netherlands has a very low risk of waterborne disease. For these three countries, the rates of outbreaks per 1000 population in the last few years were 0.59, 2.03, and 2.79, respectively (*6*, *7*). It seems that the presence of a disinfectant in the distribution system does not guarantee lower rates of disease outbreaks. However, small groundwater systems that are not chlorinated and are typically used intermittently have caused the most recent outbreaks in the United States (*6*).

An additional consideration in the debate about disinfectant residuals is the robustness of the infrastructure against contamination events. In the Netherlands, at least half of the water distribution pipes have been replaced since the 1970s; as a result, pipe networks are, on average, 33 to 37 years old (*8*). Although there are regional differences, an estimated 22% of the pipes in the United States are more than 50 years old; the average age of pipe at failure is 47 years, and only 43% of pipes are considered to be in good or excellent condition (*9*). In the United Kingdom, as much as 60% of pipe inventory does not have a record of pipe age, and estimates of average pipe age are on the order of 75 to 80 years overall (*10*). The use of a disinfectant residual is required in the United Kingdom (*11*).

Leakage is one measure of vulnerability of the distribution system. It is as low as 6% in the Netherlands, compared to 25% in the United Kingdom and 16% in the United States (*8, 12, 13*). Generally, United States distribution systems have longer retention times, which may promote microbial regrowth and disinfection byproduct formation. Maintenance of adequate pressure can provide a barrier against contaminant intrusion, but excessive water pressure, including transients, can lead to pipe breaks. In fact, drinking water infrastructure in the United States is in serious need of investment, including the replacement of lead-lined pipes or connections that are found in many households.

It should be noted that there are differences in drinking water costs between Europe and the United States. Water prices in some western European countries are on average two to three times higher than in the United States (*14*). It is clear that pricing

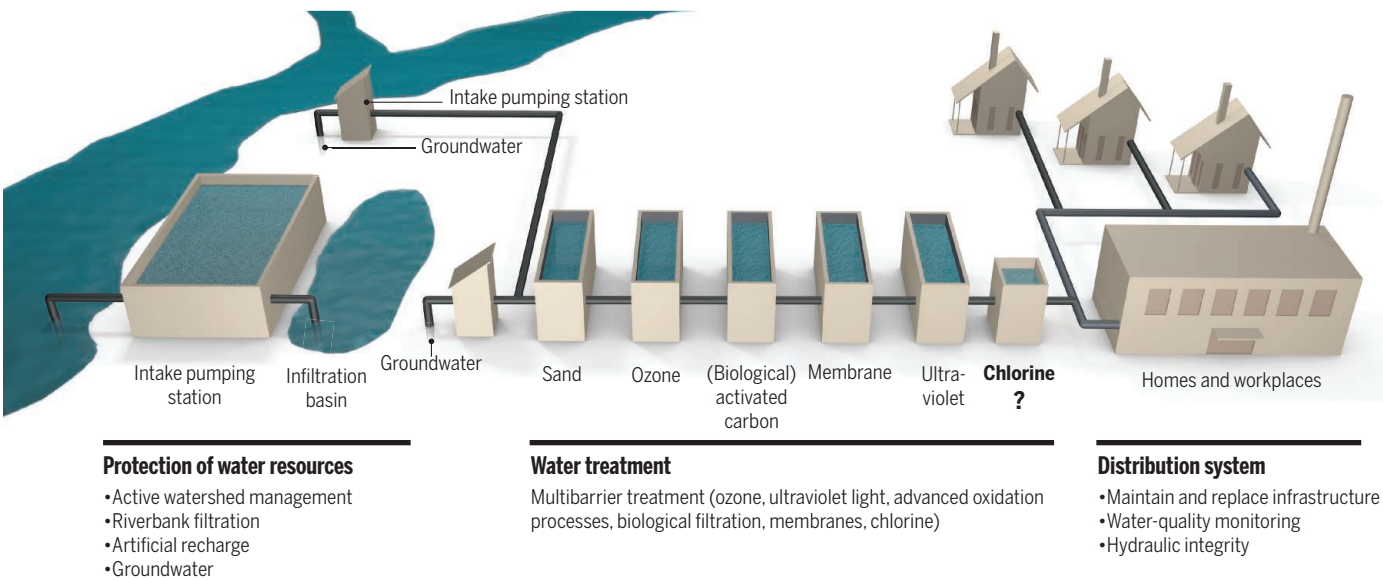

Multibarrier approach to drinking water safety. Filtering through soil and/or sand-gravel aquifers protects source waters from many microbial contaminants. Well-controlled water treatment includes particle removal, disinfection, biological filtration, and removal of natural organic matter. Water can then be distributed to consumers without addition of a disinfectant residual, but with the capacity to do so in the event of leaks or repairs.

[1]Department of Civil, Environmental and Architectural Engineering, University of Colorado, Boulder, CO 80309, USA. [2]Eawag, Swiss Federal Institute of Aquatic Science and Technology, Dübendorf 8600, Switzerland. [3]Department of Fisheries and Wildlife, Michigan State University, East Lansing, MI 48824, USA. [4]Department of Civil and Structural Engineering, University of Sheffield, Sheffield S10 2TN, UK. [5]School of Architecture, Cibil and Environmental Engineering (ENAC), Ecole Polytechique Fédérale de Lausanne, CH-1015 Lausanne, Switzerland. [6]Department of Civil and Environmental Engineering, University of Iowa, Iowa City, IO 52242, USA. E-mail: jerald-schnoor@uiowa.edu

ILLUSTRATION: P. HUEY/*SCIENCE*

Published by AAAS

for potable water also needs to be evaluated to determine how much should be spent to ensure microbiological safety and integrity of the distribution system.

To understand the long-term properties of water distribution systems, comparative data are needed on water quality, disease outbreaks, and distribution system failures from all approaches used to produce potable water. The water microbiome in distribution pipes and the definition of microbiologically safe water should be further investigated. In addition, improved monitoring and emerging sensor technology can provide warnings and alerts, helping to determine when to restore and protect extensive pipe assets. In the case of green water infrastructure, which includes water recycling, rainwater harvesting, and solar water heating, multiple barriers will be necessary to prevent opportunistic pathogens such as *Legionella*, which is higher in buildings with green water designs and longer water residence times (*15*). But the European evidence to date suggests that safe water can indeed be delivered without a disinfectant residual, as long as there are multiple barriers in operation. ■

REFERENCES AND NOTES

1. M. Hanna-Attisha, J. LaChance, R. C. Sadler, A. Champney Schnepp, *Am. J. Public Health* **106**, 283 (2015).
2. E. D. Mackey *et al.*, *Public perception of tap water chlorinous flavor* (Water Research Foundation, Denver, CO, 2005).
3. G. J. Medema, P. W. M. H. Smeets, E. J. M. Blokker, J. H. M. van Lieverloo, in *Microbial Growth in Drinking-Water Supplies: Problems, Causes, Control and Research Needs*, D. van der Kooij, P. van der Wielen, Eds., (IWA Publishing, London, 2014), pp. 95–125.
4. D. L. Sedlak, U. von Gunten, *Science* **331**, 42 (2011).
5. M. Edwards, S. Triantafyllidou, D. Best, *Environ. Sci. Technol.* **43**, 1618 (2009).
6. K. D. Beer *et al.*, *Morb. Mortal. Wkly. Rep.* **64**, 842 (2015).
7. B. Guzman-Herrador *et al.*, *Eurosurveillance* **20**, 21160 (2015).
8. Vewin, Dutch water sector, 2015; www.vewin.nl/english/dutch-water-sector.
9. S. Folkman, *Water main break rates in the USA and Canada: A comprehensive study* (Utah State University, Logan, UT, April 2012); see www.neng.usu.edu/mae/faculty/stevef/UtahStateWaterBreakRatesLR.pdf.
10. UKWIR. National sewer and water mains failure database, Issue 1.2, Project Report 08/RG/05/26, UK Water Industry Research, 2011.
11. DWI, The Water Supply Regulations, Statutory Instrument 2010 No. 991.
12. D. Carrington, "Most water companies not required to cut leaks before 2015 despite drought," *The Guardian*, 7 May 2012; www.theguardian.com/environment/2012/may/07/water-companies-cut-leaks-2015-drought.
13. USEPA. Water audits and water loss control for public water systems, Report 816-F-13-002 (2013).
14. N. Hrovatin, S. J. Bailey, *Utilities Policy* **10**, 13 (2001).
15. W. J. Rhoads, A. Pruden, M. A. Edwards, *Environ. Sci.: Water Research & Technology* **2**, 164 (2016).

ACKNOWLEDGMENTS

J.S. and F.R.-O. are grateful for sabbatical support from Eawag, Swiss Federal Institute of Aquatic Science and Technology, during work on this Perspective (F.R.-O. also received support from ETH Zurich). V.S. received support from EPSRC (EP/I029346/1). We thank J. Hering and R. Valentine for helpful suggestions on the manuscript.

10.1126/science aaf0953

WATER

Saving freshwater from salts

Ion-specific standards are needed to protect biodiversity

By **M. Cañedo-Argüelles,[1,2] C. P. Hawkins,[3] B. J. Kefford,[4] R. B. Schäfer,[5] B. J. Dyack,[4] S. Brucet,[6,1] D. Buchwalter,[7] J. Dunlop,[8] O. Frör,[5] J. Lazorchak,[9] E. Coring,[10] H. R. Fernandez,[11] W. Goodfellow,[12] A. L. González Achem,[11] S. Hatfield-Dodds,[13] B. K. Karimov,[14] P. Mensah,[15] J. R. Olson,[16] C. Piscart,[17] N. Prat,[2] S. Ponsá,[1] C.-J. Schulz,[18] A. J. Timpano[19]**

PHOTO: © KERRY WHITWORTH/ALAMY STOCK PHOTO

Many human activities—like agriculture and resource extraction—are increasing the total concentration of dissolved inorganic salts (i.e., salinity) in freshwaters. Increasing salinity can have adverse effects on human health (*1*); increase the costs of water treatment for human consumption; and damage infrastructure [e.g., amounting to $700 million per year in the Border Rivers catchment, Australia (*2*)]. It can also reduce freshwater biodiversity (*3*); alter ecosystem functions (*4*); and affect economic well-being by altering ecosystem goods and services (e.g., fisheries collapse). Yet water-quality legislation and regulations that target salinity typically focus on drinking water and irrigation water, which does not automatically protect biodiversity.

POLICY

For example, specific electrical conductivities (a proxy for salinity) of 2 mS/cm can be acceptable for drinking and irrigation but could extirpate many freshwater insect species (*3*). We argue that salinity standards for specific ions and ion mixtures, not just for total salinity, should be developed and legally enforced to protect freshwater life and ecosystem services. We identify barriers to setting such standards and recommend management guidelines.

Attempts to regulate salinization on the basis of ecological criteria can be found in the United States and Australia, where total salinity recommendations have been made (*5*, *6*). Even these criteria are insufficient to protect freshwater life, because waters with the same total amount of salts but different ionic composition can have markedly different effects on freshwater fauna (*7*). Canada and the United States are the only countries in the world that identify concentrations of a specific ion (chloride) above which freshwater life will be harmed (*6*, *8*). Globally, concentrations of other ions (e.g., Mg^{2+}, HCO_3^-) remain free from regulation in spite of their potential toxicity (*9*).

The situation will likely worsen in the future, because predicted increase in demand for freshwater will reduce the capacity of surface waters to dilute salts, and increasing resource extraction and other human activities (*10*) will generate additional saline effluents and runoff. Climate change will likely exacerbate salinization by causing seawater intrusion in coastal freshwaters, increasing evaporation, and reducing precipitation in some regions (*11*).

SETTING STANDARDS. Scientific understanding of mechanisms by which increasing salinization damages freshwater ecosystems is in its infancy, which makes it challenging to develop and implement standards protective of freshwater life. Technical challenges are exacerbated by the fact that salinization risks perceived by the public and policy-makers may be much lower than those identified by scientists. In addition, although scientific input has been

Published by AAAS

Wetland salinization. Feeder creek at Bottle Bend Lagoon, a wetland near Midura, Australia, where inadequate water management in the past has led to salinization and acid sulfate soils.

used to set standards, there has been inadequate integration of costs of salinity and benefits of controls.

Several countries have specific requirements for developing and implementing water-quality standards, e.g., the Australian and New Zealand Environmental and Conservation Council (ANZECC), the Agriculture and Resource Management Council of Australia and New Zealand (ARMCANZ), the Clean Water Act in the United States, and the Water Framework Directive and related legislation in the European Union. We draw on these experiences and recommend an integrated approach to standards development and management that includes a triple bottom line (TBL) approach, a well-established framework with multiple stakeholder input used to account for social, economic, and environmental impacts of management options. This should produce ecologically meaningful and protective salinity standards for any jurisdiction, although the amount of work needed will vary widely depending on available data and existing regulatory structures. Components are the following.

(i) *Characterize water bodies to which standards will apply*. Freshwaters naturally vary in ionic concentrations and composition because of underlying geology, proximity to the ocean, and hydrology (3). Protecting organisms adapted to widely differing ion concentrations will require locality-specific standards based on natural background ion concentrations. Such conditions can now be estimated for any water body, which makes site-specific standards possible (*12*).

(ii) *Characterize ionic composition (i.e., concentrations of specific ions and their ratios) of effluents associated with each existing driver of salinization in the region*. Also, assess the technical potential to reduce effluent loads and total flows and the social and economic impacts associated with these reductions.

(iii) *Quantify potential effects of each class of saline effluent in the region and identify thresholds for toxic effects*. Quantifying relationships between biota and ionic composition from field survey data can help identify taxa at potential risk and prioritize toxicity experiments. As with other contaminants, both laboratory bioassays (e.g., lethal concentration 50 or whole-effluent toxicity tests) and longer-term mesocosm experiments should be used to quantify toxicity of different ions to a representative set of species (e.g., fish, amphibians, invertebrates, and algae).

(iv) *Ensure that standards are informed by the best available science and understanding of costs and benefits*. Stakeholder involvement is crucial to ensuring that arrangements will be implemented and enforced in practice (*13*). This process needs to be structured to promote communication and social learning across different constituencies, so as to ensure that scientific results are understandable by policy-makers, affected stakeholders, and the public. Sound integration of insights from natural and social sciences will help all parties understand the risks and opportunities of different options for protec-

[1]University of Vic - Central University of Catalonia, Vic 08500, Spain. [2]Universitat Barcelona, Barcelona 08028, Spain. [3]Utah State University, Logan, UT 84322, USA. [4]University of Canberra, Canberra 2601, Australia. [5]University of Koblenz-Landau, 76829 Landau, Germany. [6]Catalan Institution for Research and Advanced Studies, Barcelona 08010, Spain [7]North Carolina State University, Raleigh, NC 27695, USA. [8]Queensland Government, Australia. [9]U.S. Environmental Protection Agency, Cincinnati, OH 45268, USA. [10]EcoRing, 37181 Hardegsen, Germany. [11]Instituto de Biodiversidad Neotropical, Tucumán, Argentina. [12]Exponent Inc., Alexandria, VA 22314, USA. [13]CSIRO Land and Water, Canberra 2601, Australia. [14]Uzbekistan Academy of Sciences, Uzbekistan. [15]Rhodes University, Grahamstown 6140, South Africa. [16]Desert Research Institute, Las Vegas, NV 89119, USA. [17]Université de Rennes, 35042, Rennes, France. [18]Thuringian State Institute for Environment and Geology, D-07745 Jena, Germany. [19]Virginia Polytechnic Institute and State University, Blacksburg, VA 24061, USA. *Corresponding author. E-mail: mcanedo.fem@gmail.com

Published by AAAS

tion and restoration. Such analyses should be based ideally on state-of-the-science techniques of decision support and benefit-cost analysis that account for the diversity of societal values (including market and nonmarket values) associated with the causes and consequences of salinization. Given that evidence will improve, developing standards and wider governance arrangements will require an iterative approach over time. The Australian Murray-Darling Basin salinity management strategy (*14*) is an example of how planning and consultation can lead to catchment-specific salinity targets. This strategy sits within the overall Murray-Darling Basin Plan, where legislation requires a TBL approach.

MANAGEMENT MEASURES. Several management actions could help meet existing and emerging standards and could prevent or remediate damage associated with freshwater salinization. Essential to all of these options is providing incentives for reducing salinization, such as by market-based instruments, subsidies for technology development and implementation, or load-based charges on saline effluents. Examples of good practices include the following.

(i) *Implement agriculture practices that use less water and thereby reduce salt loading to freshwaters.* For example, the Colorado River Basin Salinity Control Program has reduced salt loading to the river by an estimated 1.3 million tons/year, mostly by improving irrigation practices (*15*).

(ii) *Reduce or eliminate the use of salts as pavement deicers by making more effective application and use of the salts that are applied or by using alternative deicers.*

(iii) *Reduce point-source production and discharge of salts to freshwaters.* For example, innovative methods of resource extraction that sequester soluble minerals away from water sources have potential to reduce effluent discharge to streams.

(iv) *Implement cap-and-trade schemes.* This cost-effective approach is being used in Australia (e.g., the Hunter River Salinity Trading Scheme), where miners and power generators trade permits to discharge salt-rich effluents during moderate to high flow periods.

(v) *Develop specific management options for salt-rich effluents.* Salt-rich urban discharges could be routed to retention basins rather than treatment plants or streams. Although currently prohibitively expensive, water desalinization may become a viable treatment, particularly solar-powered systems, such as are in development in the Middle East. Recovering salts could reduce costs, e.g., using magnesium to recover ammonia and phosphate in the form of struvite, which has commercial value.

(vi) *Promote practices that reduce salinization.* Recognition of water-wise products (e.g., via eco-labels) or support for direct economic incentives to commercialize crops that demand less water (*14*) can be useful tools to alter behaviors.

Fortunately, few large-scale ecological disasters have been caused by salinization of freshwater ecosystems to date, but those that have [e.g., the fisheries collapse in the Aral Sea in Central Asia (*16*)] should be a wake-up call. International cooperation and scientific knowledge-sharing are needed to develop solutions that can be applied globally. Experiences like those near the river Werra in Germany, where a combination of total ion and ion-specific discharge requirements led to ecosystem recovery (*17*), show that rehabilitation of salt-polluted freshwater ecosystems is possible. Prevention of salt damage is much more likely if water managers, stakeholders, and scientists work together to identify social, economic, and ecological costs and the benefits that can accrue from prevention and restoration. ■

REFERENCES AND NOTES

1. A. E. Khan *et al.*, *Environ. Health Perspect.* **119**, 1328 (2011).
2. S. M. Wilson, *Dryland and Urban Salinity Costs Across the Murray-Darling Basin: An Overview and Guidelines for Identifying and Valuing the Impacts* (Murray-Darling Basin Commission, Canberra, Australia, 2004).
3. M. Cañedo-Argüelles *et al.*, *Environ. Pollut.* **173**, 157 (2013).
4. E. R. Herbert *et al.*, *Ecosphere* **6**, art206 (2015).
5. ANZECC, ARMCANZ, *Australian and New Zealand Guidelines for Freshwater and Marine Water Quality*, vol. 1, *The Guidelines* (ANZECC and ARMCANZ, 2000).
6. U.S. Environmental Protection Agency, "National recommended water quality criteria: 2002" (EPA 822-R- 02-047, Office of Water, EPA, Washington, DC, 2002).
7. J. L. Kunz *et al.*, *Environ. Toxicol. Chem.* **32**, 2826 (2013).
8. Canadian Council of Ministers of the Environment, *Canadian Water Quality Guidelines for the Protection of Aquatic Life*, in *Canadian Environmental Quality Guidelines* (CCME, Winnipeg, 1999).
9. R. A. van Dam *et al.*, *Environ. Toxicol. Chem.* **29**, 410 (2010).
10. F. Krausmann *et al.*, *Ecol. Econ.* **68**, 2696 (2009).
11. Intergovernmental Panel on Climate Change, *Climate Change 2013: The Physical Science Basis: Contribution of Working Group I to the Fifth Assessment Report of the Intergovernmental Panel on Climate Change* (Cambridge Univ. Press, New York, 2013).
12. C. P. Hawkins *et al.*, *J. N. Am. Benthol. Soc.* **29**, 312 (2010).
13. T. Dietz, E. Ostrom, P. C. Stern, *Science* **302**, 1907 (2003).
14. Murray-Darling Basin Ministerial Council, *Basin Salinity Management 2030* (Murray-Darling Basin Authority, Canberra, 2015); http://bit.ly/BasinSalinity.
15. Uinta Basin Salinity Study Team, *Final Report on Findings and Strategies, Uinta Basin, UT* (U.S. Bureau of Reclamation, 2014); http://bit.ly/ColoradoRiverSalinity.
16. P. Micklin, *Annu. Rev. Earth Planet. Sci.* **35**, 47 (2007).
17. J. Bäthe, E. Coring, *Limnologica* **41**, 125 (2011).

ACKNOWLEDGMENTS

We thank B. Brooks, C. N. Dahm, D. Penrose, E. Bernhardt, G. Pyke, J. Doolan, J. Conley, R. Thompson. and three anonymous reviewers for comments. This manuscript has been subjected to the EPA's peer and administrative review and has been approved for publication. Approval does not signify that the contents reflect the views of the agency. M.C.-A. was supported by the 7th Framework Programme of the European Union–Marie Curie Actions (REA grant agreement 600388) and Catalonia Trade and investment (ACCIÓ), Government of Catalonia, under the TECNIOspring programme.

10.1126/science.aad3488

DNA

Breaking DNA

A long-sought protein that helps to break DNA is finally discovered

By **Corentin Claeys Bouuaert** *and* **Scott Keeney**

To maintain a constant number of chromosomes from one generation to the next, sexual organisms reduce the genome complement in their gametes through the specialized cellular division of meiosis. Accurate separation of homologous chromosomes during meiosis relies on a dedicated mechanism of DNA recombination that is initiated by DNA double-strand breaks (DSBs) made by a protein called sporulation protein 11 (Spo11) (*1*). Meiotic recombination helps connect homologous chromosomes to promote their accurate segregation, and also shuffles alleles between homologous chromosomes to increase diversity. Spo11 is encoded in nearly all sequenced eukaryotic genomes, and it is likely that most species

"...meiotic cells play the risky game of forming a great deal of...self-inflicted DNA damage..."

that carry out meiotic recombination use Spo11-generated DSBs as the initiators (*2*). Spo11 is thus an ancient and fundamental part of sexual reproduction. On pages 939 and 943 of this issue, Vrielynck *et al.* (*3*) and Robert *et al.* (*4*) report the discovery of a long-sought partner of Spo11 in plants and mice, respectively.

Spo11 evolved from an ancestral type II DNA topoisomerase (Topo VI) that is found today in Archaea and a few eukaryotic lineages, including some plants (*2*). Topoisomerases create transient breaks in DNA to change DNA supercoiling or untangle intertwined DNA duplexes, thereby facilitating processes such as transcription or replication. Topo VI comprises two "A" subunits that cleave DNA and two "B" sub-

Howard Hughes Medical Institute, Molecular Biology Program, Memorial Sloan Kettering Cancer Center, 1275 York Avenue, New York, NY 10065, USA. E-mail: s-keeney@ski.mskcc.org

Downloaded from on February 25, 2016

Published by AAAS

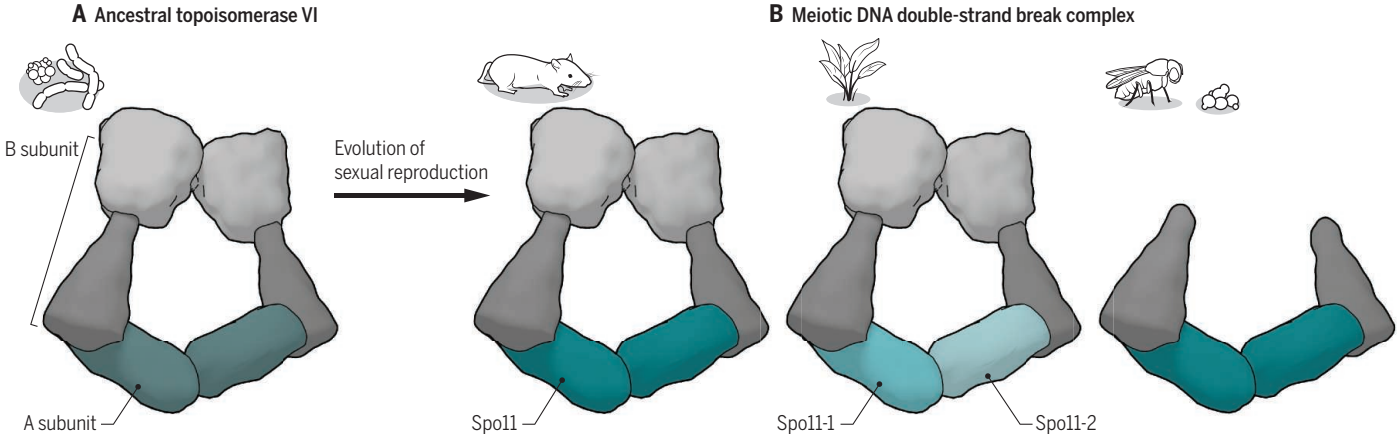

From topoisomerase to DSB-forming machine. (**A**) Topo VI uses ATP binding and hydrolysis by the B subunit to coordinate the passage of a DNA duplex through a DSB made by the A subunits, thereby altering DNA topology. (**B**) An ancestral Topo VI evolved into a meiotic DSB-forming complex that has different tertiary and quaternary structures in different organisms.

units that use adenosine triphosphate (ATP) binding and hydrolysis to control DNA cutting and to effect cycles of "gate"-closing and -opening that are needed for DNA strand passage (see the figure) (*5*).

Not surprisingly, Spo11 derives from the DNA-cleaving A subunit (*6*, *7*), but the evolutionary fate of the B subunit has been a mystery because no meiotic equivalent to the B subunit had ever been identified. This mystery has been solved with the discovery of a Topo VIB–like partner of Spo11 by Vrielynck *et al*. and Robert *et al*. This is a landmark achievement that has important implications for understanding the mechanism and regulation of meiotic DSB formation.

Vrielynck *et al*. performed a forward genetic screen in the plant *Arabidopsis thaliana*, searching for mutants with reduced fertility. The authors mapped two mutant alleles to a gene that, based on sequence similarity alone, did not reveal homology to any known functional domains. However, structural model–based homology searches revealed a match with archaeal Topo VIB. Indeed, the identified protein—named MTOPVIB for "meiotic"—retains most of the structural features of the ancestral Topo VIB, including the transducer domain that interacts with the A subunit and the ATP-binding fold (*5*). It is not known whether the latter region, known as the GHKL fold (for gyrase, Hsp90, histidine kinase, MutL), retains ATP binding and hydrolysis activity.

As expected for a bona fide partner of Spo11, Vrielynck *et al*. found that MTOPVIB is essential for DSB formation and interacts with both SPO11-1 and SPO11-2, the two Spo11 paralogs that are both required for meiotic DSB formation in *A. thaliana* (*3*). Interestingly, MTOPVIB supports an interaction between SPO11-1 and SPO11-2, which suggests that they may assemble into a heterotetrameric complex containing both SPO11 variants. This solves a long-standing puzzle as to how SPO11-1 and SPO11-2 might work together to make DSBs.

Robert *et al*. set out to identify the mouse (*Mus musculus*) MTOPVIB ortholog. Clever molecular sleuthing involving computational methods to recognize weak homology between highly diverged protein sequences led them to a meiosis-specific mouse gene that they have named *Top6bl*, for *Topo VIB–like*. As for its *A. thaliana* counterpart, mouse TOP6BL protein is predicted to be structurally similar to archaeal Topo VIB and is essential for meiotic DSB formation. TOP6BL interacts physically with mouse SPO11 and, interestingly, does so specifically with the β isoform of SPO11, a splicing variant that is responsible for the majority of DSBs in mice. Remarkably, TOP6BL does not appear to interact with SPO11α, which lacks a 38–amino acid segment in the N-terminal part of the protein that was previously suggested to be equivalent to the B subunit binding interface on archaeal Topo VIA (*5*). When coexpressed in *Escherichia coli*, TOP6BL and SPO11β can be purified as a complex that behaves as a heterotetramer.

Robert *et al*. also searched in other eukaryotes and made the surprising discovery that *Saccharomyces cerevisiae* Rec102, *Schizosaccharomyces pombe* Rec6, and *Drosophila melanogaster* MEI-P22 each have structural similarity to the archaeal B subunit. This is impressive detective work because, although the yeast and fly proteins have been known for years to be required for DSB formation and the yeast proteins had long been connected physically to Spo11 (*1*), the structural similarity to Topo VIB had never been noticed before. However, unlike the mouse and plant proteins, those from yeast and fly share homology only to the Topo VIB transducer domain and lack the GHKL fold. This points to the possibility of intriguing mechanistic variability in the core DSB machinery of these organisms or may suggest that there are as yet unidentified subunits that have taken over the (still hypothetical) ATP binding and hydrolysis activity.

The studies of Vrielynck *et al*. and Robert *et al*. change our view of the initiation of meiotic recombination by showing that the core DSB machinery resembles the ancestral topoisomerase more closely than anticipated. In principle, DNA topology-changing strand passage might no longer have been required once the ancestral topoisomerase VI had been co-opted to catalyze meiotic DSBs during the evolution of sexual reproduction. It was therefore not clear a priori that Spo11 would need to retain a B-type subunit. That it does suggests that there are new regulatory mechanisms within the DSB machinery to be revealed. So far, mechanistic studies of meiotic recombination initiation have been lacking, largely because of the insolubility of recombinant Spo11. The successful coexpression and purification of mouse TOP6BL and SPO11 may thus open new avenues for biochemical investigation.

DSBs are intrinsically dangerous, yet meiotic cells play the risky game of forming a great deal of this self-inflicted DNA damage, numbering in the hundreds of DSBs per meiotic cell in yeast and mouse (*8*). Topo VIB now finally joins Spo11 at center stage in this process. ■

ILLUSTRATION: V. ALTOUNIAN/*SCIENCE*

REFERENCES

1. I. Lam, S. Keeney, *Cold Spring Harb. Perspect. Biol.* **7**, a016634 (2015).
2. G. Bloomfield, *Semin. Cell Dev. Biol.* doi: 10.1016/j.semcdb.2016.01.026 (2016).
3. N. Vrielynck *et al*., *Science* **351**, 939 (2016).
4. T. Robert *et al*., *Science*, **351**, 943 (2016).
5. K. D. Corbett, P. Benedetti, J. M. Berger, *Nat. Struct. Mol. Biol.* **14**, 611 (2007).
6. S. Keeney, C. N. Giroux, N. Kleckner, *Cell* **88**, 375 (1997).
7. A. Bergerat *et al*., *Nature* **386**, 414 (1997).
8. F. Baudat, B. de Massy, *Chromosome Res.* **15**, 565 (2007).

10.1126/science.aaf2509

Published by AAAS

ORGANIC CHEMISTRY

Lewis acids turn unreactive substrates into pure enantiomers

Chiral organic anion binding to silyl cation provides a new platform for organocatalysis

By **Audrey Dumoulin** *and* **Geraldine Masson***

Asymmetric synthesis, reactions that produce a high proportion of one enantiomer of a chiral compound relatively to the other, are of ever-growing importance, particularly for creating pure pharmaceuticals. Asymmetric catalysis (*1*) uses a recyclable or regenerated chiral molecule to perform these reactions, but achieving high yields can be challenging if the substrate is relatively unreactive. On page 949 of this issue, Gatzenmeier *et al.* (*2*) report a highly efficient method that relies on an in situ–generated catalyst to produce complex structures in excellent yields of almost pure enantiomers from low-reactivity starting materials.

Chiral catalysts interact with substrates to create an asymmetric environment around a newly formed chiral center. Among strategies used by organic chemists to organize this interaction, Lewis acid organocatalysis, which uses chiral electron-deficient organic molecules (neutral or cationic) to address specific functional groups in substrates, has gained considerable attention because of their environmental advantages over traditional metal-centered catalysts. Nevertheless, the benefits of these organic catalysts have been tempered by the lack of sufficiently strong Lewis acids to activate unreactive substrates and by the need for large catalyst loadings. Silicon-based catalysts, whose Lewis acidity can be easily enhanced by the introduction of less Lewis basic counteranions, have been routinely used as organic Lewis acids (*3*, *4*). However, despite their high catalytic activity, few chiral silyl cationic catalysts (combining one or more chiral groups and a strong activation capacity in a single entity) have been developed. The emerging concept of asymmetric counteranion-directed catalysis (ACDC), a type of catalytic system that uses an enantiopure anion to induce enantioselectivity in a reaction arising from a cationic intermediate (*5*–*7*), allows both functions of asymmetric catalysis to be performed with separate partners, so the reactivity of each is easier to tune.

In 2009, List and co-workers (*8*) disclosed a highly enantioselective, silyl cation–catalyzed Mukaiyama aldol reaction that relies solely on the chirality of an anionic counterion (a disulfonimide anion) (see the figure, panel A) to induce asymmetry. Interestingly, extremely low catalyst loadings sufficed, thus demonstrating high catalytic performance of these new Lewis acids. However, in the Mukaiyama aldol reaction, preactivation of one substrate under the form of an *O*-silylated oxonium is required (see the figure, panel A), adding an extra step to the overall process.

Gatzenmeier *et al.* considered whether this new mode of chiral anion–directed asymmetric silyloxonium activation could be expanded to a more challenging reaction in which the silylated reagents would not be required. In this context, the Diels–Alder reaction—a [4π + 2π] cycloaddition between a diene and a dienophile for the construction of six-membered carbocycles—was selected. Despite numerous advances in enantioselective Diels–Alder reactions, some dienophiles remain poorly reactive toward this transformation, such as α,β-unsaturated esters called cinnamates (*9*).

The only previous example using cinnamates, reported by Ryu and Corey (*10*), required very high catalyst loadings. Based on their work, Gatzenmeier *et al.* performed the silylation of this unreactive α,β-unsaturated ester in situ to provide a cationic, more reactive dienophile. An enantiopure anion could then ion-pair with this cationic dienophile and create an asymmetric environment for the Diels–Alder reaction to take place (see the figure, panels B and C). The silyl-transfer reagent needs to be regenerated at the end of the process in order for it to be part of the catalytic system.

*Institut de Chimie des Substances Naturelles, CNRS UPR 2301, Université Paris-Sud, Université Paris-Saclay, Gif-sur-Yvette, France. *E-mail: geraldine.masson@cnrs.fr*

Downloaded from on February 25, 2016

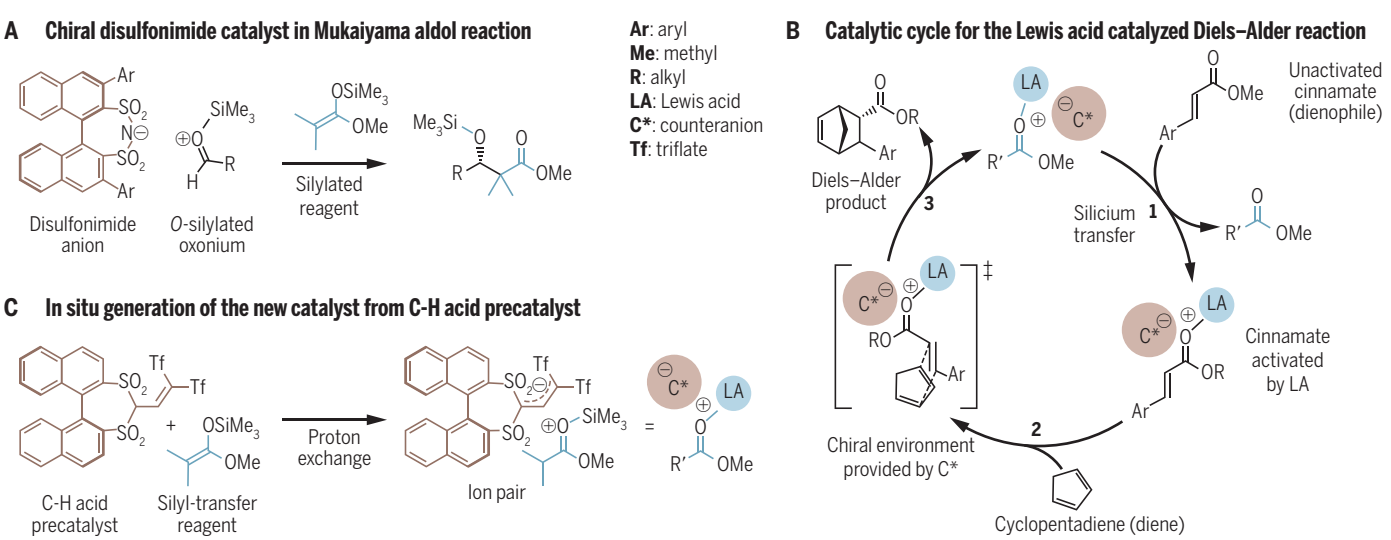

ACDC applied to the Diels–Alder reaction. Based on their previous work (**A**), Gatzenmeier *et al.* activated cinnamates via silylium-ACDC (**B**) using an in situ–generated catalyst (**C**).

ILLUSTRATION: P. HUEY/*SCIENCE*

Published by AAAS

Chiral disulfonimides were first examined as chiral counterion precursors in this reaction but had mediocre activity. Considering that the nature of counteranions strongly influences Lewis acidities of the cationic partners, Gatzenmeier *et al.* decided to investigate the Diels–Alder reaction with carbanions, which would be expected to form a combination of greater overall Lewis acidity. To evaluate those carbon-centered anions, they designed a range of enantiopure C–H acid precatalysts that would react in situ with the silyl-transfer reagent to generate an ion pair as a catalyst (see the figure, panels B and C). With respect to the substrate scope, Gatzenmeier *et al.* achieved impressive stereoinductions (up to 97:3 enantiomer ratio) and excellent yields in such a transformation. The protocol can be applied to a variety of cinnamates, including hetero-aromatic substrates, showing its wide applicability. Furthermore, this strategy cleverly combines the benefits of silylated compounds (nontoxic and air and water stable) with exceptionally low catalyst loadings (only 1 mole percent).

The work of Gatzenmeier *et al.* allows normally unreactive cinnamates to undergo Diels–Alder cyclization. This method of activation based on the tunability of Lewis acids could give rise to extensive applications in any challenging Lewis-acid–catalyzed reaction. More broadly, through its C–H acidic function, this new catalyst could turn into an effective alternative in reactions catalyzed by Brønsted acids. ■

"This method of activation based on the tunability of Lewis acids could give rise to extensive applications in any challenging Lewis-acid–catalyzed reaction."

REFERENCES

1. E. N. Jacobsen, A. Pfaltz, H. Yamamoto, *Comprehensive Asymmetric Catalysis Suppl. 1 & 2* (Springer, Berlin, Heidelberg, 2004).
2. T. Gatzenmeier *et al.*, *Science* **351**, 949 (2016).
3. H. F. T. Klare, M. Oestreich, *Dalton Trans.* **39**, 9176 (2010).
4. A. D. Dilman, S. L. Ioffe, *Chem. Rev.* **103**, 733 (2003).
5. M. Mahlau, B. List, *Angew. Chem. Int. Ed.* **52**, 518 (2013).
6. K. Brak, E. N. Jacobsen, *Angew. Chem. Int. Ed.* **52**, 534 (2013).
7. R. J. Phipps, G. L. Hamilton, F. D. Toste, *Nat. Chem.* **4**, 603 (2012).
8. P. García-García *et al.*, *Angew. Chem. Int. Ed.* **48**, 4363 (2009).
9. B. Mathieu, L. de Fays, L. Ghosez, *Tetrahedron Lett.* **41**, 9561 (2000).
10. D. H. Ryu, E. J. Corey, *J. Am. Chem. Soc.* **125**, 6388 (2003).

10.1126/science.aaf2577

IMMUNOLOGY

Maternal T_H17 cells take a toll on baby's brain

Infection produces an immune molecule that interferes with brain development

By **Myka L. Estes** *and* **A. Kimberley McAllister**

The possibility that microcephaly is caused by Zika virus has made recent alarming headlines. Although few people had previously heard of an association between infection during pregnancy and changes in brain development, epidemiologists have known about this connection for many years. Moreover, mounting evidence suggests that maternal immune activation (MIA) alone is sufficient to alter brain development and may be causally linked to autism spectrum disorder (ASD) (*1*–*3*). How could the maternal immune system, which normally serves to protect mother and child from environmental insults, cause changes in brain development? On page 933 of this issue, Choi *et al.* (*4*) uncover an important component of this immune pathway: a critical signal from a special class of cells in the mother's immune system, called T helper 17 (T_H17) cells, that alters brain development in her fetal offspring (see the figure). These findings have exciting implications for the development of new treatments to prevent ASD caused by maternal infection.

How does the mother's immune system, which has limited access to the fetal compartment, alter brain development? Cytokines, immune system signaling molecules that are generated in response to infection, can cross the placental boundary and are critical for MIA to change brain development and behavior in offspring. One of the first cytokines elevated in the serum of pregnant mice after immune activation is interleukin-6 (IL-6). This increase is necessary and sufficient for MIA to alter brain development and behavior in offspring (*5*). Choi *et al.* have now identified another cytokine, IL-17, that is necessary and sufficient to mediate the effects of MIA. But this isn't just another cytokine to add to the steadily growing list of factors implicated in MIA. Choi *et al.* convincingly show, using several genetic mouse models and targeted blockade, that IL-17 acts downstream of IL-6 in offspring after MIA. Whereas previous studies identifying cytokines involved in MIA raised more questions than they answered, Choi *et al.* present an impressive series of experiments demonstrating the role of IL-17 in mediating the effects of MIA in offspring. Moreover, the authors have identified its cellular source: IL-17 is secreted by T_H17 cells present in the mother's circulating blood, where it crosses the placenta and acts in the brain of developing offspring. IL-17 increases the cellular expression of IL-17 receptor, further increasing IL-17 signaling in the fetal brain. This sequence of events is required for MIA to cause cortical malformations and the three core behavioral abnormalities associated with ASD (*4*). How IL-17 exerts its effects, and upon which cells and with what molecular consequences, is still a mystery, especially because the literature on IL-17 signaling in the brain remains limited and contradictory.

Although IL-17 and the cells that produce it, T_H17 cells, have been implicated in ASD through both genetic associations and observations of elevated IL-17 concentration in the blood of children (*6*–*8*), there was no evidence for a role for T_H17 cells in MIA until the Choi *et al.* study. T_H17 cells protect against bacterial and fungal pathogens, especially at mucosal surfaces such as the gut, and are an important part of an inflammatory response to infection (*9*). T_H17 cells may also be critical for the development of autoimmunity and have been implicated in numerous animal models of autoimmune disorders (*10*). For their study, Choi *et al.* used a specific mouse strain that is widely used to generate animal models for experimental autoimmune encephalomyelitis and obesity-induced diabetes (*11*). This choice may have produced a more relevant and robust phenotype relative to other mouse strains commonly used to study MIA.

The strain used in Choi *et al.* exhibits a propensity for T_H17 polarization due to a distinct microbiota signature, whereas mice lacking T_H17-inducing microbiota, and therefore having barely detectable levels of T_H17

Center for Neuroscience, University of California, Davis, CA 95618, USA. E-mail: kmcallister@ucdavis.edu

Downloaded from on February 25, 2016

Published by AAAS

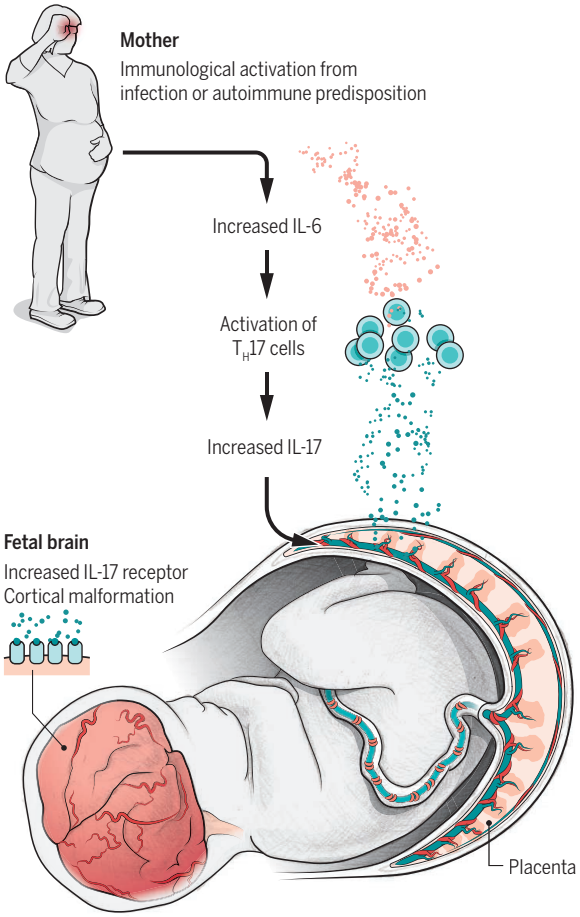

Maternal immune activation (MIA). The hypothetical model shown is based on mouse experiments and illustrates that MIA, possibly in combination with a predisposition for autoimmunity, leads to an increase in T_H17 cells in maternal blood. These cells release IL-17, which crosses the placenta and increases expression of the IL-17 receptor in the offspring's brain. This in turn leads to ASD-related cortical and behavioral abnormalities in the offspring.

cells, are often used to generate the MIA model (*9*, *11*–*13*). This altered baseline immune response may explain the surprising, long-lasting increase in IL-1β concentration in maternal blood observed by Choi *et al.* in pregnant mice after they were injected with polyinosinic-polycytidylic acid [poly(I:C)], relative to the transient increase in IL-1β blood concentration typical of other mouse strains (*14*). Poly(I:C) is a synthetic double-stranded RNA that tricks the immune system into responding as though the host is infected with a virus. Poly(I:C) injection to induce MIA did not induce T_H17 cell generation in a mouse strain that typically does not express T_H17 cells (*12*). Thus, future research should determine whether induction of T_H17 cell generation is critical for the effects of MIA regardless of genetic background, or whether it specifically mediates the effects of MIA in mice with T_H17 cell polarization. The latter possibility may be of even greater interest, as it is consistent with epidemiological studies implicating a family history of autoimmunity in ASD (*1*) and would imply that infection in pregnant women with increased T_H17 cell numbers might lead to a greater likelihood of ASD in offspring.

With their discovery that injection of a function-blocking antibody to IL-17 after MIA induction in mice decreases the severity of some ASD behaviors in offspring, Choi *et al.* raise the possibility that pharmacological intervention in the IL-17 pathway could prevent ASD caused by maternal infection. It is important to note, however, that the subset of pregnant mothers who experience a strong infection and will go on to have a child with ASD is incredibly low (*1*, *3*). Moreover, cytokines are sneakily versatile—just when you think you know what they're up to, they turn out to be integral to some unrelated process. Thus, inhibiting IL-17 in infected mothers may have consequences as detrimental as the infection itself, because many cytokines play important roles in typical brain development (*1*). The study by Choi *et al.* suggests that women with T_H17 skewing may have a much higher risk that ultimately warrants intervention. In this regard, alternative approaches to dampening T_H17 cell differentiation, such as treatment with vitamin D and/or retinoic acid (a metabolite of vitamin A) (*10*) or manipulation of intestinal microbiota (*11*, *15*), will be exciting avenues of investigation. ■

REFERENCES

1. M. L. Estes, A. K. McAllister, *Nat. Rev. Neurosci.* **16**, 469 (2015).
2. H. O. Atladottir *et al.*, *J. Autism Dev. Disord.* **40**, 1423 (2010).
3. H. O. Atladottir *et al.*, *Pediatrics* **130**, e1447 (2012).
4. G. B. Choi *et al.*, *Science* **351**, 933 (2016).
5. S. E. Smith, J. Li, K. Garbett, K. Mirnics, P. H. Patterson, *J. Neurosci.* **27**, 10695 (2007).
6. L. Y. Al-Ayadhi, G. A. Mostafa, *J. Neuroinflamm.* **9**, 158 (2012).
7. K. Suzuki *et al.*, *PLOS ONE* **6**, e20470 (2011).
8. B. van der Zwaag *et al.*, *PLOS ONE* **4**, e5324 (2009).
9. I. I. Ivanov *et al.*, *Cell Host Microbe* **4**, 337 (2008).
10. S. K. Bedoya, B. Lam, K. Lau, J. Larkin III, *Clin. Dev. Immunol.* **2013**, 986789 (2013).
11. I. I. Ivanov *et al.*, *Cell* **139**, 485 (2009).
12. M. Mandal, A. C. Marzouk, R. Donnelly, N. M. Ponzio, *Brain Behav. Immun.* **25**, 863 (2011).
13. Y. Yang *et al.*, *Nature* **510**, 152 (2014).
14. U. Meyer *et al.*, *J. Neurosci.* **26**, 4752 (2006).
15. E. Y. Hsiao *et al.*, *Cell* **155**, 1451 (2013).

10.1126/science.aaf2850

RNA

CRISPR goes retro

RNA contributes directly to the immunological memory recorded in CRISPR sequences

By **Erik J. Sontheimer**[1] *and* **Luciano A. Marraffini**[2]

Genetic invasions threaten nearly all cells and genomes. Bacteria and archaea "remember" encounters with invaders through an adaptive immunity strategy involving clustered, regularly interspaced, short palindromic repeats (CRISPRs). These repeats can store snippets of an invader's genome as "spacers" (*1*), which then constitute a heritable memory that can instruct an immune response against future encounters with foreign DNAs carrying those same sequences. The ability to form new memories of invasion depends on the ability of a CRISPR to incorporate new spacers. The mechanistic basis for this acquisition from DNA is increasingly understood (*2*) and has often been assumed to be the sole mode of CRISPR adaptation. On page 932 of this issue, Silas *et al.* (*3*) describe an intriguing twist on bacterial adaptive immunity, identifying a subset of CRISPR systems with the remarkable ability to incorporate new spacers directly from RNA.

Destruction of foreign DNA is achieved by CRISPR-associated (Cas) proteins (nucleases) that are guided to their targets by spacer-derived transcripts [CRISPR RNAs (crRNAs)]. Once crRNAs recognize the foreign DNA by base pairing, the Cas nuclease cleaves the target. CRISPR-Cas systems are exceptionally diverse (*4*). Most are classified as type I or type III, and both of these types depend on multisubunit complexes for target recognition and destruction (*1*, *4*). A type III-A system was the first to be revealed as a DNA interference pathway (*5*), and DNA targeting is now known to be a shared feature of virtually all CRISPR-Cas systems (*1*). However, type III-B systems have long been known to have RNA-targeting capacity (*6*), and this capability was later uncovered in type III-A

[1]*RNA Therapeutics Institute, Program in Molecular Medicine, University of Massachusetts Medical School, Worcester, MA 01605, USA.* [2]*Laboratory of Bacteriology, The Rockefeller University, New York, NY 10065, USA. E-mail: erik.sontheimer@umassmed.edu; marraffini@rockefeller.edu*

ILLUSTRATION: V. ALTOUNIAN/*SCIENCE*

Downloaded from on February 25, 2016

Published by AAAS

systems as well (*7*, *8*). A unified model is now emerging in which type III systems perform cotranscriptional degradation of both DNA targets and their RNA transcripts (*5*–*11*). Might this unique dual targeting mechanism of type III systems be tied to a similar duality in spacer acquisition?

Silas *et al*. explored this question by noting predicted reverse transcriptase (RT) enzymes in a subset (~8%) of bacterial type III CRISPR-Cas systems, including a type III-B system from the MMB-1 strain of the marine bacterium *Marinomonas mediterranea*. RTs use RNAs as templates for DNA synthesis and drive the reverse flow of genetic information associated with retroviruses and retroelements (genetic elements that are incorporated into a DNA genome after reverse transcription of RNA molecules) (*12*). Many of the CRISPR-associated RTs (including that from MMB-1) are fused to Cas1, a nuclease that, along with Cas2, catalyzes the integration of new spacers into the bacterial CRISPR locus (*2*, *13*). To investigate the function of this unusual RT domain in MMB-1 cells, Silas *et al*. overexpressed RT-Cas1 and Cas2 and detected new CRISPR spacers (in this case, derived from sequences appearing elsewhere in the host genome). The host sequences that gave rise to the new spacers were biased toward regions that are highly transcribed into RNA during the normal course of host gene expression. The authors showed that this bias depended on the RT activity of RT-Cas1. Furthermore, experiments with self-splicing intron-containing transgenes indicated that spliced sequences could be detected among the new spacers. Because splicing can only occur at the RNA level, these sequences must have previously passed through an RNA phase, suggesting a likely RNA source for spacer acquisition. To confirm this possibility, Silas *et al*. expressed MMB-1 RT-Cas1 and Cas2 proteins in *Escherichia coli* cells, purified them, and used them in combination to catalyze the initial steps of spacer integration using defined components in vitro, including synthetic RNAs or DNAs as spacer precursors (protospacers). Strikingly, either RNA or DNA could be ligated directly to the CRISPR-like substrate (see the figure). Furthermore, the ligation of RNA into the CRISPR locus depended on the RT domain, consistent with the results in MMB-1 cells. Most gratifying of all, when the reaction was furnished with 2′-deoxynucleotides, the RT domain catalyzed DNA synthesis of the new spacer, using the inserted RNA as a template and the opposite strand of the target CRISPR DNA as a primer. The framework established by Silas *et al*. is that DNA spacer acquisition by type III systems, although it clearly occurs, is not the whole story: The subset of systems that includes an RT module can also record RNA memories.

What does this advance mean for our broader view of the type III CRISPR pathway? RNA acquisition provides a potential source of spacers from RNA bacteriophage (*8*), even though no RNA phage-matching spacers have yet been documented in any natural CRISPR locus. Furthermore, direct RNA acquisition provides a route for CRISPR spacers to be taken selectively from transcribed regions of invasive DNA genomes. This is important not only for the RNA-targeting branch of the pathway (*6*–*8*, *14*) but for type III DNA targeting as well, because the latter can only occur with DNAs that are undergoing active transcription and with crRNA guides that are antisense to both the DNA and its transcripts (*9*–*11*, *14*, *15*). With this in mind, however, one aspect of this work only deepens the mysteries of type III interference: Both in vitro and in cells, RNA spacers can insert into the CRISPR locus in either orientation, leading to little or no antisense bias for the resulting crRNAs.

The lack of apparent directionality to RNA spacer acquisition suggests that ~50% of all new RNA-derived spacers are useless for defense. Could the system really be that profligate (perhaps buffered by recombinational spacer loss in the absence of selective pressure for retention), or are there other pieces of the type III CRISPR-Cas puzzle that we do not yet recognize? Similarly, how do the majority of type III systems that lack the RT function achieve spacer acquisition directionality? Whatever the answers to these questions, our understanding of CRISPR biology and mechanism is now greatly enriched by the elegant demonstration by Silas *et al*. that some CRISPR spacers are, in essence, retroelements. ■

REFERENCES

1. L. A. Marraffini, *Nature* **526**, 55 (2015).
2. G. Amitai, R. Sorek, *Nat. Rev. Microbiol.* **14**, 67 (2016).
3. S. Silas *et al*., *Science* **351**, aad4234 (2016).
4. K. S. Makarova *et al*., *Nat. Rev. Microbiol.* **13**, 722 (2015).
5. L. A. Marraffini, E. J. Sontheimer, *Science* **322**, 1843 (2008).
6. C. R. Hale *et al*., *Cell* **139**, 945 (2009).
7. R. H. Staals *et al*., *Mol. Cell* **56**, 518 (2014).
8. G. Tamulaitis *et al*., *Mol. Cell* **56**, 506 (2014).
9. L. Deng *et al*., *Mol. Microbiol.* **87**, 1088 (2013).
10. W. Peng, M. Feng, X. Feng, Y. X. Liang, Q. She, *Nucleic Acids Res.* **43**, 406 (2015).
11. P. Samai *et al*., *Cell* **161**, 1164 (2015).
12. A. Beauregard, M. J. Curcio, M. Belfort, *Annu. Rev. Genet.* **42**, 587 (2008).
13. J. K. Nuñez *et al*., *Nature* **519**, 193 (2015).
14. W. Jiang, P. Samai, L. A. Marraffini, *Cell* **164**, 710 (2016).
15. G. W. Goldberg *et al*., *Nature* **514**, 633 (2014).

10.1126/science.aaf2851

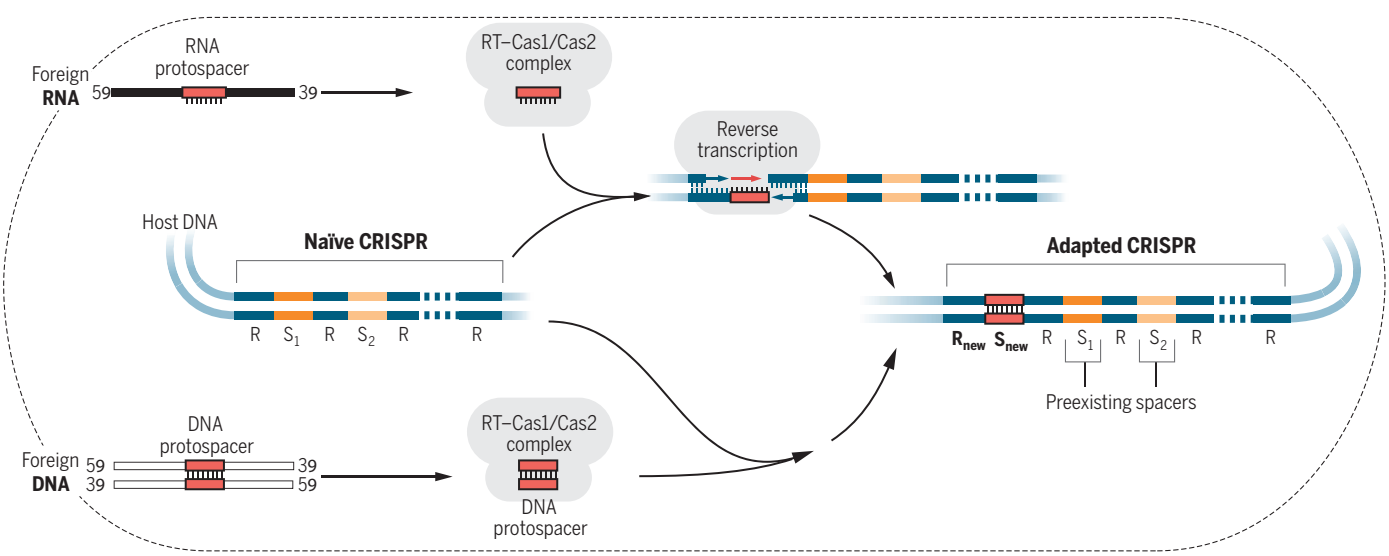

ILLUSTRATION: K. SUTLIFF/*SCIENCE*

CRISPR recordings of RNA memories. A naïve CRISPR with its repeats (R) and preexisting spacers (S_1, S_2, ...) can acquire a new spacer (S_{new}) via spacer precursors (red) that arise from either RNA (black, top left) or DNA (white, bottom left). RNA spacer precursors are directly inserted and then reverse-transcribed. Intermediate steps are omitted for clarity.

Published by AAAS

CONSERVATION

Evolution in the Anthropocene

Taking account of the evolutionary effects of human actions is crucial for humans and nonhumans

By **François Sarrazin**[1] *and* **Jane Lecomte**[2]

Most current conservation strategies focus on the immediate social, cultural, and economic values of ecological diversity, functions, and services (*1*). For example, the Intergovernmental Platform on Biodiversity and Ecosystem Services (*2*) mostly addresses the utilitarian management of biodiversity from local to global scales. However, besides urgent diagnosis and actions (*3*, *4*), processes that occur over evolutionary time scales are equally important for biodiversity conservation. Strategizing for conservation of nature at such long time scales will help to preserve the function—and associated services—of the natural world, as well as providing opportunities for it to evolve. This approach will foster a long-term, sustainable interaction that promotes both the persistence of nature and the well-being of humans.

Considering the evolutionary trajectories of nonhumans beyond human interest may also constitute a major evolutionary transition (*5*). It would be the first case in the history of life on Earth where a species cares for the evolution of other species beyond its own fitness and well-being.

Most conservation actions aim to protect particular populations, species, communities, ecosystems, or ecosystem services. Although these actions target important current issues, they also affect the evolutionary trajectories of these systems in various, generally unplanned ways. For many taxonomic groups, such as primates or island birds, anthropogenic extinctions are not phylogenetically random (*6*). Further, extinctions and population size reductions may greatly constrain the evolutionary trajectories not only of the target species, but also of other members of the community or ecosystem. Such unintended changes occur, for example, through extinction cascades (*6*), changes in direct and indirect selective pressures on genetic and phenotypic diversity, and alteration of interaction networks and coevolutionary networks. These consequences are rarely considered when actions are taken to preserve or promote specific ecosystem services (*7*). We thus know very little about how our current focus on such services will affect long-term ecosystem function, composition, and stability.

In agriculture, domestication syndrome is a tangible example of how a focus on one or a few specific desirable components of a species or system can have unexpected evolutionary consequences. In this syndrome, a consistent set of morphological traits (such as reduced brain size in animals or non-shattering seeds in plants) can emerge as a result of selection for a different set of desired traits. Thus, active selection of specific desired traits causes the retention of not only those traits, but a suite of other traits that are both unintended and currently outside of human control.

We expect a similar process to occur as we begin to enact larger-scale selection on nature for specific purposes. This is critical for the intensive exploitation of biodiversity by humans (*8*). Some nature-based solutions set up to mitigate the effects of climate change—such as planting forests for carbon storage, using biomass to produce green energy, or protecting coastal wetlands to adapt to rising sea levels—are also likely to change local ecological selection regimes, causing shifts in evolutionary trajectories. Cultural and recreational services may similarly shape evolutionary trajectories by defining particular strategies of rewilding, restoring, and perhaps even resurrecting extinct species (*9*).

Finally, advances in synthetic biology and genetic engineering are likely to lead to the emergence of new types of organisms, including some designed for environmental engineering. This particular strategy would open up an especially worrying "Pandora's box" of novel genetic and ecological interactions. Although we can manage the desirable traits or target functions of species and ecosystems, control of the evolutionary consequences of such actions is not within our power. It is therefore essential to explore how nature can be conserved for maximum evolutionary freedom.

All life, both human and nonhuman, is a product of evolution. Through evolutionary luck and niche construction, humans have reached a point where our quest for well-being goes beyond the requirements of survival and reproduction (i.e., beyond evolutionary fitness). Humans also assign intrinsic values to entities that have their own ends, and they assign instrumental values to entities that are means to achieve other ends (*10*).

Thinking about both humans and nonhumans within this kind of evolutionary and ethical framework allows us to address basic questions about different conservation scenarios (see the figure). Should we abandon attempts at biodiversity conservation? This scenario would mean pursuing a human evolutionary trajectory that ignores nonhumans in a blind Anthropocene—a choice sure to have many unintended consequences (*11*).

Alternatively, do we conserve biodiversity for the resilience of human generations, either for the immediate well-being of human individuals or for the well-being of future generations? In these scenarios, we place instrumental value only on specific, desired traits of nature—again with unintended and unknown consequences.

Finally, do we conserve biodiversity for the well-being of future human generations as well as nature? In ecological systems, the well-being of nonhumans is mostly driven by their fitness. Conservation for people and nature (*1*) must then rely not only on intrinsic values of human well-being and fitness, but also on nonhu-

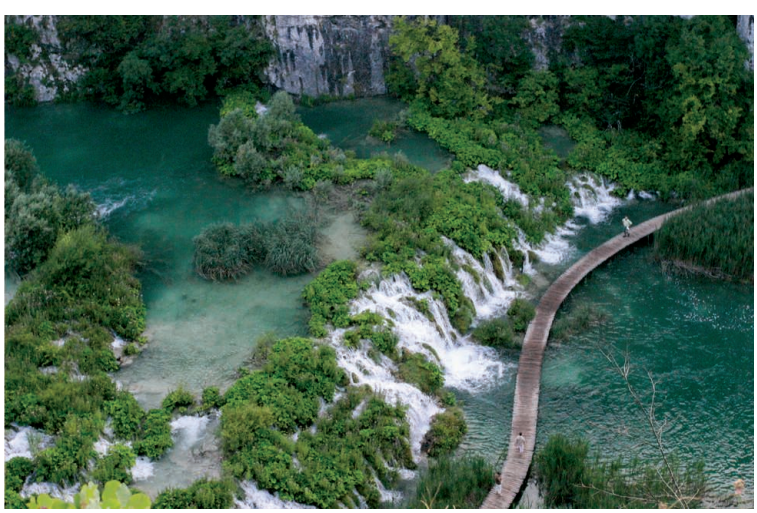

PHOTO: F. SARRAZIN

Treating nature with respect. Human-made structures that protect natural interactions reduce the impact of human visitors on biodiversity in the Plitvice Lakes National Park, Croatia.

Downloaded from on February 25, 2016

Published by AAAS

Evolutionary roots, challenges, and consequences of conservation strategies and ethics

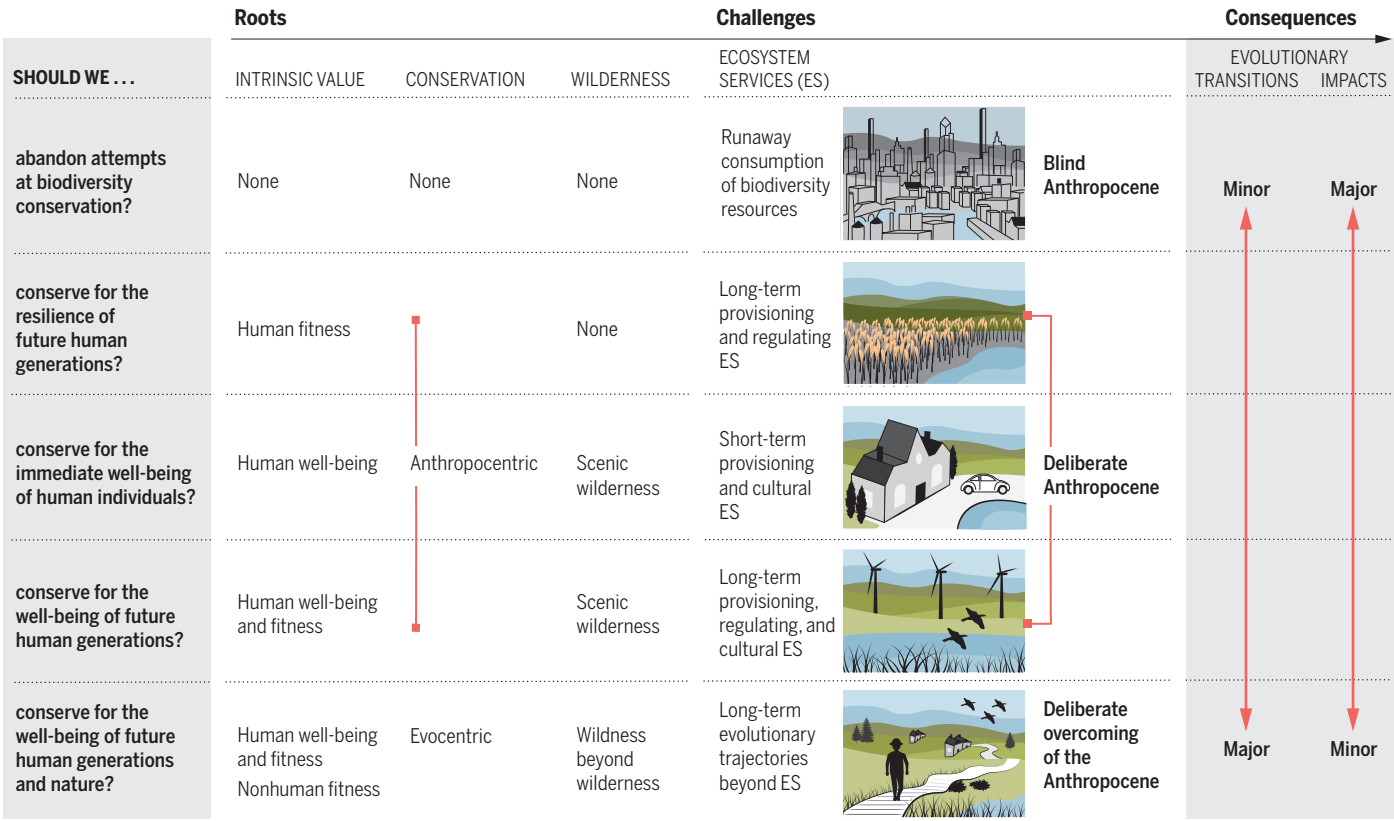

man fitness. It requires an interspecific form of altruism to achieve neutrality on nonhuman evolutionary trajectories, whatever our genetic distance toward nonhumans, the services we expect from them, their beauty, or our need for nature. Such evolution-focused or "evocentric" conservation could be part of a deliberate overcoming of the Anthropocene (see the figure).

The aim to conserve the evolutionary potential of nonhumans has many consequences. It requires us to define operational metrics of evolutionary potential that account for phylogenetic diversity and evolutionary distinctiveness (*6*); genetic, functional, and cultural diversity within populations; and networks of interactions within communities and ecosystems.

To make progress toward these goals, we must remember that biodiversity and ecosystem functioning support evolutionary processes, and not the opposite. Furthermore, it is crucial that we view adaptation to global change as a necessary means of enabling the potential evolution of nonhumans (and not merely a means of adapting natural systems solely to short-term human ends).

[1]*Sorbonne Universités, UPMC Univ Paris 06, Muséum National d'Histoire Naturelle, CNRS, CESCO, UMR 7204, 75005 Paris, France.* [2]*Ecologie Systématique Evolution, Univ. Paris-Sud, CNRS, AgroParisTech, Université Paris-Saclay, 91400 Orsay, France. E-mail: sarrazin@mnhn.fr*

The deliberate creation and stewardship of evolutionary trajectories through synthetic biology or genetic engineering should not be used to replace native life forms or affect their evolution, but only as a very last resort to reduce our evolutionary impacts on them. To reduce the spatial and temporal extent of human directional selective pressures, it is also important to maintain and restore wildness wherever possible, even outside areas of pristine wilderness.

Reducing the increasing rate at which human activities perturb nonhuman dynamics is a prerequisite to evocentric conservation (see the photo). Indeed, generation times constrain the speed of adaptive responses of most species and populations, particularly of long-lived and specialist ones. Conserving nonhuman evolutionary potential therefore requires a fundamental shift in the burden of proof from "why conserve?" to "why destroy?" biodiversity.

Many stakeholders and conservationists consider conservation for nature itself as outdated, utopian, or inefficient. They advocate a "new conservation" dedicated to people (*12*). However, at the scale of evolution, considering other life forms as resources—even in a broad sense—is not innovative. The deliberate conservation of the evolutionary potential and opportunity of nonhumans beyond the services they provide us with is, by contrast, a real novelty. It forces us to think about links between human and nonhuman evolutionary trajectories and reduces the focus on a trade-off between long-term human well-being and wildness (see the figure).

What we conserve defines what we are or pretend to be. We must establish and promote comprehensive dialogs among social scientists, ecologists, and evolutionary biologists to explore the biological and cultural roots of our interactions with nonhumans and to understand the origins of our inertia in the face of the urgency of biodiversity erosion. Addressing this major challenge for humanity may also enhance our ability to respect each other in our societies. ■

REFERENCES

1. G. M. Mace, *Science* **345**, 1558 (2014).
2. S. Díaz *et al.*, *Curr. Opin. Environ. Sustain.* **14**, 1 (2015).
3. A. D. Barnosky *et al.*, *Nature* **471**, 51 (2011).
4. S. L. Pimm *et al.*, *Science* **344**, 1246752 (2014).
5. E. Clarke, *J. Biosci.* **39**, 303 (2014).
6. S. Veron, T. J. Davies, M. W. Cadotte, P. Clergeau, S. Pavoine, *Biol. Rev.* 10.1111/brv.12228 (2015).
7. D. P. Faith *et al.*, *Curr. Opin. Environ. Sustain.* **2**, 66 (2010).
8. C. T. Darimont, C. H. Fox, H. M. Bryan, T. E. Reimchen, *Science* **349**, 858 (2015).
9. P. J. Seddon, C. J. Griffiths, P. S. Soorae, D. P. Armstrong, *Science* **345**, 406 (2014).
10. J. A. Vucetich, J. T. Bruskotter, M. P. Nelson, *Conserv. Biol.* **29**, 321 (2015).
11. W. Steffen *et al.*, *Science* **347**, 1259855 (2015).
12. R. T. Corlett, *Trends Ecol. Evol.* **30**, 36 (2015).

10.1126/science.aad6756

ILLUSTRATION: K. SUTLIFF/*SCIENCE*

Published by AAAS

BOOKS *et al.*

DATA SCIENCE

The social revolution

A team of researchers sheds light on when and how we participate in politics online

By **Arnout van de Rijt**

We like, share, and sign electronic petitions on social media—but do our online actions translate to real change?

Social media platforms, e-petitioning websites, and activists' social networks have made it easier than ever for dispersed collectives to communicate in their fight for a common cause. In *Political Turbulence*, Helen Margetts, Peter John, Scott Hale, and Taha Yasseri show how our use of these online tools leaves behind a treasure trove of digital traces that can be fruitfully employed for social scientific inquiry.

Scholars interested in working with these new data and techniques will find detailed examples and applications explaining how the authors obtained their data and how results may be replicated. The authors draw on a wide range of data sources—including laboratory, natural, and field experiments, as well as large-scale digital data captured from social media platforms—and employ both traditional social science methods and techniques imported from the computer and natural sciences.

The intellectual focus of the book is the social mechanisms through which new media allow individuals to be persuaded to join a collective effort. The authors present a number of empirical results on the susceptibility of individuals to social influence that speak to the disciplines of political science, sociology, psychology, economics, network science, and complex systems. For example, the authors find that the chance that a funding goal will be reached roughly doubles when everyone can see who has contributed in real time. Chances of funding also double when individuals can observe how much has been raised from how many others.

The authors further demonstrate how the "Big Five" personality traits—openness, conscientiousness, extroversion, agreeableness, and neuroticism—as well as how one chooses to allocate resources between oneself and another person (known as social value orientation), affect both an individual's willingness to partake in collective action and his or her susceptibility to social pressure. Extroverts in particular are more willing than others to be the first to contribute money toward a public good, and their participation in the early phase of mobilization can make or break a collective effort.

Consistent with other forms of online activity and theories of social contagion, the authors find the distributions of Internet mobilization to be extreme: Millions of initiatives typically accumulate just a handful of supporters, while just a handful of campaigns reach millions. Nearly all clicks, signatures, and donations happen in brief episodes of hyperactivity, while most of the time campaigns lie dormant.

The question that this book cannot answer is whether the social dynamism observed in Internet-facilitated communication translates into significant political action. Have social media simply replaced traditional modes of organization, or have they empowered collectives with effective instruments to achieve policy change? Are the commonly heard charges of "slacktivism" and "clicktivism"—allegations that electronic signatures are just empty gestures—unfounded? Although the findings presented in the book cannot speak to the ultimate impact on policy, the authors nonetheless suggest an affirmative answer throughout the book.

This position is advanced most forcefully in the final chapter, where the authors develop the argument that social media and modern communication technologies allow citizens with various minority beliefs and niche interests to effectively impact politics, thereby limiting the exercise of power by a dominant group or ruling organization.

This argument, however, would seem in tension with the rest of the book. The evidence presented in the earlier chapters supports a model in which people are susceptible to the opinions and actions of others and participation is triggered by the legitimacy of large crowds. Would we not expect this susceptibility to favor the loudest voices coming from the strongest forces—states and organizations funded by wealthy donors? If, as has previously been found, social media often echo traditional media, would they not increase people's vulnerability to conformity pressure, propaganda, and agenda setting?

Although the evidence presented in the book may permit a conclusion opposite to the one the authors draw, with social media serving as a tool of rather than a weapon against vested interests, it nonetheless contributes an important series of creatively and rigorously researched insights into the social mechanics of Internet-based collective action, handing researchers a new toolbox of methods and techniques in the process.

The reviewer is at the Department of Sociology, Utrecht University, Utrecht, Netherlands. E-mail: a.vanderijt@uu.nl

Political Turbulence
How Social Media Shape Collective Action
Helen Margetts, Peter John, Scott Hale, Taha Yasseri
Princeton University Press, 2016. 297 pp.

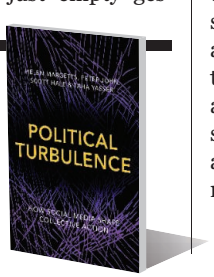

10.1126/science.aaf0971

Downloaded from on February 25, 2016

PHOTO: ASSOCIATED PRESS

Published by AAAS

ENGINEERING

Moving forward

A history of America's bridges and roadways offers lessons for the future of physical infrastructure

By **Lee Vinsel**

The Road Taken
The History and Future of America's Infrastructure
Henry Petroski
Bloomsbury, 2016. 335 pp.

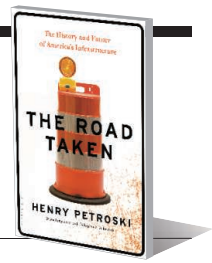

In a 2014 opinion column in *The New York Times*, the Nobel Prize–winning economist Paul Krugman declared that, with the country still in post-2008 economic doldrums, it is "a very good time to invest in infrastructure." Yet, despite a number of recent appeals to revive and improve the country's physical support systems, there is reluctance among legislators and the public to commit the necessary funds to do so. It would seem that the United States, a nation that is otherwise obsessed with technological innovation, is not so keen on maintaining the technology it has already built.

Henry Petroski examines this tension between creation and neglect in his new book, *The Road Taken*. It joins recent works, like Rosabeth Moss Kanter's *Move: Putting America's Infrastructure Back in the Lead*, in calling for better care of our built environment.

In earlier books, like *To Engineer Is Human* and *To Forgive Design*, Petroski used his critical acumen to show what we can gain from failure, even disaster. Acknowledging that "infrastructure connotes the sum of a society's physical improvements and denotes the public works," like "roads, bridges, and water supplies," as well as the "works of private enterprise," like "fiber-optic, wireless, cellular, and other information and communication networks," Petroski focuses more narrowly on roadways and other components of ground transportation in *The Road Taken*.

The book's title is a reference to Robert Frost's famous 1916 poem "The Road Not Taken," in which the narrator recalls coming to a fork in the road and arbitrarily choosing to take the path less traveled. Petroski detects the same kind of ambivalence in our attitude toward infrastructure.

The High Line park in Manhattan was built on an elevated section of a disused spur of the New York Central Railroad.

PHOTO: © BLAINE HARRINGTON III/CORBIS

Although Petroski does not use the term, *The Road Taken* is about what economists and other social scientists call "path dependence": the idea that past decisions limit present and future decisions and that chains of choices often draw us to particular results. In other words, the material world that we inherit from our forebears defines both our liabilities and our opportunities.

Several chapters of *The Road Taken* began their lives as columns that Petroski wrote for *American Scientist*, so the book does not develop a central argument but rather looks at the situation from several vantage points. Petroski begins by providing a history of our concern with infrastructural decline. In 1981, Pat Choate and Susan Walter published *America in Ruins: The Decaying Infrastructure*, which documented the precipitous drop in infrastructure investment that began in the mid-1950s. The book initiated a wave of discussion that led to the development of the American Society of Civil Engineers' (ASCE's) infrastructure report cards, which rate federal- and state-level infrastructure according to capacity, condition, funding, future need, operation and maintenance, public safety, resilience, and innovation. Since the inception of the ASCE report cards, America's highways, bridges, water resources, and waste management facilities have, on the whole, received very bad grades indeed.

Other parts of the book elucidate the origins of various components of roadway infrastructure, including histories of road construction, the American interstate highways, and the system of lines, signs, and signals. Petroski outlines the often quirky visionaries behind the things we take for granted, such as William Phelps Eno, the eccentric obsessive who created the nation's first traffic laws in New York City in 1903. But he also does a good job describing the role that government agencies played in standardizing our physical environment. Many parts of the book are lyrical and include Petroski's personal reflections on growing up in New York City and driving around many parts of the country.

The book's biggest problem is that it says almost nothing about climate change. Petroski may have felt that the topic was too far afield. Yet, Americans' heavy car use—and the infrastructure built to support it—is one of the nation's largest sources of greenhouse gases. The book's only concession to this problem comes in its 19th chapter, which features a delightful meditation on how we might repurpose bridges and roads as parks and public spaces rather than attempting to maintain the whole of the infrastructure that we have erected to date.

Despite this omission, Petroski presents one of the clearest (and most entertaining) cases yet for why we must improve the network of roads, bridges, and highways we take for granted.

The reviewer is at the College of Arts and Letters, Stevens Institute of Technology, Hoboken, NJ 07030, USA. E-mail: lee.vinsel@gmail.com

10.1126/science.aaf0845

Downloaded from on February 25, 2016

Published by AAAS

LETTERS

Edited by **Jennifer Sills**

Trading away ancient amber's secrets

IN THE SWAMPS of North Myanmar lies some of the oldest stone in the world. Burmese amber (burmite) is more than 100 million years old (*1*, *2*). Unlike more recent ambers from the Baltic Sea (*3*), Dominica (*4*), and India (*5*), burmite formed in the early Cretaceous period, when the first flowering plants were beginning to grow and major tectonic shifts were changing the positions of the continents. About 1% of burmite holds biological inclusions such as insects, plants, and fungi that have been sealed in and thus incredibly preserved. Burmite inclusions have served as the first fossil record of several species (*6*–*8*) and play an irreplaceable role in our understanding of the early evolution of animals and plants.

Unfortunately, burmite is being mined for commercial sale without regard for its paleontological significance. Its hardness, density, and color make it the most suitable amber for sculpture, jewelry manufacture, and gem collection, and from 1940 to 1989, about 83 tons of it were mined and sold (*2*). The trading boom has led to a surge in mining, depleting the store of burmite and producing a sale volume of nearly 10 tons in 2015 alone. Burmite that falls into the hands of jewelers and collectors is no longer available for study, and thus the knowledge it contains is lost.

In the past 2 years, another kind of commercialized amber—Fushun amber (50 to 53 million years old), originating from Northern China (*9*)—was nearly mined to depletion. Such blatant consumption represents a considerable loss of human knowledge, yet the mining and sale of amber, including burmite, remain unregulated. Very little of mined amber is available to scientists (only a few private organizations, such as the Fushun Institute of Amber, work to acquire burmite and offer it to scientists).

Biological inclusion sealed in a piece of Burmese amber.

We must take steps to protect this valuable source of irreplaceable knowledge before it is too late. In Myanmar, the government has little regulatory power because most mining districts are privately owned. Therefore, it may be more effective to intervene in China, where much of the amber is sold.

Shuo Wang,[1,2] Chao Shi,[3] Yun-jiao Zhang,[4] Guo-xiong Hu,[5] Li-zhi Gao[1,2]*

[1]Faculty of Environmental Science and Engineering, Kunming University of Science and Technology, Kunming 650500, China. [2]Faculty of Life Science and Technology, Kunming University of Science and Technology, Kunming 650500, China. [3]Kunming Institute of Botany, Chinese Academy of Sciences, Kunming 650201, China. [4]Department of Microbiology and Immunology, Faculty of Basic Medical Sciences, Kunming Medical University Haiyuan College, Kunming 650031, China. [5]College of Life Sciences, Guizhou University, Guiyang 550025, China.

*Corresponding author. E-mail: lgao@mail.kib.ac.cn

REFERENCES

1. F. M. Gradstein *et al.*, *A Geologic Timescale* (Cambridge Univ. Press, 2004).
2. G. H. Shi *et al.*, *Cretaceous Res.* **37**, 155 (2012).
3. E. M. Sadowski *et al.*, *Proc. Natl. Acad. Sci. U.S.A.* **112**, 1 (2015).
4. G. O. Poinar Jr., R. Singer, *Science* **248**, 1099 (1990).
5. J. Rust *et al.*, *Proc. Natl. Acad. Sci. U.S.A.* **107**, 43 (2010).
6. G. O. Poinar Jr., B. N. Danforth, *Science* **314**, 614 (2006).
7. B. Wang *et al.*, *eLife* **4**, e05447 (2015).
8. C. Y. Cai *et al.*, *Naturwissenschaften* **101**, 10 (2014).
9. B. Wang *et al.*, *Curr. Biol.* **24**, 14 (2014).

Migratory birds need coordinated protection

IN JANUARY, THE Supreme Court of Pakistan lifted the hunting ban on Houbara bustards (*1*), a bird categorized by the International Union for Conservation of Nature (IUCN) as Vulnerable (*2*). Frustrating ecologists and environmental groups, the local government argued that lifting the ban has economic benefits and direct bearing on foreign relations with Arab states (*1*). Every winter, thousands of Houbara bustards migrate from central Asia to Pakistan, where Arab dignitaries have been invited to hunt them. By crossing international borders, migratory species face particular conservation challenges, and their conservation is subject to the legislation of each country en route. Thus, it is important to consider the implications of each country's policies on migratory birds.

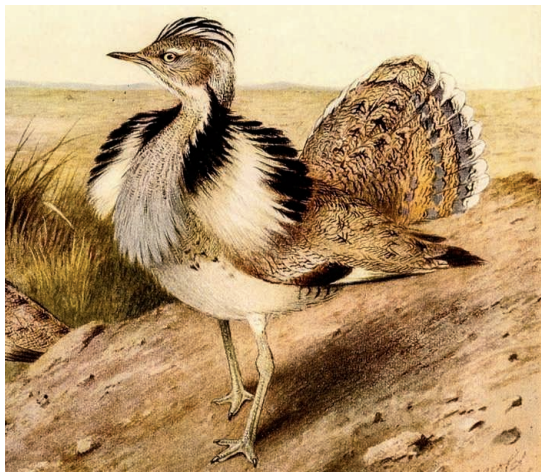

The Houbara bustard (illustrated here) migrates from central Asia to Pakistan.

The IUCN considers hunting (primarily falconry) to be the major threat responsible for diminishing the Houbara population, which currently numbers between 50,000 and 100,000 (*2*). The bird is listed on Appendix II of the Convention on the Conservation of Migratory Species of Wild Animals, to which Pakistan is a party (*3*). Biological conservation should not be sacrificed for short-term local political or economic benefits. Protecting migratory birds requires the cooperation of all countries along the species' migration route. These migratory birds should be conserved as a single unit, irrespective of jurisdictional boundaries. Therefore, Pakistan should reinstate the hunting ban and take effective measures to ensure protection of these guests within its borders. In addition, networks of critical stopover habitats of these species should be conserved in collaboration with other countries. International efforts should be coordinated to create managed protected sites and breeding facilities in selected habitats for migratory birds. Finally, governments should prioritize socioeconomic development of the local people and enlist their help to effectively implement conservation strategies.

M. Usman[1,2]* and M. Farooq[3,4]

[1]Department of Geosciences, Center for Applied Geosciences, University of Tübingen, 72074 Tübingen, Germany. [2]Institute of Soil and Environmental Sciences, University of Agriculture, Faisalabad 38040, Pakistan. [3]IRSET, University of Rennes 1, Rennes Cedex 35043, France. [4]Department of Clinical Sciences, College of Veterinary and Animal Sciences, Jhang, Pakistan.

*Corresponding author. E-mail: muhammad.usman@uaf.edu.pk

REFERENCES

1. BBC News, "How Pakistan's bustard hunting ban was shot down" (2016); www.bbc.com/news/world-asia-35384094.

PHOTO: LI-ZHI GAO AND SHUO WANG; ILLUSTRATION: HENRIK GRØNVOLD/WIKIMEDIA COMMONS

Downloaded from on February 25, 2016

Published by AAAS

2. BirdLife International, *Chlamydotis macqueenii*: The IUCN Red List of Threatened Species (2014); http://dx.doi.org/10.2305/IUCN.UK.2014-2.RLTS.T22733562A40859158.en.
3. R. Vagg, *CMS Family Guide: The Encylopaedia of the Convention on the Conservation of Migratory Species of Wild Animals* (UNEP/CMS Secretariat, Bonn, Germany, ed. 4, 2015); www.cms.int/en/node/925.

Walking the open science walk

ON 22 JANUARY, B. Owens reported that the Montreal Neurological Institute (MNI) is the first scientific institute to practice the principles of the "open science" movement ("Montreal institute going 'open' to accelerate science," In Depth, p. 329). Owens quotes the director as saying, "It's an experiment; no one has ever done this before." We commend the MNI for walking this path, but they are not the first to do so.

The Allen Institute for Brain Science, a private not-for-profit institute, has practiced a radical open-access policy since its inception in 2003. Although we reserve the right to apply for patents, all of our data that pass internal quality controls are freely and widely available both to the general public and to companies several years before the associated publications come out in the literature. This includes mouse, nonhuman primate and human brain atlases, microarrays, electrophysiological data, and associated visualization and analysis tools. Our website (www.brain-map.org) is the largest such online data repository (more than 3 petabytes). Likewise, we rapidly make our transgenic mouse lines available to the community. We are glad to see these principles being taken up by our Canadian colleagues.

Christof Koch

Allen Institute for Brain Science, Seattle, WA 98109, USA. E-mail: christofk@alleninstitute.org

TECHNICAL COMMENT ABSTRACTS

Comment on "Abrupt warming events drove Late Pleistocene Holarctic megafaunal turnover"

Sune O. Rasmussen and Anders M. Svensson

Cooper *et al.* (Research Article, 7 August 2015, p. 602) combined the annual-layer-counted Greenland Ice Core Chronology 2005 with chronological information from the Hulu Cave and Cariaco Basin records to produce a "revised" time scale. We argue that their time scale is incompatible with the nature of annual-layer-counted time scales and may lead to seriously flawed conclusions if used elsewhere at face value.
Full text at http://dx.doi.org/10.1126/science.aad3573

Response to Comment on "Abrupt warming events drove Late Pleistocene Holarctic megafaunal turnover"

Alan Cooper, Chris Turney, Konrad Hughen

Rasmussen and Svensson correctly point out that there is currently no satisfactory method to fully align the Greenland and Cariaco Basin records of climate change. However, our approach using interstadial onsets as tie-points allows direct comparison between radiocarbon dates and Greenland climate records. Crucially, both the standard Greenland and the merged Greenland-Cariaco time scales show that interstadial warming was associated with megafaunal genetic transitions.
Full text at http://dx.doi.org/10.1126/science.aad8016

TECHNICAL COMMENT

PALEOECOLOGY

Comment on "Abrupt warming events drove Late Pleistocene Holarctic megafaunal turnover"

Sune O. Rasmussen* and Anders M. Svensson

Cooper *et al*. (Research Article, 7 August 2015, p. 602) combined the annual-layer-counted Greenland Ice Core Chronology 2005 with chronological information from the Hulu Cave and Cariaco Basin records to produce a "revised" time scale. We argue that their time scale is incompatible with the nature of annual-layer-counted time scales and may lead to seriously flawed conclusions if used elsewhere at face value.

Cooper *et al*. investigated the relative timing of abrupt climate change and megafaunal extinction during the last glacial period (*1*). In the process, they created a time scale, denoted GICC05-Cariaco, based on a combination of data from marine sediments, speleothems, and ice cores, the latter presented on Greenland Ice Core Chronology 2005. Cooper *et al*. are obviously welcome to present data on their own time scale, but because they present their results as a revision of the GICC05 time scale developed by our group (*2*–*5*), we find it appropriate to discuss why we think GICC05-Cariaco represents a step in the wrong direction when it comes to time scale integration. We do not contest the megafaunal analysis: Cooper *et al*. state that the conclusions are robust to change of chronology.

When ice cores are dated by annual layer counting, the uncertainty accumulates with increasing age (*6*). Consequently, the determination of absolute ages is accurate for recent periods, whereas the accumulated uncertainty becomes large (i.e., low accuracy) in the last glacial period, compared with uncertainties of other dating methods, such as radiometric dating. However, even when the absolute accuracy is relatively low, layer counting still provides the possibility to determine event durations precisely. For example, at the onset of Greenland stadial 6 (GS-6), which according to GICC05 occurred 33.31 thousand years before 1950 C.E. (b1950), the GICC05 accumulated maximum counting error is 1191 years. In contrast, the outstanding precision allows for the determination of the duration of Greenland interstadial 6 (GI-6) and the subsequent stadial GS-6 to 1240 years, with a maximum counting uncertainty of 80 years (*4*). Thus, the duration estimate is an order of magnitude more precise than the absolute dating accuracy.

For radiometrically dated records, the situation is generally the opposite: relatively high accuracy and low precision. Cooper *et al*. uses Cariaco-derived ages of the GI/GS-6 pair that yield a duration of 2627 years with a 1 σ root mean square uncertainty of 271 years—i.e., more than twice the precise ice-core–based duration and not compatible with GICC05 within >3 σ. Even though the individual ages of the interstadial onsets are compatible between the Cariaco and GICC05 time scales within their respective error margins, the associated event durations are not. On this background, we argue that the presented set of ages from Cariaco cannot meaningfully be combined with the GICC05 event durations.

The differences in how the interstadials are expressed in the Cariaco and Greenland records are illustrated on figure S3 in (*1*). The large discrepancy between GICC05 and GICC05-Cariaco

Centre for Ice and Climate, Niels Bohr Institute, University of Copenhagen, Juliane Maries Vej 30, 2100 Copenhagen Ø, Denmark.
*Corresponding author: olander@nbi.ku.dk

Table 1. Data from (*1*) (first five columns). The GICC05-Cariaco ages (column 6) are obtained by error-weighted averaging hereof, demonstrating that interstadial durations are not needed for the construction of GICC05-Cariaco as claimed in (*1*). Column 7 shows the duration of each GI-GS pair in GICC05-Cariaco relative to GICC05. The column "Termination of interstadial" in table S3 of Cooper *et al*. is derived by adding estimated interstadial durations from (*8*) to the onset ages—i.e., assuming no stretching of interstadials. However, in the data of Fig. 1 and table S4 of Cooper *et al*., interstadials as well as stadials are stretched by the factor stated in the table. We conclude that the interstadial durations of table S3 in Cooper *et al*. are incorrect and refer to (*9*) for precise event durations. *, within GICC05 counting uncertainty.; **, not consistent with GICC05 counting uncertainty.

Event	Onset GICC05 (years b1950)	GICC05 uncertainty (years b1950)	Onset Cariaco (years b1950)	Cariaco uncertainty (years b1950)	Error-weighted mean (years b1950)	Stretching factor of GI and following GS
GI-1	14,642	93	14,600	125	14,627	0.99*
GI-2	23,290	298	23,790	268	23,566	1.03*
GI-3	27,730	416	27,855	119	27,846	0.96*
GI-4	28,850	449	28,639	126	28,654	0.72**
GI-5	32,450	566	31,599	152	31,656	0.83**
GI-6	33,690	606	34,226	224	34,162	2.02**
GI-7	35,430	661	35,357	288	35,369	0.69**
GI-8	38,170	725	38,355	194	38,343	1.09**
GI-9	40,110	790	41,368	340	41,171	1.46**
GI-10	41,410	817	42,192	197	42,149	0.75**
GI-11	43,290	868	43,808	189	43,785	0.87**
GI-12	46,810	956	47,540	211	47,506	1.06**
GI-13	49,230	1,015	50,801	691	50,303	1.16**
GI-14	54,170	1,150	53,972	719	54,028	0.75**
GI-15	55,750	1,196	55,961	672	55,910	1.19**

Downloaded from on February 25, 2016

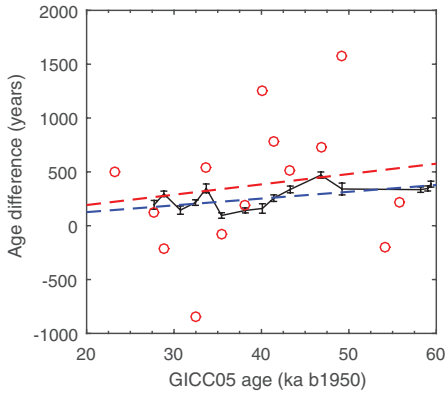

Fig. 1. Buizert *et. al* (*7*) (black and blue) and Cooper *et al*. (*1*) (red) age differences. (See the text for more details.)

suggests that uncertainties in the event identification and alignment and in the Hulu-Cariaco time scale transfer (not included by Cooper *et al.*) dominate over the analytical dating uncertainties.

If radiometric dates and annual-layer-counting results are to be meaningfully combined, we argue that the methodology must respect that radiometric dates are mutually independent with small uncertainties, whereas annual-layer-counted chronologies have large but highly correlated uncertainties. Furthermore, we argue that a combination of the two must take into account the uncertainties in aligning the records.

Cooper *et al.* claims that the interstadial durations from GICC05 have been maintained for the revised GICC05-Cariaco time scale. We see this as a step toward acknowledging that annual-layer-counted interstadial durations are indeed precisely determined, but it is unclear why Cooper *et al.* do not treat stadial durations in the same way. Furthermore, it turns out that the GICC05 interstadial durations do not actually enter the time-scale merging calculations: As demonstrated in Table 1, the ages of interstadial onsets in the GICC05-Cariaco time scale can be obtained by error-weighted averaging of the interstadial onsets in GICC05 and Cariaco. The approach assumes independent uncertainties for both records and disregards uncertainty of the alignment of events between records.

Table 1 also shows the stretching factor of each GI/GS pair in GICC05-Cariaco compared with GICC05. The maximum counting error estimates of GICC05 are below 5% at all depths, corresponding to stretching factors between 0.95 and 1.05. Back to GI/GS-3, the stretching factors are within those limits, but for older sections, interstadial-stadial durations are stretched or compressed more than what is consistent with the annual layer counting results. The extremes are GI/GS-6, whose duration is more than doubled, and GI/GS-7, which is compressed to 69% of its GICC05 duration.

As an example of how annual-layer-counted chronologies can be meaningfully combined with radiometric dates, Buizert *et al.* (*7*) combined GICC05 and Hulu ages in the construction of the West Antarctic Ice Sheet Divide time scale. Their age differences between aligned events are shown in Fig. 1 (black symbols with estimated matching uncertainties), together with the GICC05-Cariaco age differences from Cooper *et al.* (red symbols). Based on a linear fit, GICC05 was stretched by a factor of 1.0063 to, on average, align Hulu and Greenland ages (blue dashed curve in Fig. 1) (*7*). All event durations are thus increased by 0.63%, suggesting a small bias in the layer counting during the construction of GICC05. A similar analysis using data from Cooper *et al.*, which are less precise due to the matching via Cariaco, leads to a bias estimate of 0.96% (Fig. 1, red dashed line), well within the maximum counting error of GICC05.

We conclude that the GICC05-Cariaco time scale cannot be seen as a revision of GICC05 because it is not consistent with the constraints given by the annual layer counting on which GICC05 is based. We thus recommend that the GICC05-Cariaco time scale not be used for palaeoclimatic reconstructions and, in particular, not for presentation of ice-core data.

REFERENCES

1. A. Cooper *et al.*, *Science* **349**, 602–606 (2015).
2. S. O. Rasmussen *et al.*, *J. Geophys. Res.* **111**, D06102 (2006).
3. B. M. Vinther *et al.*, *J. Geophys. Res.* **111**, D13102 (2006).
4. K. K. Andersen *et al.*, *Quat. Sci. Rev.* **25**, 3246–3257 (2006).
5. A. Svensson *et al.*, *Clim. Past* **4**, 47–57 (2008).
6. A. Brauer *et al.*, *Quat. Sci. Rev.* **106**, 47–66 (2014).
7. C. Buizert *et al.*, *Clim. Past* **11**, 153–173 (2015).
8. E. W. Wolff, J. Chappellaz, T. Blunier, S. O. Rasmussen, A. Svensson, *Quat. Sci. Rev.* **29**, 2828–2838 (2010).
9. S. O. Rasmussen *et al.*, *Quat. Sci. Rev.* **106**, 14–28 (2014).

30 October 2015; accepted 19 January 2016
10.1126/science.aad3573

TECHNICAL RESPONSE

PALEOECOLOGY

Response to Comment on "Abrupt warming events drove Late Pleistocene Holarctic megafaunal turnover"

Alan Cooper,[1]* Chris Turney,[2] Konrad Hughen[3]

Rasmussen and Svensson correctly point out that there is currently no satisfactory method to fully align the Greenland and Cariaco Basin records of climate change. However, our approach using interstadial onsets as tie-points allows direct comparison between radiocarbon dates and Greenland climate records. Crucially, both the standard Greenland and the merged Greenland-Cariaco time scales show that interstadial warming was associated with megafaunal genetic transitions.

A major challenge for testing hypotheses of synchronous climate and environmental change is high-precision alignment of geochronological frameworks. Nowhere is this more problematic than in comparison of the radiocarbon (^{14}C) time scale with the Greenland ice core records of abrupt and extreme climate change during the Late Pleistocene. We thank Rasmussen and Svennson for their Comment (*1*) on our paper (*2*). It was not our intention to provide a replacement chronology for the excellent Greenland Ice Core Chronology 2005 (GICC05) time scale generated by these authors. Instead, we wished to test our observation that there was indeed a relationship between megafaunal extinctions and abrupt and extreme climate warming events, as preserved in Greenland on the GICC05 time scale [table 1 in (*2*)]. As a result, we developed a methodology that allows direct comparison between radiocarbon ages and Greenland climate. By combining the tropical Cariaco Basin (Hulu Cave) radiocarbon record of shifts in the Intertropical Convergence Zone with Greenland temperature, we were able to exploit the positive attributes of these independent records and thereby bring abrupt interstadial transitions and high-resolution radiocarbon into the same calendar time scale. This provided an alternative chronology that would allow us to test the conclusions reached by using GICC05 on its own, given the known accuracy problems of this record at greater annual ice layer counts. However, we do not advocate the use of the revised GICC05-Cariaco chronology as a replacement alternate age model for the complete GICC05 record.

As Rasmussen and Svennson remark, a full merging of chronologies has to take into account the different nature of annual-layer-counted and radiometric chronologies and their associated and very different uncertainties (i.e., independent versus dependent errors), something that is at present difficult to do in a robust, objective statistical model. Such a substantial exercise was beyond the scope of this paper, and we focused on the timing of abrupt interstadial transitions only, given our initial conclusions derived using just GICC05. We took a conservative approach by combining the strengths of GICC05 and Cariaco-Hulu to derive an alternative replicated framework for the timing of the onset of abrupt and extreme warming during Dansgaard-Oeschger events (within the uncertainties of both sequences). By taking advantage of the counting precision on the Greenland interstadial durations (*3*) (as stated explicitly in our supplementary materials), we could directly compare the calibrated megafaunal data set to climate. Given the magnitude of the uncertainties in calibrating radiocarbon ages across the full time scale, we considered the use of centennial-length durations appropriate; furthermore, as reported by Wolff *et al.* (*3*), the onset of some interstadials is difficult to precisely identify due to the complex structure of events; hence, Greenland interstadials 13 to 15 were not used in our calculations. We are sympathetic to the use of the duration of Greenland stadials and interstadials as a test of different age models, but as Rasmussen and Svensson and colleagues have previously reported, "alternative but reasonable sets of criteria could have been developed that would have given a different count and a different uncertainty" (*3*). Furthermore, it is clear that major challenges remain in capturing all missing Greenland layers, as evidenced by recent work questioning even the relatively recent Late Glacial and Holocene part of the record (*4*, *5*). Developing more precise and accurate geochronological frameworks in the future will require new approaches to alignment, incorporating all sources of error.

The key point remains that regardless of the chronology used, we reach the same conclusion: Interstadial warming events are strongly associated with the regional replacement or extinction of major genetic clades or species of megafauna.

[1]University of Adelaide, Australian Centre for Ancient DNA, School of Earth and Environmental Sciences, and Environment Institute, Adelaide, Australia. [2]Climate Change Research Centre, School of Biological, Earth and Environmental Sciences, University of New South Wales, Sydney, Australia. [3]Department of Marine Chemistry and Geochemistry, Woods Hole Oceanographic Institution, Woods Hole, MA, USA.
*Corresponding author. E-mail: alan.cooper@adelaide.edu.au

REFERENCES

1. S. O. Rasmussen, A. M. Svensson, *Science* **351**, 927 (2016).
2. A. Cooper *et al.*, *Science* **349**, 602–606 (2015).
3. E. W. Wolff, J. Chappellaz, T. Blunier, S. O. Rasmussen, A. Svensson, *Quat. Sci. Rev.* **29**, 2828–2838 (2010).
4. R. Muscheler, F. Adolphi, M. F. Knudsen, *Quat. Sci. Rev.* **106**, 81–87 (2014).
5. M. C. Torbenson, G. Plunkett, D. M. Brown, J. R. Pilcher, H. H. Leuschner, *Geology* **43**, 799–802 (2015).

17 November 2015; accepted 19 January 2016
10.1126/science.aad8016

Downloaded from on February 25, 2016

AAAS President seeks increasing support for curiosity-driven research

Studies of plant evolution can yield practical benefits, says Barbara Schaal

By **Earl Lane**

From a childhood fascination with cactus plants, to fieldwork in Brazil tracing the wild progenitor of the cassava plant, to learning the subtleties of rice cultivation from an expert farmer in the highlands of Thailand, evolutionary biologist Barbara Schaal has found science to be "just so much fun."

She brings that enthusiasm to her new role as president of AAAS, where she will argue for the value of curiosity-driven science pursued without regard for immediate application. At the same time, she has spent much of her career studying the practical benefits that can flow from a better understanding of the vast genetic diversity of the natural world.

Barbara Schaal visits a rice-growing cooperative aimed at developing local conservation practices in Gongliao District, Taiwan.

Schaal, dean of the faculty of arts and sciences at Washington University in St. Louis, called for more effective communication and public engagement by scientists in explaining their work, both to policy-makers and to the general public, across a range of topics—climate change, evolution, stem cells, and use of genetically modified organisms (GMOs) in agriculture.

"Agriculture has tremendous challenges that it is going to face," Schaal said. "We want to feed a growing population. We want to feed them better, with more nutritious food." The global population is projected to reach 9 billion by 2050. Of particular importance, Schaal said, is finding ways to lessen the environmental footprint of agriculture, which currently accounts for about 70% of U.S. water consumption. Such challenges, she said, must be addressed using the entire toolbox of methods, including genomics, cellular and molecular biology, traditional plant breeding, and genetic modification. Taken together, such tools are giving scientists a better understanding of how plants respond to drought, high temperatures, pests, and disease.

Messages by scientists about the environmental impact of agrochemicals, GMOs, and other topics often "are not well received," Schaal acknowledged. Researchers must understand the cultural context as well as the underlying science in communicating about their work. When scientists have difficulty trying to explain their research to a lay audience, she said, the tendency too often has been to just "give them more detail and say it louder."

Schaal's own pursuit of science blossomed from her childhood interest in plants. She majored in biology as an undergraduate at the University of Illinois, Chicago, where she studied with Donald A. Levin, a specialist on the origin, expansion, and demise of plant species. When Levin moved to Yale University, Schaal followed. She was accepted as a doctoral student there and began a research career in which she was among the first plant scientists to use molecular biology–based approaches to understand evolutionary processes in plants.

Schaal's interest in agricultural species was spurred when Rob Bertram, a staff member at the U.S. Agency for International Development, asked if her research on plant DNA sequences could help trace the origin of cassava, a starchy root crop that is a large source of food carbohydrates in the tropics. "I didn't know what cassava was," Schaal admitted, but she figured the question was pretty straightforward. It took a decade of work before Schaal and Kenneth M. Olsen, then a graduate student, reported finding the wild progenitor of the cassava plant in a region along the southern border of the Amazon basin.

Their exercise in phylogeography, interesting on its own merits, also identified a source of genetic diversity that could be tapped to help improve the modern cassava plant. And it showed that the domestication of cassava occurred in a place where humans have had their longest association with the wild ancestor of the plant. Such associations began when "some smart men and women 10,000 years ago began to cultivate" various plants, Schaal said.

That human selection of favorable traits continues, both through traditional crop breeding and through the more targeted use of genetic engineering. In Thailand, where Schaal studied the adaptability of ancestral varieties of rice to pests and climate change, she was impressed by the ongoing search for favorable traits by expert farmers who pay close attention to mutations in their crops. "Clearly, what is going on in these villages is artificial selection," Schaal said, "and they are modifying their crops in the same way as their ancestors did over many centuries."

In recent years, Schaal's focus has shifted from fieldwork (though she continues to follow the far-flung research projects of her students) to national and international policy issues involving science. In 2005, she was the first woman elected to the vice presidency of the National Academy of Sciences. She was elected to a second 4-year term in 2009, the same year she was appointed by President Obama to the President's Council of Advisors on Science and Technology (PCAST). She serves as chair of the Division on Earth and Life Studies at the National Research Council and also was a science envoy for the U.S. Department of State.

Schaal is eager in her new role with AAAS to become even more involved with science policy, particularly to make clear the value of basic research. She cited "the incredible advances in medicine" that have come from basic studies funded by the National Institutes of Health. She worries that budget stringencies could close "the pipeline for new discoveries" fostered by NIH, the National Science Foundation, and other science-related agencies. ■

PHOTO: KUO-FANG CHUNG

Downloaded from on February 25, 2016

Published by AAAS

RESEARCH ARTICLE SUMMARY

GENE EDITING

Direct CRISPR spacer acquisition from RNA by a natural reverse transcriptase–Cas1 fusion protein

Sukrit Silas,* Georg Mohr,* David J. Sidote, Laura M. Markham, Antonio Sanchez-Amat, Devaki Bhaya, Alan M. Lambowitz,† Andrew Z. Fire†

INTRODUCTION: Cells use a variety of mechanisms to prevent the propagation of parasitic information. A family of adaptive immune systems associated with CRISPRs in prokaryotes has been shown to protect cell populations from "selfish" DNA, including viruses and plasmids. CRISPR-mediated immunity begins with an "adaptation" phase, involving the heritable acquisition of short sequence segments (spacers) from the genome of the infectious agent by the host. This information is stored within CRISPR arrays in the host genome and is used by CRISPR-associated (Cas) nucleases in the subsequent "interference" phase to identify and disrupt infections by the same invader. CRISPR-Cas systems include those capable of interfering with DNA and RNA targets. In several characterized systems, adaptation involves acquisition from DNA templates through the action of a subset of the Cas proteins. One of these proteins (Cas1) plays a catalytic role in spacer acquisition from DNA in all systems analyzed so far.

RATIONALE: We sought to determine whether some CRISPR-Cas systems build CRISPR arrays through the acquisition of spacer sequences from RNA. CRISPR systems are phylogenetically grouped into five types (types I to V); in some type III CRISPR systems, Cas1 is naturally fused to a reverse transcriptase (RT). This suggests the possibility of a concerted spacer integration mechanism involving Cas1 integrase activity and the reverse transcription of RNA to DNA. This would enable the acquisition of new spacers from RNA, potentially generating adaptive immunity against RNA-based invaders. To test this hypothesis, we characterized the spacer acquisition machinery of the RT-Cas1–containing type III-B CRISPR system in the bacterium *Marinomonas mediterranea* (MMB-1), by means of in vivo assays and in vitro reconstitution.

RESULTS: To examine the acquisition capabilities of the MMB-1 type III-B system, we overexpressed RT-Cas1 and associated adaptation genes from MMB-1 in the native host. The resulting strains acquired a variety of new spacer elements in their type III-B CRISPR arrays. These sequences matched segments from the MMB-1 genome and our expression plasmids, with substantially more acquisitions deriving from highly transcribed genes. The transcription-associated acquisition of spacers was dependent on functional Cas1 and RT domains of the RT-Cas1 protein, supporting the idea of an RNA capture mechanism that combines Cas1 integrase activity with reverse transcription of cellular RNA. While Cas1 catalytic mutations abolished spacer acquisition, deletion or mutational inactivation of the RT domain yielded a system capable of integration with no transcriptional bias, revealing an alternative Cas1 activity on DNA substrates. To test whether the MMB-1 system can acquire sequences from RNA, we engineered a self-splicing intron into plasmid copies of two MMB-1 genes that were well sampled by RT-Cas1, simultaneously introducing mutations flanking the splice sites to yield a novel exon-junction sequence that was present as RNA but not DNA. Newly acquired spacers containing the exon-junction sequences confirmed that RT-Cas1 can acquire spacers from RNA. To investigate the relationship between the integrase and RT activities of RT-Cas1, we studied the acquisition machinery in vitro. RT-Cas1 and the associated Cas2 protein promote the precise integration of single-stranded RNA, single-stranded DNA, and double-stranded DNA oligonucleotides directly into a linear CRISPR DNA substrate, indicating that RT-Cas1 acquires spacers directly from RNA. The in vitro studies are consistent with a mechanism in which the Cas1-fused RT domain then reverse-transcribes the integrated RNA, converting it to a cDNA sequence between CRISPR repeats. The concerted integrase-RT mechanism suggested by the in vitro studies has similarities to the genomic integration mechanism used by the bacterial retrotransposons known as mobile group II introns, which encode a related RT.

ON OUR WEB SITE

Read the full article at http://dx.doi.org/10.1126/science.aad4234

CONCLUSION: We showed that a natural RT-Cas1 fusion protein in a type III CRISPR system can enable the acquisition of new spacers directly from RNA. With other type III CRISPR systems known to target RNA for degradation, RT-associated CRISPR-Cas systems would effectively generate adaptive immunity against RNA parasites. RNA spacer acquisition could also contribute to immune responses against highly transcribed regions of DNA-based invaders through targeted interference at both the DNA and RNA levels. ■

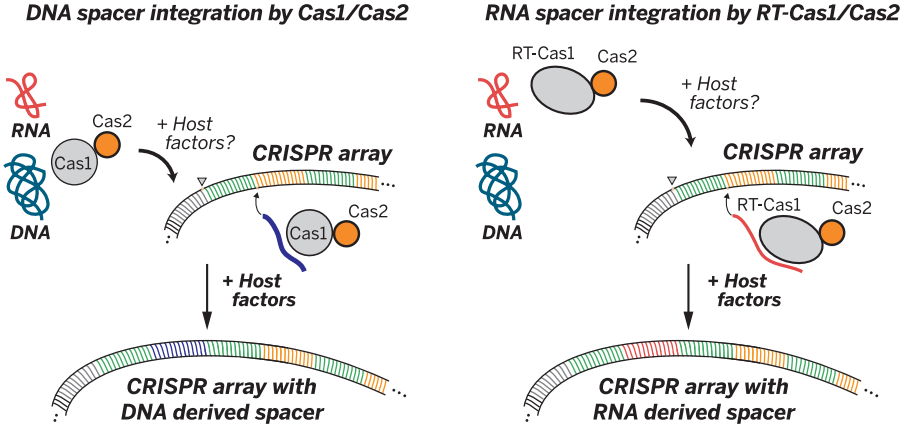

Spacer acquisition from RNA. (**Left**) Small segments of invasive DNA are assimilated into CRISPR arrays by Cas1 and Cas2 in a canonical spacer acquisition process that allows adaptive immunity in a wide variety of bacteria and archaea. (**Right**) In some type III CRISPR systems, a RT fused to Cas1 enables the acquisition of spacer sequences directly from RNA. This process might mediate adaptive immunity against RNA-based parasites.

The list of author affiliations is available in the full article online.
*These authors contributed equally to this work.
†Corresponding author. E-mail: lambowitz@austin.utexas.edu (A.M.L.); afire@stanford.edu (A.Z.F.)
Cite this article as S. Silas *et al.*, *Science* 351, aad4234 (2016). DOI: 10.1126/science.aad4234

Downloaded from on February 25, 2016

RESEARCH ARTICLE

GENE EDITING

Direct CRISPR spacer acquisition from RNA by a natural reverse transcriptase–Cas1 fusion protein

Sukrit Silas,[1,2]* Georg Mohr,[3]* David J. Sidote,[3] Laura M. Markham,[3] Antonio Sanchez-Amat,[4] Devaki Bhaya,[5] Alan M. Lambowitz,[3]† Andrew Z. Fire[1]†

CRISPR systems mediate adaptive immunity in diverse prokaryotes. CRISPR-associated Cas1 and Cas2 proteins have been shown to enable adaptation to new threats in type I and II CRISPR systems by the acquisition of short segments of DNA (spacers) from invasive elements. In several type III CRISPR systems, Cas1 is naturally fused to a reverse transcriptase (RT). In the marine bacterium *Marinomonas mediterranea* (MMB-1), we showed that a RT-Cas1 fusion protein enables the acquisition of RNA spacers in vivo in a RT-dependent manner. In vitro, the MMB-1 RT-Cas1 and Cas2 proteins catalyze the ligation of RNA segments into the CRISPR array, which is followed by reverse transcription. These observations outline a host-mediated mechanism for reverse information flow from RNA to DNA.

RNA-guided host defense mechanisms associated with CRISPR arrays exist in most bacteria and archaea (*1*, *2*). Their target specificity derives from a series of spacers—many of which are identical to DNA sequences from phage, transposon, and plasmid mobilomes—interspersed within CRISPR arrays (*3*–*5*). Transcripts from these CRISPR arrays are processed into short structured RNAs, which form a complex with CRISPR-associated (Cas) endonucleases and target invasive nucleic acids, thereby conferring immunity (*6*, *7*). CRISPR-Cas systems have been phylogenetically grouped into five types (*8*, *9*). Homologs of the *cas1* and *cas2* genes are conserved across diverse CRISPR types (*9*, *10*), with direct evidence for a role in the physical integration of new spacers from invasive DNA into CRISPR arrays in a few type I and II systems (*11*–*14*). Spacer acquisition allows the host to adapt to new threats.

The ability of type III systems to target RNA in addition to DNA (*15*–*21*) raises the possibility of natural spacer acquisition from RNA species. Direct acquisition of RNA spacers would add to the handful of known mechanisms for the reverse flow of genetic information from RNA into DNA genomes (*22*–*27*).

Examination of bacterial genomes has revealed a class of CRISPR-associated coding regions in which *cas1* is fused to a putative reverse transcriptase (RT) (*10*, *28*–*30*). These RT-Cas1 fusions raise the possibility of a concerted mechanism of spacer acquisition involving reverse transcription of RNA to DNA, a potentially host-beneficial mechanism for RNA-to-DNA information flow.

Common features of RT-Cas1 fusions

To examine the phylogenetic distribution of fused RT-Cas1–encoding genes, we used the National Center for Biotechnology Information (NCBI) Conserved Domain Architecture Retrieval Tool (CDART) to retrieve protein records containing both a Cas1 domain (Pfam domain PF01867) and a RT domain of any origin (PF00078). Of 93 RT-Cas1–bearing species, all were from bacteria and none were from archaea. RT-Cas1 fusions were most prevalent among cyanobacteria, with 21% of *cas1*-bearing cyanobacteria carrying such fusions (Fig. 1, A and B). RT-Cas1 fusions with sufficient flanking sequence for type classification were exclusively associated with type III CRISPR systems (table S1); conversely, ~8% of bacterial type III CRISPR systems carried RT-Cas1 fusions.

The Cas1-fused RT domains were most closely related to RTs encoded by mobile genetic elements (retrotransposons) known as mobile group II introns (*29*, *30*). We identified two related structural families of RT-Cas1 proteins. The more abundant family carries a canonical N-terminal RT domain with a conserved RT-0 motif characteristic of group II intron and non–long terminal repeat (non-LTR) retrotransposon RTs (*31*, *32*). The other lacks the RT-0 motif, starting instead with an additional N-terminal domain containing a putative Cas6-like RNA recognition motif of the RAMP [repeat-associated mysterious protein (*10*)] superfamily. Alignments of the retrovirus HIV-1 RT and a group II intron RT [*Thermosynechococcus elongatus* TeI4c RT (*33*)] with representatives of the two RT-Cas1 fusion families (from *Arthrospira platensis* and *Marinomonas mediterranea*) revealed that both Cas1-fused RTs contain the seven conserved sequence motifs characteristic of the finger and palm regions of retroviral RTs. Each also shares the RT-2a motif, which is conserved in group II intron RTs and related proteins but not present in retroviral RTs, such as the HIV-1 RT (*31*, *32*). The thumb/X domain, which is found in retroviral and group II intron RTs just downstream of the RT domain, appears to be missing in the Cas1-associated RTs (Fig. 1C).

The structural subcategories, limited phylogenetic distribution, and exclusive association with a subset of CRISPR types are consistent with a small number of common origins of RT-Cas1 fusions (*10*, *29*).

Spacer acquisition by the *M. mediterranea* type III-B machinery in an *E. coli* host

To test whether RT-Cas1 proteins could facilitate the acquisition of new spacers, and to determine whether such spacers might be acquired from RNA, we chose the type III-B CRISPR locus in *M. mediterranea* (MMB-1) (*34*), because this is an easily cultured, nonpathogenic member of the well-studied γ-proteobacterium class that contains a RT-Cas1–encoding gene.

We first assessed spacer acquisition after transplantation of the locus into the canonical γ-proteobacterium experimental model, *Escherichia coli*. We constructed expression vectors carrying the type III-B operon of MMB-1 in two configurations, either as a single cassette consisting of the CRISPR03 array (*35*), the genes encoding RT-Cas1 and Cas2, and an adjacent gene (encoding Marme_0670) with limited homology to the NERD (nuclease-related domain) family (*36*), or together with a second cassette additionally encoding the remaining CRISPR-associated factors, Cmr1 to Cmr6 and Marme_0671 (Fig. 2, A and B). The acquisition of new spacers into CRISPR03 was evident from polymerase chain reaction (PCR) amplification of the region between the leader sequence and the first native spacer, followed by high-throughput sequencing. We identified newly acquired spacers in transformants expressing either the full complement of Cas genes, or the subset containing only the potential "adaptation" genes (encoding RT-Cas1, Cas2, and Marme_0670). Bona fide spacer acquisition is evidenced by the precise junctions between the inserted spacer DNA and CRISPR repeats (fig. S1A) and by the diversity of acquired spacers (fig. S1, B and D).

Specificity was further tested by evaluating the requirements for RT-Cas1 and Cas2 in spacer acquisition. We constructed two point mutations, E870A and E790A, in the putative Cas1 active site of MMB-1 RT-Cas1, based on a three-dimensional homology model computed using the *Archaeoglobus fulgidus* Cas1 crystal structure (*37*). Each point mutation abolished spacer acquisition, as did a 60–amino acid C-terminal deletion in Cas2 (Fig. 2C).

The majority (~85%) of newly acquired spacers mapped to the *E. coli* genome, with the rest being

[1]Department of Pathology, Stanford University, Stanford, CA 94305, USA. [2]Department of Chemical and Systems Biology, Stanford University, Stanford, CA 94305, USA. [3]Institute for Cellular and Molecular Biology, Department of Molecular Biosciences, University of Texas–Austin, Austin, TX 78712, USA. [4]Department of Genetics and Microbiology, Universidad de Murcia, Murcia 30100, Spain. [5]Department of Plant Biology, Carnegie Institution for Science, Stanford, CA 94305, USA. *These authors contributed equally to this work. †**Corresponding author. E-mail: lambowitz@austin.utexas.edu (A.M.L.); afire@stanford.edu (A.Z.F.)**

A ***Distribution of RT-Cas1 fusions among major bacterial phyla***

	RT-Cas1		Cas6-RT-Cas1		Cas1	
	records	species	records	species	records	species
Archaea	0	0	0	0	371	231
Bacteria	112	83	10	10	6491	3551
Actinobacteria	10	10	0	0	809	478
Bacteroidetes	28	8	1	1	327	190
Chlorobi	3	3	0	0	20	15
Cyanobacteria	26	24	0	0	268	117
Firmicutes	4	4	0	0	1881	1044
Planctomycetes	3	3	1	1	14	8
Proteobacteria	38	31	5	5	2315	1227
unclassified	0	0	3	3		
all other phyla	0	0	0	0	857	472

B ***Phylogenetic tree of bacterial phyla***

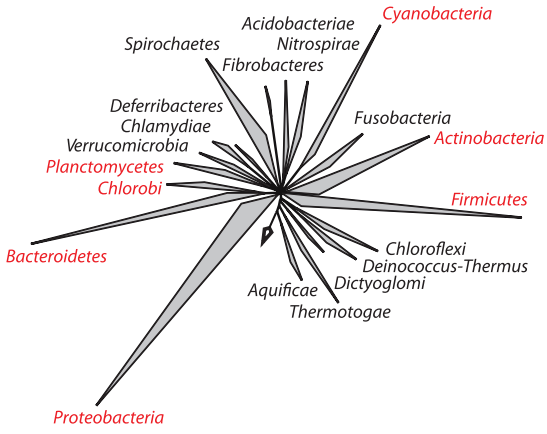

C ***Domain structure of RT-Cas1 proteins***

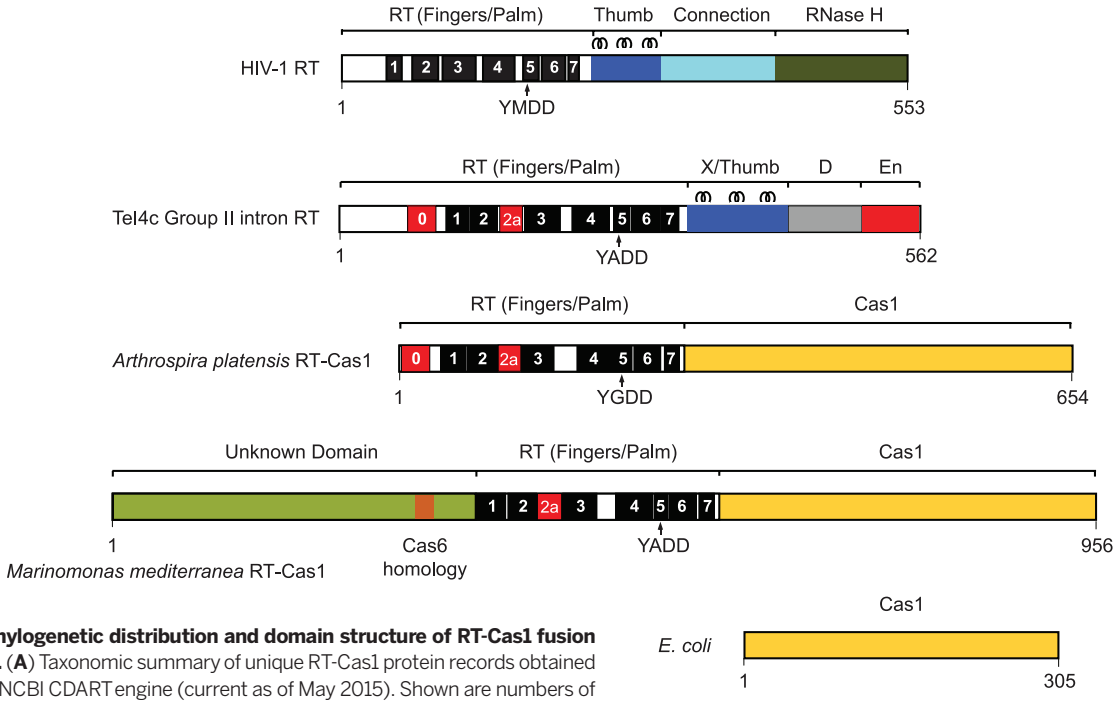

Fig. 1. Phylogenetic distribution and domain structure of RT-Cas1 fusion proteins. (**A**) Taxonomic summary of unique RT-Cas1 protein records obtained from the NCBI CDART engine (current as of May 2015). Shown are numbers of Cas1 protein records and bacterial species with (left) a fused RT domain, (center) RT and an additional N-terminal extension containing a Cas6-like motif, and (right) Cas1 with no additional annotated domain. Only phyla containing RT-Cas1 fusions are listed. (**B**) 16*S* rRNA–based tree showing major bacterial phyla, with phyla that contain RT-Cas1 in red [adapted from (*48*)]. (**C**) Schematic showing the domain organization of HIV RT (UniProtKB/Swiss-Prot P03366), a group II intron RT (Tel4c from *T. elongatus* BP-1; GenPept WP_011056164), *A. platensis* RT-Cas1 (WP_006620498), *M. mediterranea* RT-Cas1 (WP_013659858), and *E. coli* Cas1 (NP_417235). Conserved RT motifs as defined in (*49*) are labeled 1 to 7. Motifs 0 and 2a are conserved in mobile group II intron and non-LTR–retrotransposon RTs (*32*). The YXDD sequence found in motif 5 contains two aspartic acid residues at the RT active site. Three α-helices found in the thumb/X domain of HIV and group II intron RTs are indicated. Numbers below the bars indicate amino acid positions. D, DNA binding domain; En, endonuclease domain.

derived from plasmid DNA (fig. S1D). Over 70% of the spacers were 34 to 36 base pairs (bp) in length (Fig. 2D). Consistent with observations of interference mechanisms in other type III CRISPR systems (*7*), we found no evidence for a conserved protospacer-adjacent motif (PAM) or other sequence signature associated with protospacer choice (Fig. 2E). We observed no bias for the sense strand among spacers acquired from annotated *E. coli* genes (fig. S2A) and no enrichment of spacers derived from highly transcribed genes (Fig. 2F). Spacer acquisition was unhindered when the RT domain of RT-Cas1 was mutated or deleted (Fig. 2C), consistent with a DNA-based mechanism operating under these conditions. Deletion of the entire 290–amino acid conserved region of the RT domain resulted in a ~20-fold increase in spacer acquisition frequency (*38*), with no apparent differences in the characteristics of the pool of acquired spacers (Fig. 2, C to F, and figs. S2A and S3A).

Transcription-associated spacer acquisition in MMB-1 is RT-dependent

Our inability to detect RNA spacer acquisition in the ectopic *E. coli* assay could reflect the absence of required factors or conditions that are present in

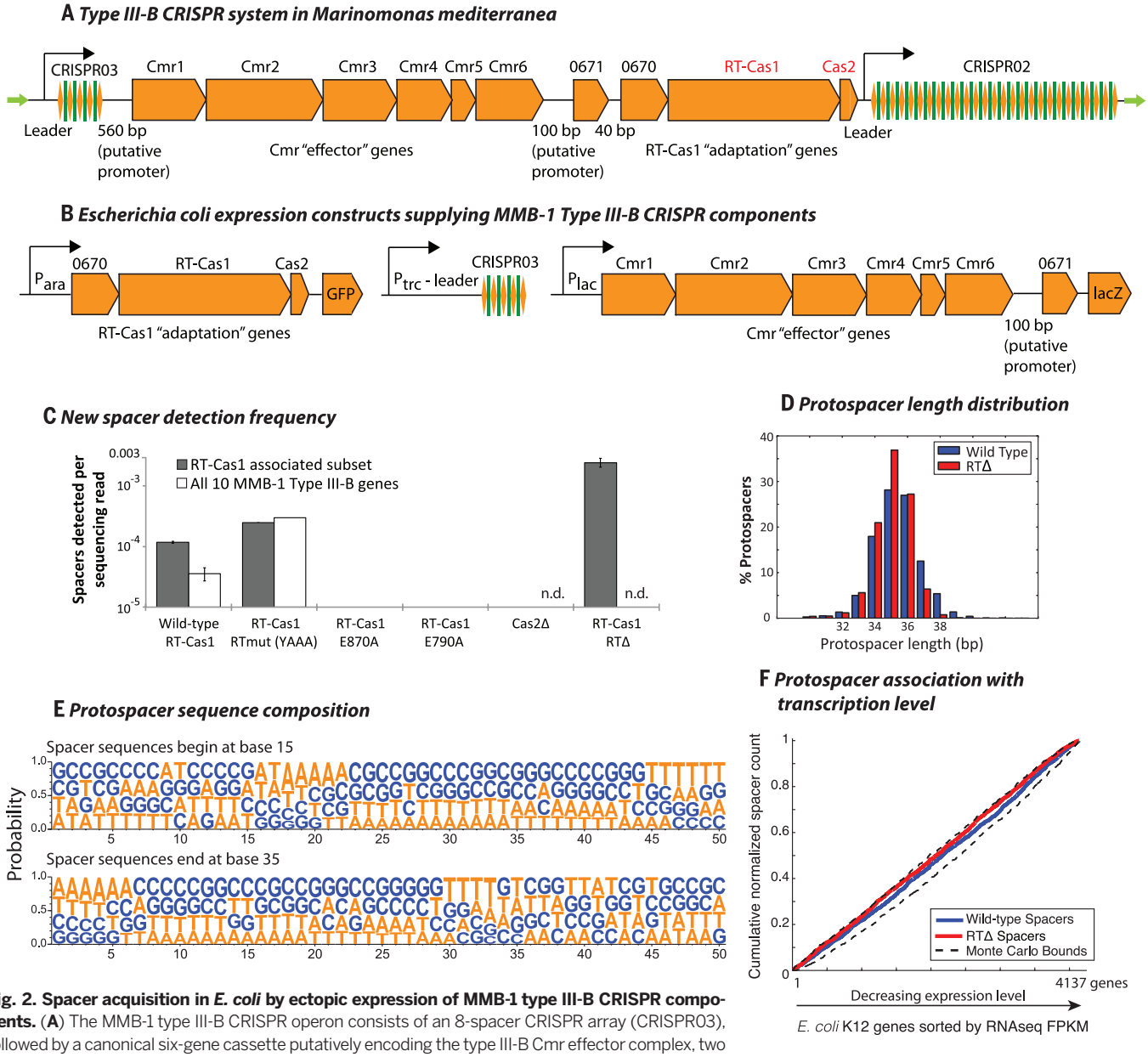

Fig. 2. Spacer acquisition in *E. coli* by ectopic expression of MMB-1 type III-B CRISPR components. (**A**) The MMB-1 type III-B CRISPR operon consists of an 8-spacer CRISPR array (CRISPR03), followed by a canonical six-gene cassette putatively encoding the type III-B Cmr effector complex, two genes of unknown function (*Marme_0671* and *Marme_0670*), the genes encoding RT-Cas1 and Cas2, and lastly a larger 58-spacer CRISPR array (CRISPR02). The locus is flanked by two ~200-bp direct repeats (green arrows). The black arrows indicate promoters. (**B**) Arrangement of MMB-1 type III-B CRISPR components under inducible promoters (P_{ara}, P_{trc}, and P_{lac}) on pBAD vectors for ectopic expression in *E. coli*. (**C**) Spacer detection frequency after overnight induction of *E. coli* carrying pBAD expression vectors with arabinose and IPTG. Wild-type RT-Cas1, RT active site mutant (YAAA), and Cas1 domain mutants E790A and E870A were tested with or without the P_{lac}-driven gene cassette encoding the Cmr effector complex. Cas2 Δ32–92 and RT domain Δ299–588 mutants (shown in the two rightmost columns) were tested without the Cmr cassette. Range bars indicate values for two biological replicates (n.d., not determined). (**D**) Histogram showing normalized counts of *E. coli* genomic protospacers from the wild-type RT-Cas1 and RTΔspacer acquisition experiments, distributed by mappable length. Pooled data from several experiments are presented. (**E**) Nucleotide probabilities at each position along the wild-type RT-Cas1–acquired protospacers in (D), including 15 bp of flanking sequence on each side. Because of varying protospacer lengths, two panels are shown with the spacer 5′ and 3′ ends anchored at positions 15 and 35, respectively. (**F**) Cumulative normalized distribution of spacers in (D) among *E. coli* protein-coding open reading frames (ORFs) sorted by expression level [normalized RNAseq read counts from (*47*); FPKM, fragments per kilobase per million reads], with the most highly expressed genes listed first. Included are 2470 wild-type RT-Cas1– and 5569 RTΔ-acquired spacers mapping to *E. coli* genes. Dashed black lines show the range of values from a Monte Carlo simulation with random assortment (no transcription-related bias).

the native host, MMB-1. To assay spacer acquisition in MMB-1, we overexpressed RT-Cas1 and Cas2 along with Marme_0670 from a broad-host-range plasmid (pKT230), using the 100-bp sequence upstream of the MMB-1 16*S* ribosomal RNA (rRNA) gene as a promoter (Fig. 3A). We recovered newly acquired spacers from the genomic copy of the CRISPR03 array and found that the vast majority (~95%) mapped to the MMB-1 genome, with an expected proportion mapping to the expression vector (figs. S1, C and D, and S4). Although the endogenous type III-B CRISPR operon was still present in these strains, we found that plasmid-driven overexpression of adaptation genes was critical for detectable acquisition of new spacers: Parallel analysis of transconjugants in which plasmid-driven RT-Cas1 had the mutation E870A or E790A at the putative

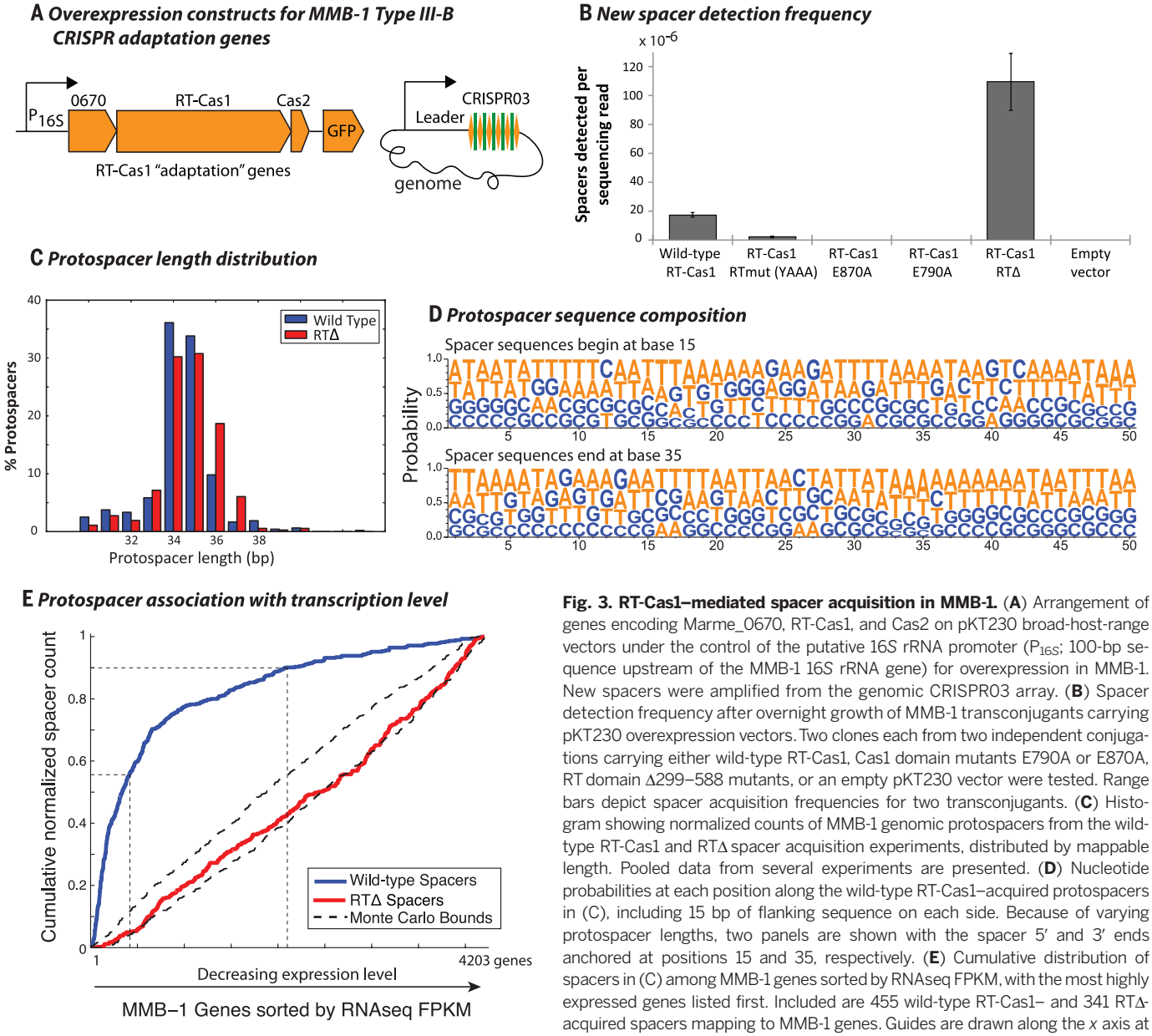

Fig. 3. RT-Cas1–mediated spacer acquisition in MMB-1. (**A**) Arrangement of genes encoding Marme_0670, RT-Cas1, and Cas2 on pKT230 broad-host-range vectors under the control of the putative 16S rRNA promoter (P_{16S}; 100-bp sequence upstream of the MMB-1 16S rRNA gene) for overexpression in MMB-1. New spacers were amplified from the genomic CRISPR03 array. (**B**) Spacer detection frequency after overnight growth of MMB-1 transconjugants carrying pKT230 overexpression vectors. Two clones each from two independent conjugations carrying either wild-type RT-Cas1, Cas1 domain mutants E790A or E870A, RT domain Δ299–588 mutants, or an empty pKT230 vector were tested. Range bars depict spacer acquisition frequencies for two transconjugants. (**C**) Histogram showing normalized counts of MMB-1 genomic protospacers from the wild-type RT-Cas1 and RTΔ spacer acquisition experiments, distributed by mappable length. Pooled data from several experiments are presented. (**D**) Nucleotide probabilities at each position along the wild-type RT-Cas1–acquired protospacers in (C), including 15 bp of flanking sequence on each side. Because of varying protospacer lengths, two panels are shown with the spacer 5′ and 3′ ends anchored at positions 15 and 35, respectively. (**E**) Cumulative distribution of spacers in (C) among MMB-1 genes sorted by RNAseq FPKM, with the most highly expressed genes listed first. Included are 455 wild-type RT-Cas1– and 341 RTΔ-acquired spacers mapping to MMB-1 genes. Guides are drawn along the *x* axis at top-10% and top-50% genes by expression level. Monte Carlo bounds were calculated as in Fig. 2F. rRNA genes have been excluded from this analysis because spacers were rarely acquired from rRNA.

Cas1 active site, or of transconjugants carrying an empty vector, failed to identify any new spacers (Fig. 3B). As in *E. coli*, most (>75%) of the new protospacers were 34 to 36 bp in length (Fig. 3C), and we did not observe a PAM-like sequence at either the 5′ or 3′ ends of the acquired spacers (Fig. 3D).

In contrast to the *E. coli* data set, the genomic regions most frequently sampled by the RT-Cas1 spacer acquisition machinery in MMB-1 appeared to be genes that are typically highly expressed in bacteria. We further investigated this association between expression and spacer capture by obtaining RNA sequencing (RNAseq) expression profiles of two independent MMB-1 transconjugants carrying the RT-Cas1 expression vector. The 10% most highly expressed genes accounted for over 50% of newly acquired spacers, with the top 50% of expressed genes accounting for 90% of newly acquired spacers (Fig. 3E). Next, we tested whether this transcriptional association was dependent on the RT domain of RT-Cas1. Deletion of the conserved RT domain of RT-Cas1 abolished the preference for highly transcribed genes (Fig. 3E and fig. S5), while maintaining a comparable length and sequence distribution for the acquired spacer repertoire (Fig. 3, B and C, and figs. S2B, S3B, and S4). Together, these data demonstrate a RT-dependent bias toward the acquisition of spacers from highly transcribed regions.

Spacers acquired from transcribed regions could conceivably be integrated into the CRISPR array in either a negative or a positive orientation. Among spacers that mapped to MMB-1 transcripts, we observed at most a limited preference for the sense strand (fig. S2, B and C). The lack of a strong bias implies a degree of directional flexibility in the integration mechanism, potentially yielding a system in which only a fraction of spacers is able to protect against a single-stranded DNA or RNA target.

RT-Cas1–mediated spacer acquisition from RNA

The observed association between the gene expression level and the frequency of spacer acquisition in MMB-1, combined with the requirement of the RT domain for this association, is consistent

with an acquisition process involving reverse transcription of an RNA molecule. Nonetheless, an alternative hypothesis is that acquisition of DNA spacers could result from increased accessibility of DNA in regions of high transcriptional activity.

The acquisition of DNA spacer sequences from an RNA molecule can be tested by placing a functional intron into a transcript, which is spliced to yield a ligated-exon junction sequence that is then captured as DNA (*25*). To test whether the RT-Cas1 complex could acquire spacers directly from RNA, we used the self-splicing *td* group I intron, a ribozyme that catalyzes its own excision from its parent transcript, leaving behind a splice junction that was not present as a DNA sequence (*39*). We produced intron-interrupted versions of two MMB-1 genes—the *ssrA* gene, encoding a small noncoding RNA [transfer-messengerRNA (tmRNA) (*40*)] and *Marme_0982*, encoding ribosomal protein S15—in both cases inserting the intron at sites that were well sampled in our spacer libraries. Each construct was designed with four or five mutations to optimize the flanking exon sequences for *td* intron splicing. These mutations allow us to unambiguously distinguish between spliced (plasmid-expressed) and native (genomic) *ssrA* and ribosomal protein S15 transcripts (Fig. 4A). After confirming self-splicing in vitro (fig. S6A), we placed the *td* intron–containing genes on our RT-Cas1 overexpression plasmids and expressed them in MMB-1 from their native promoters. To assess the transcription level of the engineered coding regions relative to their endogenous counterparts in vivo, we performed high-throughput sequencing of RT-PCR amplicons spanning the splice junctions. We found that ~30% of all ribosomal protein S15 transcripts and ~16% of all *ssrA* tmRNA transcripts were produced by splicing in the respective transconjugants (fig. S6B).

We assayed for newly integrated spacers in plasmid copies of CRISPR03, recovering 80,136 new spacers that map to the MMB-1 genome. The protospacer length, sequence composition, and bias for highly expressed genes remained consistent with our previous results in MMB-1 (fig. S7). We found two spacers spanning the splice junction of ribosomal protein S15 and six spacers spanning the splice junction of tmRNA from two independent cultures of two independent transconjugants, thereby confirming that the RT-Cas1 spacer acquisition machinery is capable of acquiring spacers from RNA molecules (Fig. 4, B and C). We observed both sense and antisense spacers spanning the synthetic splice junctions from both the *ssrA* and ribosomal protein S15 constructs (Fig. 4B), further indicating flexibility in the orientation of spacer acquisition relative to the leader. We considered the possibility that these spacers might have been acquired from an extended cDNA copy of the spliced transcripts that was generated through indiscriminate RT activity. Such cDNA sequences would have been detectable by highly sensitive targeted sequencing assays and were not observed (fig. S6C).

Whereas these experiments demonstrate the ability of this system to acquire spacers from RNA, the RT-domain deletion experiments in which spacer acquisition was not biased toward transcribed regions (Fig. 3E) indicate that the system can also acquire spacers from DNA. Nonetheless, the strong transcriptional bias observed with wild-type RT-Cas1 in MMB-1 indicates that most spacer acquisitions driven by the intact RT-Cas1 fusion protein under our conditions are from RNA.

Ligation of RNA and DNA oligonucleotides directly into CRISPR repeats by a RT-Cas1–Cas2 complex

The *E. coli* Cas1-Cas2 complex has been shown to ligate double-stranded DNA (dsDNA) directly into a supercoiled plasmid containing a CRISPR array by means of a concerted cleavage-ligation (transesterification) mechanism, analogous to that of retroviral integrases (*41*). To investigate how MMB-1 RT-Cas1 functions in spacer acquisition, we reconstituted this activity in vitro using purified RT-Cas1 and Cas2 proteins. We confirmed that wild-type RT-Cas1 protein has RT activity that is abolished by the deletion of the RT domain (RTΔ) or mutations at the RT active site (YADD to YAAA at amino acid positions 530 to 533) (fig. S8). To assay spacer acquisition, the purified RT-Cas1 and Cas2 proteins were incubated with (i) putative spacer precursors (protospacers) corresponding to DNA or RNA oligonucleotides of different lengths and (ii) a linear 268-bp internally labeled CRISPR DNA substrate containing the leader, the first two repeats, and interspersed spacer sequences from the MMB-1 CRISPR03 array (Fig. 5A). The reactions also included deoxynucleotide triphosphates (dNTPs) to enable reverse transcription of a ligated RNA oligonucleotide.

In initial assays using a dsDNA oligonucleotide, products derived from cleavage of the CRISPR substrate were readily detected in the presence of RT-Cas1 and Cas2 together but not in the presence of either protein alone (Fig. 5B). The sizes of these products were consistent with cleavage at the junctions between the leader and first repeat on the top strand and between the first repeat and spacer on the bottom strand, as expected for staggered cuts that are known to occur in type I CRISPR systems (*12*). Structural features at the leader-repeat boundary might dictate cleavage at these sites (*41*). Bands of the sizes expected for free 3′ fragments [148 and 155 nucleotides (nt)] were much weaker than those for the corresponding 5′ fragments (120 and 113 nt), reflecting their replacement with prominent bands of the sizes expected for ligation of the oligonucleotide to their 5′ ends (148 and 155 nt plus oligonucelotide). Similar products were also detected using single-stranded DNA (ssDNA) and RNA oligonucleotides of various sizes (ssDNA, 19 to 59 nt; RNA, 21 to 50 nt) (Fig. 5, B and C, and figs. S9 and S10), presumably reflecting that the more uniform spacer size of 34 to 36 bp in vivo is due to processing of the spacers prior to their integration into the CRISPR array. Additionally, a 3′-phosphate modification of the ssDNA oligonucleotide almost completely abolished the cleavage-ligation reaction, suggesting a crucial role of the 3′OH of the donor oligonucleotide in the integration reaction (Fig. 5D). The ligation of both DNA and RNA oligonucleotides into the CRISPR DNA was confirmed by their expected ribonuclease (RNase) and/or deoxyribonuclease (DNase) sensitivity in reactions with 5′-end–labeled oligonucleotides and unlabeled CRISPR DNA (Fig. 5E). The ligated RNA oligonucleotide was sensitive to RNase H, indicating its presence in an RNA-DNA hybrid, as would be expected if it was used as a template for cDNA synthesis by RT-Cas1 (Fig. 5E).

Although the MMB-1 RT-Cas1–Cas2 complex functions similarly to the *E. coli* Cas1-Cas2 complex to site-specifically integrate putative spacer precursors into CRISPR arrays, it differs in being able to use a linear CRISPR DNA substrate and to insert not only dsDNA but also ssDNA and RNA oligonucleotides. The ligation of RNA and DNA oligonucleotides into the CRISPR DNA substrate differs in two respects. First, whereas the E870A mutation at the Cas1 active site abolishes ligation of both RNA and DNA oligonucleotides, deletion of the RT domain (RTΔ) abolishes ligation of RNA but not DNA oligonucleotides (Fig. 5F). These findings mirror in vivo results showing that the E870 mutation abolishes the acquisition of both RNA and DNA spacers, whereas the RTΔ mutation abolishes the acquisition of RNA but not DNA spacers (Fig. 3, B and E). Second, dNTPs are required for ligation of RNA but not DNA oligonucleotides, with deoxyguanosine triphosphate (dGTP) or deoxyadenosine triphosphate (dATP) alone sufficient to support RNA ligation (Fig. 5G). Together, these findings suggest that the RT-Cas1 protein is modular, with the Cas1 domain catalyzing ligation of both RNA and DNA spacers into CRISPR repeats, but with ligation of RNA spacers requiring binding by the N-terminal and/or RT domains, possibly coupled to RT domain core closure and/or the initiation of reverse transcription on addition of dNTPs.

Integrated RNA oligonucleotides are reverse-transcribed by the RT-Cas1–Cas2 complex

We tested whether the RT-Cas1–Cas2 complex could reverse-transcribe an integrated RNA oligonucleotide in vitro to generate the cDNA precursor of a fully integrated RNA spacer. The cleavage-ligation reactions on either side of repeat R1 generate products with 5′ overhangs that could potentially be substrates for target DNA-primed reverse transcription (TPRT) reactions, in which the 3′ end of the opposite strand is extended to yield a DNA copy of the repeat plus the ligated RNA oligonucleotide (Fig. 6A). To detect the synthesis of such cDNAs, we incubated the CRISPR DNA with RT-Cas1–Cas2 in the presence of a 21-nt RNA oligonucleotide and supplied radioactive deoxycytidine triphosphate (dCTP) and other unlabeled dNTPs during the incubation (Fig. 6A). cDNA synthesis during the reactions was evident by the labeled products being of the same size as the two ligation products, as expected for a TPRT reaction extending through the R1 repeat and ligated RNA. The synthesis of these cDNAs depends on the presence of the RNA oligonucleotide, the CRISPR DNA, and RT-Cas1–Cas2 (Fig. 6B). The RTΔ mutant abolishes cDNA synthesis,

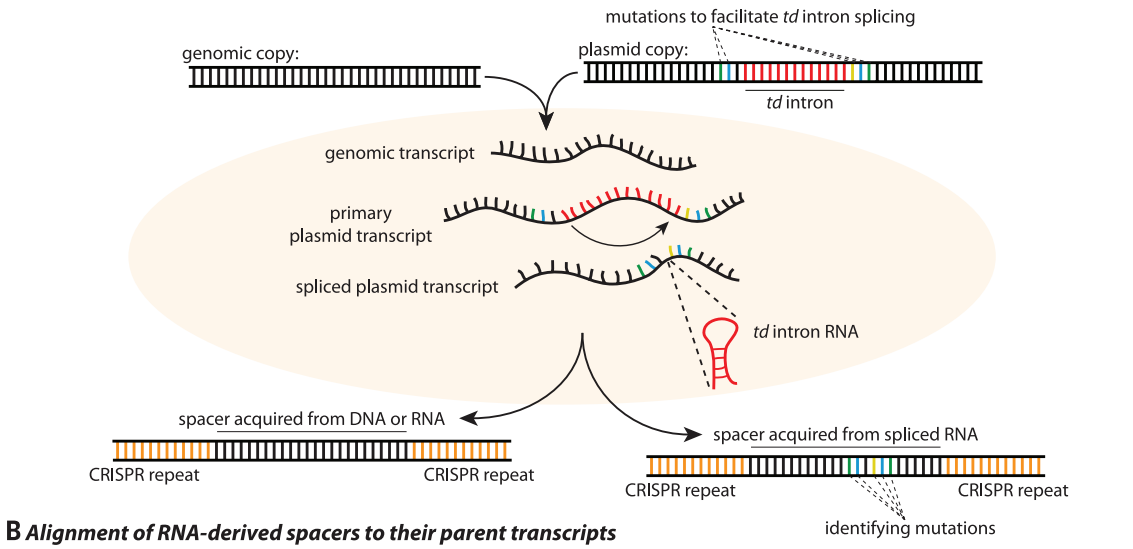

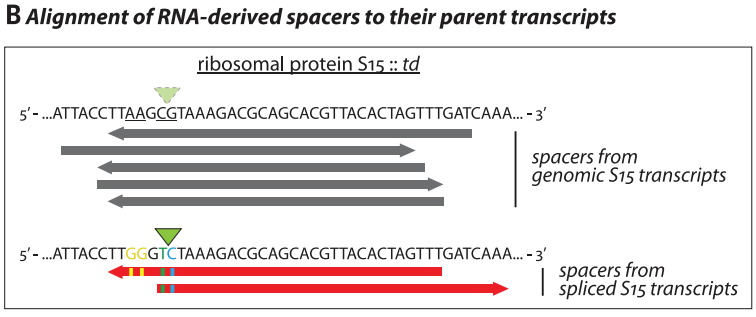

C ***Total number of spacers from genomic transcripts***

td intron Construct	Genomic Spacers	Max MM
ribosomal protein S15	37	2
ssrA tmRNA	60	3

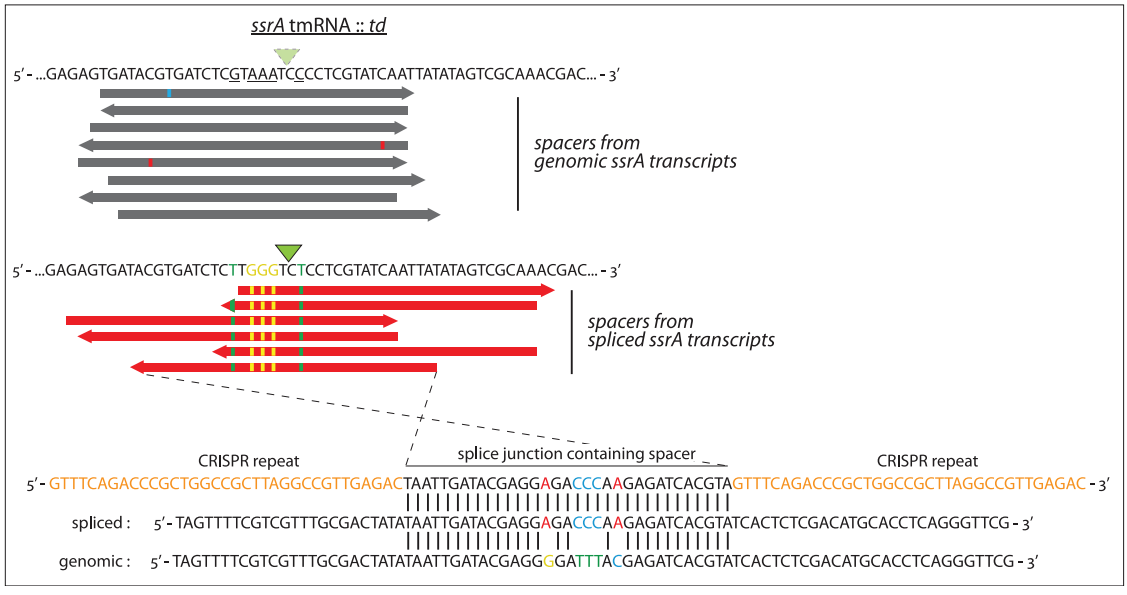

Fig. 4. Spacer acquisition from RNA in the MMB-1 type III-B system. (**A**) Spacers acquired from a host genome could conceivably originate from either RNA or DNA. To test for an RNA origin, we used an engineered self-splicing transcript, which produces an RNA sequence junction that is not encoded by DNA. Bases that were mutated to provide flanking exon sequences favorable for *td* intron splicing were separated by the 393-bp intron in the DNA template. After transcription and splicing, the two exons were brought together to form a novel junction containing the identifying mutations. Newly acquired spacers that contain this exon-junction indicate spacer acquisition from an RNA target. (**B**) Alignments of some of the genome-contiguous spacers (gray) and several newly acquired exon-junction–spanning spacers (red) to the genomic and split-gene sequences, respectively. Bases mutated to facilitate *td* intron splicing are underlined in the genomic sequences. Identifying mutations are depicted as colored bases, and the splice sites are indicated by green triangles. The highlighted *ssrA* exon-junction–spanning spacer (bottom) is antisense to the spliced tmRNA and differs from a putative DNA template by the five expected mutations. (**C**) All unique spacers spanning the *td* intron splice site that did not carry the engineered mutations. The maximum number of mismatches (MM) when these spacers were mapped to the wild-type genomic locus is indicated. None of the identifying mutations were observed among these sporadic mismatches. The spacers in (B) were in addition to four spacers (one for the S15 and three for the *ssrA* construct) that align to the unspliced exon-intron junction and could have been derived from either DNA or (nascent) RNA.

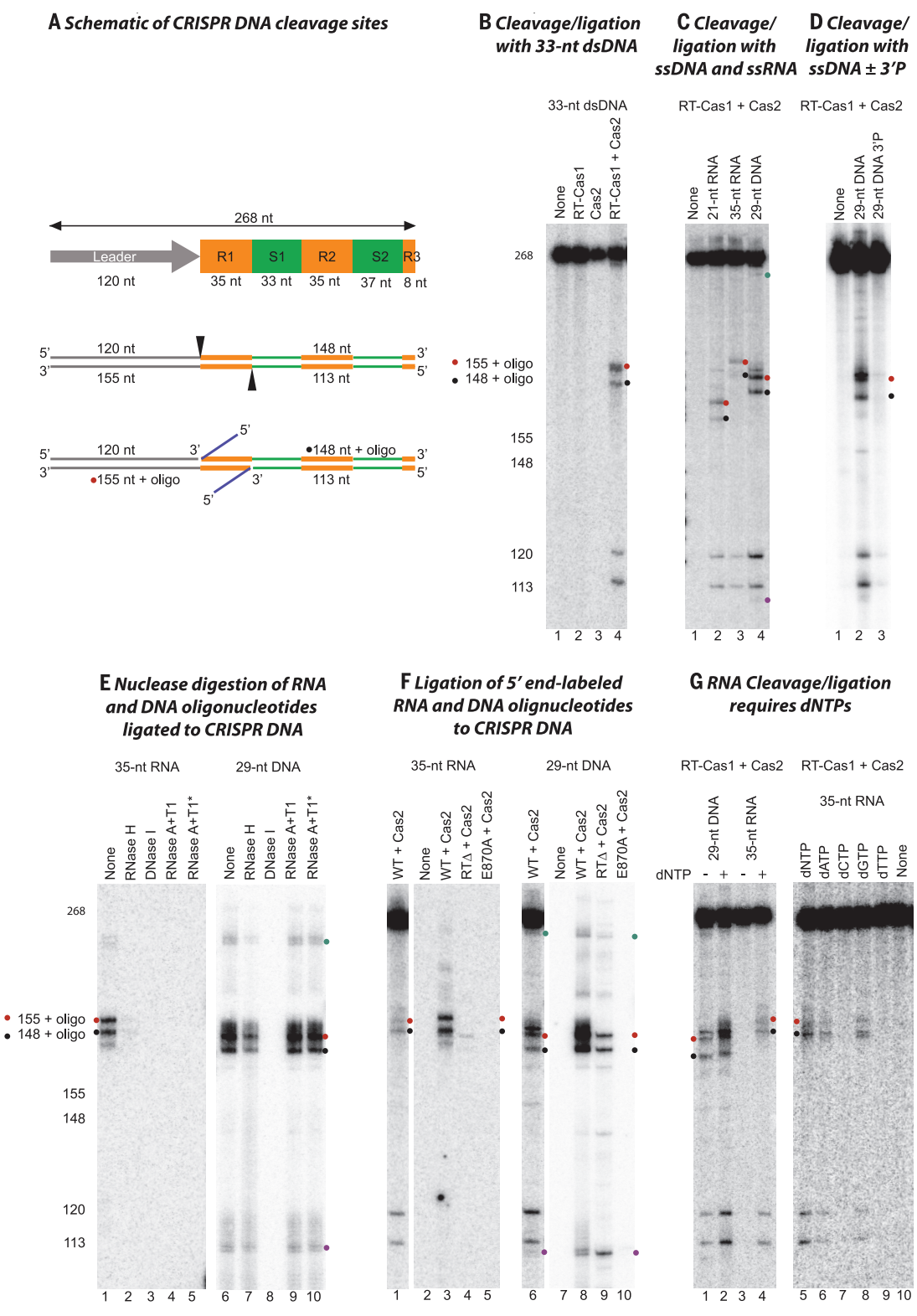

Fig. 5. Site-specific CRISPR DNA cleavage-ligation by the RT-Cas1–Cas2 complex. (**A**) Schematic of CRISPR DNA substrates and products of cleavage-ligation reactions. The substrate was a 268-bp DNA containing the leader (gray), the first two repeats (R1 and R2, orange) and spacers (S1 and S2, green), and part of the third repeat (R3, orange) of the MMB-1 CRISPR03 array. Cleavages (arrowheads) occur at the boundaries of the first repeat with concomitant ligation of a DNA or RNA oligonucleotide (oligo, blue) to the 3′ fragment, yielding products of the sizes shown. (**B**) Internally labeled CRISPR DNA and a 33-nt dsDNA were incubated with no protein (lane 1), RT-Cas1 (lane 2), Cas2 (lane 3), or a 1:2 mixture of RT-Cas1 and Cas2 (lane 4). The sizes of products determined from sequencing ladders in parallel lanes are indicated on the left. (**C**) Internally labeled CRISPR DNA was incubated with wild-type (WT) RT-Cas1 and Cas2 without (lane 1) or with a 21-nt RNA (lane 2), 35-nt RNA (lane 3), or 29-nt ssDNA (lane 4). (**D**) Internally labeled CRISPR DNA was incubated with WT RT-Cas1 plus Cas2 in the absence (lane 1) or presence of a 29-nt ssDNA with either a 3′ OH (lane 2) or a 3′ phosphate (lane 3). (**E**) Nuclease digestion of 5′-end–labeled RNA and DNA oligonucleotides ligated to CRISPR DNA. Ligation reactions were performed as in (C). After extraction with phenol-CIA and ethanol precipitation, the products were incubated with the indicated nucleases. An asterisk indicates that the sample was boiled to denature the DNA before adding the nuclease. (**F**) Ligation of 5′-end–labeled RNA and DNA oligonucleotides into CRISPR DNA by WT and mutant RT-Cas1 proteins. Lanes 1 and 6 show control reactions of internally labeled CRISPR with WT RT-Cas1 plus Cas2 and an unlabeled 35-nt ssRNA or 29-nt ssDNA oligonucleotide for comparison. Lanes 2 to 5 and 7 to 10 show reactions of unlabeled CRISPR DNA with 5′-end–labeled 35-nt ssRNA and 29-nt ssDNA, respectively, and WT, E870A, and RTΔ RT-Cas1 plus Cas2. All reactions were carried out in the presence of dNTPs. (**G**) Effect of dNTPs. In the gel on the left, internally labeled CRISPR DNA was incubated with WT RT-Cas1 plus Cas2 in the presence of a 29-nt ssDNA (lanes 1 and 2) or 35-nt ssRNA (lanes 3 and 4) in the absence (lanes 1 and 3) or presence of 1 mM dNTPs (1 mM each of dATP, dCTP, dGTP, and dTTP; lanes 2 and 4). In the gel on the right, internally labeled CRISPR DNA was incubated with WT RT-Cas1 plus Cas2 in the presence of a 35-nt ssRNA oligonucleotide in the absence (lane 10) or presence of different dNTPs (1 mM) as indicated (lanes 5 to 9). Red and black dots indicate products resulting from cleavage and ligation of oligonucleotides at the junction of the leader and repeat 1 on the top strand and the junction of repeat 1 and spacer 1 on the bottom strand, respectively; cyan and purple dots indicate products of the size expected for cleavage and ligation of the oligonucleotide at the junctions of the second CRISPR repeat (see fig. S10).

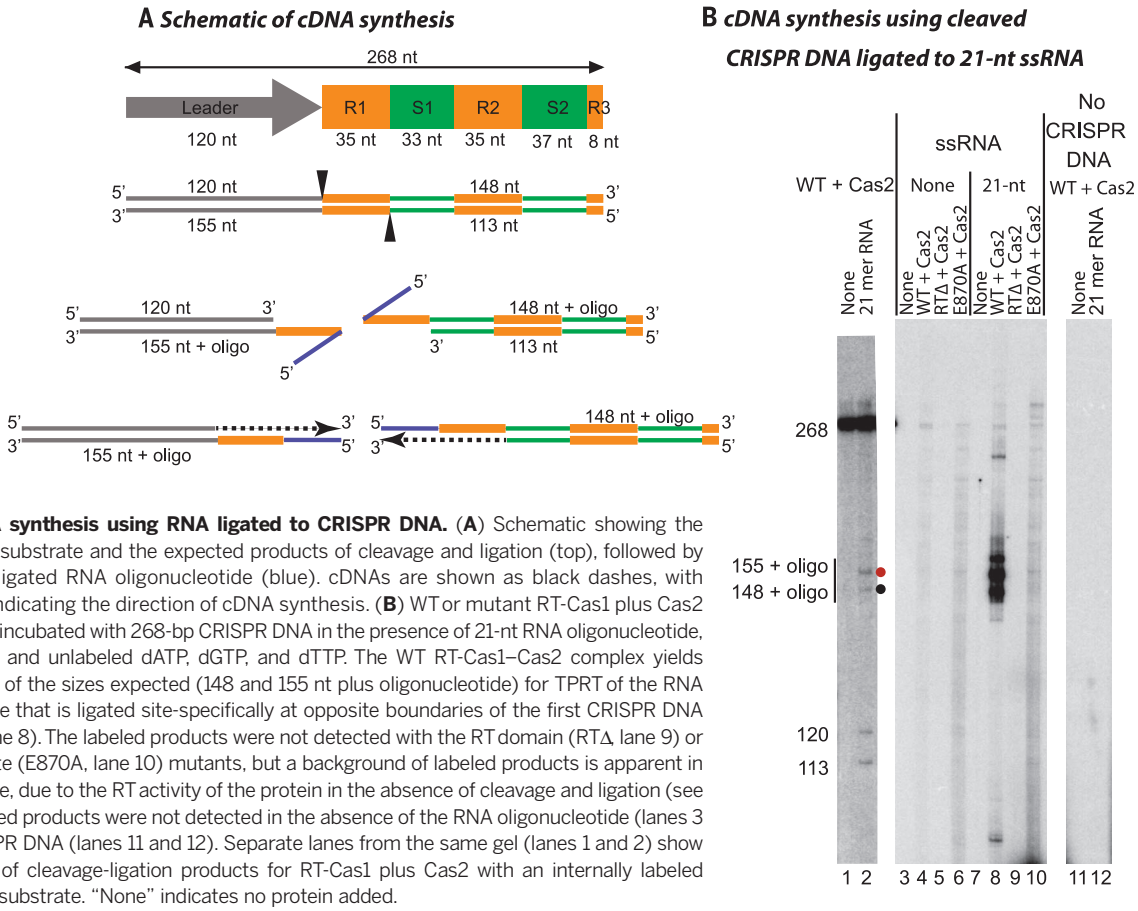

Fig. 6. cDNA synthesis using RNA ligated to CRISPR DNA. (**A**) Schematic showing the CRISPR DNA substrate and the expected products of cleavage and ligation (top), followed by TPRT of the ligated RNA oligonucleotide (blue). cDNAs are shown as black dashes, with arrowheads indicating the direction of cDNA synthesis. (**B**) WT or mutant RT-Cas1 plus Cas2 proteins were incubated with 268-bp CRISPR DNA in the presence of 21-nt RNA oligonucleotide, labeled dCTP, and unlabeled dATP, dGTP, and dTTP. The WT RT-Cas1–Cas2 complex yields labeled bands of the sizes expected (148 and 155 nt plus oligonucleotide) for TPRT of the RNA oligonucleotide that is ligated site-specifically at opposite boundaries of the first CRISPR DNA repeat (R1, lane 8). The labeled products were not detected with the RT domain (RTΔ, lane 9) or Cas1 active site (E870A, lane 10) mutants, but a background of labeled products is apparent in the E870A lane, due to the RT activity of the protein in the absence of cleavage and ligation (see fig. S8). Labeled products were not detected in the absence of the RNA oligonucleotide (lanes 3 to 6) or CRISPR DNA (lanes 11 and 12). Separate lanes from the same gel (lanes 1 and 2) show the positions of cleavage-ligation products for RT-Cas1 plus Cas2 with an internally labeled CRISPR DNA substrate. "None" indicates no protein added.

whereas the E870A mutant, which retains RT activity (fig. S8) but cannot integrate the RNA oligonucleotide or create the 3′OH required for priming cDNA synthesis (Fig. 5F), produces only a heterogeneous background of labeled products (Fig. 6B). The TPRT products detected in our assays may represent an intermediate in spacer acquisition, with additional steps potentially including digestion of the ligated RNA spacer strand by a host RNase H, synthesis of a full dsDNA containing the spacer sequence by RT-Cas1 or a host DNA polymerase, and ligation of the unattached ends of the dsDNA into the CRISPR array. Our in vivo and in vitro data suggest that this can occur in either orientation and may involve host enzymes that are present in MMB-1 but not in *E. coli*.

Conclusion

We showed that the MMB1 RT-Cas1 fusion protein can mediate the direct acquisition of spacers from donor RNA, using the Cas1 integrase activity to directly ligate an RNA protospacer into CRISPR DNA repeats. The 3′ end generated by cleavage of the opposite DNA strand is then poised for use as a primer for TPRT (*26*). This mechanism shares features with group II intron retrohoming, in which the intron RNA uses its ribozyme activity to insert itself directly into the host genome and is then converted to an intron cDNA by using the 3′ end generated by cleavage of the opposite DNA strand for TPRT (*42*). Because type III CRISPR systems are known to target RNA for degradation, and RT-Cas1–encoding genes are exclusively associated with such systems, RNA spacer acquisition makes these CRISPRs distinctively capable of generating immunity against parasitic RNA sequences, potentially including RNA phages and/or other "selfish" RNAs that maintain themselves through the action of host machinery (*43*–*46*). The acquisition of RNA spacers might also contribute to immune responses to highly transcribed regions of DNA phages and plasmids, by coupling spacers from such regions to an interference system that targets DNA, RNA, or both (*15*–*21*).

It is possible that fusion between the RT and Cas1 domains may not be necessary to facilitate uptake of RNA spacers; there are several examples of CRISPR loci in which genes encoding similar group II intron–like RTs are adjacent but not fused to *cas1* (*29*). Thus, the mechanisms described herein could potentially extend to species with separately encoded RT and Cas1 components. In addition, RNA spacer acquisition could be involved in gene regulation, providing a straightforward means for bacteria to down-regulate a set of target loci in response to activation of the CRISPR locus.

To fully assess the prevalence and importance of CRISPR adaptation to RNA, a greater understanding of the impact of invasive RNAs in bacteria is necessary. However, our knowledge of the abundance and distribution of RNA phages and other RNA parasites is limited, with the vast majority restricted to the *Escherichia* and *Pseudomonas* genera. Future research on the distribution of spacers in RT-associated CRISPR loci among natural populations of bacteria and their environments might help shed light on this topic.

Materials and methods

RT-Cas1 genomic neighborhood analysis

The genomic neighborhoods (up to 20 kb) of RT-Cas1–encoding genes were retrieved from 50 bacterial strains with a custom BioPython script that uses the NCBI tblastn software. The HMMER 3.0 algorithm was then used to identify whether the RT-Cas1–encoding genes were associated with type I, II, or III CRISPR systems, using Cas3 (TIGR 01587, 01596, 02562, 02621, and 03158), Cas9 (TIGR 01865 and 3031), and Cas10 (TIGR 02577 and 02578) hidden Markov models as "signature" genes for each type, respectively (*8*). Each result was assessed manually by iterative runs of BLAST (Basic Local Alignment Search Tool, NCBI) and the CRISPRfinder online suite.

Monte Carlo simulation of expected spacer acquisition characteristics for random sampling of all genes

We used a Monte Carlo simulation to evaluate a null hypothesis based on random assortment of

spacer acquisitions from genomic DNA, with no dependence on gene expression level. For each system, a series of samples of 500 spacers each were randomly chosen in silico from a list of all genes, based on the sizes of the individual genes using the stochastic universal sampling algorithm. Sets of 1000 such trials were used to generate a range of null relationships between gene expression and spacer acquisition. The Monte Carlo bounds (black dotted lines in Figs. 2 and 3 and figs. S2, S5, and S7) depict the envelope of such simulated random assortments. Traces above this envelope indicate preferential spacer acquisition from highly expressed genes; traces below the envelope indicate spacer acquisition from poorly expressed genes more often than expected by random chance. RNAseq data from *E. coli* K12 were obtained from (*47*) (data set without computational background subtraction). MMB-1 expression data were generated by RNAseq analysis of the transconjugants used in this study (Fig. 3).

Construction of expression vectors

Plasmids for inducible overexpression of the MMB-1 type III-B CRISPR operon in *E. coli* were built on the pBAD/Myc–His B backbone (Life Technologies). RT-Cas1–associated genes [*Marme_0670*, *Marme_0669* (RT-Cas1), and *Marme_0668* (Cas2)] and green fluorescent protein (GFP) were driven by P_{ara}, and the CRISPR03 array was driven by P_{trc}. The other seven genes [*Marme_0677* to *_0672* (Cmr1 to Cmr6) and *Marme_0671*] and lacZα were driven by P_{lac}. GFP and lacZα ORFs enabled verification of expression of the transcripts containing RT-Cas1–associated adaptation genes and Cmr effector genes, respectively. Point mutants of the Cas1 (E790A or E870A) and RT domains (YADD to YAAA at amino acid positions 530 to 533) of RT-Cas1 were tested with overexpression of the RT-Cas1–associated subset, with and without the remaining seven genes. Deletion mutants of the RT domain of RT-Cas1 (Δ299–588), and Cas2 [Δ32–92] were tested with overexpression of the RT-Cas1–associated subset only.

Plasmids for the overexpression of the RT-Cas1–associated genes in MMB-1 cells were built on the pKT230 backbone (a gift from L. Banta, Williams College). The genes were driven by the 100-bp promoter–containing sequence (positions 306,879 to 306,978) upstream of a MMB-1 16*S* rRNA gene. Cas1 point mutants (E790A or E870A) and the RTΔ mutant were also tested. For experiments with *td* intron–containing constructs, a copy of the CRISPR03 array with its leader sequence was also placed on the pKT230 vector to increase the concentration of CRISPR arrays per unit input DNA in the PCR amplification step, and thus increase the efficiency of our spacer detection assay.

Plasmids for protein expression and purification were built on the pMal-c2X backbone [New England Biolabs (NEB)] for RT-Cas1 (wild type and mutants) and on the pET14b backbone (Novagene) for Cas2. Variants of RT-Cas1 were expressed with an N-terminal maltose-binding protein tag attached via a noncleavable rigid linker (*50*). Cas2 was expressed with an N-terminal 6xHis tag.

All plasmids were verified by sequencing. Plasmid structures are available upon request.

Strains and culture conditions

All bacterial strains used in this study were stored in 20% glycerol at −80°C. Two clones from each conjugation were maintained for each plasmid (referred to as independent transconjugants).

pBAD plasmids (Amp^R) encoding MMB-1 type III-B operon components were transformed into chemically competent TOP10F' cells (Life Technologies). TOP10F'-derived strains were grown at 37°C on Luria-Bertani (LB) agar plates (10 g/l tryptone, 5 g/l yeast extract, 10 g/l NaCl, 15 g/l agar) with 100 μg/ml of ampicillin, 0.1% w/v arabinose, and 0.1 mM IPTG (isopropyl-β-D-thiogalactopyranoside) overnight.

pKT230 plasmids (Kan^R) encoding MMB-1 type III-B operon components were mobilized into a spontaneous rifampicin-resistant mutant of MMB-1 (strain ATCC 700492) from a donor *E. coli* strain carrying the pRL443 conjugal plasmid (a gift from M. Davison, Carnegie Institution), as described in (*51*). All transformed MMB-1 strains were grown on 2216 marine agar (Difco) with 50 μg/ml of kanamycin for 16 hours at 25°C.

For experiments with MMB-1 transconjugants carrying *td* intron constructs, 150-ml cultures were subsequently prepared in 2216 broth (Difco) with 50 μg/ml of kanamycin and shaken at 26° to 27°C in 1-liter flasks for 20 hours before midiprep.

E. coli strain DH5α (Life Technologies) was used for cloning, and Rosetta2 and Rosetta2(DE3) (Novagen) were used for protein expression. Bacteria were grown in LB medium with shaking at 200 rpm. Antibiotics were added when needed (ampicillin, 100 mg/l; chloramphenicol, 25 mg/l).

Nucleic acid extraction

Plasmid DNA from *E. coli* strains was extracted using the QIAprep Spin Miniprep Kit (QIAGEN). Genomic DNA from MMB-1 strains was extracted using a modified SDS–proteinase K method: Briefly, cells were scraped from plates and resuspended in 1 ml of lysis buffer (10 mM tris, 10 mM EDTA, 400 μg/ml proteinase K, 0.5% SDS) and incubated at 55°C for 1 hour. Batches of the digest (50 to 100 μl) were subsequently purified using the Genomic DNA Clean & Concentrator Kit (Zymo Research).

Total RNA was extracted from MMB-1 strains using a combined trizol–RNeasy method: Briefly, cells were scraped from plates and homogenized directly in 1 ml of trizol (Life Technologies) by vortexing, and total RNA was extracted with 200 μl of chloroform. Ethanol (500 μl) was added to an equal volume of the aqueous phase containing RNA, and the mixture was purified using the RNeasy Kit (QIAGEN) with on-column DNase digestion according to the manufacturer's instructions. This protocol selects RNA >200 nt and thus depletes transfer RNAs.

Plasmid DNA was purified from large MMB-1 cultures using a custom midiprep method. Cells were harvested from 150- to 200-ml confluent cultures (3000*g*, 30 min, 4°C) and homogenized in 12 ml of alkaline lysis buffer (40 mM glucose, 10 mM tris, 4 mM EDTA, 0.1 N NaOH, 0.5% SDS) at 37°C by pipetting until clear (10 to 15 min). Chilled neutralization buffer (8 ml) was added (3 M CH_3COOK, 2 M CH_3COOH), and lysates were immediately transferred to ice to prevent digestion of genomic DNA. Samples were mixed by inverting, and the genomic DNA–containing precipitate was removed by centrifugation (20,000*g*, 20 min, 4°C). Clarified lysates were extracted twice with a 1:1 mixture of tris-saturated phenol (Life Technologies) and $CHCl_3$ (Fisher Scientific) and once with $CHCl_3$ in heavy phase lock gel tubes (5 Prime). Ethanol (50 ml) was added and DNA was pelleted by centrifugation (16,000*g*, 20 min, 4°C), washed twice in 80% ethanol, and resuspended in 500 μl of elution buffer (10 mM tris, pH 8.5). Samples were treated with 20 μg/ml RNase A (Life Technologies) at 37°C for 30 min, further digested with 150 μg/ml of protease K in 0.5% SDS at 50°C for 30 min, and purified by organic extraction. Plasmid DNA was resuspended in 0.5 ml of elution buffer, desalted with Illustra NAP-5 G-25 Sephadex columns (GE Healthcare), and eluted with 1 ml of water. Batches of 100 μl were linearized with PvuII-HF (NEB) to aid denaturation during PCR. Last, each digest was purified using a Genomic DNA Clean & Concentrator column (Zymo Research).

DNA and RNA preparations were quantified using a fluorometer (Qubit 2.0, Life Technologies).

Spacer sequencing

Leader proximal spacers were amplified by PCR from 3 to 4 ng of genomic DNA per μl of PCR mix using forward primer AF-SS-119 (CGACGCTCTTCCGATCTNNNNNCTGAAATGATTGGAAAAAATAAGG) anchored in the leader sequence and reverse primer AF-SS-121 (ACTGACGCTAGTGCATCACGTGGCGGAGATCTTTAA) in the first native spacer. For each sample, 96 10-μl reactions were pooled. Sequencing adaptors were then attached in a second round of PCR with 0.5 μl of the previous reaction as a template in a 50-μl reaction, using AF-SS-44:55 (CAAGCAGAAGACGGCATACGAGAT NNNNNNNN GTGACTGGAGTTCAGACGTGTGCTCTTCCGATCACTGACGCTAGTGCATCA) and AF-KLA-67:74 (AATGATACGGCGACCACCGAGATCTACAC NNNNNNNN ACACTCTTTCCCTACACGACGCTCTTCCGATCT), where the $(N)_8$ barcodes correspond to reverse-complemented TruSeq HT indexes D701 to D712 and D501 to D508, respectively (Illumina). Template matching regions in primers are underlined. Phusion High-Fidelity PCR Master Mix with HF Buffer (Fisher Scientific) was used for all reactions. Cycling conditions for round 1 were as follows: one cycle at 98°C for 1 min; two cycles at 98°C for 10 s, 50°C for 20 s, and 72°C for 30 s; 24 cycles at 98°C for 15 s, 65°C for 15 s; and 72°C for 30 s; and one cycle at 72°C for 9 min. Conditions for round 2 were one cycle at 98°C for 1 min; two cycles at 98°C for 10 s, 54°C for 20 s, and 72°C for 30 s; five cycles at 98°C for 15 s, 70°C for 15 s, and 72°C for 30 s; and one cycle at 72°C for 9 min. The dominant amplicons containing the first native spacer from unmodified CRISPR templates after rounds 1 and 2 were 123 bp and 241 bp, respectively. We

prepared sequencing libraries by blind excision of gel slices at 300 to 320 bp (70 bp above the 241-bp band, consistent with the expected size of an amplicon from an expanded CRISPR array) after agarose electrophoresis (3%, 4.2 V/cm, 2 hours) of the round 2 amplicons.

When amplifying spacers from plasmids, 1 ng of DNA was used per microliter of PCR mix, synthesis time was shortened to 15 s, and 20 and nine cycles were used in rounds 1 and 2 instead of 24 and five, respectively. Additionally, round 1 amplicons were purified by blind excision of gel slices at 180 to 200 nt after denaturing PAGE (polyacrylamide gel electrophoresis) [pre-run TBE-Urea 10% gels (Novex), 180 V, 80 min in XCell SureLock Mini-Cells (Life Technologies)], and agarose gel–purified libraries were further PAGE-purified by blind excision of gel slices at 300 to 320 nt (pre-run TBE-Urea 6% gels, 180 V, 90 min as above). In this way, spacer detection efficiency was increased ~100-fold. Libraries were quantified by Qubit and sequenced with MiSeq v3 kits (Illumina) (150 cycles, read 1; 8 cycles, index 1; and 8 cycles, index 2).

Spacers were trimmed from reads using a custom Python script and considered identical if they differed only by one nucleotide. Protospacers were mapped using Bowtie 2.0 ("–very-sensitive-local" alignments). These methods preserve strand information.

Directional RNAseq profiling of MMB-1 strains

Total RNA (1 μg) was incubated at 95°C in alkaline fragmentation buffer (2 mM EDTA, 10 mM Na_2CO_3, 90 mM $NaHCO_3$; pH ~9.3) for 45 min and PAGE-purified [pre-run 15% TBE-Urea precast gels, 200 V, 45 min in Mini-PROTEAN electrophoresis cells (Bio-Rad)] to select 30- to 80-nt fragments. RNA fragments were 3′-dephosphorylated with T4 polynucleotide kinase (NEB) at 37°C for 60 min in the supplied buffer, then desalted by ethanol precipitation. Desphosphorylated RNA was denatured again in adenylated ligation buffer [3.3 mM dithiothreitol (DTT), 10 mM $MgCl_2$, 10 μg/ml acetylated BSA, 8.3% glycerol, 50 mM HEPES-KOH; pH ~8.3) for 1 min at 98°C and ligated to preadenylated adaptor AF-JA-34 (/5rApp/NNNNNNAGATCGGAAGAGCACACGTCT/3ddC/) at 22°C for 4 hours using 10 U T4 RNA Ligase I (NEB). The $(N)_6$ barcode for each RNA fragment allowed us to computationally collapse PCR bias. Excess adaptor was removed by treatment with 5′ deadenylase (NEB) followed by $RecJ_f$ (NEB) treatment and organic extraction to purify ligation products. RNA was reverse-transcribed using primer AF-JA-126 (/5Phos/AGATCGGAAGAGCGTCGTGT/iSp18/CACTCA/iSp18/GTGACTGGAGTTCAGACGTGTGCTCTTCCGATCT) with SuperScript II (Life Technologies) and subsequently hydrolyzed in 0.2 M NaOH at 70°C for 15 min. cDNA was PAGE-purified (pre-run 10% TBE-urea gels, 200 V, 45 min in Mini-PROTEAN electrophoresis cells) to select 90- to 150-nt fragments and circularized with 50U CircLigase I (Epicentre). Libraries were prepared by six to 14 cycles of PCR with universal adaptor AF-JA-158 (AATGATACGGCGACCACCGAGATCTACACTCTTTCCCTACACGACGCTCTTCCGATCT) and indexing primers AF-JA-118:125 (CAAGCAGAAGACGGCATACGAGAT NNNNNN GTGACTGGAGTTCAGACGTGTGCTCTTCCG) where the $(N)_6$ barcodes correspond to TruSeq LT indexes AD001 to AD008 (Illumina). Amplicons of 160 to 200 bp were gel-purified by agarose electrophoresis.

Construction and validation of td intron constructs

Constructs with the following features were ordered as gBlocks (Integrated DNA Technologies) and cloned downstream of the T7 promoter in pCR-Blunt II-TOPO (Life Technologies). Bases 208 to 216 (CTTAAGCGT) of the ribosomal protein S15 gene (*Marme_0982*) and bases 67 to 75 (CGTAAATCC) of the *ssrA* tmRNA gene (*Marme_R0008*) were replaced with the wild-type *td* intron splice junction (CTTGGGT|CT). The 393-bp intron sequence was inserted at the exon junction '|'. Included were 128 bp of upstream sequence for *Marme_0982* and 183 bp of upstream sequence and 30 bp of downstream sequence for *Marme_R0008*. Transcripts were generated from linearized plasmids using the MEGAscript T7 Transcription kit (Life Technologies). Mostly unspliced RNA was obtained by arresting the transcription reaction after 5 min at 37°C and subsequently extracted with acidified phenol:$CHCl_3$ (Life Technologies). One-third of the reaction product was incubated in a splicing buffer (40 mM tris, pH 7.5; 6 mM $MgCl_2$; 100 mM KCl; 1 mM ribo-GTP) at 37°C for 30 min and desalted by ethanol precipitation. Spliced and unspliced transcripts were visualized by 1/4x tris-acetate-EDTA native agarose gel electrophoresis, with a 100-bp Quickload dsDNA ladder (NEB) providing approximate sizing. Intron-containing genes were then transferred to pKT230-derived MMB-1 overexpression vectors carrying RT-Cas1–associated genes and a copy of the CRISPR03 array. One clone each from two independent conjugations was isolated for each vector.

In vivo splicing efficiency was measured by high-throughput sequencing as follows. Total RNA was extracted and 1 μg was reverse-transcribed (SuperScript III, high GC content protocol; Life Technologies) with gene-specific primers downstream of the splice junctions that would bind both spliced and unspliced transcripts: AF-SS-238 (CTTAGCGACGTAGACCTAGTTTTT) for *Marme_0982* and AF-SS-241 (GGTTATTAAGCTGCTAAAGCGTAG) for *Marme_R0008*. cDNA was treated with RNase H, and libraries were prepared by a two-round PCR method adapted from the CRISPR spacer sequencing method described above. Round 1 of PCR was performed at annealing temperatures of 48° and 65°C for two and 19 cycles, respectively, with primers AF-SS-242 (CGACGCTCTTCCGATCTNNNNNGATTCGCATGGTAAAC) and AF-SS-243 (ACTGACGCTAGTGCATCAAACTAGTGTAACGTGCTG) for *Marme_0982*, and for two and 16 cycles, respectively, with primers AF-SS-247 (CGACGCTCTTCCGATCTNNNNNCACGAACCTGAGGTG) and AF-SS-248 (ACTGACGCTAGTGCATCACGTCGTTTGCGACTATATAATTGA) for *Marme_R0008*. This approach simultaneously generated amplicons of identical length for both spliced and unspliced transcripts, which were then attached to flowcell adaptors (Illumina) with a second round of PCR as before.

The presence of exon-junction sequences corresponding to the *td* intron constructs in DNA form outside the CRISPR arrays was also tested by high-throughput sequencing. Libraries consisting of the ~100-bp region containing the *td* intron insertion sites in *Marme_R0008* and *Marme_0982* were prepared by a two-round PCR method identical to the one described above for measuring splicing efficiency by RT-PCR, using 100 ng of genomic DNA (~2×10^7 copies) as a template instead of reverse-transcribed cDNA. Round 1 of PCR was performed at annealing temperatures of 57°C and 68°C for two and 16 cycles, respectively, with primers AF-SS-318 (CGACGCTCTTCCGATCTNNNNNCACATTCATGACCACCATTCTCG) and AF-SS-309 (ACTGACGCTAGTGCATCACTTCGGTCTTAGCGACGTAGAC) for *Marme_0982* and primers AF-SS-310 (CGACGCTCTTCCGATCTNNNNNGGGGTGACATGGTTTCGACG) and AF-SS-311 (ACTGACGCTAGTGCATCAGCAGGTTATTAAGCTGCTAAAGCG) for *Marme_R0008*. The amplicons were then attached to flowcell adaptors (Illumina) with a second round of PCR as before. Each library was sequenced to a depth of ~5 million reads. To ensure that the PCR was not bottlenecked, we also included a spike-in (1 molecule per 1000 copies of the MMB-1 genome) of synthetic ssDNA templates—AF-SS-312 (TAAAAACATTGAAGGTCTACAAGGTCACTTTAAAGCTCACATTCATGACCACCATTCTCGTCGCNNNNNNNNNNNNNATGGTAAACCAACGTCGTAAGTTGTTGGATTACCAGCTGCGTAAAGACGCAGCACGTTACACTAGTTTGANNNNNNNNNNNNGTCTACGTCGCTAAGACCGAAG) for *Marme_0982* and AF-SS-313 (GGGGTGACATGGTTTCGACGNNNNNNNNNNNNNCCTGAGGTGCATGTCGAGAGTGATACGTGATCTCAGCTGTCCCCTCGTATCAATTATATAGTCGCAAANNNNNNNNNNNNCGCTTTAGCAGCTTAATAACCTGCTAGTGTGCTGCCCTCAGGTTGCTTGTAGCCCGAGATTCCGCAGT) for *Marme_R0008*—that could be amplified concomitantly by the same primer sets to yield identically sized amplicons.

The spike-in–derived reads are easily identified by sequence, with the diversity of randomized $(N)_{12}$ segments used to evaluate the degree to which distinct reads in the amplified pool represent independent molecules from the pre-amplification mixture. A large number of spike-in barcodes (ideally a different barcode for every spike-in read) indicate that a high fraction of reads from the amplified pool represent unique molecules in the initial sample, whereas repeated appearances of a small number of $(N)_{12}$ barcodes in the amplified pool would be indicative of bottleneck formation during PCR (and hence a less than optimal relationship between read counts and molecules in the initial pool). For the purpose of estimating the number of molecules sampled from an initial pool, we calculated a nonredundancy fraction, which is the ratio of spike-in–derived barcodes to total spike-in–derived reads. The nonredundancy

fraction provides a multiplier that can be used to correct raw read counts from an amplified pool to obtain an estimate of the contributing number of molecules from the initial pool. This is particularly applicable for estimating a minimal incidence of a rare class (i.e., setting a detection limit for spliced copies of the *td* intron–containing DNA constructs in this work). Given nonredundancy fractions of >0.45 for all samples in these experiments, the observed totals of control (nonspliced, genomic) sequence reads (fig. S6C) would have been sufficient to detect the presence of extended spliced *td* intron–containing DNA molecules, even at the low incidence of 10^{-6}.

The same cultures of MMB-1 were used to assess both splicing efficiency and the presence of exon-junction sequences in DNA form.

PCR fidelity

Analyzing sequence distributions through PCR and sequencing entails certain best practices in terms of both experimental protocols and analysis. In particular, several precautions were observed in constructing sequencing libraries for spacer sequencing. PCR titrations were performed to ensure that the amplification kinetics were in the linear range of the reactions before any size selection step (e.g., band excision from native agarose gels); this avoids renaturation artifacts in complex sequence pools. The overall error rate was empirically determined for every experiment by analyzing the distribution of mismatches in the sequences obtained from the first native spacer in the CRISPR03 array; this enabled the estimation of the error rate in the region of the sequencing reads that contained newly acquired spacers. PCR bottlenecking was also measured as the number of repeat occurrences of any given new spacer. All synthetic sequences that could lead to confounding contamination issues were avoided: No sequences from *E. coli*, MMB-1, or other sources have been synthesized as amplifiable substrates. As a benchmark for recovery of individual sequences, a nonbacterial sequence was synthesized as a spacer flanked by the appropriate CRISPR repeats. This repeat-flanked spacer sequence (CTGGGACATATAATATCGTCCCCGTAGATGCCTAT; a segment of the phage MS2) was recovered effectively in experiments with an *E. coli* transformant carrying a plasmid with the indicated template. Appearances of MS2 sequences in other trials were limited to this single sequence, indicating a likely source due to a low level of cross-sample "bleeding."

Protein purification

Expression plasmids were transformed into *E. coli* strains Rosetta2 (pMal derivatives) or Rosetta2(DE3) (pET14b derivatives), and single transformed colonies were grown in LB medium supplemented with appropriate antibiotics over night at 37°C with shaking. Six flasks each containing 1 liter LB were inoculated with 1% of the overnight culture and grown at 37°C with shaking to log phase. After the culture reached an optical density at 600 nm of ~0.8, IPTG was added to 1 mM final concentration and the cultures were incubated at 19°C for 20 to 24 hours. Cells were harvested by centrifugation, and the pellet was dissolved in A1 buffer (25 mM KPO_4, pH 7; 500 mM NaCl; 10% glycerol; 10 mM ß-mercaptoethanol; 10 ml/g cell paste) on ice. Lysozyme was added to 1 mg/ml final concentration and incubated at 4°C for 0.5 hours. Cells were then sonicated (Branson Sonifier 450; three bursts of 15 s each with 15 s between each burst). The lysate was cleared by centrifugation (29,400*g*, 25 min, 4°C), and polyethyleneimine (PEI) was added to the supernatant in six steps on ice with stirring to a final concentration of 0.4%. After 10 min, precipitated nucleic acids were removed by centrifugation (29,400*g*, 25 min, 4°C), and proteins were precipitated from the supernatant by adding ammonium sulfate to 60% saturation on ice and incubating for 30 min. Proteins were collected by centrifugation (29,400*g*, 25 min, 4°C), dissolved in 20 ml A1 buffer, and filtered through a 0.45-µm polyethersulfone membrane (Whatman Puradisc).

Protein purification was achieved by using a BioLogic fast protein liquid chromatography system (BioRad). RT-Cas1 was purified by loading the filtered crude protein onto an amylose column (30 ml; NEB Amylose High Flow resin), washing with 50 ml of A1 buffer, followed by 30 ml A1 plus 1.5 M NaCl and 30 ml of A1 buffer. Bound proteins were eluted with 50 ml of 10 mM maltose in A1 buffer. Fractions containing RT-Cas1 were identified by SDS-PAGE, pooled, and diluted to 250 mM NaCl. The protein was then loaded onto a 5-ml heparin-Sepharose column (HiTrap Heparin HP column; GE Healthcare) and eluted with a 0.1- to 1-M NaCl gradient. Peak fractions (~700 mM NaCl) were identified by SDS-PAGE, pooled, and dialyzed into A1 buffer. The dialyzed protein was concentrated to >10 µM using an Amicon Ultra Centrifugal Filter (Ultracel-50K). The protein was stable in A1 buffer on ice for about 3 months.

The initial steps in the Cas2 purification were similar, except that the cell paste was resuspended in N1 buffer (25 mM tris-HCl, pH 7.5; 500 mM KCl; 10 mM imidazole; 10% glycerol; 10 mM DTT) and the ammonium sulfate precipitation step was omitted. Instead, the Cas2 PEI supernatant was loaded directly onto a 5-ml nickel column (HiTrap Nickel HP column; GE Healthcare) and eluted with an imidazole gradient (60 ml 10 to 500 mM in N1 buffer). Peak fractions containing Cas2 were identified by SDS-PAGE and pooled. After adjusting the KCl concentration to 200 mM, the pooled fractions were loaded onto two 5-ml heparin-Sepharose columns arranged in tandem. The protein was eluted with a linear KCl gradient (50 ml, 100 mM to 1 M), and Cas2 peak fractions (~800 mM KCl) were identified by SDS-PAGE and stored on ice in elution buffer. The protein was stable on ice for several months.

All protein concentrations were measured using the Qubit Protein assay kit (Life Technologies) according to the manufacturer's protocol. Proteins were >80% pure based on densitometry.

Formation of RTCas1+Cas2 complex

Purified RTCas1 (2500 pMol) was mixed with a twofold excess of purified Cas2 in 250 mM KCl, 250 mM NaCl, and 12.5 mM tris-HCl (pH 7.5); 12.5 mM KPO_4 (pH 7); 5 mM DTT; 5 mM BME; and 10% glycerol and incubated on ice for >16 hours prior to reactions.

RT assay

RT assays with poly(rA)/oligo$(dT)_{24}$ were performed by preincubating poly(rA)/oligo$(dT)_{24}$ (80 µM and 50 µM, respectively) in 200 mM KCl, 50 mM NaCl, 10 mM $MgCl_2$, and 20 mM tris-HCl (pH 7.5); 1 mM unlabeled deoxythymidine triphosphate (dTTP); and 5 µCi [α-^{32}P]-dTTP (3000 Ci/mmol; PerkinElmer) for 2 min at the desired temperature, then initiating the reaction by adding the RT-Cas1 proteins (1 to 2 µM final concentration). The reactions (20 to 30 µl) were incubated for times up to 30 min. A 3-µl sample was withdrawn at each time point and added to 10 µl of stop solution (0.5% SDS, 25 mM EDTA). Reaction products were spotted onto Whatman DE81 paper (10- × 7.5-cm sheets; GE Healthcare Biosciences), which was then washed three times with 0.3 M NaCl and 0.03 M sodium citrate, dried, and scanned with a PhosphorImager (Typhoon Trio Variable Mode Imager; GE Healthcare Biosciences) to quantify the bound radioactivity.

CRISPR DNA cleavage/ligation assay

MMB-1 CRISPR DNA substrate was a PCR product amplified with primers MMB1crisp5b (CACTCGACCGGAATTATCGACGAA) and MMB1crisp3 (TCTGAAACTCTGAATACTAACGAAAAATAG) using Phusion High-Fidelity DNA polymerase according to the manufacturer's protocol (NEB or Thermo Scientific). The resulting 268-bp PCR fragment contains 120 bp of the leader, 35 bp of repeat 1, 33 bp of spacer 1, 35 bp of repeat 2, 37 bp of spacer 2, and 8 bp of repeat 3. Internally labeled substrate was prepared by adding 25 µCi [α-^{32}P]-dTTP or dCTP (Perkin Elmer) and 40 µM dTTP or dCTP, respectively, to the PCR reactions. Labeled DNA was purified by electrophoresis in a native 6% polyacrylamide gel, cutting out the labeled band, and electroeluting the DNA using midi D-Tube dialyzer cartridges (Novagen). The eluted DNA was extracted with phenol:chloroform:isoamyl alcohol (phenol-CIA), ethanol-precipitated, and quantitated using a Qubit dsDNA assay kit (Life Technologies).

CRISPR DNA cleavage-ligation assays contained RTCas1–Cas2 complex (500 nM final), MMB-1 CRISPR substrate (1 nM), 20 mM tris (pH 7.5), and 7.5 mM free $MgCl_2$. DNA or RNA oligonucleotides and an equimolar solution of dNTPs and Mg^{2+} were added at 2.5 µM and 1 mM final concentrations as indicated for individual experiments. Reactions were incubated at 37°C for 1 hour and stopped by adding phenol-CIA. The supernatant was mixed at a 2:1 ratio with loading dye (90% formamide, 20 mM EDTA, and 0.25 mg/ml bromophenol blue and xyan cyanol), and nucleic acids were analyzed in a 6% polyacrylamide 7 M urea gel. Gels were dried and scanned with a phosphorimager.

Labeled DNA or RNA oligonucleotide ligation assays were performed as described above but using 22.5 µM unlabeled CRISPR PCR fragment

and ~0.25 μM 5′-end–labeled gel-purified oligonucleotides. Control assays were performed without adding CRISPR PCR fragment. For nuclease treatment of oligonucleotide ligation to CRISPR DNA, reactions were scaled up fourfold, treated with phenol-CIA, and ethanol-precipitated. The precipitated nucleic acids were dissolved in 30 μl of water. Equal amounts were then either untreated or treated with RNase H (2 units, Invitrogen), DNase I (RNase-free, 10 units, Roche), and RNase A/T1 mix [0.5 μg RNase A (Sigma) and 500 units RNase T1 (Ambion)] in 40 mM tris (pH 7.9), 10 mM NaCl, 6 mM $MgCl_2$, and 1 mM $CaCl_2$ for 20 min at 37°C. Samples were extracted with phenol-CIA to terminate the reaction and analyzed by electrophoresis in a denaturing polyacrylamide gel, as described above.

Labeled cDNA extension reactions were carried out as above but using cold CRISPR DNA and oligonucleotides with 0.25 mM unlabeled dATP, dGTP, and dTTP and 5 μCi [α-^{32}P]-dCTP (3000 Ci/mMol, PerkinElmer).

Oligonucleotides for cleavage/ligations assays were as follows: 29-nt DNA (TTTGGATCCTCATCTTTTAGGGCTCCAAG), 33-nt dsDNA-top (GATGCTTATGGTTATTGCAGCTACCCTCGCCCT), 33-nt dsDNA-bottom (AGGGCGAGGGTAGCTGCAATAACCATAAGCATC), 21-nt RNA (GCCGCUUCAGAGAGAAAUCGC), and 35-nt RNA (UUACGGUGCUUAAAACAAAACAAAACAAAACAAAA).

REFERENCES AND NOTES

1. R. Barrangou *et al*., CRISPR provides acquired resistance against viruses in prokaryotes. *Science* **315**, 1709–1712 (2007). doi: 10.1126/science.1138140; pmid: 17379808
2. L. A. Marraffini, E. J. Sontheimer, CRISPR interference: RNA-directed adaptive immunity in bacteria and archaea. *Nat. Rev. Genet.* **11**, 181–190 (2010). doi: 10.1038/nrg2749; pmid: 20125085
3. A. Bolotin, B. Quinquis, A. Sorokin, S. D. Ehrlich, Clustered regularly interspaced short palindrome repeats (CRISPRs) have spacers of extrachromosomal origin. *Microbiology* **151**, 2551–2561 (2005). doi: 10.1099/mic.0.28048-0; pmid: 16079334
4. F. J. Mojica, C. Díez-Villaseñor, J. García-Martínez, E. Soria, Intervening sequences of regularly spaced prokaryotic repeats derive from foreign genetic elements. *J. Mol. Evol.* **60**, 174–182 (2005). doi: 10.1007/s00239-004-0046-3; pmid: 15791728
5. C. Pourcel, G. Salvignol, G. Vergnaud, CRISPR elements in *Yersinia pestis* acquire new repeats by preferential uptake of bacteriophage DNA, and provide additional tools for evolutionary studies. *Microbiology* **151**, 653–663 (2005). doi: 10.1099/mic.0.27437-0; pmid: 15758212
6. S. J. Brouns *et al*., Small CRISPR RNAs guide antiviral defense in prokaryotes. *Science* **321**, 960–964 (2008). pmid: 18703739
7. J. van der Oost, E. R. Westra, R. N. Jackson, B. Wiedenheft, Unravelling the structural and mechanistic basis of CRISPR-Cas systems. *Nat. Rev. Microbiol.* **12**, 479–492 (2014). doi: 10.1038/nrmicro3279; pmid: 24909109
8. K. S. Makarova *et al*., Evolution and classification of the CRISPR-Cas systems. *Nat. Rev. Microbiol.* **9**, 467–477 (2011). doi: 10.1038/nrmicro2577; pmid: 21552286
9. K. S. Makarova *et al*., An updated evolutionary classification of CRISPR-Cas systems. *Nat. Rev. Microbiol.* **13**, 722–736 (2015). doi: 10.1038/nrmicro3569; pmid: 26411297
10. K. S. Makarova, N. V. Grishin, S. A. Shabalina, Y. I. Wolf, E. V. Koonin, A putative RNA-interference-based immune system in prokaryotes: Computational analysis of the predicted enzymatic machinery, functional analogies with eukaryotic RNAi, and hypothetical mechanisms of action. *Biol. Direct* **1**, 7 (2006). doi: 10.1186/1745-6150-1-7; pmid: 16545108
11. I. Yosef, M. G. Goren, U. Qimron, Proteins and DNA elements essential for the CRISPR adaptation process in *Escherichia coli*. *Nucleic Acids Res.* **40**, 5569–5576 (2012). doi: 10.1093/nar/gks216; pmid: 22402487
12. K. A. Datsenko *et al*., Molecular memory of prior infections activates the CRISPR/Cas adaptive bacterial immunity system. *Nat. Commun.* **3**, 945 (2012). doi: 10.1038/ncomms1937; pmid: 22781758
13. Y. Wei, R. M. Terns, M. P. Terns, Cas9 function and host genome sampling in Type II-A CRISPR-Cas adaptation. *Genes Dev.* **29**, 356–361 (2015). doi: 10.1101/gad.257550.114; pmid: 25691466
14. R. Heler *et al*., Cas9 specifies functional viral targets during CRISPR-Cas adaptation. *Nature* **519**, 199–202 (2015). doi: 10.1038/nature14245; pmid: 25707807
15. L. A. Marraffini, E. J. Sontheimer, CRISPR interference limits horizontal gene transfer in staphylococci by targeting DNA. *Science* **322**, 1843–1845 (2008). doi: 10.1126/science.1165771; pmid: 19095942
16. C. R. Hale *et al*., RNA-guided RNA cleavage by a CRISPR RNA-Cas protein complex. *Cell* **139**, 945–956 (2009). doi: 10.1016/j.cell.2009.07.040; pmid: 19945378
17. C. R. Hale *et al*., Essential features and rational design of CRISPR RNAs that function with the Cas RAMP module complex to cleave RNAs. *Mol. Cell* **45**, 292–302 (2012). doi: 10.1016/j.molcel.2011.10.023; pmid: 22227116
18. G. Tamulaitis *et al*., Programmable RNA shredding by the type III-A CRISPR-Cas system of *Streptococcus thermophilus*. *Mol. Cell* **56**, 506–517 (2014). doi: 10.1016/j.molcel.2014.09.027; pmid: 25458845
19. G. W. Goldberg, W. Jiang, D. Bikard, L. A. Marraffini, Conditional tolerance of temperate phages via transcription-dependent CRISPR-Cas targeting. *Nature* **514**, 633–637 (2014). doi: 10.1038/nature13637; pmid: 25174707
20. W. Peng, M. Feng, X. Feng, Y. X. Liang, Q. She, An archaeal CRISPR type III-B system exhibiting distinctive RNA targeting features and mediating dual RNA and DNA interference. *Nucleic Acids Res.* **43**, 406–417 (2015). doi: 10.1093/nar/gku1302; pmid: 25505143
21. P. Samai *et al*., Co-transcriptional DNA and RNA cleavage during Type III CRISPR-Cas immunity. *Cell* **161**, 1164–1174 (2015). doi: 10.1016/j.cell.2015.04.027; pmid: 25959775
22. D. Baltimore, RNA-dependent DNA polymerase in virions of RNA tumour viruses. *Nature* **226**, 1209–1211 (1970). doi: 10.1038/2261209a0; pmid: 4316300
23. H. M. Temin, S. Mizutani, RNA-dependent DNA polymerase in virions of Rous sarcoma virus. *Nature* **226**, 1211–1213 (1970). doi: 10.1038/2261211a0; pmid: 4316301
24. C. W. Greider, E. H. Blackburn, Identification of a specific telomere terminal transferase activity in tetrahymena extracts. *Cell* **43**, 405–413 (1985). doi: 10.1016/0092-8674(85)90170-9; pmid: 3907856
25. J. D. Boeke, D. J. Garfinkel, C. A. Styles, G. R. Fink, Ty elements transpose through an RNA intermediate. *Cell* **40**, 491–500 (1985). doi: 10.1016/0092-8674(85)90197-7; pmid: 2982495
26. S. Zimmerly, H. Guo, P. S. Perlman, A. M. Lambowitz, Group II intron mobility occurs by target DNA-primed reverse transcription. *Cell* **82**, 545–554 (1995). doi: 10.1016/0092-8674(95)90027-6; pmid: 7664334
27. M. Liu *et al*., Reverse transcriptase-mediated tropism switching in *Bordetella* bacteriophage. *Science* **295**, 2091–2094 (2002). doi: 10.1126/science.1067467; pmid: 11896279
28. K. K. Kojima, M. Kanehisa, Systematic survey for novel types of prokaryotic retroelements based on gene neighborhood and protein architecture. *Mol. Biol. Evol.* **25**, 1395–1404 (2008). doi: 10.1093/molbev/msn081; pmid: 18391066
29. D. M. Simon, S. Zimmerly, A diversity of uncharacterized reverse transcriptases in bacteria. *Nucleic Acids Res.* **36**, 7219–7229 (2008). doi: 10.1093/nar/gkn867; pmid: 19004871
30. N. Toro, R. Nisa-Martínez, Comprehensive phylogenetic analysis of bacterial reverse transcriptases. *PLOS ONE* **9**, e114083 (2014). doi: 10.1371/journal.pone.0114083; pmid: 25423096
31. H. S. Malik, W. D. Burke, T. H. Eickbush, The age and evolution of non-LTR retrotransposable elements. *Mol. Biol. Evol.* **16**, 793–805 (1999). doi: 10.1093/oxfordjournals.molbev.a026164; pmid: 10368957
32. F. J. Blocker *et al*., Domain structure and three-dimensional model of a group II intron-encoded reverse transcriptase. *RNA* **11**, 14–28 (2005). doi: 10.1261/rna.7181105; pmid: 15574519
33. G. Mohr, E. Ghanem, A. M. Lambowitz, Mechanisms used for genomic proliferation by thermophilic group II introns. *PLOS Biol.* **8**, e1000391 (2010). pmid: 20543989
34. F. Solano, A. Sanchez-Amat, Studies on the phylogenetic relationships of melanogenic marine bacteria: Proposal of *Marinomonas mediterranea* sp. nov. *Int. J. Syst. Bacteriol.* **49**, 1241–1246 (1999). doi: 10.1099/00207713-49-3-1241; pmid: 10425786
35. Of the two RT-Cas1–associated type III-B CRISPR arrays in this system, CRISPR03 was chosen for spacer acquisition assays, because the other array (CRISPR02) has unusual truncated repeats at the leader-proximal end (*1*).
36. M. Grynberg, A. Godzik, NERD: A DNA processing-related domain present in the anthrax virulence plasmid, pXO1. *Trends Biochem. Sci.* **29**, 106–110 (2004). doi: 10.1016/j.tibs.2004.01.002; pmid: 15055202
37. T. Y. Kim, M. Shin, L. Huynh Thi Yen, J. S. Kim, Crystal structure of Cas1 from *Archaeoglobus fulgidus* and characterization of its nucleolytic activity. *Biochem. Biophys. Res. Commun.* **441**, 720–725 (2013). doi: 10.1016/j.bbrc.2013.10.122; pmid: 24211577
38. One potential contributor to increased spacer acquisition frequency (Fig. 2C) after RT deletion could be the higher growth rate that was observed for the cells expressing the RTΔ mutant.
39. M. Belfort, P. S. Chandry, J. Pedersen-Lane, Genetic delineation of functional components of the group I intron in the phage T4 *td* gene. *Cold Spring Harb. Symp. Quant. Biol.* **52**, 181–192 (1987). doi: 10.1101/SQB.1987.052.01.023; pmid: 3331339
40. S. D. Moore, R. T. Sauer, The tmRNA system for translational surveillance and ribosome rescue. *Annu. Rev. Biochem.* **76**, 101–124 (2007). doi: 10.1146/annurev.biochem.75.103004.142733; pmid: 17291191
41. J. K. Nuñez, A. S. Lee, A. Engelman, J. A. Doudna, Integrase-mediated spacer acquisition during CRISPR-Cas adaptive immunity. *Nature* **519**, 193–198 (2015). doi: 10.1038/nature14237; pmid: 25707795
42. A. M. Lambowitz, S. Zimmerly, Mobile group II introns. *Annu. Rev. Genet.* **38**, 1–35 (2004). doi: 10.1146/annurev.genet.38.072902.091600; pmid: 15568970
43. T. Blumenthal, G. G. Carmichael, RNA replication: Function and structure of Qbeta-replicase. *Annu. Rev. Biochem.* **48**, 525–548 (1979). doi: 10.1146/annurev.bi.48.070179.002521; pmid: 382992
44. C. K. Biebricher, L. E. Orgel, An RNA that multiplies indefinitely with DNA-dependent RNA polymerase: Selection from a random copolymer. *Proc. Natl. Acad. Sci. U.S.A.* **70**, 934–938 (1973). doi: 10.1073/pnas.70.3.934; pmid: 4577140
45. M. M. Konarska, P. A. Sharp, Replication of RNA by the DNA-dependent RNA polymerase of phage T7. *Cell* **57**, 423–431 (1989). doi: 10.1016/0092-8674(89)90917-3; pmid: 2720777
46. R. Flores, S. Gago-Zachert, P. Serra, R. Sanjuán, S. F. Elena, Viroids: Survivors from the RNA world? *Annu. Rev. Microbiol.* **68**, 395–414 (2014). doi: 10.1146/annurev-micro-091313-103416; pmid: 25002087
47. B. J. Haas, M. Chin, C. Nusbaum, B. W. Birren, J. Livny, How deep is deep enough for RNA-Seq profiling of bacterial transcriptomes? *BMC Genomics* **13**, 734 (2012). doi: 10.1186/1471-2164-13-734; pmid: 23270466
48. W. Ludwig, H. P. Klenk, in *Bergey's Manual of Systematic Bacteriology*, G. M. Garrity, Ed. (Springer, vol. 2, 2001), pp. 49–65.
49. Y. Xiong, T. H. Eickbush, Origin and evolution of retroelements based upon their reverse transcriptase sequences. *EMBO J.* **9**, 3353–3362 (1990). pmid: 1698615
50. S. Mohr *et al*., Thermostable group II intron reverse transcriptase fusion proteins and their use in cDNA synthesis and next-generation RNA sequencing. *RNA* **19**, 958–970 (2013). doi: 10.1261/rna.039743.113; pmid: 23697550
51. F. Solano, P. Lucas-Elío, E. Fernández, A. Sanchez-Amat, *Marinomonas mediterranea* MMB-1 transposon mutagenesis: Isolation of a multipotent polyphenol oxidase mutant. *J. Bacteriol.* **182**, 3754–3760 (2000). doi: 10.1128/JB.182.13.3754-3760.2000; pmid: 10850991

ACKNOWLEDGMENTS

We thank J. Shor, S. Cohen, M. Bagdasarian, C. Pourcel, L. Mindich, C.P. Wolk, M. Poranen, and laboratory colleagues for help and advice; the Howard Hughes Medical Institute and Stanford for fellowship support (S.S.); NIH (grants R01-GM37706 to A.Z.F., R01-GM37949 to A.M.L., and R01-GM37951 to A.M.L.); and the Welch Foundation (grant F-1607 to A.M.L.). Sequencing data are archived in the Sequence Read Archive under SRA ID-SRP066108. S.S. and A.Z.F. conceived the project. S.S., G.M., A.M.L., and A.Z.F. designed experiments, analyzed data, and wrote the paper with inputs from other authors. S.S. performed all genetics experiments. G.M., D.J.S., and L.M.M. performed all biochemistry experiments. A.S.-A. and D.B. provided protocols and conceptual guidance.

SUPPLEMENTARY MATERIALS

www.sciencemag.org/content/351/6276/aad4234/suppl/DC1
Figs. S1 to S10
Tables S1 and S2
Reference (*52*)

11 September 2015; accepted 7 January 2016
10.1126/science.aad4234

EXTENDED PDF FORMAT
SPONSORED BY

www.rndsystems.com

Direct CRISPR spacer acquisition from RNA by a natural reverse transcriptase–Cas1 fusion protein

Sukrit Silas *et al.*

Science **351**, (2016);
DOI: 10.1126/science.aad4234

This copy is for your personal, non-commercial use only.

If you wish to distribute this article to others, you can order high-quality copies for your colleagues, clients, or customers by clicking here.

Permission to republish or repurpose articles or portions of articles can be obtained by following the guidelines here.

The following resources related to this article are available online at www.sciencemag.org (this information is current as of February 25, 2016):

Updated information and services, including high-resolution figures, can be found in the online version of this article at:
/content/351/6276/aad4234.full.html

Supporting Online Material can be found at:
/content/suppl/2016/02/24/351.6276.aad4234.DC1.html

A list of selected additional articles on the Science Web sites **related to this article** can be found at:
/content/351/6276/aad4234.full.html#related

This article **cites 49 articles**, 15 of which can be accessed free:
/content/351/6276/aad4234.full.html#ref-list-1

This article has been **cited by** 1 articles hosted by HighWire Press; see:
/content/351/6276/aad4234.full.html#related-urls

This article appears in the following **subject collections:**
Molecular Biology
/cgi/collection/molec_biol

Downloaded from on February 25, 2016

Science (print ISSN 0036-8075; online ISSN 1095-9203) is published weekly, except the last week in December, by the American Association for the Advancement of Science, 1200 New York Avenue NW, Washington, DC 20005. Copyright 2016 by the American Association for the Advancement of Science; all rights reserved. The title *Science* is a registered trademark of AAAS.

RESEARCH ARTICLES

NEUROIMMUNOLOGY

The maternal interleukin-17a pathway in mice promotes autism-like phenotypes in offspring

Gloria B. Choi,[1]* Yeong S. Yim,[1]* Helen Wong,[2,3]* Sangdoo Kim,[4] Hyunju Kim,[4] Sangwon V. Kim,[5] Charles A. Hoeffer,[2,3]† Dan R. Littman,[5,6]† Jun R. Huh[4,5]†

Viral infection during pregnancy has been correlated with increased frequency of autism spectrum disorder (ASD) in offspring. This observation has been modeled in rodents subjected to maternal immune activation (MIA). The immune cell populations critical in the MIA model have not been identified. Using both genetic mutants and blocking antibodies in mice, we show that retinoic acid receptor–related orphan nuclear receptor gamma t (RORγt)–dependent effector T lymphocytes [for example, T helper 17 (T_H17) cells] and the effector cytokine interleukin-17a (IL-17a) are required in mothers for MIA-induced behavioral abnormalities in offspring. We find that MIA induces an abnormal cortical phenotype, which is also dependent on maternal IL-17a, in the fetal brain. Our data suggest that therapeutic targeting of T_H17 cells in susceptible pregnant mothers may reduce the likelihood of bearing children with inflammation-induced ASD-like phenotypes.

Several studies have suggested that viral infection of women during pregnancy correlates with an increased frequency of autism spectrum disorder (ASD) in the offspring (*1*–*6*). In the rodent maternal immune activation (MIA) model of this phenomenon (*7*), offspring from pregnant mice infected with virus or injected intraperitoneally with synthetic double-stranded RNA (dsRNA) [poly(I:C)], a mimic of viral infection, exhibit behavioral symptoms reminiscent of ASD: social deficits, abnormal communication, and repetitive behaviors (*8*). T helper 17 (T_H17) cells are responsible for immune responses against extracellular bacteria and fungi, and their dysregulation is thought to underlie numerous inflammatory and autoimmune diseases (*9*), such as asthma, rheumatoid arthritis, psoriasis, inflammatory bowel disease (IBD), and multiple sclerosis. The transcription factor retinoic acid receptor–related orphan nuclear receptor gamma t (RORγt) is expressed in several cell types in the immune system. It is a key transcriptional regulator for the development of T_H17 cells, as well as γδ T cells and innate lymphoid cells (such as ILC3) that express T_H17 cell–like cytokines, in both humans and mice (*10*–*13*).

T_H17 cells and their cytokine mediators have been suggested to have a role in ASD. For example, elevated levels of interleukin-17a (IL-17a), the predominant T_H17 cytokine, have been detected in the serum of a subset of autistic children (*14*, *15*). A genome-wide copy number variant (CNV) analysis identified *IL17A* as one of many genes enriched in autistic patients (*16*). Similarly, in the MIA mouse model, $CD4^+$ T lymphocytes from affected offspring produced higher levels of IL-17a upon in vitro activation (*17*, *18*). Although these data suggest that T_H17 cells may be involved in ASD patients, whether T_H17 cells are the specific immune cell population that is necessary for MIA phenotypes is unknown. Here, we show that maternal RORγt-expressing proinflammatory T cells, a major source of IL-17a, are required in the MIA model for induction of ASD-like phenotypes in offspring. Consistent with this notion, antibody blockade of IL-17a activity in pregnant mice protected against the development of MIA-induced behavioral abnormalities in the offspring. Also, we found atypical cortical development in affected offspring, and this abnormality was rescued by inhibition of maternal T_H17–IL-17a pathways.

Elevated fetal brain IL-17Ra mRNA follows increased maternal IL-17a in MIA

Pregnant mothers injected with poly(I:C) on embryonic day 12.5 (E12.5) had strong induction of serum cytokines IL-6, tumor necrosis factor-α (TNF-α), interferon-β (IFN-β), and IL-1β at 3 hours, compared with phosphate-buffered saline (PBS)–injected control dams (Fig. 1A and fig. S1, A to C). Additionally, poly(I:C) injection resulted in a strong increase of serum IL-17a at E14.5 (Fig. 1B). On the other hand, poly(I:C) did not affect the levels of the anti-inflammatory cytokine IL-10 in the serum nor in placenta and decidua extracts (fig. S1D). It was previously shown that the pro-inflammatory effector cytokine IL-6, a key factor for T_H17 cell differentiation (*19*), is required in pregnant mothers for MIA to produce ASD-like phenotypes in the offspring (*7*). We found that poly(I:C) injection into pregnant dams lacking IL-6 [IL-6 knockout (KO)] failed to increase the serum levels of IL-17a at E14.5, consistent with IL-6 acting upstream of IL-17a. Conversely, recombinant IL-6 injections into wild-type (WT) mothers were sufficient to induce IL-17a levels comparable to those of poly(I:C)-injected WT mothers (fig. S1E). Placenta- and decidua-associated mononuclear cells, isolated from poly(I:C)-treated animals at E14.5 and cultured for 24 hours, expressed amounts of IL-6 mRNA similar to those of PBS controls (Fig. 1C). In contrast, IL-17a mRNA expression in these cells was strongly up-regulated by poly(I:C) injection (Fig. 1D). This increase in mRNA expression was correlated with enhanced secretion of IL-17a by placenta- and decidua-associated mononuclear cells from poly(I:C)-treated dams (Fig. 1E), upon ex vivo stimulation with phorbol-myristate acetate (PMA) and ionomycin, which mimics T cell receptor (TCR) activation. IL-17a induction was specific to the placenta and decidua, as small intestine mononuclear cells from poly(I:C)-treated pregnant dams did not secrete more IL-17a than those from PBS-treated controls (fig. S1F).

We also observed that expression of the IL-17a receptor subunit A (IL-17Ra) mRNA, but not subunit C (IL-17Rc) mRNA, was strongly augmented in the fetal brain upon induction of MIA (Fig. 1, F and G). By in situ hybridization, IL-17Ra mRNA was detected in the mouse cortex, and its expression was strongly up-regulated in E14.5 fetal brains after poly(I:C) injection of pregnant dams (Fig. 1, H and I). The in situ probe detecting endogenous expression of IL-17Ra was specific, as it did not produce detectable signal in E14.5 fetal brain that lacks IL-17Ra (fig. S2).

Maternal IL-17a promotes abnormal cortical development in offspring

We next investigated if pathological activation of the IL-17 pathway in pregnant mothers affects fetal brain development and subsequently contributes to the ASD-like behavioral phenotypes in offspring. To test this hypothesis, we pretreated pregnant mothers with isotype control or IL-17a–blocking antibodies before injecting them with PBS or poly(I:C) (fig. S3). We then examined cortical development in the fetus for the following reasons: (i) Poly(I:C) injection of mothers increases IL-17Ra expression in the cortex of the fetal brain (Fig. 1, H and I); (ii) cortical development starts at about E11 (*20*), which aligns well with the time points of potential fetal exposure to MIA (*7*); (iii) disorganized cortex and focal patches of abnormal laminar cytoarchitecture have been found in

[1]The McGovern Institute for Brain Research, Department of Brain and Cognitive Sciences, Massachusetts Institute of Technology, Cambridge, MA 02139, USA. [2]Center for Neural Science, New York University, New York, NY 10003, USA. [3]Institute for Behavioral Genetics, Department of Integrated Physiology, University of Colorado, Boulder, CO 80303, USA. [4]Division of Infectious Diseases and Immunology and Program in Innate Immunity, Department of Medicine, University of Massachusetts Medical School, Worcester, MA 01605, USA. [5]The Kimmel Center for Biology and Medicine of the Skirball Institute, New York University School of Medicine, New York, NY 10016, USA. [6]Howard Hughes Medical Institute, New York, NY 10016, USA.
*These authors contributed equally to this work. †Corresponding author. E-mail: charles.hoeffer@colorado.edu (C.A.H.); dan.littman@med.nyu.edu (D.R.L.); jun.huh@umassmed.edu (J.R.H.)

Downloaded from on February 25, 2016

the brains of ASD patients (*21*, *22*); and (iv) MIA has been shown to affect cortical development (*23*, *24*). We analyzed cortical lamination, an orderly layered structure of the cortex, in fetal brains at E14.5 and E18.5, as well as in the adult brain, using antibodies specific for proteins expressed in the cortex in a layer-specific manner (*25*): special AT-rich sequence-binding protein 2 (SATB2) (*26*), T-brain-1 (TBR1) (*27*), and chicken ovalbumin upstream promoter transcription factor–interacting protein 2 (CTIP2) (*28*). MIA led to delayed expression of SATB2 at E14.5 compared with fetuses of control animals (Fig. 2, A and C). At E18.5, MIA resulted in a patch of disorganized cortical cytoarchitecture (Fig. 2, B and D to G) but did not affect cortical thickness of the fetal brains (Fig. 2H). This singular patch of disorganized cortex occurred at a similar medial-lateral position in a majority of E18.5 fetal brains (Fig. 2, E and G) derived from mothers injected with poly(I:C) but not those injected with PBS. The abnormal expression patterns of SATB2, TBR1, and CTIP2 were maintained in adult MIA offspring (fig. S4). Note that normal expression of these cortical layer–specific markers, as well as laminar cortical organization, were largely preserved in the offspring of poly(I:C)-injected mothers pretreated with IL-17a–blocking antibody (Fig. 2, A to D, and fig. S4).

Pretreatment with IL-17a–blocking antibody also suppressed the MIA-mediated increase in IL-17Ra mRNA expression in fetal brain at E14.5 (Fig. 1F). This suppression was accompanied by a reduction in maternal serum IL-17a (Fig. 1B), which indicated that the up-regulation of IL-17Ra mRNA in fetal brains requires maternal IL-17a signaling. Of note, IL-17a antibody blockade of the IL-17a–IL-17Ra signaling pathway did not result in a concomitant increase of the serum IL-10 levels, and IL-17a mRNA expression was not detected in fetal brain at E14.5, regardless of poly(I:C) injection. Together, these data demonstrate that the maternal IL-17a–dependent pathway mediates disorganized cortical phenotypes in offspring after in utero MIA and suggest that this may be due to exposure of the fetus and its brain to increased levels of IL-17a.

Maternal IL-17a promotes ASD-like behavioral abnormalities in offspring

We next tested the functional relevance of the maternal IL-17a pathway for MIA-induced ASD-like behavioral abnormalities in offspring (fig. S3). We first assessed MIA offspring for abnormal communication by measuring pup ultrasonic vocalization (USV) responses (*29*). After separation from mothers, pups from poly(I:C)-injected mothers pretreated with immunoglobulin G (IgG) isotype control antibody emitted more USV calls than those from PBS-injected mothers (Fig. 3A), in agreement with previous studies (*29*, *30*). Some studies have reported reduced USV calls upon MIA (*8*, *31*), but these opposite effects may reflect differences in methodological approaches, including dose and number of exposures to poly(I:C), as well as timing of poly(I:C) administration. Altogether, these results indicate that MIA induces abnormal USV in offspring. Pretreating poly(I:C)-injected mothers with IL-17a–blocking antibody resulted in offspring that emitted a similar number of USV calls as the pups from PBS-injected control mothers (Fig. 3A), which demonstrated that IL-17a–mediated signaling events are necessary for the MIA-induced abnormal USV phenotype. As previously reported (*7*, *8*), we found that prenatal exposure to MIA also caused social interaction deficits in adult offspring (Fig. 3B). This defect was fully rescued in offspring from poly(I:C)-injected

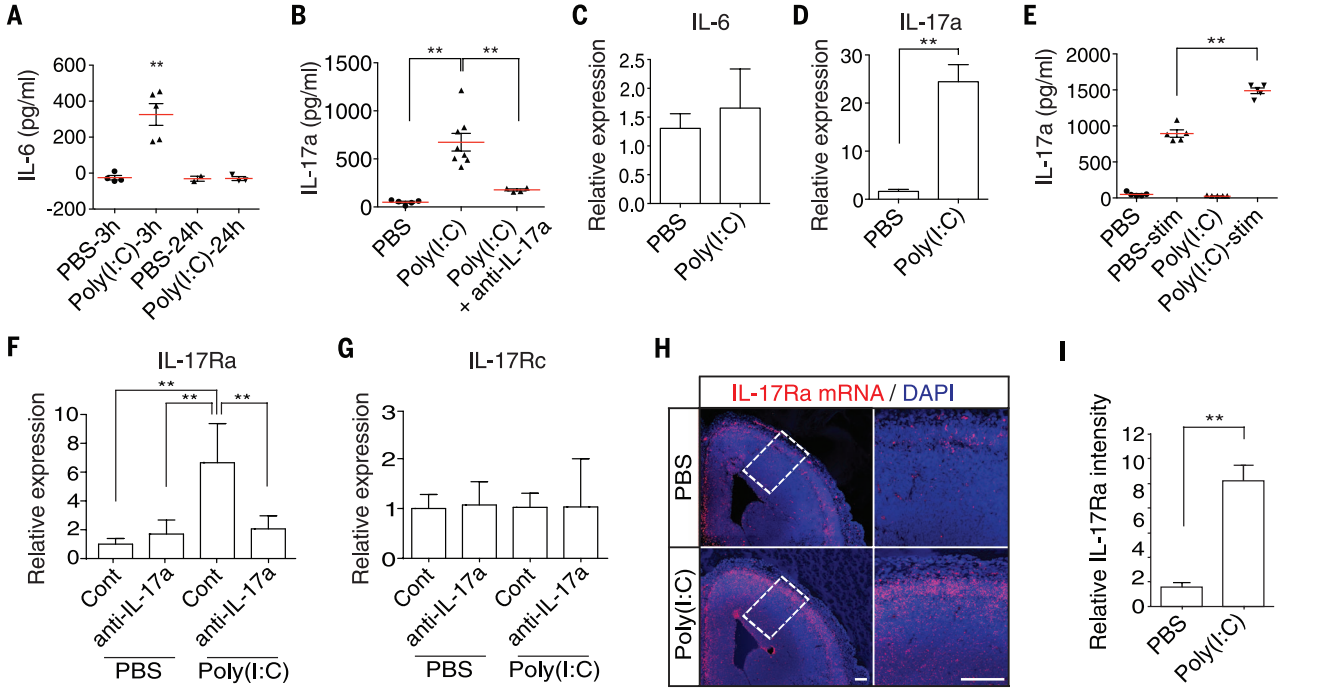

Fig. 1. IL-17a increase in mothers subjected to MIA leads to elevated IL-17Ra mRNA expression in the offspring. (**A**) Serum concentrations of IL-6 (n = 3 to 5 mice per group, two independent experiments) at 3 or 24 hours after PBS or poly(I:C) injection into pregnant dams at E12.5. (**B**) Serum concentrations of maternal IL-17a (n = 4 to 8 mice per group, two independent experiments) at E14.5 in PBS- or poly(I:C)-injected mothers, pretreated with or without anti–IL-17a. (**C** and **D**) Relative IL-6 (C) and IL-17a (D) mRNA expression in cells isolated from placenta or decidua of PBS- or poly(I:C)-treated mothers at E14.5 and cultured in vitro for 24 hours. The results are representative of three independent experiments. For each probe set, relative mRNA expression of one biological replicate from PBS-treated dams was set at 1. Real-time PCR analysis of relative expression of indicated genes compared with the level of glyceraldehyde-3-phosphate dehydrogenase in cells from PBS-treated dams. (**E**) Supernatant concentrations of IL-17a from ex vivo cultured mononuclear cells, isolated from placenta or decidua of PBS- or poly(I:C)-treated pregnant dams. Stim refers to PMA and ionomycin stimulation. (**F** and **G**) Relative IL-17Ra (F) and IL-17Rc (G) mRNA levels in E14.5 male fetal brain, derived from PBS- or poly(I:C)-injected mothers, pretreated with isotype control (Cont) or anti–IL-17a. The relative mRNA fold change, compared with the PBS- and Cont-treated groups, is plotted on the y axis (n = 7 for all groups; two or three independent experiments). (**H**) In situ hybridization with an IL-17Ra RNA probe in E14.5 male fetal brains derived from PBS- or poly(I:C)-injected mothers. Images are representative of four independent experiments. DAPI, 4′,6′-diamidino-2-phenylindole. (**I**) Relative signal intensity for images shown in (H). Scale bar, 100 μm. (A), (B), (E), (F), and (G) One-way analysis of variance (ANOVA) with Tukey's post hoc tests. (C), (D), and (I) Student's t test. $^{**}P < 0.01$. Means ± SEM.

mothers pretreated with IL-17a–blocking antibody (Fig. 3B). Repetitive and perseverative behaviors are another core feature in ASD that we tested next in our experimental mice using the marble-burying assay (*32*). Offspring from poly (I:C)-injected mothers displayed enhanced marble burying compared with offspring from PBS-injected mothers (Fig. 3C), consistent with previous studies (*7*, *29*). Pretreatment with IL-17a–blocking antibody of poly(I:C)-injected mothers rescued marble-burying behavior in the offspring (Fig. 3C). Notably, distinct behavioral phenotypes

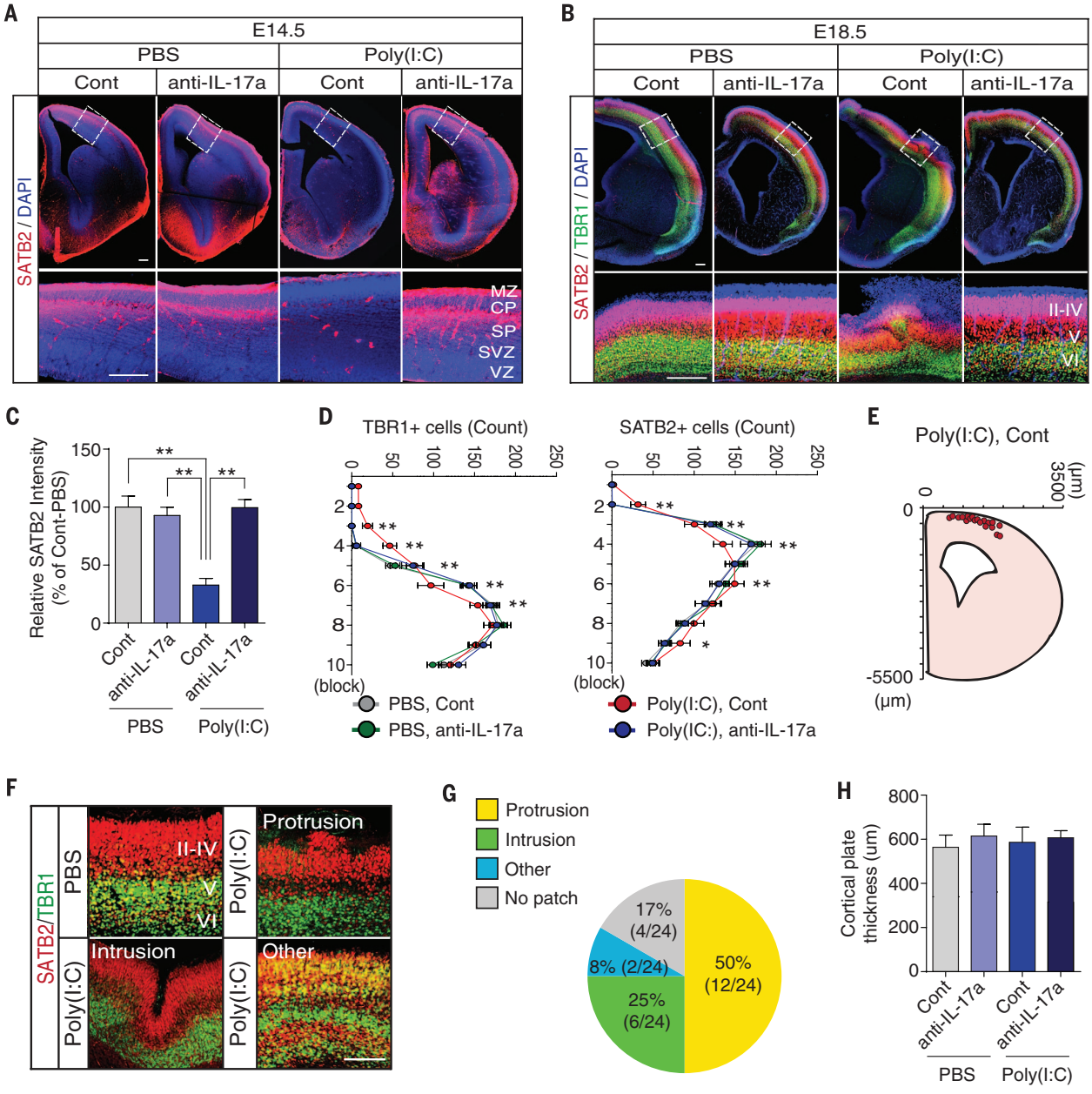

Fig. 2. The IL-17a pathway promotes abnormal cortical development in the offspring of pregnant dams after MIA. (**A**) Immunofluorescence staining of SATB2 (a marker of postmitotic neurons in superficial cortical layers) in E14.5 male fetal brain, derived from PBS- or poly(I:C)-injected mothers, pretreated with isotype control (Cont) or anti–IL-17a. MZ, marginal zone; CP, cortical plate; SP, subplate; SVZ, subventricular zone; VZ, ventricular zone. (**B**) Staining of SATB2 and TBR1 (a marker restricted to deeper cortical layers) in E18.5 male fetal brains from animals treated as in (A). Cortical layers: II to IV, V, and VI. (**C**) Quantification of SATB2 intensity in the cortical plate of E14.5 fetal brains (n = 8 for all groups; three independent experiments). (**D**) Quantification of TBR1- and SATB2-positive cells in a 300 × 300 μm^2 region of interest (ROI) centered on the malformation in the cortical plate of E18.5 fetal brains {n = 20 (PBS, Cont); n = 20 (PBS, anti–IL-17a); n = 24 [poly(I:C), Cont]; n = 20 [poly(I:C), anti–IL-17a]; five independent experiments}. (**E**) The spatial location of the cortical patch in E18.5 male fetal brains from poly(I:C)-injected mothers pretreated with control antibodies {n = 20 [poly(I:C), Cont]}. (**F**) The disorganized patches of cortex observed in fetuses from poly(I:C)-injected mothers were categorized into groups based on morphology: Protrusions, intrusions, or other abnormal patterns and their representative images are shown. (**G**) Percentage of the cortical patches in each category {n = 24 [poly(I:C), Cont]}. (**H**) Thickness of the cortical plate in E18.5 fetal brains, derived from PBS- or poly(I:C)-injected mothers, pretreated with isotype control or anti–IL-17a (n = 20 for all groups; five independent experiments). Scale bars in (A), (B), and (F), 100 μm. One-way ANOVA (C) and (H) and two-way ANOVA (D) with Tukey's post hoc tests. $^{**}P < 0.01$ and $^{*}P < 0.05$. Means ± SEM.

observed among different treatment groups were not due to differences in activity or arousal, as total distances moved during the sociability test were indistinguishable (Fig. 3D). Moreover, different treatment groups displayed comparable gender ratios, litter sizes, and weights (fig. S5). Taken together, these data indicate that the IL-17a pathway in pregnant mice is crucial in mediating the MIA-induced behavioral phenotypes in offspring.

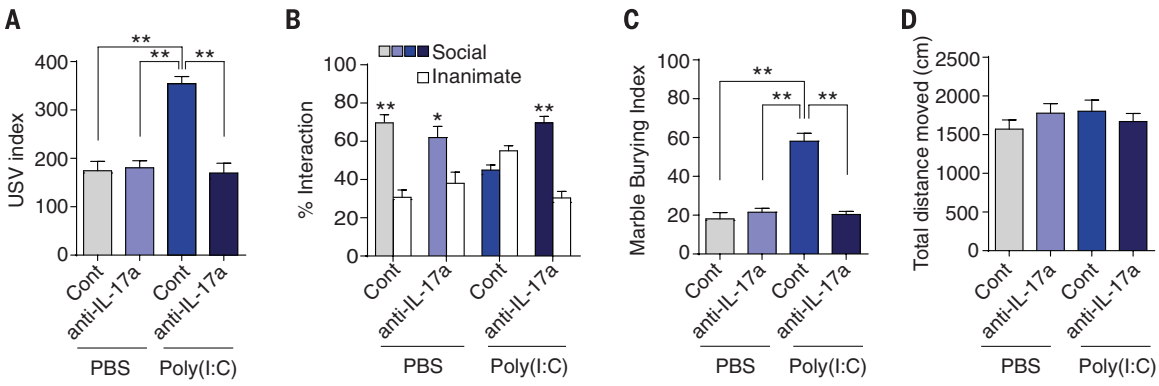

Fig. 3. The IL-17a pathway promotes ASD-like phenotypes in the MIA offspring. (**A**) USV assay. At P9, pups from the indicated experimental groups were separated from their mothers to elicit USV calls. The number of pup calls is plotted on the *y* axis {*n* = 25 (PBS, Cont); *n* = 28 (PBS, anti–IL-17a); *n* = 38 [poly(I:C), Cont]; *n* = 34 [poly(I:C), anti–IL-17a]; from six or seven independent experiments}. (**B**) Social approach behavior. Graphed as a social preference index (% time spent investigating social or inanimate stimulus out of total object investigation time) {*n* = 15 (PBS, Cont); *n* = 15 (PBS, anti–IL-17a); *n* = 16 [poly(I:C), Cont]; *n* = 20 [poly(I:C), anti–IL-17a]; from six or seven independent experiments}. (**C**) Marble-burying behavior. Percentage of the number of buried marbles is plotted on the *y* axis {*n* = 15 (PBS, Cont), *n* = 15 (PBS, anti–IL-17a), *n* = 15 [poly(I:C), Cont]; *n* = 20 [poly(I:C), anti–IL-17a]; from six or seven independent experiments}. (**D**) Total distance traveled during social approach behavior. (A), (C), and (D) One-way ANOVA with Tukey's post hoc tests. (B) Two-way ANOVA with Tukey's post hoc tests. $^{**}P < 0.01$ and $^{*}P < 0.05$. Means ± SEM.

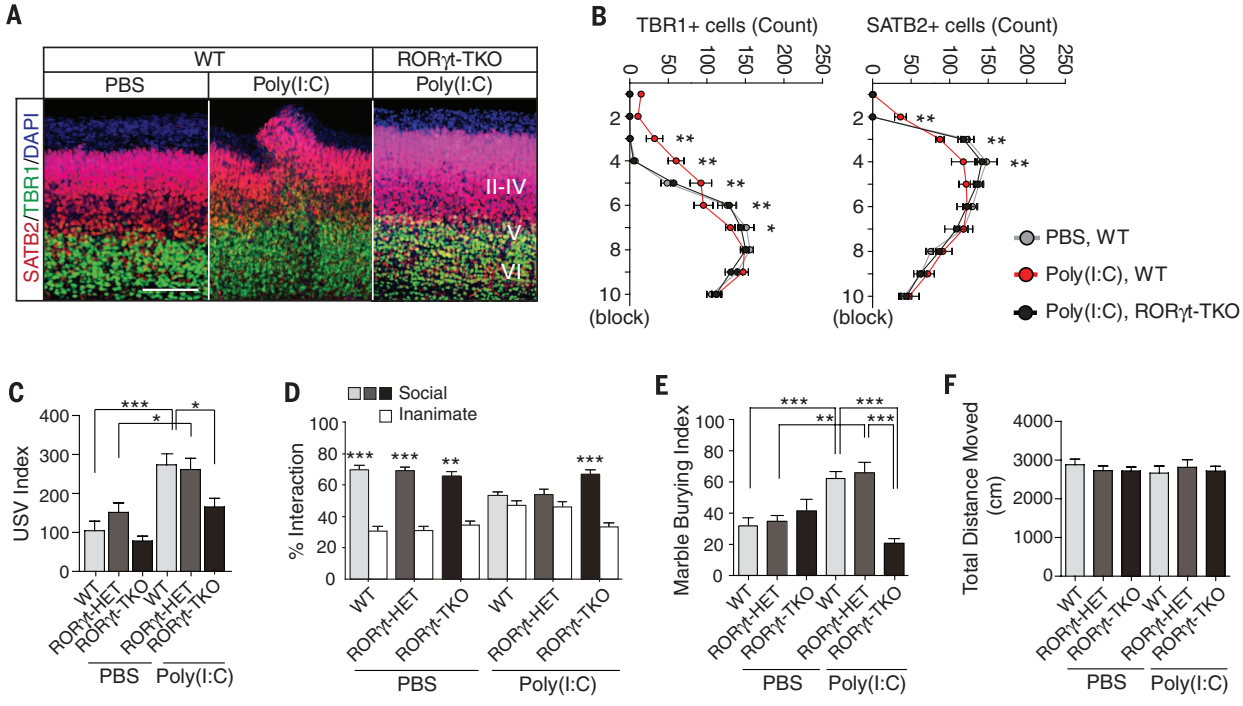

Fig. 4. RORγt expression in maternal T cells is required for manifestation of ASD-like phenotypes in the MIA model. (**A**) SATB2 and TBR1 staining in the cortex of E18.5 male fetal brains after MIA induction with poly(I:C) in mothers with the indicated genotypes. Cortical layers: II to IV, V, and VI. Images are representative of three independent experiments. Scale bar, 100 μm. (**B**) Quantification of TBR1- and SATB2-positive cells in a 300 × 300 μm^2 ROI centered on the malformation in the cortical plate of E18.5 male fetal brains (*n* = 6 for all groups). (**C**) Number of USVs emitted by P9 pups. Total USVs emitted during test period (3 min) are plotted on the *y* axis [*n* = 16, 18, and 15 offspring from PBS-treated WT, RORγt HET, and RORγt TKO mothers, respectively; *n* = 15, 11, and 28 from poly(I:C)-treated WT, RORγt HET, and RORγt TKO mothers, respectively; data from four to seven independent dams]. (**D**) Social approach behavior is shown as a social preference index as in Fig. 3. [*n* = 21, 15, and 15 adult offspring from PBS-treated WT, RORγt HET, and RORγt TKO mothers, respectively; *n* = 36, 15, and 21 from poly(I:C)-treated WT, RORγt HET, and RORγt TKO mothers, respectively; data from four to seven independent dams]. (**E**) Marble-burying behavior as in Fig. 3 [*n* = 14, 19, and 15 adult offspring from PBS-treated WT, RORγt HET, and RORγt TKO mothers, respectively; *n* = 32, 15, and 25 from poly(I:C)-treated WT, RORγt HET, and RORγt TKO mothers, respectively; data from four to seven independent dams]. (**F**) Total distance moved by offspring tested for social behavior. RORγt HET and RORγt TKO refer to *RORγ*$^{Neo/+}$; *CD4-Cre/+* and *RORγt*^{FL}/*RORγ*^{Neo}; *CD4-Cre/+*, respectively. (C) One-way ANOVA with Holm-Sidak post hoc tests. (B) and (D) Two-way ANOVA with Tukey's post hoc tests. (E) and (F) One-way ANOVA with Tukey's post hoc tests. $^{***}P < 0.001$, $^{**}P < 0.01$, and $^{*}P < 0.05$. Means ± SEM.

RORγt expression in maternal T cells is required for ASD-like phenotypes in the MIA offspring.

As RORγt is a critical regulator of the IL-17a pathway (*13*), we next investigated the role of maternal RORγt in MIA-induced behavioral phenotypes in offspring. Note that T_H17 cells and IL-17a have been detected in the decidua, as well as in the serum, during pregnancy in humans (*33*–*35*). $CD45^+$ mononuclear cells, including $CD4^+$ T cells, isolated from placenta and decidua of immune-activated WT mothers, but not from immune-activated mothers lacking both RORγt and the closely related RORγ isoform (RORγ KO), produced IL-17a upon ex vivo activation with PMA and ionomycin (fig. S6, A and B). Cells isolated from WT and RORγ KO mice secreted similar amounts of IFN-γ, consistent with the specific effect of RORγt on IL-17a expression (fig. S6C). In line with this observation, poly(I:C) treatment increased placenta- and decidua-associated T_H17, but not regulatory T, cells in pregnant dams, compared with PBS treatment (fig. S6, D and E). RORγ KO mice lack RORγ and γt expression not only in $CD4^+$ T cells but also in other lymphoid and non-immune system cells, and they have defective development of secondary and tertiary lymphoid organs (*36*, *37*). To determine whether RORγt function specifically in T cells mediates MIA-induced phenotypes, we bred $ROR\gamma t^{FL}$ animals (fig. S7) to CD4-Cre mice to selectively inactivate *rorc(t)* in the T cells of pregnant mothers (RORγt TKO) (*38*). In these animals, the functions of T_H17 cells ($CD4^+ROR\gamma t^+$ cells) and other RORγt-expressing αβT cells are inhibited, but there is no effect in RORγt-expressing innate (or innate-like) immune cells, including γδT, lymphoid tissue-inducer cells, and ILC3 cells (*11*, *12*), as well as in RORγ-expressing nonlymphoid cells. We found that RORγt TKO mothers failed to produce IL-17a even after poly(I:C) injection (fig. S6F). Note that poly(I:C)-induced malformation of the cortex was prevented in offspring from RORγt TKO mothers (Fig. 4, A and B), similar to the results from anti–IL-17a treatment (Fig. 2, B and D). Moreover, we found that prenatal exposure to MIA increased USV calls in pups derived from WT or RORγt heterozygous (HET) mothers, but offspring of RORγt TKO mothers had normal USV behavior (Fig. 4C). T cell–specific deletion of maternal RORγt also abrogated the MIA-induced social interaction deficit and excessive marble burying in offspring (Fig. 4, D and E). These results were not due to general activity defects in the offspring of WT, RORγt HET or TKO mothers (Fig. 4F). Because these offspring were derived from mating RORγt WT, HET and TKO female with WT male mice, they all carried at least one copy of functional RORγt. Therefore, the rescue of MIA-induced phenotypes observed in the offspring of RORγt TKO mothers was not likely due to the lack of T_H17 cells in the offspring. Taken together, these data indicate that maternal $CD4^+$ T lymphocytes expressing RORγt (i.e., T_H17 cells) are necessary for the MIA-mediated expression of cortical abnormalities and three ASD-like behaviors modeled in mouse offspring.

IL-17a administration to the fetal brain promotes abnormal cortical development and ASD-like behavioral phenotypes

To determine whether IL-17a acts on receptors in the mother or the fetus to induce the MIA phenotype, we injected poly(I:C) into IL-17Ra WT, HET, or KO mothers that had been bred to IL-17Ra WT or HET males (*39*). Removing one or both copies of *il17ra* in the mother was sufficient to rescue the MIA-induced sociability deficit in offspring, regardless of their genotypes (fig. S8A). Moreover, we found that reduced expression of maternal IL-17Ra in *il17ra* HET mothers led to reduced serum IL-17a in poly(I:C)-treated mothers (fig. S8B). Thus, it is difficult, if not impossible, to test the functional significance of the IL-17Ra in offspring with a full germline *il17ra* KO without affecting maternal T_H17 cell activity. To circumvent this problem, we asked if increasing IL-17Ra activity in the offspring, by introducing IL-17a directly into the fetal brain in the absence of maternal inflammation, would be sufficient to induce MIA phenotypes. Injection of recombinant IL-17a protein into the ventricles of the fetal brain at E14.5 in the absence of MIA (Fig. 5A) led to the appearance of disorganized cortical patches in a similar location to those induced by MIA (Fig. 5, B to E). Unlike poly(I:C) injection, however, intraventricular injection of IL-17a resulted in thinned cortical plates at the medial but not lateral part of the brain (fig. S9). This effect may reflect

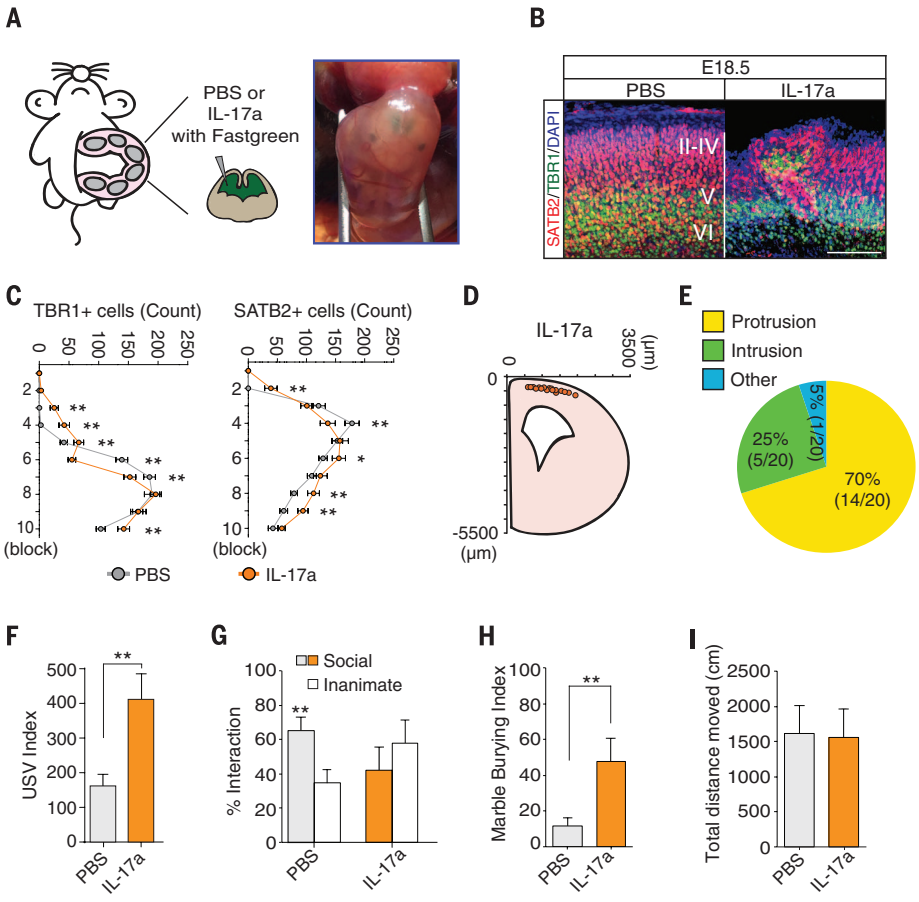

Fig. 5. IL-17a administration to the fetus promotes abnormal cortical development and ASD-like behavioral phenotypes. (**A**) Schematic diagram of the experimental method. Each embryo was injected intraventricularly at E14.5 with PBS or recombinant IL-17a protein mixed with Fastgreen dye. (**B**) SATB2 and TBR1 staining in the cortex of E18.5 male fetal brains treated as in (A). Images are representative of five independent experiments. (**C**) Quantification of TBR1- and SATB2-positive cells in a 300-μm-wide ROI corresponding to the region of the cortical plate containing the malformation in E18.5 male fetal brain [n = 20 (PBS), n = 20 (IL-17a)]. (**D**) The spatial location of the disorganized cortical patch in E18.5 fetal brain [n = 20 (IL-17a)]. (**E**) Percentage of the cortical patches in each category [n = 20 (IL-17a)]. (**F**) USV assay, the number of pup calls [n = 15 (PBS), n = 17 (IL-17a); from five or six independent dams per treatment]. (**G**) Social approach behavior is shown as a social preference index as in Fig. 3 [n = 12 (PBS), n = 18 (IL-17a); from five or six independent experiments]. (**H**) Marble-burying behavior. Percentage of the number of buried marbles is plotted on the y axis [n = 12 (PBS), n = 18 (IL-17a); from five or six independent experiments]. (**I**) Total distance traveled during social approach test. (C) Two-way ANOVA with Tukey's post hoc tests. (F), (H), and (I) Student's t tests. (G) One-way ANOVA with Tukey's post hoc test. $^{**}P < 0.01$; $^{*}P < 0.05$; and ns, not significant. Means ± SEM.

differences in the levels or types of inflammation associated with poly(I:C) versus IL-17a injections or the time points at which poly(I:C) (E12.5) and IL-17a (E14.5) were administered. We also found that, compared with sham injection, IL-17a injections led to an enhanced USV phenotype, social approach deficit, and increased marble-burying behavior, all similar in magnitude to those observed in MIA-exposed offspring (Fig. 5, F to H). These behavioral abnormalities were not due to group differences in mobility (Fig. 5I). Neither cortical disorganization nor enhanced USV phenotypes were observed after IL-17a injections into the ventricles of IL-17Ra KO fetuses or upon IL-6 injections into WT fetal brains (fig. S10, A to C), which suggests that IL-17a, but not IL-6, acts directly in the fetal brain to induce these phenotypes. Of note, in agreement with previous reports (*7*, *40*), IL-6 injection into pregnant WT mothers was sufficient to produce MIA-associated behavioral (enhanced USV) and cortical phenotypes in the offspring (fig. S10, D to F). Yet, pretreatment of pregnant mothers with IL-17a–blocking antibody prevented the phenotypes induced by maternal IL-6 injection (fig. S10, D to F). Last, IL-17a injection into brains of fetuses from poly(I:C)-injected IL-6 KO mothers was sufficient to elicit increased pup USVs compared with PBS-injected controls (fig. S10G). These data collectively demonstrate that activation of the IL-17Ra pathway in the fetal brain, induced by intraventricular injection of IL-17a into the fetus or by intraperitoneal injection of poly(I:C) or IL-6 into pregnant mothers, results in MIA-associated phenotypes in the offspring.

Therapeutic treatment with IL-17a–blocking antibody in pregnant dams ameliorates MIA-associated behavioral abnormalities

Our results suggest that pathological activation of the T_H17 cell–IL-17a pathway during gestation in mothers with some inflammatory conditions may alter fetal brain development and contribute to the ASD-like behavioral phenotypes in offspring (fig. S11). T_H17 cells require RORγt for their differentiation and exert their functions by secreting multiple cytokines, including IL-17a. Abrogation of RORγt expression in maternal αβ T cells or blockade of the IL-17a pathway in pregnant dams resulted in the complete rescue of cortical developmental abnormalities and ASD-like behavioral phenotypes in offspring in the MIA rodent model. Thus, RORγt and T_H17 cells (as well as their cytokines) may serve as good therapeutic targets to prevent the development of ASD phenotypes in the children of susceptible mothers. To further test this idea, we administered IL-17a–blocking antibody to pregnant mice in a time window after MIA induction (Fig. 6A). We injected pregnant mothers with PBS or poly(I:C) at E12.5, followed by injection of IgG isotype control or IL-17a–blocking antibody at E14.5, when the delayed expression of SABT2 manifests in MIA-exposed fetal brains (Fig. 2, A and C). Compared with PBS injection followed by control antibody treatment, poly(I:C) injection followed by IL-17a–blocking antibody administration partially rescued USV and marble-burying phenotypes (Fig. 6, B and D). However, MIA-induced social interaction deficits were not corrected (Fig. 6C). These effects were not due to group differences in mobility (Fig. 6E). Thus, treating pregnant mothers with IL-17a–blocking antibody after MIA can correct some of the ASD-like features, but pretreatment with this antibody may have greater therapeutic potential.

Conclusions

Our results identify a specific maternal immune cell population that may have direct roles in inducing ASD-like phenotypes by acting on the developing fetal brain. These findings raise the possibility that modulation of the activity of a cytokine receptor, IL-17Ra, in the central nervous system can influence neuronal development, with implications as to specification of neuronal cell types and their connectivity. Furthermore, note that the loss of certain genes that induce ASD-like phenotypes were also found in mice with defects in cortical lamination (*41*, *42*). These observations raise the possibility that some genetic and environmental factors that have roles in the etiology of ASD function by way of similar physiological pathways. A related question is whether IL-17Ra signaling has a normal physiological function in the fetal and adult brain, especially given the structural similarities observed between the IL-17 family cytokines and neurotrophin proteins (e.g., nerve growth factor) (*43*, *44*). Elucidating further downstream pathways of maternal IL-17a–producing T cells, both in MIA mothers and their offspring, will likely yield a better understanding of the mechanisms by which inflammation in utero contributes to the development of neurodevelopmental disorders, such as ASD,

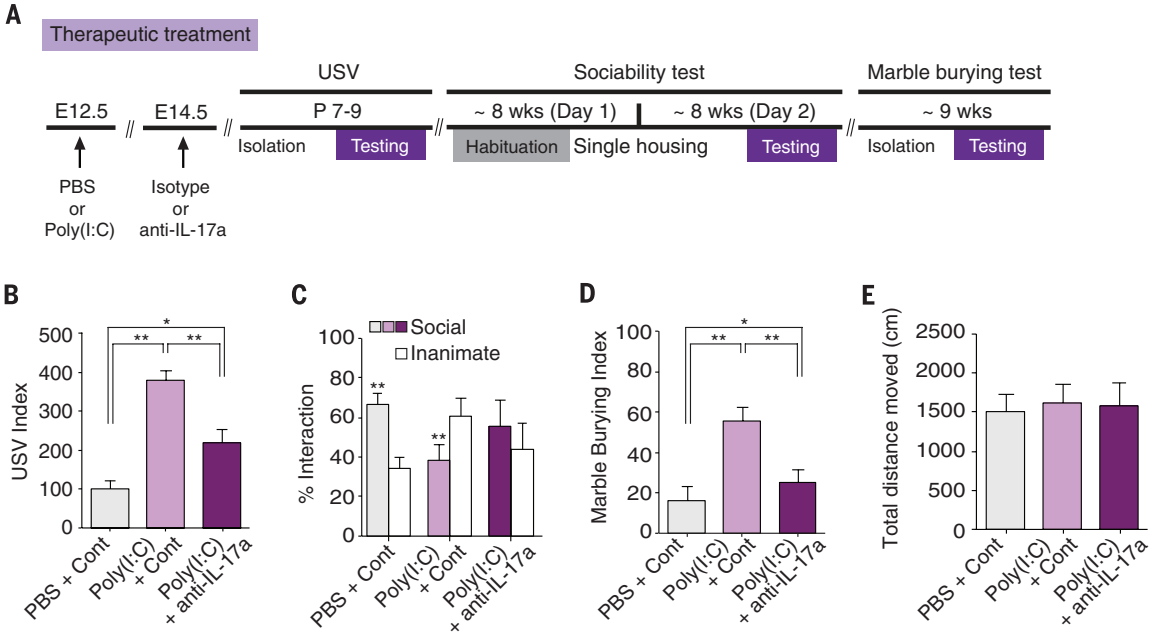

Fig. 6. Therapeutic effects of blocking IL-17a signaling in pregnant dams. (**A**) Schematic diagram of the experimental design. At E12.5, pregnant mothers were injected with PBS or poly (I:C) to induce MIA. Two days later (E14.5), the pregnant mothers were treated with isotype or anti–IL-17a. At P7 to ~P9, pups were separated from the mothers to measure USV calls. At ~8 weeks, male offspring were subjected to the social approach test and marble-burying test. (**B**) USV assay. The number of pup calls is plotted on the *y* axis {*n* = 17 (PBS, Cont); *n* = 17 [poly(I:C), Cont]; *n* = 27 [poly(I:C), anti–IL-17a]; from three or four independent dams per treatment}. (**C**) Social approach behavior is shown as a social preference index (Fig. 3) {*n* = 12 (PBS, Cont), *n* = 10 [poly(I:C), Cont], *n* = 17 [poly(I:C), anti–IL-17a]; from three or four independent dams per treatment}. (**D**) Marble-burying behavior as in Fig. 3 {*n* = 12 (PBS, Cont), *n* = 10 [poly(I:C), Cont], *n* = 17 [poly(I:C), anti–IL-17a]; from three or four independent dams per treatment}. (**E**) Total distance traveled during social approach behavior. (B), (D), and (E) One-way ANOVA with Tukey's post hoc tests. (C) Two-way ANOVA with Tukey's post hoc test. $^{**}P < 0.01$ and $^{*}P < 0.05$. Means ± SEM.

and, additionally, may provide insights into the roles of cytokine receptors in the central nervous system.

REFERENCES AND NOTES

1. H. O. Atladóttir *et al.*, *J. Autism Dev. Disord.* **40**, 1423–1430 (2010).
2. P. H. Patterson, *Behav. Brain Res.* **204**, 313–321 (2009).
3. A. S. Brown *et al.*, *Mol. Psychiatry* **19**, 259–264 (2014).
4. H. O. Atladóttir *et al.*, *Pediatrics* **124**, 687–694 (2009).
5. P. Ashwood, S. Wills, J. Van de Water, *J. Leukoc. Biol.* **80**, 1–15 (2006).
6. B. K. Lee *et al.*, *Brain Behav. Immun.* **44**, 100–105 (2015).
7. S. E. P. Smith, J. Li, K. Garbett, K. Mirnics, P. H. Patterson, *J. Neurosci.* **27**, 10695–10702 (2007).
8. N. V. Malkova, C. Z. Yu, E. Y. Hsiao, M. J. Moore, P. H. Patterson, *Brain Behav. Immun.* **26**, 607–616 (2012).
9. C. M. Wilke, K. Bishop, D. Fox, W. Zou, *Trends Immunol.* **32**, 603–611 (2011).
10. N. Manel, D. Unutmaz, D. R. Littman, *Nat. Immunol.* **9**, 641–649 (2008).
11. H. Spits, J. P. Di Santo, *Nat. Immunol.* **12**, 21–27 (2011).
12. M. Lochner *et al.*, *J. Exp. Med.* **205**, 1381–1393 (2008).
13. I. I. Ivanov *et al.*, *Cell* **126**, 1121–1133 (2006).
14. L. Y. Al-Ayadhi, G. A. Mostafa, *J. Neuroinflammation* **9**, 158 (2012).
15. K. Suzuki *et al.*, *PLOS ONE* **6**, e20470 (2011).
16. B. van der Zwaag *et al.*, *PLOS ONE* **4**, e5324 (2009).
17. M. Mandal, A. C. Marzouk, R. Donnelly, N. M. Ponzio, *J. Reprod. Immunol.* **87**, 97–100 (2010).
18. E. Y. Hsiao, S. W. McBride, J. Chow, S. K. Mazmanian, P. H. Patterson, *Proc. Natl. Acad. Sci. U.S.A.* **109**, 12776–12781 (2012).
19. V. K. Kuchroo, A. Awasthi, *Eur. J. Immunol.* **42**, 2211–2214 (2012).
20. C. Dehay, H. Kennedy, *Nat. Rev. Neurosci.* **8**, 438–450 (2007).
21. M. F. Casanova *et al.*, *Acta Neuropathol. Commun.* **1**, 67 (2013).
22. R. Stoner *et al.*, *N. Engl. J. Med.* **370**, 1209–1219 (2014).
23. J. De Miranda *et al.*, *MBio* **1**, e00176-10, e00176-19 (2010).
24. S. E. Smith, R. M. Elliott, M. P. Anderson, *J. Neuroimmune Pharmacol.* **7**, 529–532 (2012).
25. B. J. Molyneaux, P. Arlotta, J. R. Menezes, J. D. Macklis, *Nat. Rev. Neurosci.* **8**, 427–437 (2007).
26. E. A. Alcamo *et al.*, *Neuron* **57**, 364–377 (2008).
27. C. Englund *et al.*, *J. Neurosci.* **25**, 247–251 (2005).
28. M. Leid *et al.*, *Gene Expr. Patterns* **4**, 733–739 (2004).
29. J. J. Schwartzer *et al.*, *Transl. Psychiatry* **3**, e240 (2013).
30. N. Yee, R. K. Schwarting, E. Fuchs, M. Wöhr, *J. Psychiatr. Res.* **46**, 1199–1205 (2012).
31. E. Y. Hsiao *et al.*, *Cell* **155**, 1451–1463 (2013).
32. C. A. Hoeffer *et al.*, *Neuron* **60**, 832–845 (2008).
33. H. X. Wu, L. P. Jin, B. Xu, S. S. Liang, D. J. Li, *Cell. Mol. Immunol.* **11**, 253–262 (2014).
34. A. Nakashima *et al.*, *Am. J. Reprod. Immunol.* **63**, 104–109 (2010).
35. E. A. Martínez-García *et al.*, *Am. J. Reprod. Immunol.* **65**, 99–103 (2011).
36. G. Eberl, D. R. Littman, *Science* **305**, 248–251 (2004).
37. Z. Sun *et al.*, *Science* **288**, 2369–2373 (2000).
38. J. R. Huh *et al.*, *Nature* **472**, 486–490 (2011).
39. Y. Iwakura, H. Ishigame, S. Saijo, S. Nakae, *Immunity* **34**, 149–162 (2011).
40. E. Y. Hsiao, P. H. Patterson, *Brain Behav. Immun.* **25**, 604–615 (2011).
41. L. A. Orosco *et al.*, *Nat. Commun.* **5**, 4692 (2014).
42. O. Peñagarikano *et al.*, *Cell* **147**, 235–246 (2011).
43. S. G. Hymowitz *et al.*, *EMBO J.* **20**, 5332–5341 (2001).
44. X. Zhang, P. Angkasekwinai, C. Dong, H. Tang, *Protein Cell* **2**, 26–40 (2011).

ACKNOWLEDGMENTS

We thank E. Kurz, D. Montgomery, and Y. Cai for assistance with experiments and J. Koll for providing the *il17ra*^{KO} mouse line, which was originally developed by Amgen. The *il17ra*^{KO} line will be available from D.R.L. under a material transfer agreement with Amgen. We also thank M. Sellars for critical reading of the manuscript. The data presented in this paper are tabulated in the main text and in the supplementary materials. This work was supported by the Simons Foundation Autism Research Initiative (D.R.L.); the Simons Foundation to the Simons Center for the Social Brain at Massachusetts Institute of Technology (Y.S.Y. and G.B.C.); Robert Buxton (G.B.C.); the National Research Foundation of Korea grants MEST-35B-2011-1-E00012 (S.K.); and NRF-2014R1A1A1006089 (H.K.); the Crohn's and Colitis Foundation of America grant 329388 (S.V.K.); the Smith Family Foundation (J.R.H.); the Searle Scholars Program (J.R.H.); Alzheimer's Association MNIRGDP-12-258900 (C.A.H.); Brain and Behavior Research Foundation (NARSAD) 21069 (C.A.H.); and NIH grants F31NS083277 (H.W.), R00DK091508 (J.R.H.), and R01NS086933 (C.A.H.); and the Howard Hughes Medical Institute (D.R.L.). D.R.L. and J.R.H. are inventors on a patent application filed by New York University, related to the studies reported here.

SUPPLEMENTARY MATERIALS

www.sciencemag.org/content/351/6276/933/suppl/DC1
Materials and Methods
Supplementary Text
Figs. S1 to S11
References (*45*–*47*)

17 July 2015; accepted 14 January 2016
Published online 28 January 2016
10.1126/science.aad0314

MEIOSIS

A DNA topoisomerase VI–like complex initiates meiotic recombination

Nathalie Vrielynck,[1] Aurélie Chambon,[1] Daniel Vezon,[1] Lucie Pereira,[1] Liudmila Chelysheva,[1] Arnaud De Muyt,[1]* Christine Mézard,[1] Claudine Mayer,[2,3,4] Mathilde Grelon[1]†

The SPO11 protein catalyzes the formation of meiotic DNA double strand breaks (DSBs) and is homologous to the A subunit of an archaeal topoisomerase (topo VI). Topo VI are heterotetrameric enzymes comprising two A and two B subunits; however, no topo VIB involved in meiotic recombination had been identified. We characterized a structural homolog of the archaeal topo VIB subunit [*meiotic topoisomerase VIB–like* (*MTOPVIB*)], which is essential for meiotic DSB formation. It forms a complex with the two *Arabidopsis thaliana* SPO11 orthologs required for meiotic DSB formation (SPO11-1 and SPO11-2) and is absolutely required for the formation of the SPO11-1/SPO11-2 heterodimer. These findings suggest that the catalytic core complex responsible for meiotic DSB formation in eukaryotes adopts a topo VI–like structure.

Meiotic recombination is the key step in sexual reproduction leading to the production of haploid gametes and is therefore essential for the fertility of most eukaryotes. It is initiated by the induction of DNA double strand breaks (DSBs), which are catalyzed by the evolutionarily conserved SPO11 protein (*1*). SPO11 shows sequence similarities to the A subunit of the archaeal type II DNA topoisomerase, topoisomerase VI (topo VI) (*2*). Topo VI enzymes relax DNA supercoils by cutting both DNA strands of a DNA helix in an adenosine 5′-triphosphate (ATP)–dependent manner, forcing the passage of another DNA duplex through the generated break and eventually religating the break, regenerating an intact DNA molecule (*3*). Topo VI enzymes are active as heterotetramers, composed of two A and two B subunits. The two topo VIA subunits carry the catalytically active tyrosines and associate as a dimer to form the catalytic core of the topo VI enzyme (*2*). The topo VIB subunits contain an ATP-binding domain known as the Bergerat fold, which is characteristic of the GHKL (Gyrase, HSP90, histidine kinase, MutL) superfamily (*2*, *4*). Topo VIB also possess a C-terminal transducer domain that transfers the conformational changes induced by ATP binding and hydrolysis from the GHKL to the catalytic A subunits (*5*). On the basis of the similarity between SPO11 and topo VIA, and because SPO11 can be purified covalently associated with the meiotic DSB ends (*6*), it was proposed that at the onset of meiotic recombination, SPO11 dimerizes to form the catalytic core responsible for DNA DSB formation. In *Arabidopsis thaliana*, genetic analyses revealed that two nonredundant SPO11 homologs (SPO11-1 and SPO11-2) are absolutely required for DSB formation (*7*–*9*), suggesting that meiotic DSBs are catalyzed by a SPO11-1/SPO11-2 heterodimer rather than a homodimer. Although most eukaryotic lineages possess at least one SPO11 protein, until now no topo VIB homolog involved in meiotic recombination had been identified. Here, we present the first characterization of a structural homolog of the archaeal topo VIB subunit required for meiotic DSB formation. We show that it mediates the formation of the SPO11-1/SPO11-2 heterodimer, changing our view of the nature of the core complex involved in meiotic DSB formation.

In a screen for *A. thaliana* mutants with reduced fertility, we identified two allelic lines,

[1]Institut Jean-Pierre Bourgin (IJPB), INRA, AgroParisTech, CNRS, Université Paris-Saclay, RD10, 78026 Versailles Cedex, France. [2]Institut Pasteur, 25 rue du Dr Roux, 75015, Paris, France. [3]CNRS, UMR 3528, 75724 Paris cedex 15, France. [4]Université Paris Diderot, Sorbonne Paris Cité, Paris, France. *Present address: Institut Curie, PSL Research University, CNRS, UMR3664, F-75005, Paris, France. **†Corresponding author. E-mail: mathilde.grelon@versailles.inra.fr**

Downloaded from on February 25, 2016

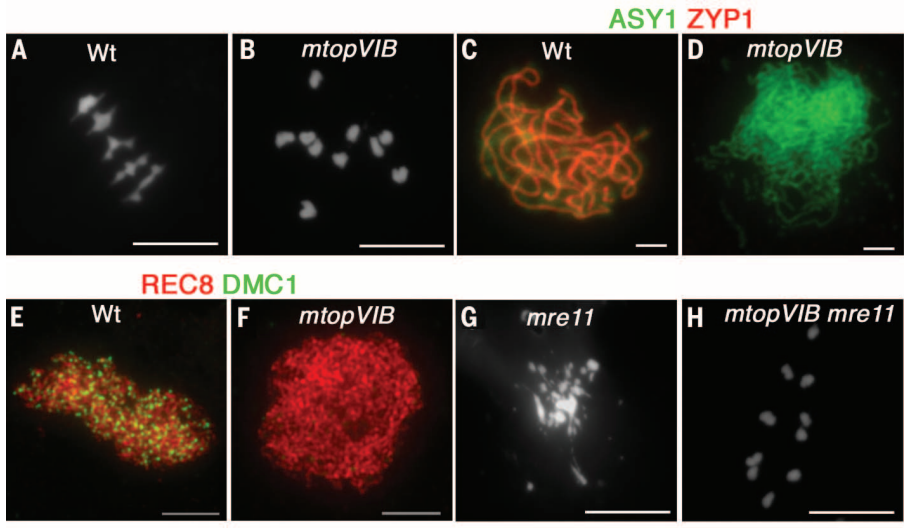

Fig. 1. *mtopVIB* mutants are DSB-deficient. (**A** and **B**) DAPI staining of meiotic chromosomes during the metaphase I/anaphase I transition shows that in (A) wild type (Wt), the 10 *A. thaliana* chromosomes associate into five bivalents that align at the metaphase plate. (B) In *mtopVIB* (*mtopVIB-2*), 10 randomly arranged univalents are observed. Scale bar, 10 μm. (**C** and **D**) Co-immunolocalization of the axis protein ASY1 (green) and the synaptonemal complex transverse filament protein ZYP1 (red). (C) In wild-type pachytene cells, ZYP1 connects the axial element of the homologous chromosomes along their whole length, as revealed by the perfect colocalization of ZYP1 with the axis protein ASY1. (D) In *mtopVIB*, no ZYP1 staining is detected, showing a complete absence of synapsis (*mtopVIB-2*). Scale bar, 2 μm. (**E** and **F**) Co-immunolocalization of the meiotic-specific cohesin REC8 (red) together with the meiotic specific recombinase DMC1 (green). (E) In wild type (Wt), ~250 recombination sites are detected by using antibodies against DMC1, whereas (F) none are visible in *mtopVIB* (*mtopVIB-2*). Scale bar, 5 μm. (**G** and **H**) DAPI staining of meiotic chromosomes during the metaphase I/anaphase I transition in (G) *mre11-4* (*mre11*) and (H) *mtopVIB-1mre11-4* (*mtopVIBmre11*). (G) The *mre11* mutant, which is defective in meiotic DSB repair, shows severe chromosome fragmentation at the first meiotic division, but (H) this phenotype is completely abolished in the *mtopVIB* mutant background. Scale bar, 10 μm.

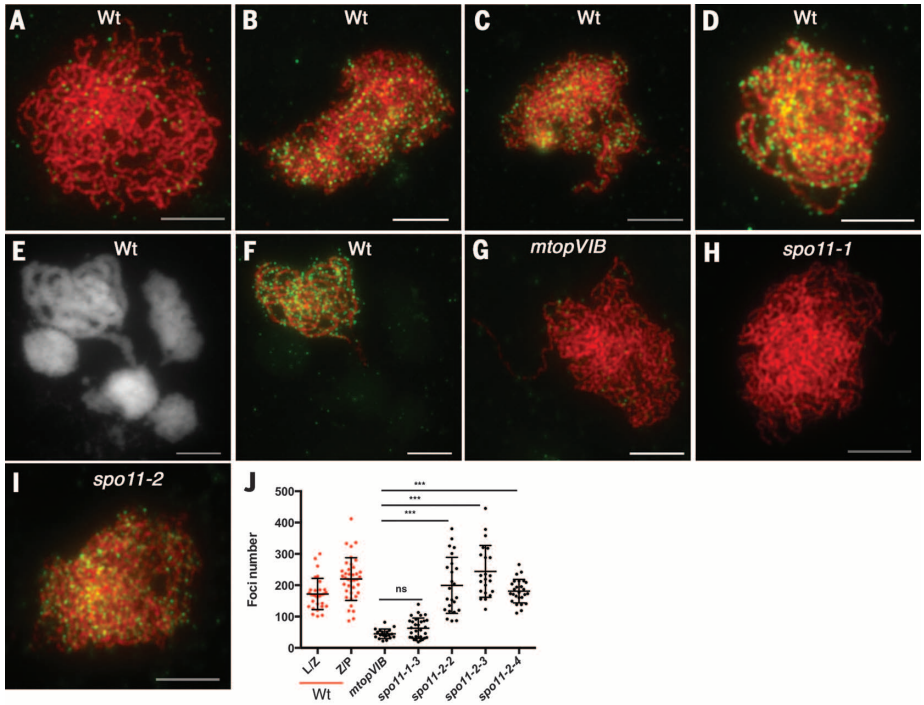

Fig. 2. MTOPVIB forms foci on meiotic chromosomes from leptotene to pachytene. (**A** to **J**) Co-immunolocalization of the REC8 cohesin (red signal) and MTOPVIB (green signal) in [(A) to (F)] wild-type Col-0, (G) *mtopVIB-2*, (H) *spo11-1-3*, and (I) *spo11-2-3* mutants. (E) DAPI staining is shown in white. The MTOPVIB signal was not detected in (A) G2/early leptotene cells but forms numerous foci associated with the REC8 signal at (B) leptotene, (C) zygotene, and (D) pachytene. DAPI staining in (E) reveals five nuclei, four of which are not labeled, with either REC8 or MTOPVIB (F) showing that MTOPVIB is specifically expressed in meiocytes. No MTOPVIB signal was seen in (G) meiocytes from the *mtopVIB* mutant, or in (H) the *spo11-1* mutant, but (I) foci were visible in *spo11-2*. (J) The number of MTOPVIB foci detected in wild type (L/Z, leptotene or early zygotene; Z/P, late zygotene or pachytene), in *mtopVIB* (*mtopVIB-2*), and in *spo11* mutants (*spo11-1-3*, *spo11-2-2*, *spo11-2-3*, and *spo11-2-4*). *P* values from an ordinary one-way analysis of variance are indicated. ns, not statistically different. ***$P < 0.0001$. Scale bar, 5 μm.

mtopVIB-1 and *mtopVIB-2*, that show a quasi-sterile phenotype (4% of the wild-type level of seeds) (fig. S1, A and B) correlated with male and female gamete developmental defects (fig. S1, C to E). Staining *mtopVIB* male meiocyte chromosome spreads with 4′,6-diamidino-2-phenylindole (DAPI) showed a considerable reduction in bivalent formation at metaphase I (Fig. 1, A and B, and figs. S2 and S3); in wild type, five bivalents were observed in 100% of cases (n = 94 cells), whereas only univalents were observed in 86% of *mtopVIB-1* and 100% of *mtopVIB-2* meiocytes (n = 141 and n = 52 cells, respectively) (fig. S3). In addition, synapsis of homologous chromosomes was completely abolished in *mtopVIB* (n = 47 cells) (Fig. 1, C and D), and no signal above background could be detected for the meiotic recombinase DMC1 (n = 29 cells) (Fig. 1, E and F). Meiotic recombination rates also fell considerably in *mtopVIB*, to only a few percent of the wild-type level, which is an effect comparable with that measured for the *spo11-1* mutation (table S1). These meiotic defects observed in *mtopVIB* mutants could be indicative of either defects in meiotic DSB formation (as in *spo11* mutants) or in DSB repair, using the homologous chromosome as the repair template (as seen in the *dmc1* mutants) (*10*). To distinguish between these two hypotheses, we introduced the *mtopVIB* mutation into two DSB-repair–deficient mutants, *rad51* and *mre11* (*11*, *12*). We observed that the *mtopVIB* mutation suppressed all the fragmentation defects observed in these backgrounds (Fig. 1 and fig. S2). Taken together, these data show that *mtopVIB* mutants display the same meiotic defects as both *spo11-1* (*7*) and *spo11-2* mutants (*8*, *9*) and establish an essential role for MTOPVIB in meiotic DSB formation.

Immunolocalized MTOPVIB forms numerous foci in meiotic cells from leptotene (172 ± 9 foci,

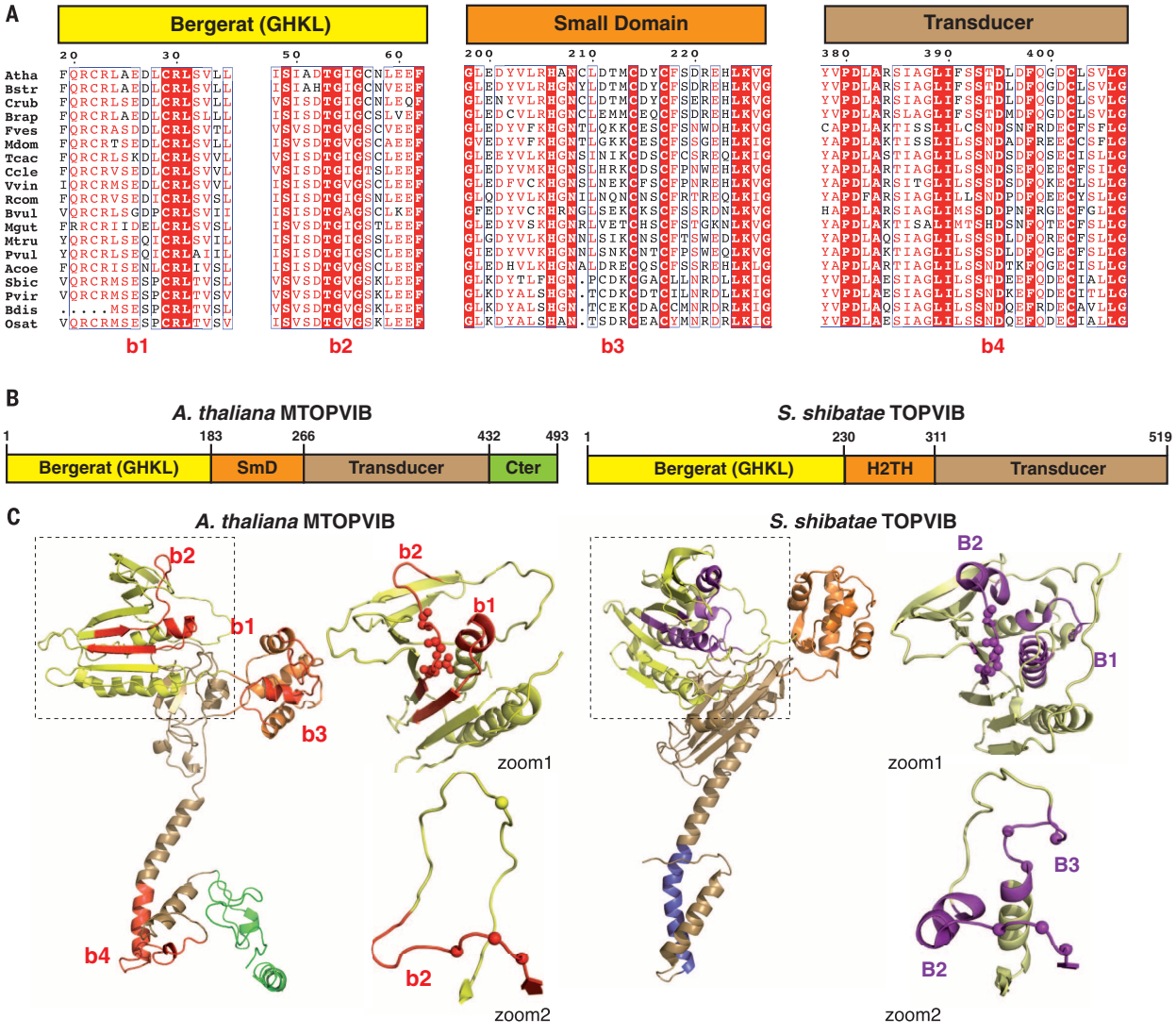

Fig. 3. Sequence and model structure of *A. thaliana* MTOPVIB. (**A**) Multiple sequence alignment of the plant MTOPVIB protein family showing the four conserved amino acid regions in MTOPVIB (b1 to b4). Two are in the GHKL domain, one is in the small domain, and one is in the transducer domain. Identical amino acids are in red. The 19 sequences used for the alignment are listed in the legend for fig. S5A. (**B**) Domain organization of the *A. thaliana* MTOPVIB and the *S. shibatae* topoisomerase VIB subunit (*S. shibatae* TOPVIB). Homologous domains are shown in the same color: yellow, GHKL domain; orange, Helix-2Turn-Helix (H2TH) domain and small domain (SmD); brown, transducer domain; green, C-terminal (Cter) domain. The amino acid numbers indicate the domain borders. (**C**) Proposed model structure of *A. thaliana* MTOPVIB and crystal structure of *S. shibatae* TOPVIB. The four conserved amino acid regions of MTOPVIB are indicated by b1 to b4 and are in red. On the *S. shibatae* TOPVIB crystal structure, the three GHKL conserved motifs [B1 to B3, as defined in (*2*)] are indicated in purple. The A-B interaction surface of the transducer is indicated in dark blue. Domains are color-coded as in (B). For each structure, two different zooms of the GHKL domains (dashed boxes) are given. For MTOPVIB and *S. shibatae* TOPVIB GHKL zooms 1, the aspartate and the two glycines of the DxGxG motif (b2 for MTOPVIB and B2 for *S. shibatae* TOPVIB) are represented in small CPK. Zooms 2 correspond to the ATP-lids, in which the Cα of the aspartate and glycines of the b2 or B2 motif (DxGxG), the single glycine in MTOPVIB, and the glycines of the B3 GxxGxG motif of *S. shibatae* TOPVIB are represented by small spheres.

mean ± SEM, n = 30 cells) to pachytene, with a slight but significant increase (219 ± 11, n = 38 cells, P = 0.002 unpaired t test) (Fig. 2, A to F and J). The MTOPVIB signal was not detected in G2/early leptotene cells or in somatic nuclei (Fig. 2, A, E, and F) and only partially colocalized with the axis signal. We also examined MTOPVIB foci in a series of *spo11* mutants characterized by a near complete absence of recombination (fig. S3) (*8*, *9*). Foci were not detected above the background level in *spo11-1* mutants but were still present in the three different *spo11-2* alleles investigated (Fig. 2, H to J); because *spo11-2* mutants are DSB-defective, this suggests that MTOPVIB foci do not mark active DSBs, at least in these backgrounds. Whether this is the case in wild type remains to be seen. Further, if SPO11-1—but not SPO11-2—is essential for MTOPVIB loading onto chromosomes, then this is the first evidence of a functional difference between SPO11-1 and SPO11-2 during meiotic recombination initiation.

The *MTOPVIB* gene (*At1g60460*) (gene and mutant molecular characterization are provided in fig. S4) encodes a 493-amino-acid protein with clear orthologs among the flowering plants (*Magnoliophyta*) (Fig. 3A and fig. S5A). The MTOPVIB protein family is characterized by four highly conserved motifs (b1 to b4) (Fig. 3A and fig. S5A). The MTOPVIB protein sequence has no obvious similarity to known functional domains. However, HHpred searches using this protein family as a query revealed clear structural homology with the two archaeal topo VIB proteins with known crystal structures [*Sulfolobus shibatae*, PDB code 2ZBK, probability = 98.5%, expect value (E) = 4.2 × 10^{-6} and *Methanosarcina mazei*, PDB code 2Q2E, probability = 95.0%, E = 0.0094]. On the basis of sequence and structure comparisons, MTOPVIB proteins comprise four domains

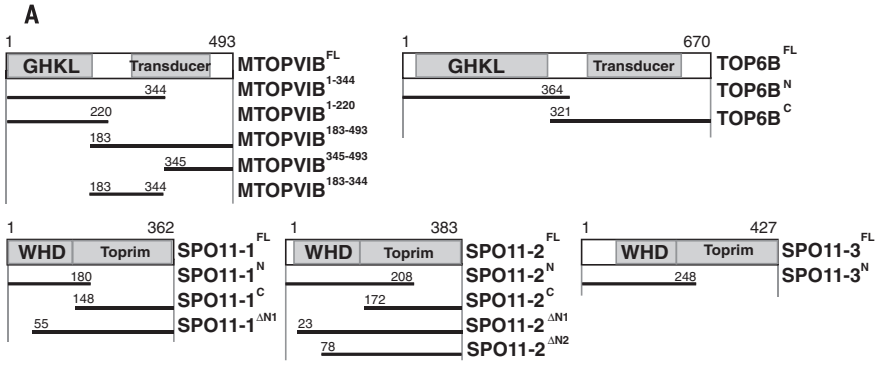

B

	SPO11-1				SPO11-2					SPO11-3	
	FL	N	C	ΔN1	FL	N	C	ΔN1	ΔN2	FL	N
MTOPVIB FL	++	++	–	–	+	++	–	–	–	++	++
MTOPVIB 1-344	–	–		–	–	–		–	–	–	–
MTOPVIB 1-220	–	–	–	–	–	–	–	–	–		
MTOPVIB 183-493	++	+	–	–	–	+	–	–	–	+	+
MTOPVIB 345-493	+	+		–	–	+		–	–	+	+
MTOPVIB 183-344		–				–					–
TOP6B FL	–			–	–			–	–	++	
TOP6B N		–				–					–
TOP6B C	–	–		–	–	–		–	–	++	+

C

	SPO11-1 FL			SPO11-2 FL			SPO11-3 FL		
SPO11-1 FL	–	–	–	–	+	–	–	–	–
SPO11-2 FL	–	+	–	–	–	–	–	–	–
SPO11-3 FL	–	–	–	–	–	–	+	+	+

In presence of :
empty pARC352
MTOPVIB
TOP6B

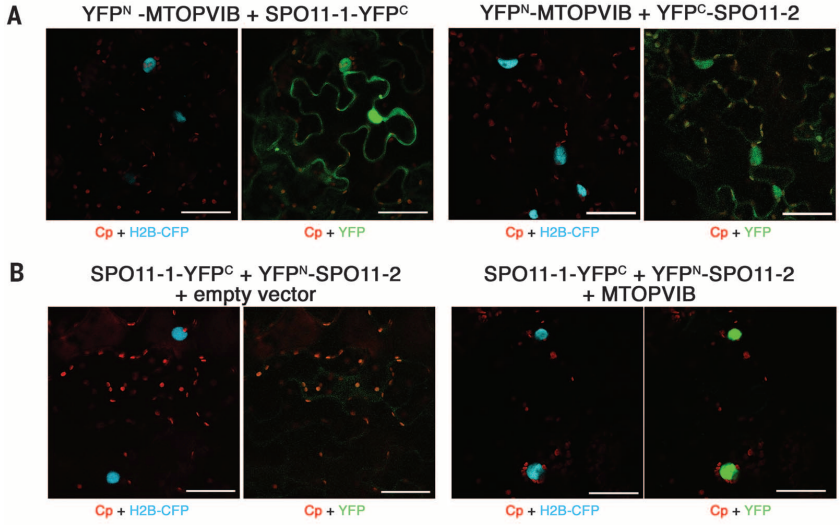

Fig. 4. MTOPVIB mediates the formation of a SPO11-1/SPO11-2 heterodimer in yeast cells. (**A**) Schematic representation of the full-length (FL) and truncated proteins used in this study. MTOPVIB and TOP6B GHKL and transducer domains are indicated. SPO11's N-terminal WHD and its C-terminal Toprim domains are shown. (**B**) Summary of the yeast two-hybrid assay results. Detailed results are given in fig. S7A. "++" indicates growth on SD-LWHA medium for at least one of the combinations tested. "+" indicates growth on SD-LWH medium for at least one of the combinations tested. "–" indicates that none of the combinations tested confer auxotrophy. Gray boxes indicate the interaction was not tested. (**C**) Summary of the yeast three-hybrid assay results. Detailed results are given in fig. S7C. Interactions among FL SPO11 proteins were tested by using the GAL4-based system (supplementary materials, materials and methods) in the presence or absence of one of the *A. thaliana* topo VIB subunits (light gray boxes, MTOPVIB; dark gray boxes, somatic TOP6B; white boxes, no B subunit). "–" indicates no growth on SD-LWHA, and "+" indicates growth on SD-LWHA.

Fig. 5. MTOPVIB mediates the formation of a SPO11-1/SPO11-2 heterodimer in plant cells. (**A** and **B**) Single-section confocal images of *N. benthamiana* epidermal cells constitutively expressing a fluorescent nuclear protein [H2B–cyan fluorescent protein (CFP), blue channel], co-infiltrated with *Agrobacterium* cultures expressing two complementary YFP [N-terminal (YFP^N) or C-terminal (YFP^C)] fusions. A YFP fluorescence signal (right panel in each pair, green) reveals an interaction between the two tested fusion proteins. The full list of combinations tested is in fig. S7D. All images correspond to merged signals of chloroplast autofluorescence (red) with either the CFP signal (blue) or the YFP signal (green). Scale bar, 50 μm. (A) MTOPVIB interacts with SPO11-1 (left) and SPO11-2 (right) in *N. benthamiana* epidermal cells. (B) SPO11-1 and SPO11-2 do not interact in *N. benthamiana* epidermal cells except if MTOPVIB is co-expressed with the split-YFP SPO11 constructs.

(Fig. 3B and fig. S5B). Overall, the structure of the first domain, the GHKL/Bergerat fold, is highly conserved (Fig. 3C). Among the motifs that constitute the GHKL signatures (Fig. 3C and fig. S5B) (*2*), two correspond to MTOPVIB motifs b1 and b2 and include the conserved B2 motif DxGxG, which is important for ATP-binding (*13*). However, the glycine-rich Bergerat fold motif B3 localized in the ATP-lid is poorly conserved, and only the first glycine of this motif is present (Fig. 3C and figs. S5B and S6C), suggesting that the ATP hydrolysis mechanism could be different in MTOPVIB. The second MTOPVIB domain is a small domain (SmD), the borders of which are more difficult to define, and structural similarity with the archaea topo VIB H2TH domain is low (Fig. 3 and figs. S5B and S6A). The third domain is the transducer domain. This long α-helix structure is shorter than in the topo VIB subunits but still very well conserved (Fig. 3C and fig. S6, A and D). This domain contains the strictly conserved W (dWxxY motif) and another conserved region (b4) (Fig. 3), which are both present in the topo VIB family (fig. S5B). The most conserved

region (b4) in the MTOPVIB transducer domain corresponds to the region of interaction between the A and B subunits of the topo VI heterotetramer (Fig. 3 and fig. S5B) (*14*). Last, the MTOPVIB C-terminal extension is different from those found in some topo VIB proteins (10).

The similarity of SPO11s to the archaeal topo VIA and of MTOPVIB to the topo VIB, together with their requirement in meiotic DSB formation, prompted us to investigate whether these proteins could associate into a topo VI–like complex. The combination of yeast two-hybrid and bimolecular fluorescence complementation [BiFC, or Split–yellow fluorescent protein (YFP)] (*15*) assays revealed that MTOPVIB interacts directly with the winged-helix domain (WHD)–containing N-terminal regions of both SPO11-1 and SPO11-2 (Figs. 4B and 5A and fig. S7). The last 149 amino acids of MTOPVIB (MTOPVIB$^{345\text{-}493}$) (Fig. 4A) are sufficient to establish the interaction with the N-terminal regions of SPO11-1 and SPO11-2 (Fig. 4B and fig. S7), which is in agreement with the known topo VI structure (figs. S5B and S6D) (*14*, *16*). The topo VI structure also predicts that the two A subunits should self-associate, but such a direct interaction between SPO11 proteins was not found in either yeast two-hybrid or BiFC assays (Figs. 4C and 5B and fig. S7C) (*8*). However, coexpression of MTOPVIB in both yeast triple-hybrid and BiFC assays showed that it mediates SPO11 heterodimerization (Figs. 4C and 5B and fig. S7C). MTOPVIB could only mediate the interaction between SPO11-1 and SPO11-2 but did not facilitate the formation of either SPO11-1 or SPO11-2 homodimers (Fig. 4C and fig. S7, C and D). Thus, we propose that the catalytic complex required for meiotic DSB formation adopts a structure comparable with that of the archaeal topo VI complex, involving two MTOPVIB subunits and the two SPO11 subunits. Searches for MTOPVIB orthologs outside flowering plants identified the presence of functionally and structurally conserved homologs in distant phyla (*17*), suggesting that the requirement for a topo VI–like complex for meiotic DSB formation is a common feature among eukaryotes.

All eukaryotic genomes encode at least one meiotic topo VIA–like protein—SPO11—but plant genomes are also one of the rare eukaryotic genomes to encode a topo VIB subunit homolog, *TOP6B/TOPVIB* (*3*, *18*). *A. thaliana top6B* mutants have strong pleiotropic phenotypes that exclusively affect somatic development but not meiosis (*19*–*21*). These phenotypes are indistinguishable from *spo11-3* mutants, which are disrupted in the third *SPO11* homolog found in the *Arabidopsis* genome (*19*–*21*). It is therefore likely that SPO11-3 and TOP6B are two subunits of an *A. thaliana* somatic topo VI complex. In further yeast two-hybrid assays, we found that MTOPVIB interacts with the somatic topo VIA subunit SPO11-3, but that the somatic B subunit TOP6B cannot interact with either meiotic SPO11-1 or SPO11-2 (Fig. 4B) or mediate the formation of the SPO11-1/SPO11-2 meiotic catalytic heterodimer (Fig. 4C). This points toward an important role for the interacting surfaces of the A subunits in conferring specificity to interactions between the two *A. thaliana* topo VI complexes. In addition, we found that in contrast to the meiotic *A. thaliana* SPO11 homologs, SPO11-3 self-associates in yeast two-hybrid assays without the need for a topo VIB–like subunit (Fig. 4C), as is the case for the archaeal topo VI complexes, in which the A subunits self-associate (*22*).

Future studies will further characterize the biochemical activity of the meiotic DSB catalytic complex and examine how it compares in detail with classical topo VI. However, we have clearly shown that the meiotic topo VIB subunit has acquired a crucial role in mediating the assembly of the catalytic portion of the meiotic complex. Compared with the original archaeal topo VI, this represents an additional regulatory capacity, which may be crucial for avoiding erratic DSB formation in gamete mother cells.

REFERENCES AND NOTES

1. B. de Massy, *Annu. Rev. Genet.* **47**, 563–599 (2013).
2. A. Bergerat *et al.*, *Nature* **386**, 414–417 (1997).
3. P. Forterre, S. Gribaldo, D. Gadelle, M.-C. Serre, *Biochimie* **89**, 427–446 (2007).
4. R. Dutta, M. Inouye, *Trends Biochem. Sci.* **25**, 24–28 (2000).
5. A. D. Bates, J. M. Berger, A. Maxwell, *Nucleic Acids Res.* **39**, 6327–6339 (2011).
6. S. Keeney, C. N. Giroux, N. Kleckner, *Cell* **88**, 375–384 (1997).
7. M. Grelon, D. Vezon, G. Gendrot, G. Pelletier, *EMBO J.* **20**, 589–600 (2001).
8. F. Hartung *et al.*, *Plant Cell* **19**, 3090–3099 (2007).
9. N. J. Stacey *et al.*, *Plant J.* **48**, 206–216 (2006).
10. A. De Muyt *et al.*, *PLOS Genet.* **5**, e1000654 (2009).
11. W. Li *et al.*, *Proc. Natl. Acad. Sci. U.S.A.* **101**, 10596–10601 (2004).
12. J. Puizina, J. Siroky, P. Mokros, D. Schweizer, K. Riha, *Plant Cell* **16**, 1968–1978 (2004).
13. K. D. Corbett, J. M. Berger, *Structure* **13**, 873–882 (2005).
14. M. Graille *et al.*, *Structure* **16**, 360–370 (2008).
15. C.-D. Hu, Y. Chinenov, T. K. Kerppola, *Mol. Cell* **9**, 789–798 (2002).
16. K. D. Corbett, P. Benedetti, J. M. Berger, *Nat. Struct. Mol. Biol.* **14**, 611–619 (2007).
17. T. Robert *et al.*, *Science* **351**, 943–949 (2016).
18. F. Hartung, H. Puchta, *Gene* **271**, 81–86 (2001).
19. Y. Yin *et al.*, *Proc. Natl. Acad. Sci. U.S.A.* **99**, 10191–10196 (2002).
20. F. Hartung *et al.*, *Curr. Biol.* **12**, 1787–1791 (2002).
21. K. Sugimoto-Shirasu, N. J. Stacey, J. Corsar, K. Roberts, M. C. McCann, *Curr. Biol.* **12**, 1782–1786 (2002).
22. M. D. Nichols, K. DeAngelis, J. L. Keck, J. M. Berger, *EMBO J.* **18**, 6177–6188 (1999).

ACKNOWLEDGMENTS

We are grateful to D. Gadelle, P. Forterre, R. Mercier, and R. Kumar for helpful discussions and constructive reading of the manuscript. We thank O. Grandjean and L. Gissot from the Imaging and Cytology platform of IJPB for providing help and technical support for the BiFC experiments. We also thank F. Hartung for providing the *TOP6B* cDNA and L. Gebbie (LKG Scientific Editing & Translation) for correcting the manuscript. IJPB benefits from the support of the Labex Saclay Plant Sciences–SPS (ANR-10-LABX-0040-SPS).

SUPPLEMENTARY MATERIALS

www.sciencemag.org/content/351/6276/939/suppl/DC1
Materials and Methods
Figs. S1 to S7
Tables S1 to S5
References (*23*–*48*)

25 September 2015; accepted 7 January 2016
10.1126/science.aad5196

Downloaded from on February 25, 2016

MEIOSIS

The TopoVIB-Like protein family is required for meiotic DNA double-strand break formation

T. Robert,[1] A. Nore,[1] C. Brun,[1] C. Maffre,[1] B. Crimi,[1] H.-M. Bourbon,[2]* B. de Massy[1]*

Meiotic recombination is induced by the formation of DNA double-strand breaks (DSBs) catalyzed by SPO11, the ortholog of subunit A of TopoVI DNA topoisomerase (TopoVIA). TopoVI activity requires the interaction between A and B subunits. We identified a conserved family of plant and animal proteins [the TOPOVIB-Like (TOPOVIBL) family] that share strong structural similarity to the TopoVIB subunit of TopoVI DNA topoisomerase. We further characterize the meiotic recombination proteins Rec102 (*Saccharomyces cerevisiae*), Rec6 (*Schizosaccharomyces pombe*), and MEI-P22 (*Drosophila melanogaster*) as homologs to the transducer domain of TopoVIB. We demonstrate that the mouse TOPOVIBL protein interacts and forms a complex with SPO11 and is required for meiotic DSB formation. We conclude that meiotic DSBs are catalyzed by a complex involving SPO11 and TOPOVIBL.

Sexual reproduction involves the formation of haploid gametes through a specialized cell cycle called meiosis. In most species, proper chromosome segregation at the first meiotic division requires connections between homologous chromosomes mediated by meiotic recombination. Meiotic recombination is initiated by programmed double-strand break (DSB) induction at the beginning of meiotic prophase and involves several evolutionarily conserved genes (*1*), including *Spo11*. This gene encodes a protein predicted to catalyze DSB formation, on the basis of two observations: (i) the similarity

[1]Institute of Human Genetics, UPR 1142 CNRS, 141 Rue de la Cardonille, 34396 Montpellier cedex 05, France. [2]Centre de Biologie du Développement, Université Fédérale de Toulouse, Paul Sabatier Campus, 118 Route de Narbonne, 31062 Toulouse, France.
*Corresponding author. E-mail: bernard.de-massy@igh.cnrs.fr (B.d.M.); henri-marc.bourbon@univ-tlse3.fr (H.-M.B.)

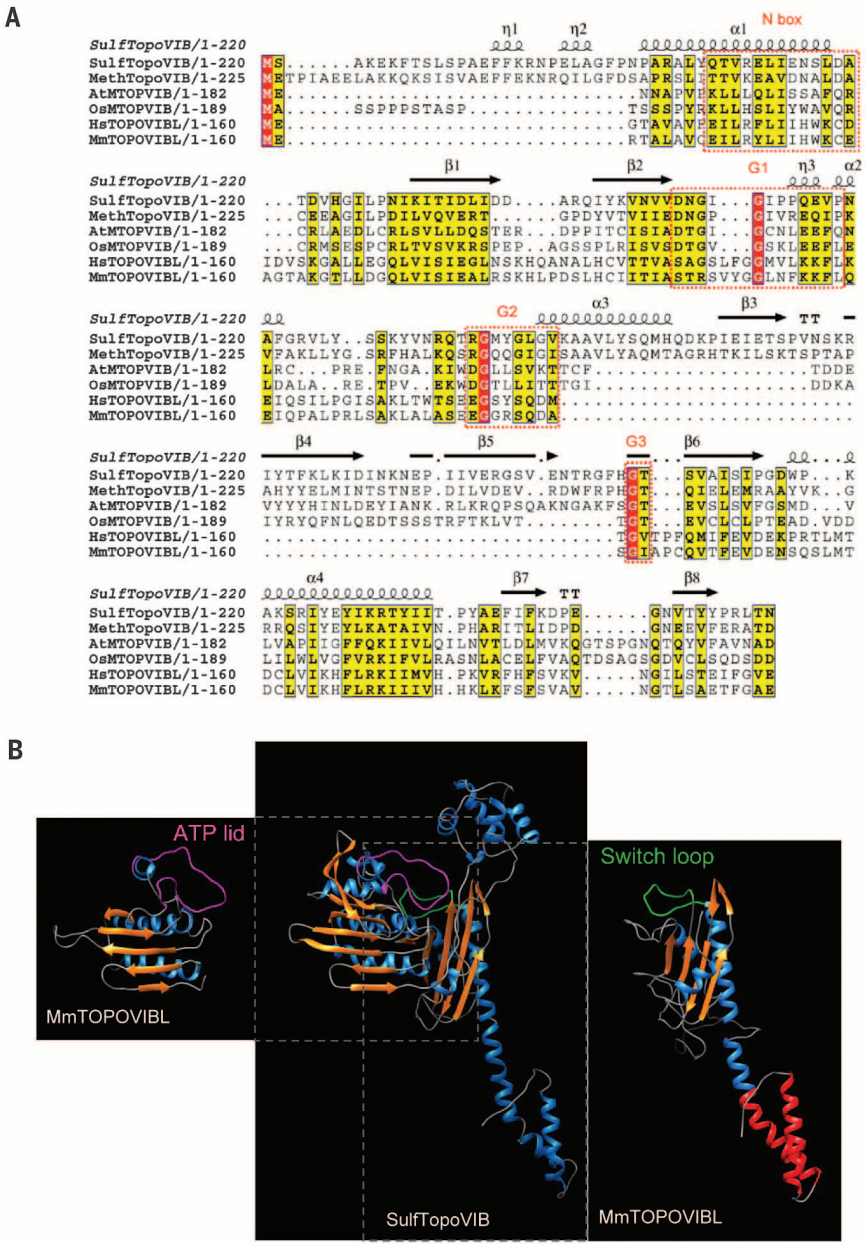

Fig. 1. TopoVIBL contains the conserved motifs and structure of the GHKL domain. (**A**) GHKL domain conservation among the B subunits of type IIB topoisomerases. Images show alignment of the sequences of the archaeal *S. shibatae* (Sulf) and *Methanosarcina mazei* (Meth) TopoVIB ATPase domains with their plant and mammalian TopoVIBL counterparts. AtMTOPVIB: *A. thaliana*; Os: *Oryza sativa*; Hs: *Homo sapiens* C11orf80; MmTOPOVIBL: *M. musculus Gm960* product. The secondary structural elements of SulfTopoVIB (Protein Data Bank ID: 2zbk_B) are shown above the alignment. The four core elements of the ATP-binding Bergerat fold (*11*) are indicated by red dashed boxes. Fully conserved amino acid residues are depicted in white on a red background, whereas partially conserved residues are in bold within yellow boxes (*18*). (**B**) Comparison of the models of the mouse TOPOVIBL GHKL and transducer domain structures with the *S. shibatae* TopoVIB structure from which they were derived. Orange, β strands; blue, α helices; pink, ATP lid; green, switch loops; red, helical regions predicted to interact with mouse SPO11.

between SPO11 and the catalytic subunit of the TopoVI family of type II DNA topoisomerases (TopoVIA), including the presence of an essential and conserved tyrosine involved in the transesterification reaction for DNA break formation (*2*), and (ii) the detection of covalent SPO11-DNA intermediates in meiotic cells (*3*, *4*). TopoVI belongs to the type IIB family of topoisomerases, and its activity promotes relaxation of negative and positive supercoiled DNA and DNA decatenation through cleavage and ligation cycles (*5*, *6*). TopoVI is composed of two subunits (A and B) that form a heterotetramer. Subunit B (TopoVIB) contains an adenosine triphosphate (ATP) binding domain and a transducer domain that communicates with the ATP binding site and interacts with TopoVIA (*7*, *8*). DNA cleavage by TopoVI requires both subunits and ATP binding (*9*). Subunit B, through ATP binding and hydrolysis, is involved in the conformational change of the complex and regulates the interaction between TopoVIA and TopoVIB homodimers for strand passage. The specific properties of this complex mechanism that are conserved in SPO11-catalyzed DSB formation remain unknown. Moreover, whether SPO11 functions alone or through association with another subunit has remained an open question for the past 18 years.

A conserved family of TopoVIB-Like proteins

While searching for a mammalian ortholog of the *MTOPVIB* gene, which is required for meiotic DSB formation in *Arabidopsis thaliana* (*10*), we identified a family of proteins sharing similarity with TopoVIB from archaea to chordates. Specifically, we performed PSI-BLAST (Position-Specific Iterative Basic Local Alignment Search Tool) searches, using *A. thaliana* MTOPVIB (AtMTOPVIB) as a query, to identify the product of the mouse gene *Gm960* (homolog of human C11orf80) that has four small regions displaying strong similarity to AtMTOPVIB (fig. S1A). Further alignments along full-length plant and mammalian proteins (fig. S1B) and analysis using HHpred (http://toolkit.tuebingen.mpg.de/hhpred) for detecting structural conservation enabled us to identify archaeal TopoVIB members with high significance (P = 99.1%, Expect value $E = 3.4 \times 10^{-9}$ for *Sulfolobus shibatae*). We named this protein family TopoVIB-Like (TopoVIBL), with plant and animal (chordates, ascidians, mollusks, and sea urchins) members (fig. S2) qualified on the basis of the conservation of the main TopoVIB domains: the GHKL domain (Bergerat fold), found in the GHKL (Gyrase, Hsp90, Histidine kinase, MutL) superfamily of adenosine triphosphatases (ATPases) (*11*), and the transducer domain (*7*, *8*) (Figs. 1 and 2 and fig. S1C). Despite an overall low level of identity and similarity [11 and 19%, respectively, between *Mus musculus* TOPOVIBL (encoded by *Gm960*, hereafter named *Top6bl*) and *S. shibatae* TopoVIB over 140 residues], key motifs (N box and the G1, G2, and G3 glycine-containing motifs) were identified within the GHKL domain, and the predicted secondary structure was conserved (Fig. 1A and fig. S3A). The Bergerat fold motifs play an important role in coordinating interaction with Mg^{2+} ions and with ATP; additionally, these motifs provide flexibility to the structure for ATP binding. On the basis of protein alignments, we predicted the structure of mouse TOPOVIBL that shares strong similarity with that of *S. shibatae* TopoVIB (Fig. 1B and fig. S3B) [root mean square deviation (RMSD) = 1.75 Å over 140 Cα atoms]. Comparison of the two structures highlighted the conservation of the ATP lid (a flexible loop that coordinates ATP binding), including a poorly conserved G2 motif. Some TopoVIB structural elements—such as the N-terminal helix (involved in dimerization) and

helix α3 (*12*)—were not detected in the TopoVIBL family, suggesting potential differences in the activity of the GHKL domain.

The transducer domain in the C-terminal region of TopoVIBL proteins also displayed marked similarity (conserved motifs or residues and structural elements) to that of TopoVIB, despite an overall high level of sequence divergence (11% identity and 22% similarity between mouse TOPOVIBL and *S. shibatae* TopoVIB over 206 residues) (Fig. 2A and fig. S4A). In particular, we detected stronger conservation at a motif that we named WOC (for WKxY-containing octapeptide) and over the C-terminal helices α11 and α12 that, in TopoVIB, interact with TopoVIA (*7*, *8*) (Fig. 2, A and B). A flexible loop was also predicted on the modeled structure of mouse TOPOVIBL in the region corresponding to the switch loop of TopoVIB that interacts with ATP bound to the GHKL domain, thus regulating phosphate release and complex conformation (*12*) (fig. S4B) (RMSD = 1.78 Å over 206 Cα atoms). The overall organization of the GHKL and transducer domains (the two primary domains of mouse TOPOVIBL) indicates that this protein shares structural similarity with *S. shibatae* TopoVIB, except for the intermediate helix–two turns–helix (H2TH) domain with unknown function (fig. S5, A and B). We also detected strong divergence at the C terminus of the proteins (C-terminal domain; see fig. S1B) after the two conserved helices of the transducer domain, with extensions of variable length among species.

Further PSI-BLAST searches for homologs in fungi led us to the identification of a predicted protein from the glomerale *Rhizophagus irregularis*, with conserved motifs overlapping the WOC motif and counterparts of archaeal β strand 14, as well as helices α11 and α12 described above, but without an obvious GHKL domain (fig. S6, A and B). The glomerale protein was then incorporated in a series of PSI-BLAST searches that identified fungal homologs in mucorales, basidiomycetes, and ascomycetes [including *Saccharomyces cerevisiae* (Rec102) and *Schizosaccharomyces pombe* (Rec6)], which contained the WOC motif, the switch loop, and the α11 and α12 helices (Fig. 2A and figs. S7, A and C, and S8). Rec102 and Rec6 (new annotation in fig. S7B) are required for meiotic DSB formation (*1*) and physically interact with Spo11 (*13*–*15*). This interaction is supported by the predicted structure of the Rec102-Spo11 complex (Fig. 2B). Additional PSI-BLAST searches and secondary structure predictions enabled detection of significant structural homologies between the TopoVIBL transducer domain and the evolutionarily conserved C-terminal region of *Drosophila melanogaster* MEI-P22 (fig. S9), which is also required for meiotic DSB formation (*16*). The absence of a detectable GHKL-type ATPase domain in fungal and insect homologs indicates that an alternative protein substitutes for this domain or that the molecular mechanism of DSB formation displays distinct properties in these species. Overall, structural modeling predicts an interaction between

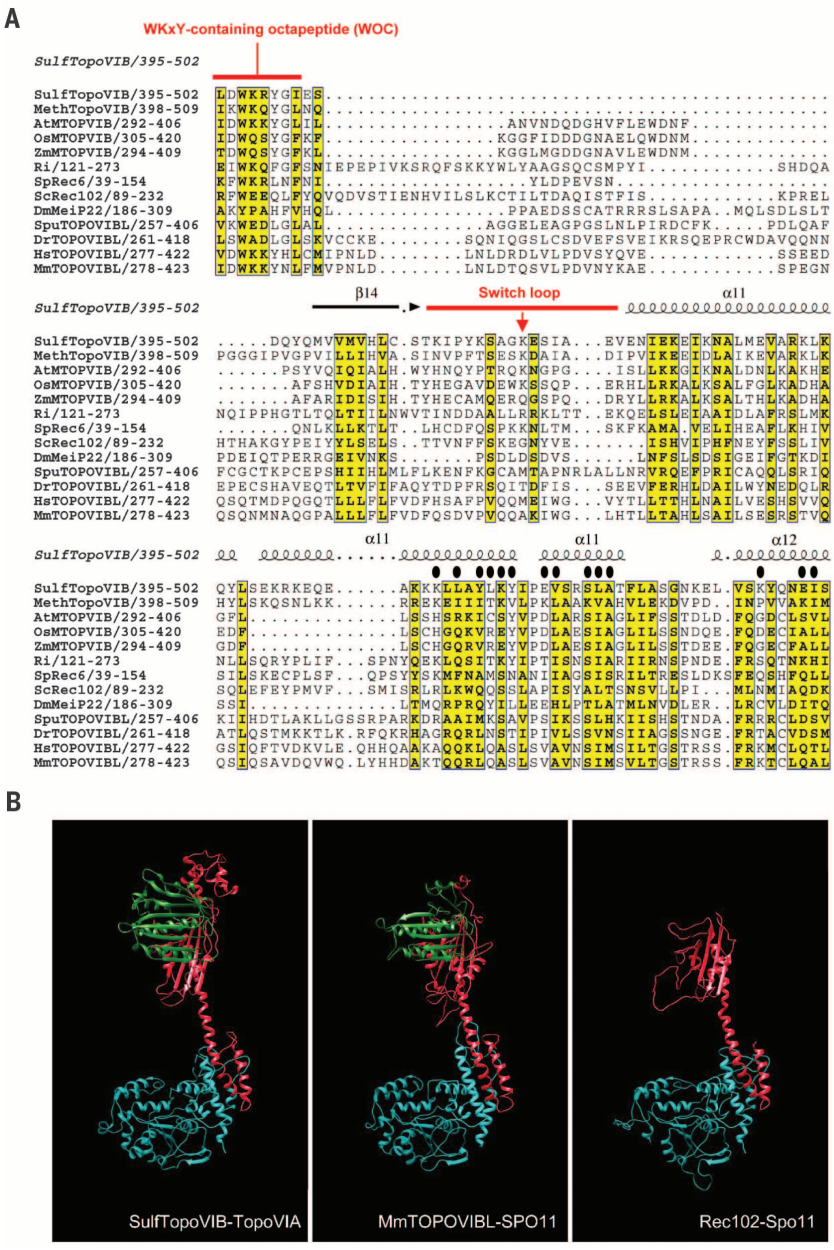

Fig. 2. The transducer domain of TopoVIBL and its interaction with Spo11 are widely conserved. (**A**) Transducer domain conservation. Images show alignment of the sequences of the long α-helical regions of archaeal TopoVIB transducer domains with their plant, fungal, and metazoan TopoVIBL counterparts. The secondary structural elements of SulfTopoVIB are shown above the alignment. The positions of the conserved WOC motif and the switch loop are indicated. Black ovals indicate the *S. shibatae* residues involved in the interaction with SulfTopoVIA. Zm, *Zea mays*; Ri, *R. irregularis*; Sp, *S. pombe*; Sc, *S. cerevisiae*; Dm, *D. melanogaster*; Spu, *Strongylocentrotus purpuratus*; Dr, *Danio rerio*. Other abbreviations and symbols are as in Fig. 1. (**B**) Comparison of the archaeal TopoVIA-B heterodimer structure (left) to mouse TOPOVIBL-SPO11β (middle) and yeast Rec102-Spo11 (right) models. Green, GHKL domain; red, transducer domain; blue, TopoVIA/Spo11.

TopoVIBL and SPO11 to form a heterodimer (Fig. 2B), and potentially a heterotetramer, for DSB formation.

Mouse TOPOVIBL and SPO11 interact

The conserved features and the structure analyses presented above predict that TOPOVIBL interacts directly with SPO11. In mice, there are two major SPO11 splice variants (α and β). SPO11β contains an additional 38 amino acids in the N terminus that correspond to the TopoVIA region interacting with TopoVIB (*7*, *8*). Analysis of mice expressing only *Spo11β* showed that this isoform is proficient in meiotic DSB formation (*17*). Using the yeast two-hybrid assay, we found that mouse TOPOVIBL interacts with SPO11β but not with SPO11α. This highlights the essential role of the aforementioned SPO11β 38–amino

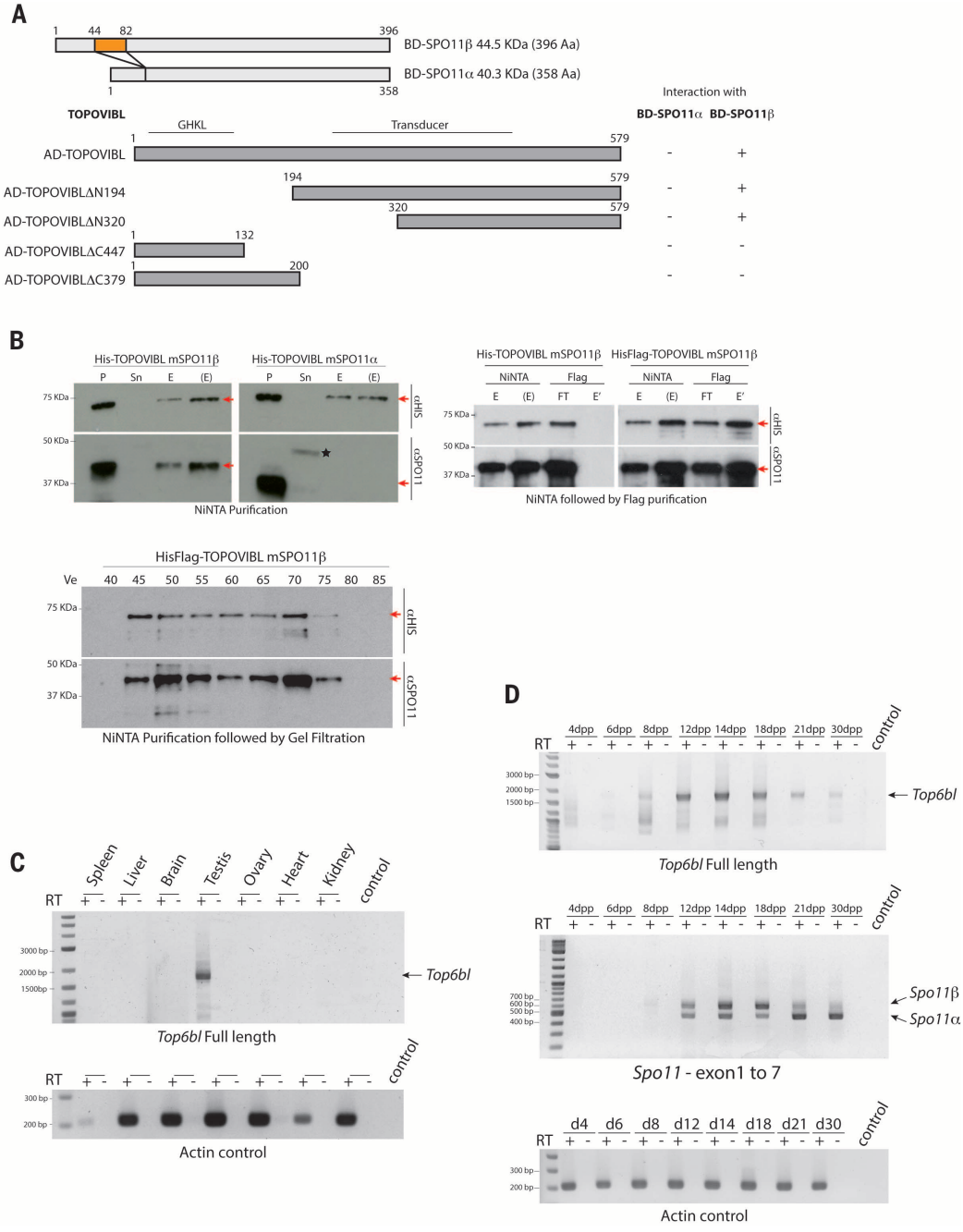

Fig. 3. Mouse TOPOVIBL interacts with SPO11 and is expressed in testis upon entry into meiosis. (**A**) TOPOVIBL C-terminal region interacts with SPO11β in a yeast two-hybrid assay. TOPOVIBL and SPO11 were fused to Gal4AD (AD) and Gal4BD (BD), respectively. The 38 residues specific to SPO11β are shown in orange, and the positions of the GHKL and transducer domains are indicated above full-length TOPOVIBL. – denotes no interaction; + indicates interaction. Aa, amino acids. (**B**) TOPOVIBL and SPO11β form a soluble complex of 150 to 250 kDa. (Top panels) His_6-TOPOVIBL and SPO11β or SPO11α, as well as His_6-Flag-TOPOVIBL and SPO11β, were coexpressed in *E. coli* and affinity-purified. P, pellet; Sn, supernatant; E, nickel nitrilotriacetic acid (NiNTA) elution; (E), concentrated NiNTA elution; FT, flow-through; E′, Flag elution. (Bottom panel) His_6-Flag-TOPOVIBL and SPO11β were affinity-purified, and proteins were analyzed by gel filtration chromatography. Anti-His or anti-SPO11 antibodies were used for detections. (**C**) *Top6bl* expression by RT-PCR using RNA extracted from various adult mouse tissues. Control, sample without RNA; RT with (+) or without (–) reverse transcriptase. Actin was used as a positive control of PCR amplification (bottom panel). (**D**) RT-PCR analysis of *Top6bl* (top panel) and *Spo11β* and *Spo11α* (middle panel) in RNA from testes of mice at various ages (4 to 30 dpp). (Bottom panel) Controls were as in (C).

acid region, which overlaps with the N-terminal α helix, in such interaction. By deletion analysis, we also determined that the TOPOVIBL C-terminal region, which includes the transducer domain, is involved in the interaction (Fig. 3A and figs. S10 and S11). Moreover, coexpression of TOPOVIBL and SPO11β in *Escherichia coli* suggested the formation of a complex. Affinity purification of His-tagged TOPOVIBL allowed the copurification of TOPOVIBL with SPO11β but not with SPO11α and was dependent on the presence of the tag used (Fig. 3B, top panels). Furthermore, upon gel filtration chromatography and glycerol gradient sedimentation, the size of the complex including TOPOVIBL and SPO11β was estimated at 150 to 250 kDa, compatible with the assembly of a heterotetramer (217 kDa) (Fig. 3B, bottom panel, and fig. S12).

Top6bl is required for meiotic DSB formation

To evaluate *Top6bl* biological function during meiosis, we first assessed its expression in tissues from adult mice. *Top6bl* was expressed in testis but not in other tissues (Fig. 3C and fig. S13A). The temporal expression profile of genes during meiosis can be determined by taking advantage of the synchronous first wave of entry of spermatogonia into meiosis, which takes place ~8 days postpartum (dpp). Spermatocytes then progress into meiotic prophase from 10 to 20 dpp and reach the first meiotic division around 21 dpp. *Top6bl* expression could not be detected in testis RNA from mice on 4 and 6 dpp but only from 8 dpp onward, with a peak of expression around 12 to 14 dpp, at the beginning of meiotic prophase. This temporal pattern is similar to that of *Spo11β* expression (Fig. 3D). In female mice, *Top6bl* transcripts were detected in embryonic ovaries when oocytes proceeded through meiotic prophase (fig. S13B). Sequencing of the reverse transcription polymerase chain reaction (RT-PCR) products led us to revise the annotation of the mouse reference genome, yielding a protein of 579 amino acids and 63.8 kDa (fig. S14).

To investigate whether *Top6bl* has a role in meiotic DSB formation in mice, we generated point mutations in exon 9 of the *Top6bl* gene by means of CRISPR-Cas9 DSB targeting. Upon deletion or insertion, this led to a frameshift and a potential truncated protein of 279 amino acids without the transducer domain (*18*) (fig. S15). Male *Top6bl*$^{-/-}$ mice developed normally and reached adulthood but had smaller testes compared with wild-type (WT) mice (table S1). No phenotypic alteration could be detected in heterozygous *Top6bl*$^{+/-}$ mice. Histological analysis of *Top6bl*$^{-/-}$ testis sections showed that spermatogenesis was disrupted in most seminiferous tubules. Spermatogonia were present at the periphery of tubules like in WT mice; however, spermatocytes were strongly depleted and spermatids could not be detected, suggesting a defect during meiotic prophase (Fig. 4A).

To more precisely identify the meiotic defect, we monitored meiotic prophase by immunocytochemical analysis of spread spermatocytes using various markers to detect potential alterations in DSB formation or repair. Based on the phenotypes of *Spo11* mutant mice (*19*, *20*), defects in DSB formation have several consequences during prophase, particularly the reduction of phosphorylated H2AFX (γH2AFX) due to defective ATM kinase activation. The lack of DSBs also results in defective loading of DSB repair proteins (such as RPA and DMC1 that bind to single-stranded DNA present on processed DSB ends), as well as a defect in homologous synapsis (*21*). *Top6bl*$^{-/-}$ spermatocytes at leptotene- and zygotene-like stages showed reduced γH2AFX levels and undetectable RPA foci, consistent with a deficiency in DSB formation (Fig. 5A and fig. S16B). The nuclear localization of γH2AFX was also altered. In *Top6bl*$^{-/-}$ spermatocytes, γH2AFX did not accumulate specifically around the sex chromosomes but instead was enriched in subdomains (Fig. 5A) that could correspond to unsynapsed axes. Monitoring the loading of SYCP1, a component of the central element of the synaptonemal complex, indicated that synapsis formation was strongly altered in *Top6bl*$^{-/-}$ spermatocytes. Many chromosomes remained unsynapsed, and the axes containing synapsed stretches were often involved in interactions with several partners, suggesting interactions between nonhomologous chromosomes (Fig. 5B and fig. S16A). The presence of unsynapsed chromosomes is known to trigger the MSUC (meiotic silencing of unsynapsed chromatin) response, which leads to accumulation of γH2AFX on unsynapsed axes, even in the absence of meiotic DSB formation (*22*, *23*), which is thus compatible with the detection of residual γH2AFX in *Top6bl*$^{-/-}$ spermatocytes. Similar defects in DSB and homologous synapsis formation were observed in a *Top6bl*$^{-/-}$ mutant generated independently (*18*) (founder 53614, figs. S15 and S17). To evaluate progression into meiotic prophase, we determined the expression of the testis-specific histone H1 variant (H1t) that is normally detected from mid-pachytene. *Top6bl*$^{-/-}$ spermatocytes were devoid of or showed only low H1t expression, indicating failure to progress through prophase and arrest before or at mid-pachytene

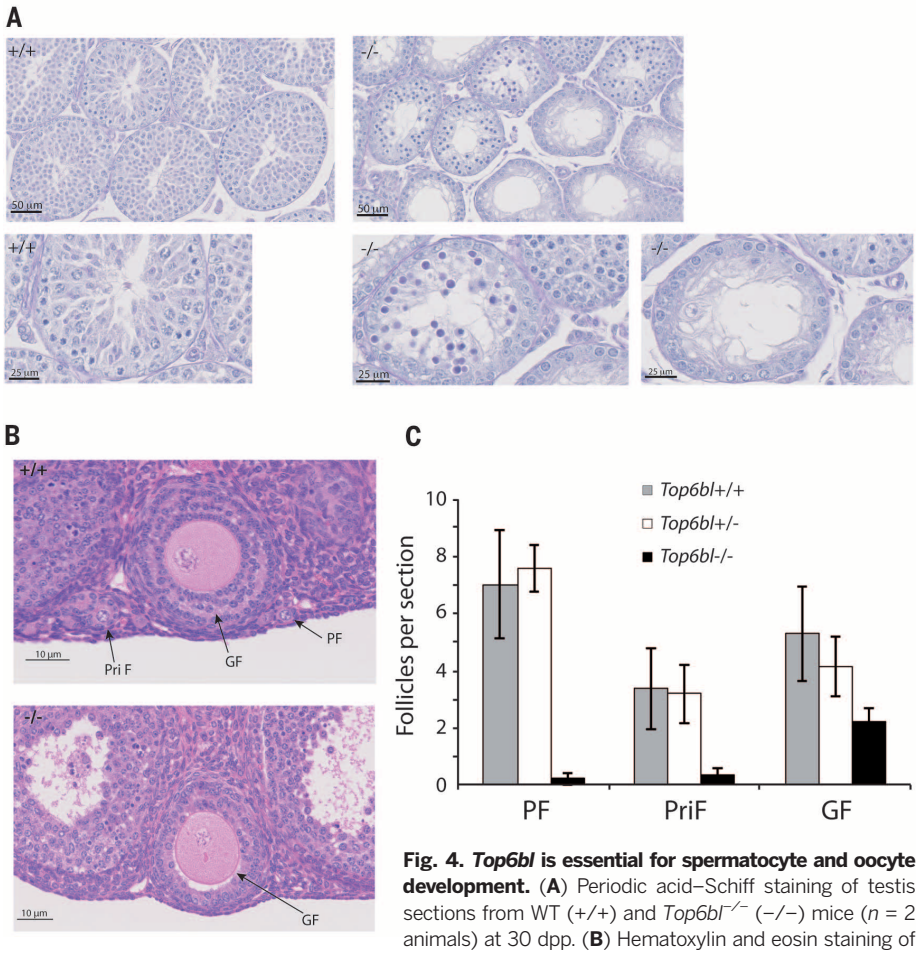

Fig. 4. *Top6bl* is essential for spermatocyte and oocyte development. (**A**) Periodic acid–Schiff staining of testis sections from WT (+/+) and *Top6bl*$^{-/-}$ (−/−) mice (n = 2 animals) at 30 dpp. (**B**) Hematoxylin and eosin staining of ovary sections from WT (+/+) (n = 1) and *Top6bl*$^{-/-}$ (−/−) (n = 4) mice at 30 dpp. PF, primordial follicles; PriF, primary follicles; GF, growing follicles. (**C**) Mean number with SD of primordial follicles, primary follicles, and growing follicles in *Top6bl*$^{+/+}$ (n = 1) (gray bars), *Top6bl*$^{+/-}$ (n = 1) (white bars), and *Top6bl*$^{-/-}$ (n = 4) (black bars) ovaries at 30 dpp. *Top6bl*$^{+/+}$ and *Top6bl*$^{+/-}$ were not significantly different (z test, P > 0.05), whereas *Top6bl*$^{+/+}$ and *Top6bl*$^{-/-}$ were statistically different (z test, P < 0.0002).

(fig. S18). This finding also provides a possible explanation for the lack of late spermatocytes and later stages in testis sections (Fig. 4A). Notably, all phenotypes observed in *Top6bl*$^{-/-}$ spermatocytes are those predicted for a DSB formation defect and are identical to those reported in *Spo11*$^{-/-}$ mice (*19*,*20*). DSB formation also requires *Mei1* and *Mei4*, which may act indirectly on *Spo11* activity through unknown mechanisms (*24*). MEI4 localization on chromosome axes is *Mei1*-dependent and is correlated and required for efficient DSB activity (*25*, *26*). As MEI4 localization was similar in *Top6bl*$^{-/-}$ and WT mice at leptotene (Fig. 5C), we could exclude the hypothesis that *Top6bl* indirectly affects DSB formation by altering MEI4 localization. Moreover, in *Top6bl*$^{-/-}$ spermatocytes at zygotene-like stages, MEI4 foci were persistent, as in *Spo11*$^{-/-}$ spermatocytes but unlike in WT spermatocytes, where they disappear upon DSB formation (*26*). MEI4 persistence in *Top6bl*$^{-/-}$ spermatocytes thus provides additional independent evidence for the lack of DSB formation. Finally, histological analysis of ovaries from *Top6bl*$^{-/-}$ females at 30 dpp showed that they were largely depleted of primordial and primary follicles compared with WT ovaries (Fig. 4, B and C). We therefore conclude that *Top6bl* is required for meiotic DSB formation during male and female meiosis.

As evidenced by our study and the one performed on *A. thaliana* (*10*), the conserved structure and function of TOPOVIBL proteins demonstrate the notable evolutionary and biochemical relationship between the type IIB family of topoisomerases and meiotic DSB activity. On the basis of the phylogeny of several meiotic functions, it has become clear that sexual reproduction and meiosis have evolved very early during eukaryote evolution (*27*). As proposed for SPO11, the TOPOVIB family could also have expanded and diversified by gene duplication (*28*). Moreover, the presence of a TOPOVIBL subunit that interacts with SPO11 dramatically changes our view of how the biochemical step of DSB formation may work: In TopoVI, the B subunit is involved in strand passage and controlling dimer interfaces (*29*, *30*). Although the involvement of a second DNA duplex is not expected for a SPO11-induced cleavage, the TOPOVIBL subunit may be involved in the regulation of DNA cleavage, through the direct

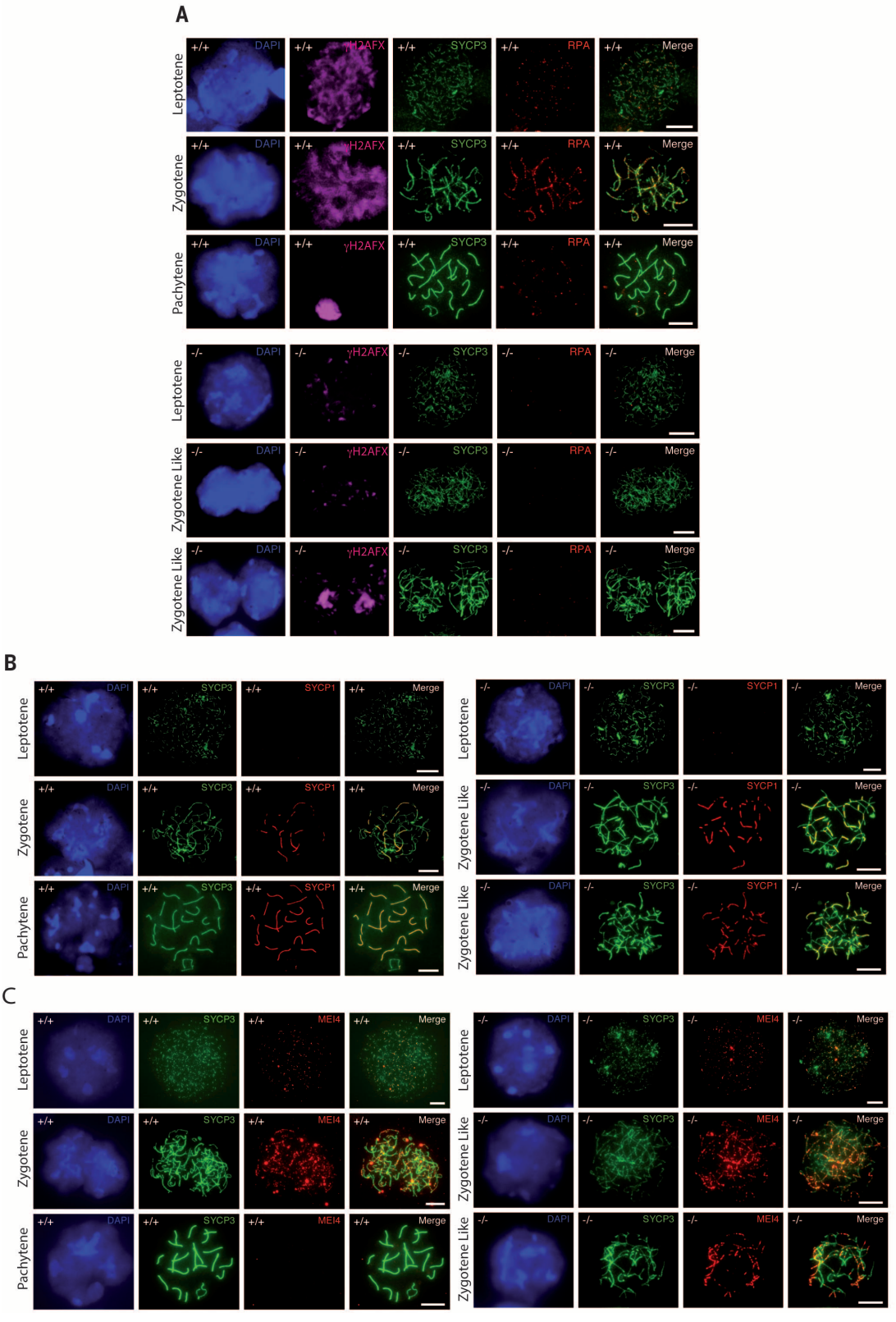

Fig. 5. *Top6bl* is required for meiotic DSB formation. (**A**) Immunocytochemical analysis with anti-γH2AFX, anti-SYCP3, and anti-RPA antibodies of spread spermatocytes from WT (+/+) and *Top6bl*$^{-/-}$ (−/−) mice (n = 2) at 30 dpp. Merged images of anti-SYCP3 and anti-RPA staining are shown. Scale bars, 10 μm. DAPI, 4′,6-diamidino-2-phenylindole. (**B**) Immunocytochemical analysis with anti-SYCP3 and anti-SYCP1 antibodies of spread spermatocytes from (+/+) and (−/−) mice (n = 2) at 30 dpp. Scale bars, 10 μm. (**C**) Immunocytochemical analysis with anti-SYCP3 and anti-MEI4 antibodies of spread spermatocytes from (+/+) and (−/−) mice (n = 2) at 30 dpp. Scale bars, 10 μm.

interaction between the transducer domain and SPO11. The GHKL domain may be involved in the stabilization of the complex upon DNA cleavage, which could allow the reversibility of the reaction. However, SPO11 monomers may not need to be stably interacting upon DSB formation, and TOPOVIBL proteins that lack the GHKL domain, as observed in yeasts and *Drosophila*, may have lost the ability to maintain the complex upon DNA cleavage. As opposed to a TopoII-induced DNA cleavage, the challenge for SPO11-induced breaks is to be properly engaged in DSB

repair by homologous recombination for maintenance of the stability of the genome, which also requires the coordinated involvement of several additional partners.

REFERENCES AND NOTES

1. B. de Massy, *Annu. Rev. Genet.* **47**, 563–599 (2013).
2. A. Bergerat *et al.*, *Nature* **386**, 414–417 (1997).
3. S. Keeney, C. N. Giroux, N. Kleckner, *Cell* **88**, 375–384 (1997).
4. M. J. Neale, J. Pan, S. Keeney, *Nature* **436**, 1053–1057 (2005).
5. D. Gadelle, J. Filée, C. Buhler, P. Forterre, *BioEssays* **25**, 232–242 (2003).
6. D. Gadelle, M. Krupovic, K. Raymann, C. Mayer, P. Forterre, *Nucleic Acids Res.* **42**, 8578–8591 (2014).
7. K. D. Corbett, P. Benedetti, J. M. Berger, *Nat. Struct. Mol. Biol.* **14**, 611–619 (2007).
8. M. Graille *et al.*, *Structure* **16**, 360–370 (2008).
9. C. Buhler, D. Gadelle, P. Forterre, J. C. Wang, A. Bergerat, *Nucleic Acids Res.* **26**, 5157–5162 (1998).
10. N. Vrielynck *et al.*, *Science* **351**, 939–943 (2016).
11. R. Dutta, M. Inouye, *Trends Biochem. Sci.* **25**, 24–28 (2000).
12. K. D. Corbett, J. M. Berger, *Structure* **13**, 873–882 (2005).
13. K. Jiao, L. Salem, R. Malone, *Mol. Cell. Biol.* **23**, 5928–5938 (2003).
14. S. Maleki, M. J. Neale, C. Arora, K. A. Henderson, S. Keeney, *Chromosoma* **116**, 471–486 (2007).
15. T. Miyoshi *et al.*, *Mol. Cell* **47**, 722–733 (2011).
16. H. Liu, J. K. Jang, N. Kato, K. S. McKim, *Genetics* **162**, 245–258 (2002).
17. L. Kauppi *et al.*, *Science* **331**, 916–920 (2011).
18. Materials and methods are available as supplementary materials on *Science* Online.
19. F. Baudat, K. Manova, J. P. Yuen, M. Jasin, S. Keeney, *Mol. Cell* **6**, 989–998 (2000).
20. P. J. Romanienko, R. D. Camerini-Otero, *Mol. Cell* **6**, 975–987 (2000).
21. F. Baudat, Y. Imai, B. de Massy, *Nat. Rev. Genet.* **14**, 794–806 (2013).
22. J. M. Turner *et al.*, *Nat. Genet.* **37**, 41–47 (2005).
23. P. S. Burgoyne, S. K. Mahadevaiah, J. M. Turner, *Nat. Rev. Genet.* **10**, 207–216 (2009).
24. R. Kumar, B. De Massy, *Genes* **1**, 521–549 (2010).
25. R. Kumar, H. M. Bourbon, B. de Massy, *Genes Dev.* **24**, 1266–1280 (2010).
26. R. Kumar *et al.*, *J. Cell Sci.* **128**, 1800–1811 (2015).
27. M. A. Ramesh, S. B. Malik, J. M. Logsdon Jr., *Curr. Biol.* **15**, 185–191 (2005).
28. S. B. Malik, M. A. Ramesh, A. M. Hulstrand, J. M. Logsdon Jr., *Mol. Biol. Evol.* **24**, 2827–2841 (2007).
29. A. D. Bates, J. M. Berger, A. Maxwell, *Nucleic Acids Res.* **39**, 6327–6339 (2011).
30. B. H. Schmidt, N. Osheroff, J. M. Berger, *Nat. Struct. Mol. Biol.* **19**, 1147–1154 (2012).

ACKNOWLEDGMENTS

We thank M. Grelon for communicating information about the sequence of the *A. thaliana MTOPVIB* gene before publication, D. Gadelle and P. Forterre for numerous discussions and technical advice, all laboratory members for stimulating discussions and suggestions, M. A. Handel for the anti-H1t antibody, J. Cau from Montpellier RIO Imaging for image analysis, and the Cryopréservation Distribution Typage Archivage Animal Transgénèse et Archivage d'Animaux Modèles and Réseau d'Histologie Expérimentale de Montpellier facilities for services. H.-M.B. was funded by grants from CNRS. B.d.M. was funded by grants from CNRS and the European Research Council Executive Agency under the European Community's Seventh Framework Programme [FP7/2007-2013 grant agreement no. 322788]. T.R., H.-M.B., and B.d.M. supervised the project and wrote the manuscript. T.R., H.-M.B, A.N., C.M., B.C., and C.B. performed experiments.

SUPPLEMENTARY MATERIALS

www.sciencemag.org/content/351/6276/943/suppl/DC1
Materials and Methods
Figs. S1 to S18
Tables S1 and S2
References (*31*–*33*)

26 September 2015; accepted 7 January 2016
10.1126/science.aad5309

REPORTS

ORGANIC LEWIS ACIDS

Asymmetric Lewis acid organocatalysis of the Diels–Alder reaction by a silylated C–H acid

Tim Gatzenmeier,* Manuel van Gemmeren,* Youwei Xie, Denis Höfler, Markus Leutzsch, Benjamin List†

Silylium ion equivalents have shown promise as Lewis acid catalysts for a range of important C–C bond-forming reactions. Here we describe chiral C–H acids that upon in situ silylation, generate silylium-carbanion pairs, which are extremely active Lewis acid catalysts for enantioselective Diels–Alder reactions of cinnamates with cyclopentadiene. Enantiomeric ratios of up to 97:3 and diastereomeric ratios of more than 20:1 are observed across a diverse set of substitution patterns with 1 mole percent (mol %) of C–H acid catalyst and 10 mol % of a silylating reagent. The results show promise for broad applications of such C–H acid–derived silylium ion equivalents in asymmetric Lewis acid catalysis.

Lewis acid catalysis enables key reactions in chemical synthesis, such as the Diels–Alder, Friedel–Crafts, and various aldol, Mannich, and Michael reactions. Consequently, substantial efforts have been directed toward enantiopure Lewis acids, which have enabled important asymmetric variations of such reactions (*1*, *2*). Despite the plethora of elegant catalysts and methodologies developed in this context, a key limitation of enantioselective Lewis acid catalysis is the frequent need for relatively high catalyst loadings, which result from issues such as insufficient Lewis acidity (keeping some substrate classes completely out of reach), product inhibition, hydrolytic instability, and the competition with nonenantioselective background catalysis (*3*, *4*). With respect to these issues, we are now envisioning an alternative approach to asymmetric Lewis acid catalysis (Fig. 1). Conventional chiral Lewis acids typically consist of a metal (loid) complex with chiral ligands or substituents (*5*–*9*). Their activity can often be increased by rendering the complexes cationic and combining them with weakly coordinating, achiral counteranions. By inverting the chiral entities within the ion pair, a conceptually different strategy results.

We have recently developed in situ silylated disulfonimide Lewis acid organocatalysts for highly enantioselective Mukaiyama-type reactions involving silylated nucleophiles with catalyst loadings as low as 10 parts per million (ppm) (*10*–*15*). As an example of asymmetric counteranion-directed catalysis (ACDC) (*16*–*19*), these reactions proceed via silylation of an electrophile, generating a cationic reactive species that ion pairs with an enantiopure counteranion and reacts with a silylated nucleophile. We became interested in expanding this silylium ion–ACDC to, in principle, all types of Lewis acid–catalyzed reactions, including those that do not involve stoichiometric amounts of silylated reagents. We hypothesized that the use of a suitable enantiopure precatalyst and a catalytic amount of a silylating reagent should effect the formation of a catalytically competent silylium ion equivalent. If successful, silylium ion–ACDC, catalytic in silicon, would provide an efficient approach to alleviating challenges in modern asymmetric Lewis acid catalysis. Here we report the realization of this idea. We have developed chiral C–H acids that, upon in situ silylation, become extremely active Lewis acid catalysts for highly enantioselective Diels–Alder reactions of cinnamates with cyclopentadiene.

Enantioselective Diels–Alder reactions of α,β-unsaturated ester dienophiles are generally challenging, and only a few have been reported. For example, Ghosez applied chiral silylium ion equivalents in combination with triflimide as achiral counteranion to catalyze Diels–Alder reactions of α,β-unsaturated esters with moderate enantioselectivity (*6*, *7*). Corey has reported that triflimide-activated chiral oxazaborolidine Lewis acids (*8*, *9*) give excellent results with acrylates and crotonates as dienophiles. Cinnamates, with their highly conjugated π-electron system, represent an even more challenging substrate class for asymmetric Diels–Alder reactions, and in a reported example, activated trifluoroethyl cinnamate required 20 mole percent (mol %) of the protonated oxazaborolidine catalyst to react (*9*, *20*).

Given the superb reactivity observed in silylium ion–ACDC in Mukaiyama-type reactions (*10*, *13*), we were curious to explore if our strategy would also be suitable for the activation of cinnamates in enantioselective Diels–Alder reactions. We anticipated that a highly Brønsted-acidic precatalyst

Max-Planck-Institut für Kohlenforschung, Kaiser-Wilhelm-Platz 1, 45470 Mülheim an der Ruhr, Germany.
*These authors contributed equally to this work. **†Corresponding author. E-mail: list@kofo.mpg.de**

Downloaded from on February 25, 2016

would be activated in situ with a catalytic amount of a silylating reagent such as a silyl ketene acetal. The resulting silylium ion equivalent would then activate the cinnamate, while he chiral counteranion would induce the enantioselectivity.

We began our studies by exploring various previously developed chiral disulfonimide precatalysts in the reaction of cinnamate **1a** with cyclopentadiene **2** (Fig. 2A). Disappointingly, their observed high activity was insufficient toward this substrate class, indicating that catalysts of even higher Lewis acidity would be required (see table S3 for further details). Inspired by the activity trends known for achiral silylium ion equivalents in solution (Fig. 2B), which indicate that the use of a carbon-centered counteranion leads to higher Lewis acidities (*21*), we became interested in developing chiral, enantiopure C–H acids as precatalysts. After considerable synthetic efforts, we accessed compounds of sufficient C–H acidity and could identify binaphthyl-allyl-tetrasulfones (BALTs) as promising candidates for the enantioselective catalysis of our target reaction (Fig. 2C). These catalysts were designed based on the notion that the Lewis acidity of the silylium ion equivalent should increase on rendering the catalyst-derived counteranion less Lewis basic. This goal was achieved by exploiting the principle of vinylogy: In BALT anions, the negative charge is highly delocalized (onto eight oxygen atoms and two carbon atoms), leading to a low charge density and thus Lewis basicity on every position of the anionic substructure, and therefore to the excellent catalytic activities observed with this catalyst class.

The optimized reaction conditions involve the use of a 9-fluoroenylmethyl cinnamate ester, which enables higher stereoselectivities but is not required for catalytic activity; 9-phenanthryl groups as 3,3′-substituents on the catalyst; and the use of only 1 mol % of catalyst **6b**, alongside 10 mol % of silyl ketene acetal **4b** to effect the initial catalyst silylation. The Brønsted acidic catalyst **6b** itself was found to be inactive for this transformation (see table S9 for further details). Under the optimal conditions, our model reaction proceeded smoothly, giving the desired product **3a** in 94% yield and an enantiomeric ratio (e.r.) of 97:3 (Fig. 3). Using these conditions, we proceeded to explore the scope of the reaction. We found that the transformation proceeds smoothly in the presence of both strongly electron-donating substituents (**3b**: 93%; e.r. = 95:5), as well as strongly electron-withdrawing groups (**3c**: 90%; e.r. = 95:5). Halide substituents were well tolerated, and the corresponding products **3d–3g** were all obtained in high to excellent yields and with excellent stereocontrol. We proceeded to assess the influence of regioisomeric substitution on the cinnamate substrate and found that methyl substituents in para, meta, and ortho position are tolerated, and the corresponding products **3h–j** were obtained with yields ≥90% and enantiomeric

Conventional approaches to enantioselective Lewis acid catalysis:

- chirality directly attached to Lewis acid
- complexation between chiral catalyst and substrate
- achiral counteranion present, if Lewis acid is cationic

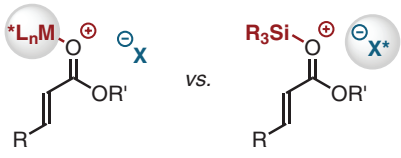

Asymmetric counteranion-directed catalysis with catalytic silylium ion equivalents (silylium ion–ACDC):

- chirality at the counteranion
- Coulomb interaction between chiral anion and activated substrate
- silylium ion equivalent = highly active Lewis acid catalyst

Fig. 1. Comparing silylium ion–ACDC with conventional approaches to enantioselective Lewis acid catalysis.

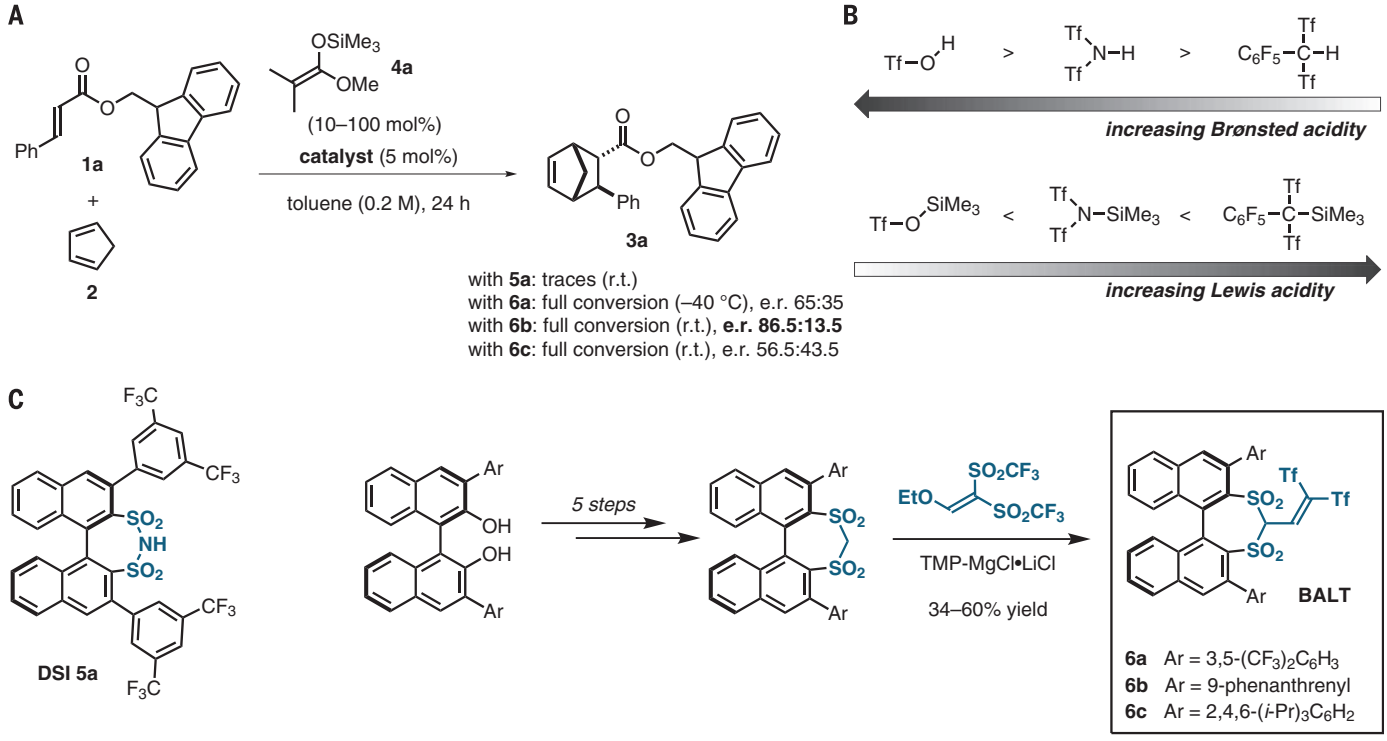

Fig. 2. Initial catalyst screening and optimization. (**A**) Model reaction of an unactivated cinnamate ester **1a** with cyclopentadiene **2**. (**B**) Trends of Lewis and Brønsted acidities in solution for silylium ion equivalents bearing CF_3SO_2 (Tf)–substituted O-, N-, and C-centered counteranions and the corresponding Brønsted acids (*21*). (**C**) Precatalysts: disulfonimides (DSI) and chiral C–H acids (BALTs).

ratios ≥95.5:4.5. To further demonstrate the tolerance of substituents in various positions of the aryl-ring, the meta-nitro-substituted product **3k** was prepared in 91% yield and with an e.r. of 97:3, a result that compares very well to the one obtained for the para-substituted analog **3c**. Furthermore, we studied substrates with extended π-surfaces, and the corresponding 1- and 2-naphthyl–substituted products (**3l** and **3m**) were obtained with excellent results. Finally, we synthesized the 2-furyl– and 2-thiophenyl–substituted products **3n** and **3o**, which were both obtained in good yields and with high stereoselectivities, thus revealing that our methodology can be applied to hetero-aromatic substrates. All Diels–Alder adducts described in this work were obtained with excellent endo-diastereoselectivities (d.r. >25:1 in virtually all cases).

Having studied the scope of our reaction, we were interested in probing the mode of action proposed at the outset of our studies. To do so, we applied ^{1}H nuclear magnetic resonance (NMR) spectroscopy to monitor the in situ activation of the BALT catalyst, using the 3,3′-unsubstituted variant **6d** and silyl ketene acetal **4a** as model compounds (Fig. 4A). We found that over a period of ~70 min, the signals corresponding to the precatalyst disappeared, and a new species emerged lacking the signal corresponding to the acidic proton (H-1). In comparison to the precatalyst (two diastereotopic naphthyl groups with sharp ^{1}H NMR signals), the newly formed species showed relatively broad signals at room temperature. Increasing the temperature to 55°C allowed us to observe pseudohomotopic naphthyl groups in the activated species, an observation in good agreement with expectations for the formation of a silylium BALT–anion pair such as **7d**. The anionic character of the BALT motif in this activated species was corroborated by the spectral similarities to the features observed for a BALT-derived tetraalkyl ammonium salt (see fig. S6 for further details).

On the basis of these observations and previous studies (*22*–*25*), we propose a catalytic cycle (Fig. 4B), which involves ionic species and thus represents a case of asymmetric counteranion-directed catalysis.

After the initial catalyst activation, achieved via protodesilylation of a catalytic amount of silyl ketene acetal **4**, the resulting silylium BALT–anion pair **7** could exchange the Lewis base, thus forming species **9**, which is activated by lowering of the lowest unoccupied molecular orbital (LUMO-lowering). Traces of water that may be present in the reaction mixture will presumably immediately hydrolyze ion pair **7**, furnishing C–H acid **6**, which in turn is reactivated by silyl ketene acetal **4**. The Diels–Alder reaction of **9** with cyclopentadiene (**2**), proceeding through a transition state such as **A**$^{\neq}$, would then result in

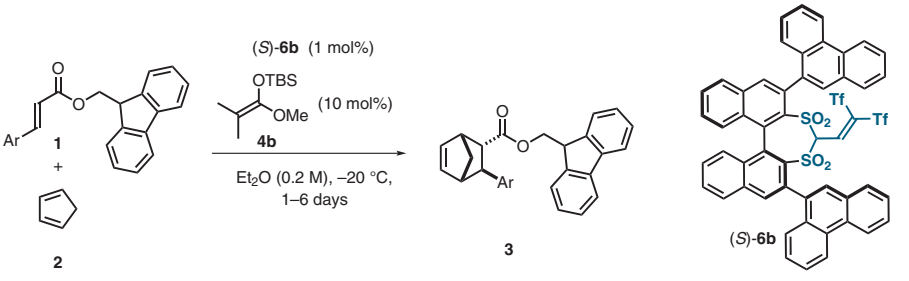

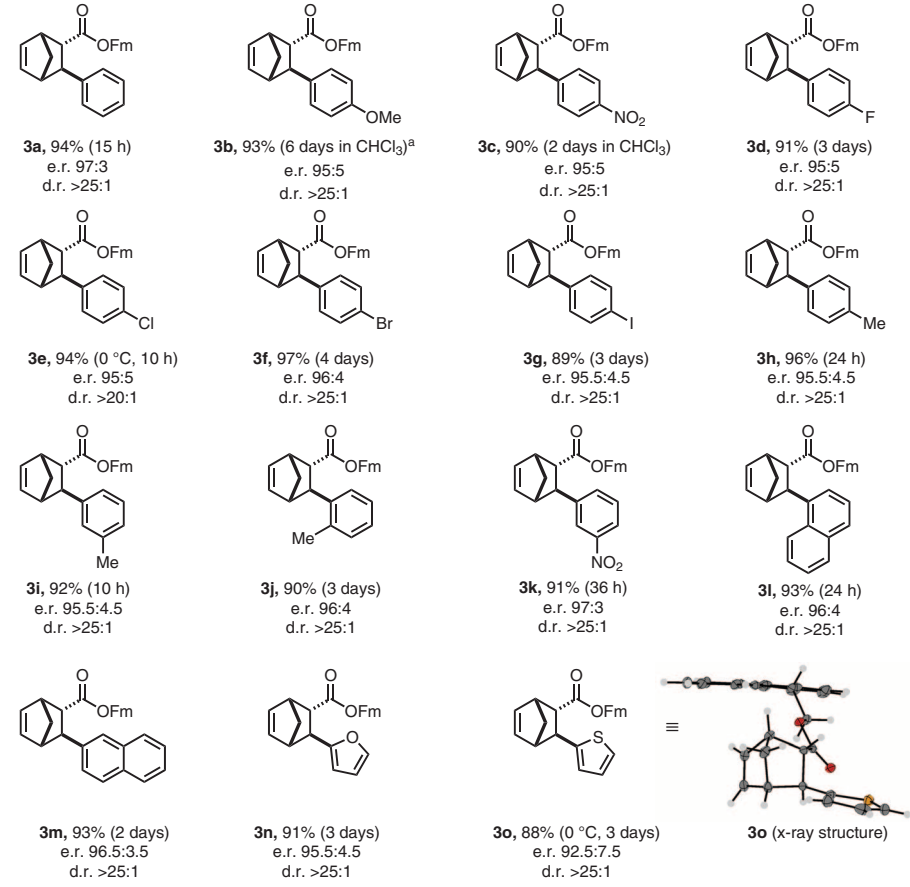

3a, 94% (15 h)
e.r. 97:3
d.r. >25:1

3b, 93% (6 days in $CHCl_3$)[a]
e.r. 95:5
d.r. >25:1

3c, 90% (2 days in $CHCl_3$)
e.r. 95:5
d.r. >25:1

3d, 91% (3 days)
e.r. 95:5
d.r. >25:1

3e, 94% (0 °C, 10 h)
e.r. 95:5
d.r. >20:1

3f, 97% (4 days)
e.r. 96:4
d.r. >25:1

3g, 89% (3 days)
e.r. 95.5:4.5
d.r. >25:1

3h, 96% (24 h)
e.r. 95.5:4.5
d.r. >25:1

3i, 92% (10 h)
e.r. 95.5:4.5
d.r. >25:1

3j, 90% (3 days)
e.r. 96:4
d.r. >25:1

3k, 91% (36 h)
e.r. 97:3
d.r. >25:1

3l, 93% (24 h)
e.r. 96:4
d.r. >25:1

3m, 93% (2 days)
e.r. 96.5:3.5
d.r. >25:1

3n, 91% (3 days)
e.r. 95.5:4.5
d.r. >25:1

3o, 88% (0 °C, 3 days)
e.r. 92.5:7.5
d.r. >25:1

3o (x-ray structure)

Fig. 3. Scope of the Diels–Alder reaction (Tf: SO_2CF_3; Fm: fluorenylmethyl; TBS: tert-butyldimethylsilyl). All yields are isolated. Enantiomeric ratios (e.r.) were determined via high-performance liquid chromatography (HPLC). Diastereomeric ratios (d.r.) were determined by ^{1}H-NMR. *Using 3 instead of 1 mol % of catalyst loading gave full conversion after 3 days with identical enantiomeric and diastereomeric ratios.

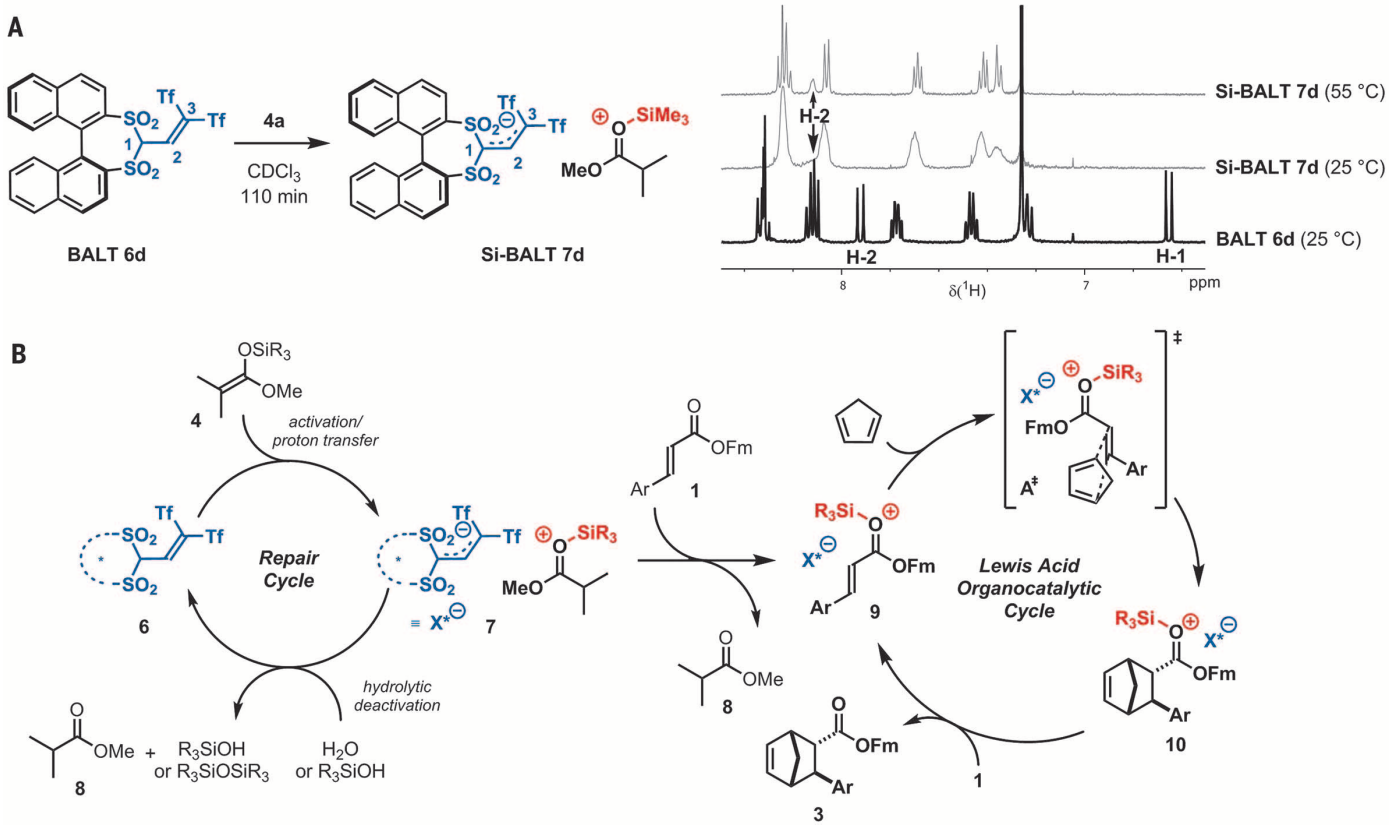

Fig. 4. Proposed catalytic cycle and mechanistic considerations. (**A**) In situ NMR spectroscopic study of catalyst activation. 3,3′-Unsubstituted BALT catalyst **6d** was treated with an excess of silyl ketene acetal **4a** to give the silylium BALT–anion pair **7d**. (Right) ^{1}H-NMR spectra of the starting material and of the product at different temperatures. (**B**) Catalyst activation and proposed catalytic cycle.

a product complex **10**. The asymmetric induction in transition state $\mathbf{A}^{\neq}$ would result largely from the stereochemical communication between the achiral cationic moiety and the enantiopure BALT anion. After the enantio-determining step, the final product ***3*** could be liberated by direct Lewis base exchange with another molecule of substrate **1**, or via the intermediate formation of the activated complex **7** with **8**, in both cases resulting in the concomitant closing of the catalytic cycle.

An important and unique feature of our silylium ion–ACDC approach arises from the possibility of a repair pathway upon hydrolytic deactivation of the Lewis acid catalyst, enabled by simply adjusting the amount of the silylating reagent. The valuable source of chirality is hydrolytically stable and can only switch between the anionic state (active Lewis acid) and the Brønsted acidic state, thus allowing very low catalyst loadings.

Our findings immediately suggest widespread applications of this activation mode to other reactions susceptible to Lewis acid catalysis. Furthermore, our studies constitute a proof of principle for the feasibility of enantioselective C–H acid catalysis and likely pave the way for the application of such catalysts in enantioselective Brønsted acid catalysis. We believe that our C–H acid-based catalyst design may furnish solutions for addressing limitations remaining with current O–H– and N–H–based organocatalysts, and in ACDC in general.

REFERENCES AND NOTES

1. H. Yamamoto, *Lewis Acids in Organic Synthesis* (Wiley-VCH, Weinheim, Germany, ed. 1, 2000), vols. 1 and 2.
2. K. T. Hollis, W. Oderkirk, N. P. Robinson, J. Whelan, B. Bosnich, *Tetrahedron* **49**, 5415–5430 (1993).
3. E. M. Carreira, R. A. Singer, *Tetrahedron Lett.* **35**, 4323–4326 (1994).
4. T. K. Hollis, B. Bosnich, *J. Am. Chem. Soc.* **117**, 4570–4581 (1995).
5. D. A. Evans, K. T. Chapman, J. Bisaha, *J. Am. Chem. Soc.* **110**, 1238–1256 (1988).
6. B. Mathieu, L. de Fays, L. Ghosez, *Tetrahedron Lett.* **41**, 9561–9564 (2000).
7. Z. Tang, B. Mathieu, B. Tinant, G. Dive, L. Ghosez, *Tetrahedron* **63**, 8449–8462 (2007).
8. D. H. Ryu, T. W. Lee, E. J. Corey, *J. Am. Chem. Soc.* **124**, 9992–9993 (2002).
9. D. H. Ryu, E. J. Corey, *J. Am. Chem. Soc.* **125**, 6388–6390 (2003).
10. P. García-García, F. Lay, P. García-García, C. Rabalakos, B. List, *Angew. Chem. Int. Ed.* **48**, 4363–4366 (2009).
11. M. van Gemmeren, F. Lay, B. List, *Aldrichim Acta* **47**, 3–13 (2014).
12. T. James, M. van Gemmeren, B. List, *Chem. Rev.* **115**, 9388–9409 (2015).
13. L. Ratjen, M. van Gemmeren, F. Pesciaioli, B. List, *Angew. Chem. Int. Ed.* **53**, 8765–8769 (2014).
14. Q. Wang, B. List, *Synlett* **11**, 807–809 (2015).
15. Q. Wang, B. List, *Synlett* **26**, 1525–1527 (2015).
16. S. Mayer, B. List, *Angew. Chem. Int. Ed.* **45**, 4193–4195 (2006).
17. M. Mahlau, B. List, *Angew. Chem. Int. Ed.* **52**, 518–533 (2013).
18. R. J. Phipps, G. L. Hamilton, F. D. Toste, *Nat. Chem.* **4**, 603–614 (2012).
19. K. Brak, E. N. Jacobsen, *Angew. Chem. Int. Ed.* **52**, 534–561 (2013).
20. E. J. Corey, *Angew. Chem. Int. Ed.* **48**, 2100–2117 (2009).
21. A. Hasegawa, K. Ishihara, H. Yamamoto, *Angew. Chem. Int. Ed.* **42**, 5731–5733 (2003).
22. For a mechanistically unclear case relying partially on an acidified C–H bond, see (*23*).
23. A. Hasegawa, Y. Naganawa, M. Fushimi, K. Ishihara, H. Yamamoto, *Org. Lett.* **8**, 3175–3178 (2006).
24. H. Yanai, Y. Sasaki, Y. Yamamoto, T. Matsumoto, *Synlett* **26**, 2457–2461 (2015).
25. M. Sai, M. Akakura, H. Yamamoto, *Chem. Commun. (Camb.)* **50**, 15206–15208 (2014).

ACKNOWLEDGMENTS

Generous support from the Max Planck Society, the Stiftung Industrieforschung (Fellowship to T.G.), the Fonds der Chemischen Industrie (Kekulé Fellowship to M.v.G.), and the European Research Council (Advanced Grant "High Performance Lewis Acid Organocatalysis, HIPOCAT") are gratefully acknowledged. This work is part of the Cluster of Excellence RESOLV (EXC 1069) funded by Deutsche Forschungsgemeinschaft. We thank S. Dehn and A. Döhring for superb technical support. We are also very thankful to our analytical scientists at the institute, especially J. B. Lingnau and C. Farès (NMR department) for excellent structural assignments, A. Deege (HPLC), and all the other members of our HPLC, gas chromatography, NMR, mass sprectrometry, and x-ray departments. Metrical parameters for the structure of 3o are available free of charge from the Cambridge Crystallographic Data Centre under accession number CCDC 1448254.

SUPPLEMENTARY MATERIALS

www.sciencemag.org/content/351/6276/949/suppl/DC1
Materials and Methods
Supplementary Text
Figs. S1 to S7
Tables S1 to S14
References (*26*–*30*)
Analytical Data

4 December 2015; accepted 20 January 2016
10.1126/science.aae0010

QUANTUM SIMULATION

Site-resolved imaging of a fermionic Mott insulator

Daniel Greif, Maxwell F. Parsons, Anton Mazurenko, Christie S. Chiu, Sebastian Blatt,* Florian Huber, Geoffrey Ji, Markus Greiner†

The complexity of quantum many-body systems originates from the interplay of strong interactions, quantum statistics, and the large number of quantum-mechanical degrees of freedom. Probing these systems on a microscopic level with single-site resolution offers important insights. Here we report site-resolved imaging of two-component fermionic Mott insulators, metals, and band insulators, using ultracold atoms in a square lattice. For strong repulsive interactions, we observed two-dimensional Mott insulators containing over 400 atoms. For intermediate interactions, we observed a coexistence of phases. From comparison to theory, we find trap-averaged entropies per particle of 1.0 times the Boltzmann constant (k_B). In the band insulator, we find local entropies as low as 0.5 k_B. Access to local observables will aid the understanding of fermionic many-body systems in regimes inaccessible by modern theoretical methods.

Detection and control of quantum many-body systems at the level of single lattice sites and single particles gives access to correlation functions and order parameters on a microscopic level. These capabilities promise insights into a number of complex and poorly understood quantum phases, such as spin liquids, valence-bond solids, and *d*-wave superconductors (*1*, *2*). Site-resolved detection and control of the wave function remain elusive in conventional solid-state systems, but are possible in synthetic matter with ultracold atoms in optical lattices, because the associated length scales are accessible with high-resolution optical microscopy (*3*). Site-resolved imaging of bosonic quantum gases has enabled studies of the superfluid–to–Mott insulator (MI) transition on a single-site level (*4*, *5*), an experimental realization of Ising and Heisenberg spin chains (*6*, *7*), a direct measurement of entanglement entropy (*8*), and studies of dynamics of charge and spin degrees of freedom of quantum systems (*9*, *10*). The extension of site-resolved imaging to fermionic atoms may enable exploration of the rich phase diagram of the Hubbard model, thought to describe a variety of strongly correlated quantum-mechanical phenomena, including high-temperature superconductivity (*11*). Recently, site-resolved imaging of fermionic atoms has been demonstrated with different atomic species (*12*–*15*), and a single-spin band insulator has been observed (*16*). Although fermionic MIs and short-range antiferromagnetic spin correlations have been observed using conventional imaging techniques (*17*–*26*), site-resolved imaging of interacting many-body states of fermions is an outstanding challenge.

Here we demonstrate site-resolved observations of fermionic metals, MIs, and band insulators. A fermionic MI is a prime example of a strongly interacting many-body state, where repulsive interactions between fermionic particles in two different spin states give rise to insulating behavior in a half-filled energy band. This behavior is well described by the Hubbard model. For low temperatures, a theoretical analysis of the phase diagram becomes difficult owing to the fermion sign problem (*27*). At temperatures above the magnetic exchange energy, spin order is absent, and a density-order crossover from a metallic state to a MI occurs when the ratio of interaction to kinetic energy is increased. Whereas the metallic state has a gapless excitation spectrum, is compressible, and shows a large variance in the site-resolved lattice occupation, the MI has a finite energy gap, is incompressible, and shows a vanishing variance in the occupation. Observing these characteristic properties of a MI requires temperatures well below the energy gap. For lower interactions and large filling, an incompressible band insulator of doublons (two particles on a site) appears because of the Pauli exclusion principle. This behavior is in contrast to the bosonic case, where the absence of the Pauli exclusion principle allows higher fillings, and a ring structure of MI states with different integer fillings appears (*4*, *5*).

The starting point of the experiment is a low-temperature, two-dimensional gas of fermionic ^{6}Li atoms with repulsive interactions in an equal mixture of the two lowest hyperfine ground states. After the preparation and cooling of the cloud, we set the *s*-wave scattering length to values $a = 37\ a_0 - 515\ a_0$ by adjusting a magnetic bias field in the vicinity of the Feshbach resonance located at 832 G, where a_0 denotes the Bohr radius (*28*). We then load the atoms into a square optical lattice using a 30-ms long linear ramp of the laser beam powers. The system is well described by a single-band two-dimensional Hubbard model on a square lattice with nearest-neighbor tunneling $t_x/h = 0.279(10)$ kHz and $t_y/h = 0.133(4)$ kHz along the two lattice directions with a corresponding bandwidth $8\bar{t} = 1.65(7)$kHz and $U/h = 1.81(3)$ to $25.2(5)$kHz. The explored ratios of $U/8\bar{t}$ thus range from the metallic ($U \sim 8\bar{t}$) to the MI ($U >> 8\bar{t}$) regime. In the experiment, an overall harmonic confinement is present, with frequencies $\omega_x/2\pi = 0.691(9)$ kHz and $\omega_y/2\pi = 0.604(3)$ kHz. For more details, see (*29*).

We detect the many-body state of the system by measuring the occupation of each lattice site with single-site resolution. For the detection, we first rapidly increase all lattice depths to pin the atomic distribution and then image the fluorescence of the atoms with a high-resolution microscope onto an intensified charge-coupled device camera. Atoms on doubly occupied sites are removed during the imaging as a consequence of light-assisted collisions (*30*). We apply a deconvolution algorithm to the images to determine the occupation of every individual lattice site n_{det}, which is unity for a single particle of either spin and zero for the case of an empty or doubly occupied site. Our imaging technique allows a reliable determination of the site-resolved occupation, with an estimated imaging fidelity of $97.5(3)\%$ (*14*, *29*).

We directly observed the metal–to-MI transition on a site-resolved level. Single images show a drastic change in the occupation distribution when increasing the interaction, $U/8\bar{t}$, at constant atom number (Fig. 1). For the weakest interactions $[U/8\bar{t} = 1.1(1)]$, we observed a purely metallic state with a large occupation variance over the entire cloud. The maximum detected value for the variance was 0.25, which is consistent with equal occupation probabilities of all four possible states per lattice site. The occupation decreases gradually for larger distances from the center because of the underlying harmonic confinement. In contrast, for the strongest interactions, $[U/8\bar{t} = 15.3(7)]$ we observed a large half-filled MI region containing about 400 atoms (*29*). The energy gap, U, suppresses the variance in occupation in the center of the cloud to values below 0.02, with thermal excitations appearing as an increased variance in the occupation at the edge of the cloud.

The underlying harmonic trap causes a spatially varying chemical potential, which can lead to the appearance of different phases within the same atomic cloud. For intermediate interactions $[U/8\bar{t} = 2.5(1)$ and $U/8\bar{t} = 3.8(2)]$, where the chemical potential $\mu > U$, we observe a wedding-cake structure, where metallic, MI, and band-insulating (BI) phases coexist. A BI core of doubly occupied sites forms in the center, visible as an extended region of empty sites with low occupation variance. This region is surrounded by a MI with a small number of defects. At the interface of these two phases and at the outer edge of the MI, there is a metallic phase with large occupation variance. For increasing interaction strength, the MI ring broadens owing to the increased energy cost for double occupation. At the same time, the BI region decreases in size, until it disappears entirely for the largest interaction, where $\mu < U$. Figure 1C shows radial profiles of the average

Department of Physics, Harvard University, Cambridge, MA 02138, USA.
*Present address: Max-Planck-Institut für Quantenoptik, 85748 Garching, Germany. †Corresponding author. E-mail: greiner@physics.harvard.edu

Downloaded from on February 25, 2016

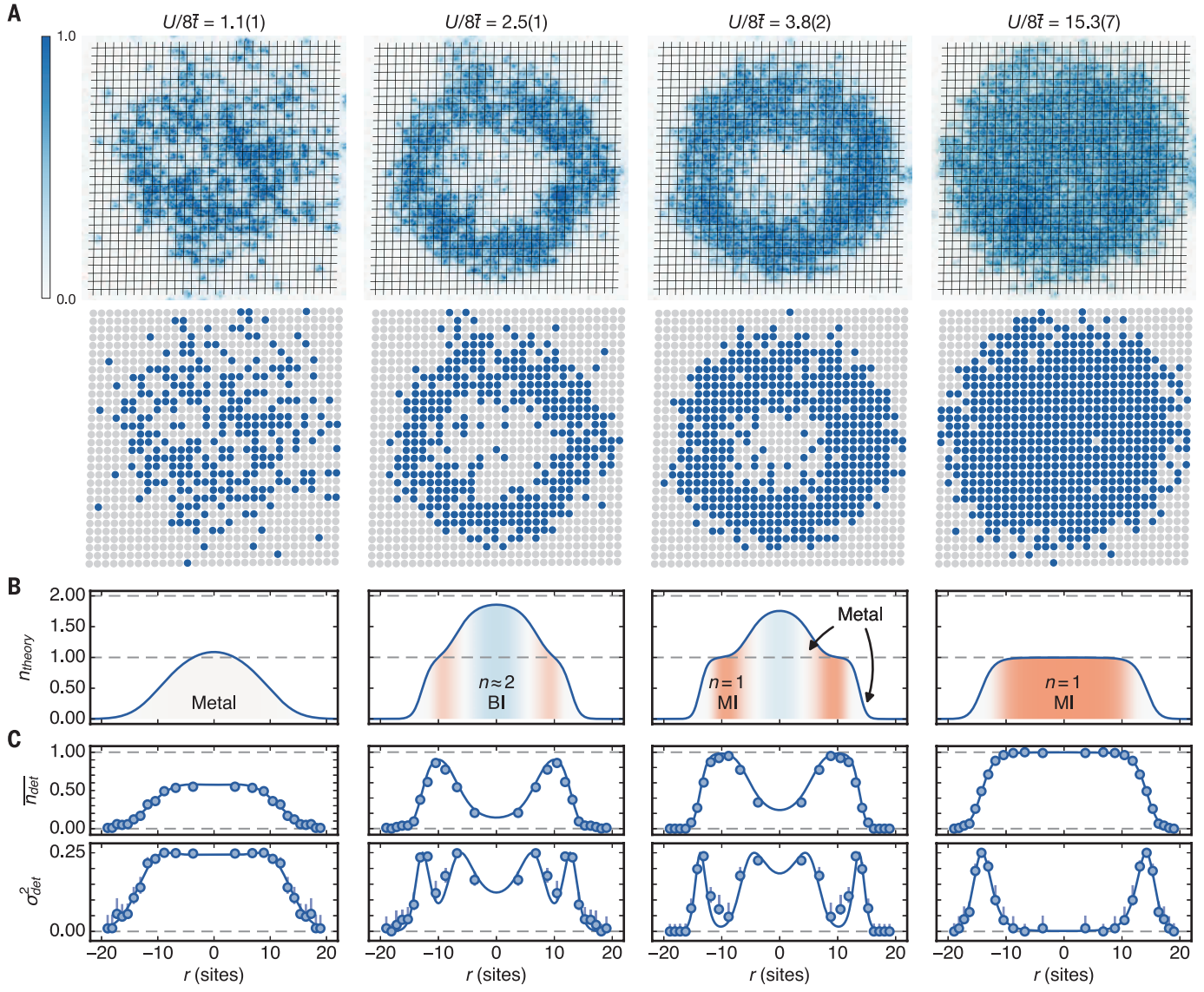

Fig. 1. Site-resolved images of the fermionic metal-to-MI transition. (**A**) Single experimental images of the atoms in the square lattice are shown for varying interactions $U/8\bar{t}$, along with the extracted site occupation. Doublons are detected as empty sites because of light-assisted collisions during imaging. The color bar shows the normalized number of detected photons. (**B**) Calculated full density profiles for the experimental parameters in (A), obtained by fits to the experimental data. Depending on the interaction, we observe MI, BI, and metallic states. The MI appears for strong interactions as an extended spatial region with filling $n_{\mathrm{theory}} = 1$. In the BI, the filling approaches 2. Metallic regions connect the different insulating states, where the filling changes by an integer. (**C**) By applying azimuthal averages to the corresponding single images, we obtain radial profiles (mirrored at $r = 0$) for the detected occupation $\overline{n_{\mathrm{det}}}$ and variance σ^2_{det}. The variance is strongly reduced in the insulating phases. The radial profiles $\overline{n_{\mathrm{det}}}(r)$ were fit using a high-temperature series expansion of the single-band Hubbard model, with temperature and chemical potential as free parameters (solid lines). This gives temperatures $k_{\mathrm{B}}T/U = 1.6(3), 0.22(3), 0.12(2)$, and $0.050(7)$ from left to right, which are used for calculating the full density profiles in (B) and correspond to average entropies per particle of $S/N = 2.2(3), 1.00(8), 0.99(7)$, and $1.15(7)\ k_{\mathrm{B}}$. The large values of temperature and entropy at $U/8\bar{t} = 1.1$ may be caused by non-adiabatic loading of the lattice at small interactions. Error bars are computed from a sampled Bernoulli distribution (*29*).

detected occupation, $\overline{n_{\mathrm{det}}}(r)$, and variance, $\sigma^2_{\mathrm{det}}(r)$, obtained from single experimental images by exploiting the symmetry of the trap and taking azimuthal averages over equipotential regions (*29*).

An essential requirement for a MI state is a temperature well below the energy gap $k_{\mathrm{B}}T << U$, where k_{B} denotes the Boltzmann constant. We perform thermometry of the atomic gas in the lattice by comparing the detected radial occupation and variance profiles obtained from single images to theoretical calculations based on a second-order high-temperature series expansion of the Fermi-Hubbard model (*31*). The effect of the harmonic trap is taken into account using a local density approximation, where the chemical potential varies locally (*32*). The temperature and chemical potential are obtained from a fit to the detected density distribution $\overline{n_{\mathrm{det}}}(r)$, and all other parameters are calibrated independently. We find excellent agreement with theory for all interactions and measure temperatures as low as $k_{\mathrm{B}}T/U = 0.05$ for the largest interaction, corresponding to an average entropy per particle of $S/N = 1.15\ k_{\mathrm{B}}$. For weaker interactions, we find values as low as $S/N = 0.99\ k_{\mathrm{B}}$. When repeating the experiment with the same parameters, we find a shot-to-shot variance in entropy consistent with fit errors (*29*). The agreement with theory shows that the entire system is well described by a thermally equilibrated state, and the underlying trapping potential is well described by a harmonic trap.

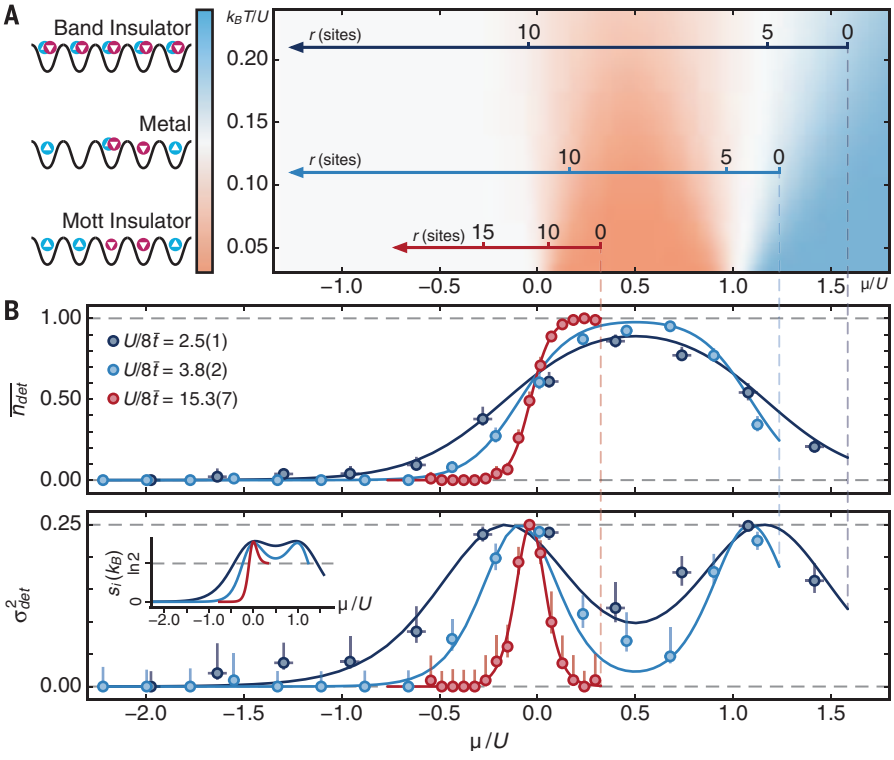

Fig. 2. Cuts through the 2D Hubbard phase diagram. (**A**) Schematic of the (μ/U, k_BT/U) phase diagram of the Hubbard model at $U >> \bar{t}$, which is the relevant regime for all three data sets shown. The intensity of the shading reflects the normalized variance of the site occupation, and the colors distinguish between MI and BI regimes. The arrows denote radial cuts through the trap for different interactions corresponding to the profiles shown in (B). (**B**) Detected site occupation and variance versus chemical potential, obtained from the radial profiles in Fig. 1, with fits as solid lines (*29*) and error bars as in Fig. 1. The distributions are symmetric around $\mu = U/2$ (half-filling) from particle-hole symmetry. (Inset, bottom left) Calculated local entropy per site s_i.

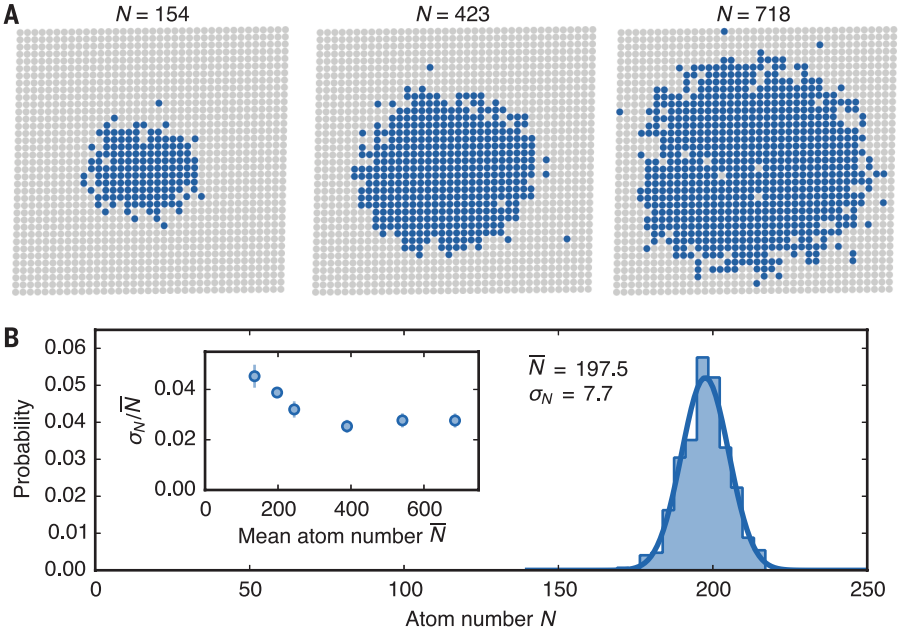

Fig. 3. Controlling the size of a MI. (**A**) Single images of MIs with varying detected atom numbers N (without doublons) for $U/8\bar{t} = 15.3(7)$. (**B**) Histogram of detected atom numbers after 400 experiment repetitions with the average atom number $\overline{N}$ and standard deviation σ_N (68% confidence). The solid line shows the Gaussian distribution for the obtained $\overline{N}$ and σ_N. The inset shows the experimental stability of preparing samples with fixed atom number, characterized by the relative standard deviation for different $\overline{N}$ obtained from ≥50 images. Error bars denote the respective standard errors.

In Fig. 2B, we show $\overline{n_{det}}$ and σ^2_{det} as a function of μ/U, which corresponds to a scan along a single line in the $(\mu/U, k_BT/U)$ phase diagram of the Hubbard model at $t << U$. These data are directly obtained from the respective radial profiles in Fig. 1. The MI is identified by an extended region in μ/U, with constant occupation $\overline{n_{det}} = 1$ and a strongly reduced variance. Because in this regime the total and detected fillings are approximately equal (see Fig. 1B, right panel), the compressibility in the range just below half-filling ($\mu < U/2$) can be obtained from $\kappa = \partial n_{det}/\partial\mu$, which is small in the MI region. The metallic regions are signaled by an enhanced compressibility, with a peak in the variance distribution. The width of each peak is determined by the temperature and is smallest for the largest interactions, as k_BT/U decreases for increasing interactions in the experiment.

Two contributions reduce the filling from one particle per site in the MI region: the finite temperature of the gas and the imaging fidelity. We determined a lower bound on the filling by averaging over 50 images, resulting in $\overline{n_{det}} =$ 96.5(2)%, limited by our finite imaging fidelity of 97.5(3)%. This filling gives an upper bound on the charge entropy (i.e., entropy involving density excitations in the atomic cloud) of 0.175 k_B (*29*). Because the fermionic particles are in two different spin states, the total entropy also contains a contribution from the spin entropy. From the fitted temperatures we calculate the total entropy per site as a function of μ/U for the different interactions (Fig. 2B, inset). In the MI region we find $s_i = 0.70(1)\ k_B$, consistent with $s_i = k_B \ln 2$, which corresponds to the entropy of

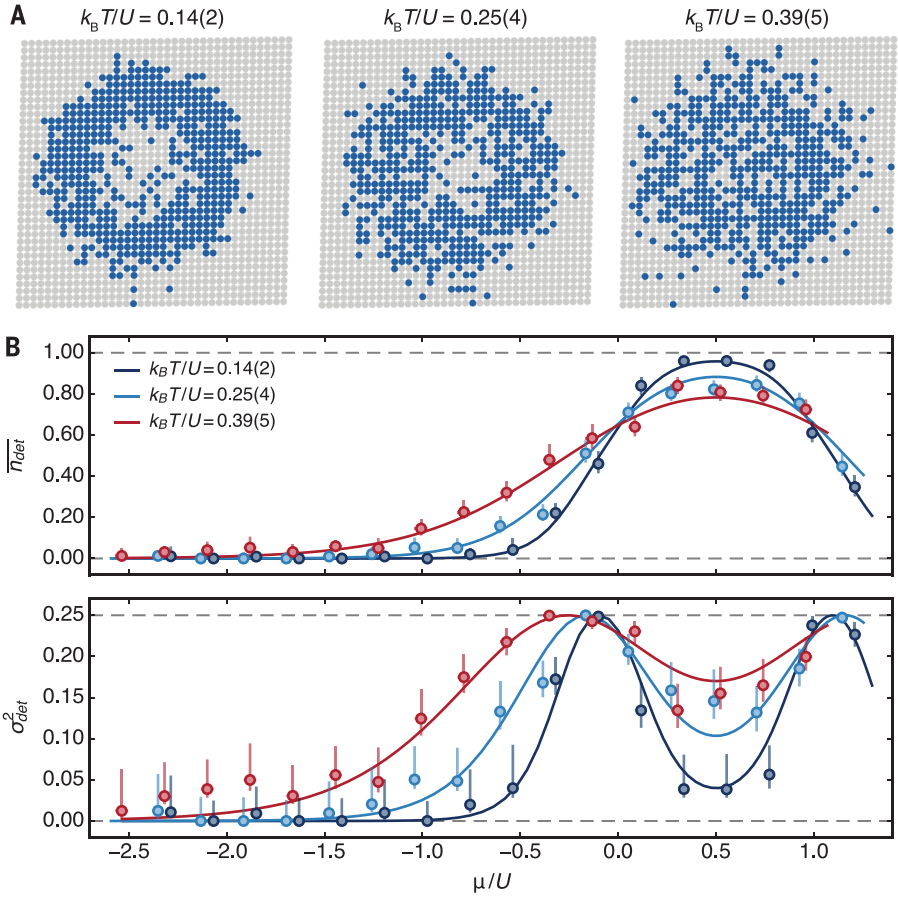

Fig. 4. Melting a fermionic MI. (**A**) Detected site occupations from single images at different temperatures for $U/8\bar{t} = 3.8(2)$. The clouds are heated by holding the atom cloud in a crossed dipole trap before lattice ramp-up. Hold times, from left to right, are 0, 1, and 3 s. (**B**) Corresponding occupations and variance profiles versus chemical potential, with error bars as in Fig. 1. The dark blue, light blue, and red curves are theory fits used to determine the temperature.

a paramagnetic MI. In the BI region the entropy drops below k_B ln2, as in this case 78(1)% of the lattice sites are occupied with doublons. In the BI, the charge entropy can be estimated from the measured average density of excitations corresponding to sites with one particle. This gives $0.53(2)\ k_B$, in good agreement with the calculated value of $0.5(1)\ k_B$ from the theory fit. The variation in local entropy over the atomic cloud indicates that there is not only mass transport, but also efficient transport of entropy over many sites when loading the atoms into the lattice. This entropy transport could be the starting point for generating other low-temperature phases of matter using entropy redistribution or other cooling schemes (*33*–*36*).

An accurate experimental study of the low-temperature Hubbard model generally requires large system sizes. By adjusting the evaporation, we experimentally control the size of the MI with detected total atom numbers (without doublons) ranging from $N = 154$ to $N = 718$ (Fig. 3). In all cases we find high values for the detected central occupation $\overline{n_{det}} > 0.92$ (*28*). To investigate the reproducibility, we repeated the same experiment and found that the standard deviation corresponds to $< 5\%$ of the mean atom number.

Whereas for temperatures $k_B T << U$ a large MI with a sharp occupation distribution appears, the insulator is expected to gradually melt with increasing temperatures and eventually disappear. We experimentally controlled the temperature while keeping the atom number approximately constant by adjusting the evaporation and preparation of the atomic cloud (*29*). We observed a clear change in the occupation and variance distribution from single images, which is also apparent in the respective distributions as a function of μ/U (Fig. 4). For higher temperatures, the occupation distribution broadens significantly, whereas the variance flattens and is only weakly suppressed at the highest detected occupations ($\mu = U/2$). The temperatures determined from theory comparison are in the range $k_B T/U = 0.14$ to 0.55, which corresponds to entropies of $S/N = 0.97$ to $1.58\ k_B$. This shows that temperatures $k_B T << U$ are required for MI states.

For the lowest detected entropy value $S/N = 0.97\ k_B$, we expect strong antiferromagnetic correlations on nearest-neighbor sites (*37*–*40*). This should be detectable in single images by measuring the spin correlation function via spin-sensitive imaging. Additionally, our experiment is well suited for studying the competition of ferromagnetic and antiferromagnetic domains in the regime of weak lattices and large scattering lengths (*41*), investigating the phase diagram of polarized samples with repulsive or attractive interactions (*42*–*45*), and testing various entropy distribution schemes (*33*–*35*).

REFERENCES AND NOTES

1. L. Balents, *Nature* **464**, 199–208 (2010).
2. P. W. Anderson, *Science* **235**, 1196–1198 (1987).
3. K. D. Nelson, X. Li, D. S. Weiss, *Nat. Phys.* **3**, 556–560 (2007).
4. W. S. Bakr *et al.*, *Science* **329**, 547–550 (2010).
5. J. F. Sherson *et al.*, *Nature* **467**, 68–72 (2010).
6. J. Simon *et al.*, *Nature* **472**, 307–312 (2011).
7. T. Fukuhara *et al.*, *Nat. Phys.* **9**, 235–241 (2013).
8. R. Islam *et al.*, *Nature* **528**, 77–83 (2015).
9. P. M. Preiss *et al.*, *Science* **347**, 1229–1233 (2015).
10. T. Fukuhara *et al.*, *Nature* **502**, 76–79 (2013).
11. P. A. Lee, N. Nagaosa, X.-G. Wen, *Rev. Mod. Phys.* **78**, 17–85 (2006).
12. E. Haller *et al.*, *Nat. Phys.* **11**, 738–742 (2015).
13. L. W. Cheuk *et al.*, *Phys. Rev. Lett.* **114**, 193001 (2015).
14. M. F. Parsons *et al.*, *Phys. Rev. Lett.* **114**, 213002 (2015).
15. G. J. A. Edge *et al.*, *Phys. Rev. A* **92**, 063406 (2015).
16. A. Omran *et al.*, *Phys. Rev. Lett.* **115**, 263001 (2015).
17. R. Jördens, N. Strohmaier, K. Günter, H. Moritz, T. Esslinger, *Nature* **455**, 204–207 (2008).
18. U. Schneider *et al.*, *Science* **322**, 1520–1525 (2008).
19. R. Jördens *et al.*, *Phys. Rev. Lett.* **104**, 180401 (2010).
20. S. Taie, R. Yamazaki, S. Sugawa, Y. Takahashi, *Nat. Phys.* **8**, 825–830 (2012).
21. T. Uehlinger *et al.*, *Phys. Rev. Lett.* **111**, 185307 (2013).
22. P. M. Duarte *et al.*, *Phys. Rev. Lett.* **114**, 070403 (2015).
23. M. Messer *et al.*, *Phys. Rev. Lett.* **115**, 115303 (2015).
24. D. Greif, T. Uehlinger, G. Jotzu, L. Tarruell, T. Esslinger, *Science* **340**, 1307–1310 (2013).
25. R. A. Hart *et al.*, *Nature* **519**, 211–214 (2015).
26. D. Greif, G. Jotzu, M. Messer, R. Desbuquois, T. Esslinger, *Phys. Rev. Lett.* **115**, 260401 (2015).
27. M. Troyer, U.-J. Wiese, *Phys. Rev. Lett.* **94**, 170201 (2005).
28. G. Zürn *et al.*, *Phys. Rev. Lett.* **110**, 135301 (2013).
29. See the supplementary materials on *Science* Online.
30. M. T. DePue, C. McCormick, S. L. Winoto, S. Oliver, D. S. Weiss, *Phys. Rev. Lett.* **82**, 2262–2265 (1999).
31. J. Oitmaa, C. Hamer, W. Zheng, *Series Expansion Methods for Strongly Interacting Lattice Models* (Cambridge Univ. Press, Cambridge, 2006).
32. V. W. Scarola, L. Pollet, J. Oitmaa, M. Troyer, *Phys. Rev. Lett.* **102**, 135302 (2009).
33. J.-S. Bernier *et al.*, *Phys. Rev. A* **79**, 061601 (2009).
34. T.-L. Ho, Q. Zhou, *Proc. Natl. Acad. Sci. U.S.A.* **106**, 6916–6920 (2009).
35. M. Lubasch, V. Murg, U. Schneider, J. I. Cirac, M.-C. Bañuls, *Phys. Rev. Lett.* **107**, 165301 (2011).
36. W. S. Bakr *et al.*, *Nature* **480**, 500–503 (2011).
37. S. Fuchs *et al.*, *Phys. Rev. Lett.* **106**, 030401 (2011).
38. B. Tang, T. Paiva, E. Khatami, M. Rigol, *Phys. Rev. Lett.* **109**, 205301 (2012).
39. J. P. F. LeBlanc, E. Gull, *Phys. Rev. B* **88**, 155108 (2013).
40. J. Imriška, E. Gull, M. Troyer, Thermodynamics of the Hubbard model on stacked honeycomb and square lattices, http://arxiv.org/abs/1509.08919 (2015).
41. P. N. Ma, S. Pilati, M. Troyer, X. Dai, *Nat. Phys.* **8**, 601–605 (2012).
42. M. Snoek, I. Titvinidze, C. Toke, K. Byczuk, W. Hofstetter, *New J. Phys.* **10**, 093008 (2008).
43. B. Wunsch, L. Fritz, N. T. Zinner, E. Manousakis, E. Demler, *Phys. Rev. A* **81**, 013616 (2010).
44. A. Koetsier, F. van Liere, H. T. C. Stoof, *Phys. Rev. A* **81**, 023628 (2010).
45. J. Gukelberger, S. Lienert, E. Kozik, L. Pollet, M. Troyer, Fulde-Ferrell-Larkin-Ovchinnikov pairing as leading instability on the square lattice, http://arxiv.org/abs/1509.05050 (2015).

ACKNOWLEDGMENTS

We acknowledge insightful discussions with I. Bloch, S. Dickerson, M. Endres, G. Jotzu, and A. Kaufman. We acknowledge support

from the Army Research Office Defense Advanced Research Projects Agency Optical Lattice Emulator, the Air Force Office of Scientific Research, the Multi University Research Initiative, the Office of Naval Research Defense University Research Instrumentation Program, and NSF. D.G. acknowledges support from the Harvard Quantum Optics Center and the Swiss National Foundation. M.P, A.M. and C.C acknowlege support from the NSF Graduate Research Fellowship Program. The authors declare no competing financial interests.

SUPPLEMENTARY MATERIALS
www.sciencemag.org/content/351/6276/953/suppl/DC1
Supplementary Text
Figs. S1 to S7
Table S1
Reference (*46*)

18 November 2015; accepted 27 January 2016
10.1126/science.aad9041

THIN FILMS

Superlubricity of graphene nanoribbons on gold surfaces

Shigeki Kawai,[1,2]*† Andrea Benassi,[3,4]*† Enrico Gnecco,[5,6] Hajo Söde,[3] Rémy Pawlak,[1] Xinliang Feng,[7] Klaus Müllen,[8] Daniele Passerone,[3] Carlo A. Pignedoli,[3] Pascal Ruffieux,[3] Roman Fasel,[3,9] Ernst Meyer[1]

The state of vanishing friction known as superlubricity has important applications for energy saving and increasing the lifetime of devices. Superlubricity, as detected with atomic force microscopy, appears when sliding large graphite flakes or gold nanoclusters across surfaces, for example. However, the origin of the behavior is poorly understood because of the lack of a controllable nanocontact. We demonstrated the superlubricity of graphene nanoribbons when sliding on gold with a joint experimental and computational approach. The atomically well-defined contact allows us to trace the origin of superlubricity, unraveling the role played by ribbon size and elasticity, as well as by surface reconstruction. Our results pave the way to the scale-up of superlubricity and thus to the realization of frictionless coatings.

Graphene offers distinctive properties as a solid lubricant (*1*) and has the potential to be used as an ultrathin coating material on surfaces, almost suppressing energy consumption in mechanical components. The interpretation of such superlubric behavior is based on the premise that (*2*–*5*) (i) the high lateral stiffness of graphene makes a commensurable contact with most solid surfaces nearly impossible, and (ii) combined with the weak interaction with most materials, incommensurability leads to a state of ultralow friction when graphene slides over a different material. To substantiate this hypothesis and establish a connection with the tribological properties observed on macro- and mesoscales, it is highly desirable to measure the mechanical response of a graphene flake down to the nanometer level. In such measurements, one has to ensure that both of the contacting surfaces are atomically well defined, that their common interface is free from contaminants, and that the ultralow forces accompanying the sliding motion can be distinguished from the background noise. Whereas clean atomically flat surfaces as substrates can reliably be obtained in ultrahigh vacuum (UHV), atomically defined graphene systems as sliding objects are rarely prepared. Carbon nanotubes have exceptional superlubric properties up to a length scale

[1]Department of Physics, University of Basel, Klingelbergstrasse 82, CH-4056 Basel, Switzerland. [2]PRESTO (Precursory Research for Embryonic Science and Technology), Japan Science and Technology Agency, 4-1-8 Honcho, Kawaguchi, Saitama 332-0012, Japan. [3]nanotech@surfaces Laboratory, Empa, Swiss Federal Laboratories for Materials Science and Technology, Überlandstrasse 129, 8600 Dübendorf, Switzerland. [4]Institute for Materials Science and Max Bergmann Center of Biomaterials, Technische Universität Dresden, 01062 Dresden, Germany. [5]Instituto Madrileño de Estudios Avanzados en Nanociencia, 28049 Madrid, Spain. [6]Otto Schott Institute of Materials Research, Friedrich Schiller University Jena, 07743 Jena, Germany. [7]Department of Chemistry and Food Chemistry, Center for Advancing Electronics Dresden, Technische Universität Dresden, 01062 Dresden, Germany. [8]Max Planck Institute for Polymer Research, 55124 Mainz, Germany. [9]Department of Chemistry and Biochemistry, University of Bern, Freiestrasse 3, 3012 Bern, Switzerland.
***Corresponding author. E-mail: shigeki.kawai@unibas.ch (S.K.); andrea.benassi@nano.tu-dresden.de (A.B.)** †These authors contributed equally to this work.

Downloaded from on February 25, 2016

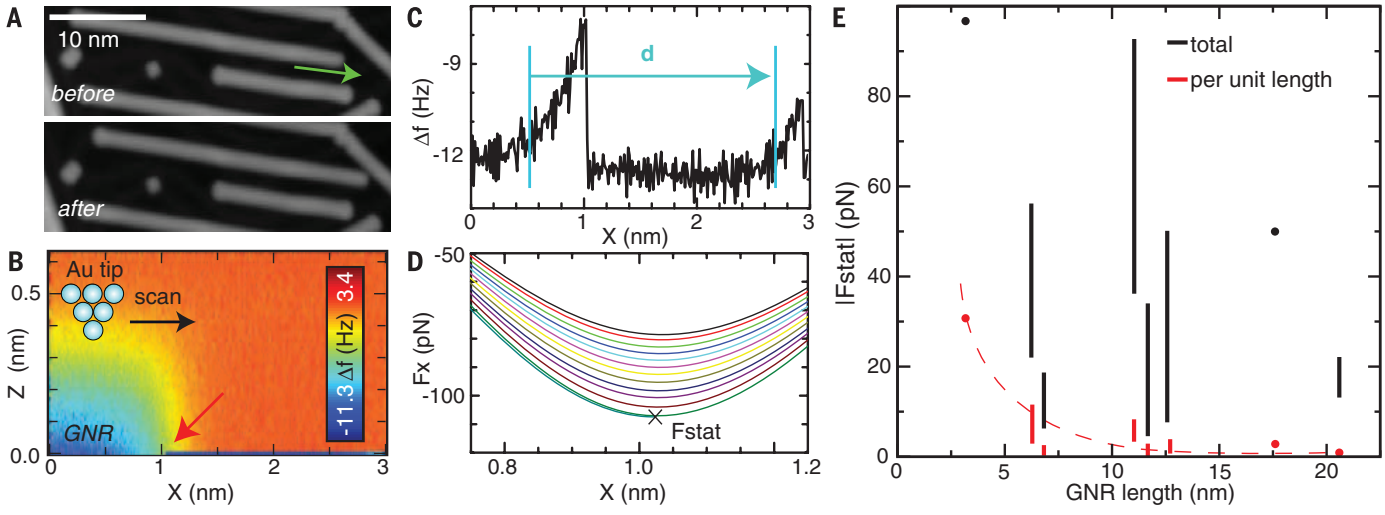

Fig. 1. Static friction force measurement. (**A**) STM topographies of GNRs on Au(111) before and after a tip-induced lateral manipulation (the green arrow indicates the sliding direction). (**B**) 2D Δf map along the longitudinal axis of the manipulated GNR. (**C**) Distance dependence of Δf before, during, and after the GNR displacement. (**D**) Calculated lateral force. The cross symbol corresponding to the red arrow in (B) shows the position at which the GNR starts moving and the corresponding value of the static friction force F_{stat}. (**E**) The absolute value of F_{stat} as a function of the GNR length (black) and F_{stat} per unit length (red). Dots correspond to single measurements, whereas bars connect the largest and the smallest values measured while manipulating the same ribbon on different surface regions. Measurement parameters: tunneling current I = 2 pA, bias voltage V = −200 mV (A); oscillation amplitude A = 34 pm [(B) to (D)].

of a few centimeters (*6*), but their curvature makes them difficult to manipulate in a controlled way. Nevertheless, the problem can be overcome by using graphene nanoribbons (GNRs), which recently have been synthetized on a metal substrate by means of an on-surface chemical reaction (*7*). Their structure is well defined by the precursor molecule, as confirmed by high-resolution scanning tunneling microscopy (STM) and atomic force microscopy (AFM). For this reason, GNRs are an appropriate candidate for our goal. Apart from that, GNRs are also very promising in a series of applications [e.g., nanoelectromechanical systems (*8*), nanofillers (*9*), transistors (*10*), and other electronic and spintronic devices (*11*)] for which assessing their mechanical stability is pivotal.

We investigated the frictional, adhesive, and elastic properties of GNRs by means of lateral manipulation on an Au(111) substrate, using dynamic AFM in UHV at a low temperature (4.8 K). The ends of selected GNRs were anchored to the probing tip and dragged back and forth in a controlled way while the friction force was recorded. An accompanying computational experiment allowed us to relate the origin of the measured superlubricity to the molecular dynamics occurring at the interface.

Our measurements originate from the unintentional manipulation of GNRs aligned along the [–1,0,1] direction of the Au(111) substrate, when the GNRs were imaged by STM using a gold tip. The GNRs were always displaced along their longitudinal axis, even with a relatively large separation, indicating high diffusivity (figs. S1 to S4). To measure the static friction force (F_{stat}), we switched to AFM, using the same tip. After imaging a sample area covered by GNRs (Fig. 1A), we acquired a two-dimensional (2D) frequency shift map while the tip was scanned laterally along a GNR (x direction) at different constant z distances (Fig. 1B and fig. S5). Following the method of Ternes *et al.* (*12*), we reduced the tip-GNR distance stepwise during scanning until we observed an abrupt decrease in the frequency shift (Δf) at the distance defined as $z = 0$ (Fig. 1C). We found that the GNR was displaced by a distance d = 2.2 nm (Fig. 1A). We also observed that the $\Delta f(x)$ profile was repeated after the same distance. Langewisch *et al.* reported a similar observation in their manipulation experiments on perylenetetracarboxylic dianhydride molecules (*13*). We found that d varied with both the GNR length and the adsorption site. Furthermore, jumps with smaller d values were rarely observed, and the GNRs were never dragged continuously, meaning that the junction formed between the tip and the GNRs is weak. To quantify F_{stat}, we first estimated the energy landscape experienced by the tip by integrating two times the $\Delta f(z)$ sections extracted from Fig. 1B. Then we differentiated the 2D potential map along the x direction and multiplied the result by the factor $-2k_c/f$ = -0.15 N m^{-1} Hz^{-1}, where k_c = 1800 N m^{-1} is the spring constant, and f = 24.7 kHz is the resonance frequency of the free tuning fork. The manipulation occurred when $F_{stat} \approx -105$ pN (Fig. 1D). F_{stat} is exceptionally low, considering that the linear size of the GNR is well above that of the single atoms and conventional molecules that are typically manipulated by AFM (*12*, *14*, *15*). This result is a strong confirmation of the superlubric properties of graphene on the nanoscale, as observed in previous friction measurements taken on graphene flakes of undefined size (*16*–*18*). Another signature of superlubricity is the decrease of the friction force per unit of contact area with increasing size of the contact (*19*–*21*). To look for this, in our quasi-1D system, we repeated the measurements on GNRs of different lengths (Fig. 1E). In spite of the spread in the measured data (due to the surface reconstruction, discussed below) the force per unit length was found to decrease with increasing GNR length.

We estimated the diffusion barrier (ΔE) for the GNR by assuming a simple sinusoidal interaction as $\Delta E \approx F_{stat}\, a/\pi \approx 40$ meV, where a = 0.41 nm is the lattice constant of the Au(111) substrate (*15*). This low value means that a single isolated GNR would diffuse spontaneously at room temperature, making measurements challenging. We also observed a rotation of short GNRs (2 nm), although we always scanned the tip exactly along the GNR axis (fig. S6). This behavior is predicted theoretically for graphene flakes dragged on graphite (*22*). We even observed a vertical motion of the shortest GNRs (1 nm) before the start of lateral manipulation (fig. S7). We could not perform reliable static friction force measurements on GNRs longer than 22 nm, because other GNRs were often found nearby, and the measured forces were considerably affected by the interaction with those neighbors. Nevertheless, superlubricity allowed us to manipulate GNRs up to 55 nm long (figs. S8 and S9).

Although our measurements allow a precise estimation of the static friction force, they do not provide any details on the complex dynamics of the sliding motion of the GNRs. To gain more insight, we applied the procedure that some of us previously introduced for polymer chains (*23*) and succeeded in attaching a short edge of a GNR to an Au-coated tip. We then oscillated the GNRs along the [–1,0,1] direction of the Au(111) surface with the tip kept at a constant distance (z) from the substrate. We repeated the measurements several times at increasing values of z (Fig. 2A). The corresponding variations in Δf are shown in Fig. 2, C to F, for increasing values of z. We found

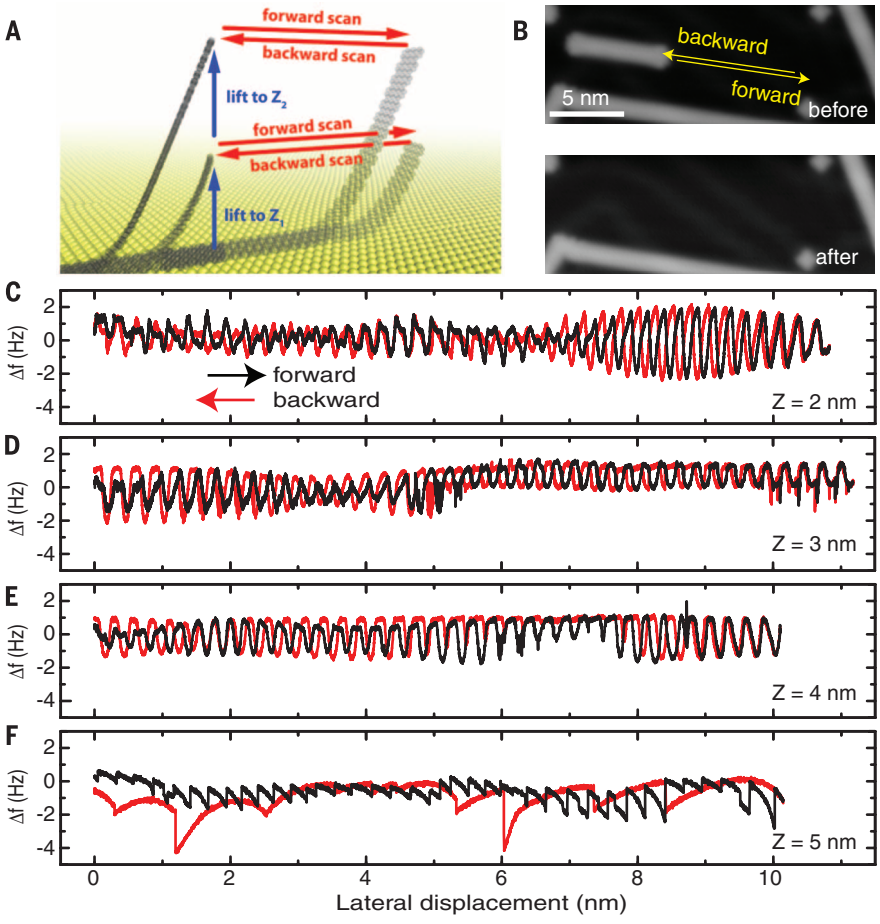

Fig. 2. Frequency shift versus pulling height. (**A**) Schematic drawing of the lateral manipulation procedure. (**B**) STM topographies before and after a GNR has been displaced on the Au(111) surface in the direction of the yellow arrows. The length of the GNR is 6.28 nm, corresponding to seven connected monomers. (**C** to **F**) Frequency shifts accompanying the lateral motion at different heights (z = 2, 3, 4, and 5 nm). Oscillation amplitude A = 38 pm.

that the frequency shift oscillated with a periodicity of 0.28 nm, except when the GNR was driven backward with a tip-surface distance of z = 5 nm. The amplitude of the Δf oscillations was not constant along x but modulated on distances of a few nanometers, varying by a factor of 2. We observed curves with roughly half-periodicity at a small scanning distance of z = 1 to 2 nm (figs. S10 and S11). We also imaged the sample at the end of the process to ensure that we manipulated only the target ribbon (Fig. 2B and fig. S12).

Figure 3 and fig. S13 show the variations of the normal force F_z and lateral force F_x, calculated by molecular dynamics (MD) simulations, as the tip drives the GNR parallel to the unreconstructed Au(111) surface at a low separation (z = 2 nm). Two characteristic lengths of 0.06 and 0.11 nm correspond to the lateral shift between three stable configurations (Fig. 3C). We estimated Δf as recorded in the AFM measurements by multiplying the force derivative $[F_z(x, z+\Delta z)-F_z(x, z)]/\Delta z$ by the conversion factor 0.15 N m^{-1} (Δz = 0.05 nm). The obtained profile (Fig. 3B) maintains the same periodicities of the manipulation curves, allowing comparison between simulations and experiments, although the relative heights of the peaks are different.

The regular profile (Fig. 3B) is considerably modified by the herringbone reconstruction, which deforms the top Au(111) layer and makes it slightly wavy (0.02-nm corrugation). The commensurability degree between the GNR and the substrate is modulated correspondingly, and the same modulation appears in the friction (or frequency shift) profiles. We studied via our simulations the effect of the reconstruction starting at three different locations on the surface (Fig. 3, D to G). The friction force is reduced if the whole GNR lies on the face-centered cubic (FCC) or hexagonal close-packed (HCP) regions (red arrows), is still small when the GNR crosses the boundary between the FCC and HCP regions (green arrow), but increases and reaches a maximum value when the free edge of the GNR or the point of detachment from the substrate sits over the boundary between the FCC and HCP regions (blue arrows). The GNR short edge binds more strongly to the substrate than to the inner atoms, and this effect is more pronounced in the boundary regions between HCP and FCC, where the substrate structure becomes more commensurate with that of the GNR. We established further support for this behavior by means of additional measurements taken on different GNRs (fig. S10); it is also supported by theoretical studies on the pinning role of the nanostructure edges (*24*). The role of the herringbone reconstruction is confirmed by a

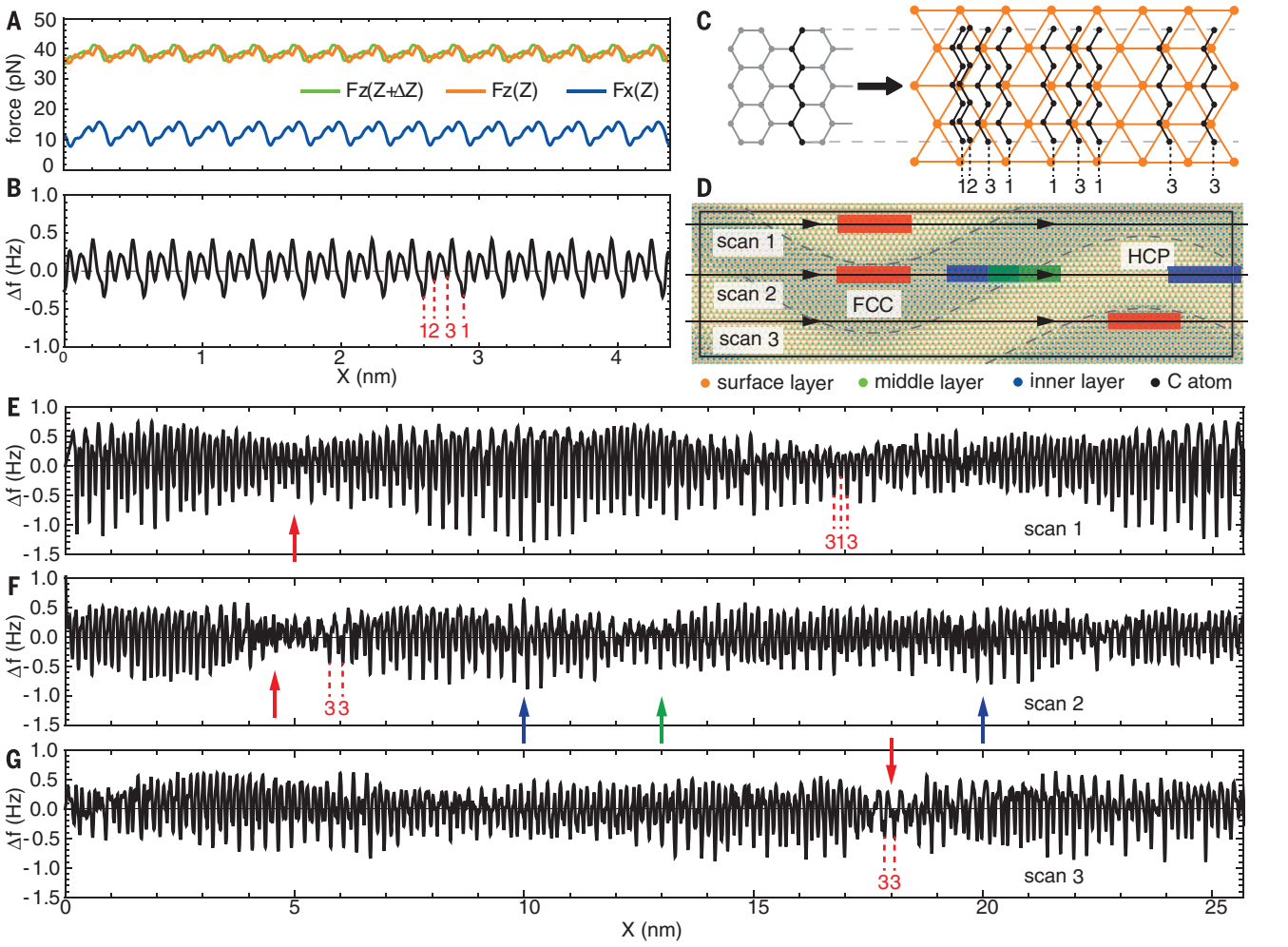

Fig. 3. Simulated sliding behavior. (**A**) Lateral force $F_x(x,z)$ (blue curve) and normal force $F_z(x,z)$ (orange curve) while pulling the 6.28-nm GNR along its longitudinal axis at a distance z = 2 nm from an unreconstructed Au(111) surface. The force F_z has been also calculated at z = 2.05 nm (green curve), which allows us to estimate the frequency shift variation $\Delta f(x)$ shown in (**B**). (**C**) Sketch of a generic row of C atoms in the GNR (black), showing that most of the time, the atoms sit in three nonequivalent configurations marked as 1, 2, and 3 (also marked in other panels); these configurations give rise to a periodicity of ~0.06 nm for short jumps from 1 to 2 or ~0.11 nm for long jumps from 2 to 3 or 3 to 1 (Au atoms are shown in orange). (**D**) Tip trajectories on reconstructed Au(111) for the scan of panels and GNR configurations corresponding to minimum and maximum friction (the simulation cell size is 25.7 × 7.0 nm). Dashed lines represent the boundaries between the HCP and FCC regions, and rectangles represent the attached portion of the GNR during the scan (with red, green, and blue colors corresponding to increasing lateral force). In the background, dots indicate C atoms and surface, middle, and inner layers. (**E** to **G**) Frequency shift $\Delta f(x)$ along the scan lines in (D). The corresponding lateral force profiles are shown in fig. S13.

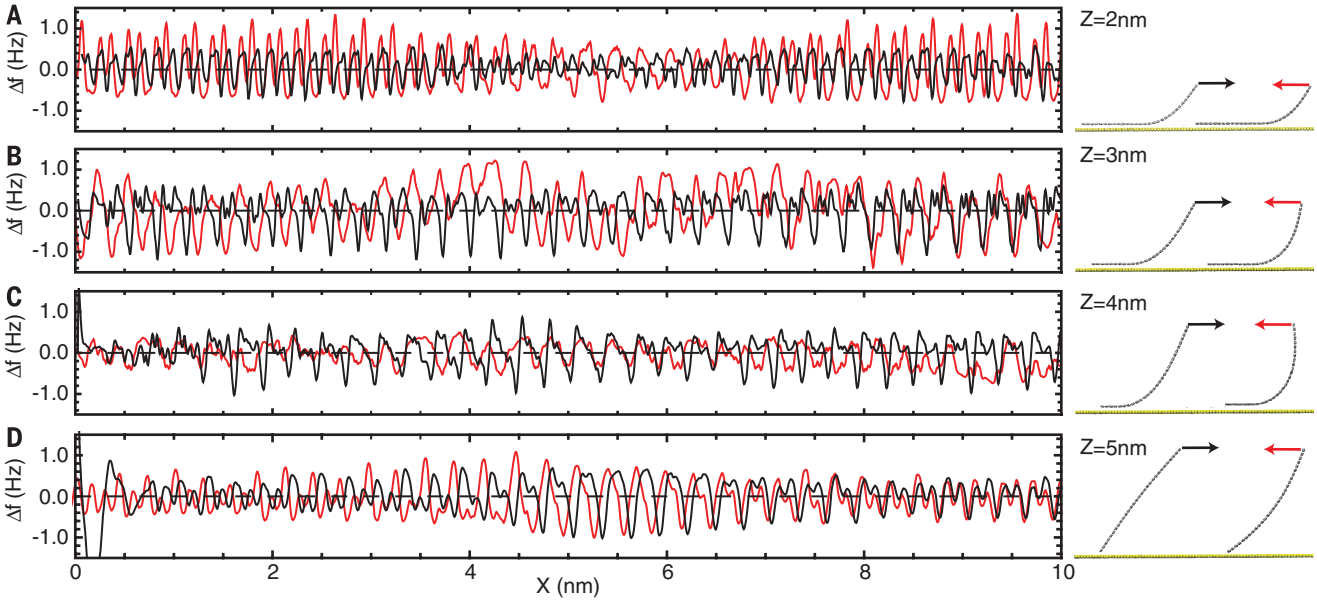

Fig. 4. Simulated frequency shifts at different pulling heights. (**A** to **D**) Frequency shifts for forward and backward scans at z = 2, 3, 4, and 5 nm. Note that the half-periodicity disappears if z > 2 nm. The diagrams on the right show the different bending of the detached portion of the GNR in the forward (black) and backward (red) scans. The corresponding friction force loops are shown in fig. S16.

similar experiment that we attempted on an unreconstructed Ag(111) surface. In this case, the GNRs merged and formed a moiré pattern with the substrate (fig. S14). Manipulation with force values similar to those used on Au(111) was not possible in this case.

Configuration 2 of the GNR (Fig. 3C) becomes unstable as the transitions from 1 to 2 and from 2 to 3 are suppressed. This leads to the half-periodicity that we sometimes observed while scanning at very close separations. Just before a "slip" from 1 to 3 or 3 to 1 occurs, the GNR becomes almost insensitive to the substrate, except for its short edge, which is still attached to the substrate (fig. S15). Because a C atom at this edge lies in a potential well U_0 a few milli–electron volts deep, and it is essentially driven by the spring k = 1.5 N m^{-1} that connects the GNR to the tip apex [C-C bonds have an estimated stiffness of a few hundred newtons per meter (*25*)], we can apply a well-known result of the Prandtl-Tomlinson model for atomic-scale friction and estimate the characteristic parameter $\eta = 4\pi^2 U_0/(ka^2)$ (*26*). The resulting value of η is well below 1 and indicates a continuous transition between the two equilibrium states (this is valid strictly at the particular instant that we have considered). When the GNR is pinned in configuration 1 or 3 and is pulled by the spring at the same time, all C atoms in contact with the substrate oppose a certain resistance, but the overall value of the friction force remains very small (a few hundred piconewtons). Thus, our MD simulations are fully consistent with the commonly accepted interpretation of the superlubricity of graphene. Because of its exceptional lateral stiffness, this material is not prone to stretch and adapt to the substrate lattice while sliding. Combined with the weak interaction between graphene and the substrate, the resulting incommensurability leads to the almost frictionless sliding of the GNR.

We plotted $\Delta f(x)$ curves at increasing separations z from the surface and also reversed the direction of motion (Fig. 4). Configuration 1 becomes unstable when z > 2 nm, and only the 3-to-3 transitions remain (corresponding to the more frequently measured periodicity of 0.28 nm). Lastly, we noticed that the forward and backward scan traces can be either in phase or in antiphase. MD simulations allow us to attribute this effect to the different bending of the suspended portion of the GNR in the two directions (Fig. 4). In the substrate regions with a large friction force, the bending of this portion can be much larger when scanning backward, thus leading to a delay in the slip events (fig. S16). If z = 5 nm (i.e., when the GNR is close to complete detachment), the agreement between the model and experimental results becomes weak; this is presumably due to the fact that the H atoms passivating the GNR edges, which are neglected in the MD simulations, start to play an important role at this point.

The pinning and releasing processes that occur in a sliding contact, as described here, are pivotal in the development of friction between two solid surfaces in reciprocal sliding (*27*). The GNR-Au(111) contact is almost superlubric, with static and kinetic friction force values in the range of 100 pN. The detailed dynamics of the sliding motion are nevertheless influenced by local surface properties, such as the variable degree of commensurability caused by the surface reconstruction. These details are clearly observable when the tip-surface separation z is small but tend to disappear as z increases and the bending (elastic) properties of the suspended piece of GNR become important. Our findings will aid in understanding and improving AFM-based nanomanipulation techniques and will motivate the design of novel nano-functionalized interfaces for friction control.

REFERENCES AND NOTES

1. D. Berman, A. Erdemir, A. V. Sumant, *Mater. Today* **17**, 31–42 (2014).
2. G. S. Verhoeven, M. Dienwiebel, J. W. M. Frenken, *Phys. Rev. B* **70**, 165418 (2004).
3. M. H. Müser, *Europhys. Lett.* **66**, 97–103 (2004).
4. K. Matsushita, H. Matsukawa, N. Sasaki, *Solid State Commun.* **136**, 51–55 (2005).
5. O. Hod, *Phys. Rev. B* **86**, 075444 (2012).
6. R. Zhang *et al.*, *Nat. Nanotechnol.* **8**, 912–916 (2013).
7. J. Cai *et al.*, *Nature* **466**, 470–473 (2010).
8. D. Wei *et al.*, *J. Am. Chem. Soc.* **131**, 11147–11154 (2009).
9. M. A. Rafiee *et al.*, *ACS Nano* **4**, 7415–7420 (2010).
10. X. Li, X. Wang, L. Zhang, S. Lee, H. Dai, *Science* **319**, 1229–1232 (2008).
11. M. Terrones *et al.*, *Nano Today* **5**, 351–372 (2010).
12. M. Ternes, C. P. Lutz, C. F. Hirjibehedin, F. J. Giessibl, A. J. Heinrich, *Science* **319**, 1066–1069 (2008).
13. G. Langewisch, J. Falter, A. Schirmeisen, H. Fuchs, *Adv. Mater. Interfaces* **1**, 1300013 (2014).
14. H.-Q. Mao, N. Li, X. Chen, Q.-K. Xue, *J. Phys. Condens. Matter* **24**, 084004 (2012).
15. G. Langewisch, J. Falter, H. Fuchs, A. Schirmeisen, *Phys. Rev. Lett.* **110**, 036101 (2013).
16. M. Dienwiebel *et al.*, *Phys. Rev. Lett.* **92**, 126101 (2004).
17. X. Feng, S. Kwon, J. Y. Park, M. Salmeron, *ACS Nano* **7**, 1718–1724 (2013).
18. E. Koren, E. Lörtscher, C. Rawlings, A. W. Knoll, U. Duerig, *Science* **348**, 679–683 (2015).
19. M. Peyrard, S. Aubry, *J. Phys. C Solid State Phys.* **16**, 1593–1608 (1983).
20. M. Ma, A. Benassi, A. Vanossi, M. Urbakh, *Phys. Rev. Lett.* **114**, 055501 (2015).
21. D. Dietzel, M. Feldmann, U. D. Schwarz, H. Fuchs, A. Schirmeisen, *Phys. Rev. Lett.* **111**, 235502 (2013).
22. A. E. Filippov, M. Dienwiebel, J. W. M. Frenken, J. Klafter, M. Urbakh, *Phys. Rev. Lett.* **100**, 046102 (2008).
23. S. Kawai *et al.*, *Proc. Natl. Acad. Sci. U.S.A.* **111**, 3968–3972 (2014).
24. N. Varini *et al.*, *Nanoscale* **7**, 2093–2101 (2015).
25. S. Balasubramanian, M. L. Klein, J. I. Siepmann, *J. Chem. Phys.* **103**, 3184–3195 (1995).
26. A. Socoliuc, R. Bennewitz, E. Gnecco, E. Meyer, *Phys. Rev. Lett.* **92**, 134301 (2004).

27. A. Vanossi, N. Manini, M. Urbakh, S. Zapperi, E. Tosatti, *Rev. Mod. Phys.* **85**, 529–552 (2013).

ACKNOWLEDGMENTS

This work was supported in part by the Japan Science and Technology Agency PRESTO program, under the project "Molecular technology and creation of new function;" the National Center of Competence in Research Nanoscale Science program; grant CRSII2 136287/1 from the Swiss National Science Foundation; the Swiss Nanoscience Institute; COST (European Cooperation in Science and Technology) Action MP1303; the European Commission, under the Graphene Flagship (award no. CNECT-ICT-604391); the U.S. Office of Naval Research Basic Research Challenge program; and Comunidad de Madrid, under the MAD2D-CM (S2013/MIT-3007) project. The Partnership for Advanced Computing in Europe (project 2012071262) and the Empa high-performance computing facility Hypatia are acknowledged for computational resources. All data are tabulated in the main text and the supplementary materials.

SUPPLEMENTARY MATERIALS

www.sciencemag.org/content/351/6276/957/suppl/DC1
Materials and Methods
Supplementary Text
Figs. S1 to S16
References (*28*–*44*)

3 September 2015; accepted 25 January 2016
10.1126/science.aad3569

ORGANIC CHEMISTRY

An aromatic ion platform for enantioselective Brønsted acid catalysis

Chirag D. Gheewala, Bridget E. Collins, Tristan H. Lambert*

Chiral acid catalysts are useful for the synthesis of enantioenriched small molecules, but the standard catalysts require laborious and expensive preparations. Here, we describe a chiral Brønsted acid prepared in one step from naturally occurring (–)-menthol and readily available 1,2,3,4,5-pentacarbomethoxycyclopentadiene. Aromatic stabilization serves as a key contributing factor to the potent acidity of the resulting compound, which is shown to catalyze both Mukaiyama-Mannich and oxocarbenium aldol reactions with high efficiency and enantioselectivity. Catalyst loadings as low as 0.01 mole percent and preparative scalability (25 grams) are demonstrated. Alternative amide catalysts are also shown to be promising platforms. In addition to proton catalysis, a chiral anion pathway is demonstrated to be viable with this catalyst system.

Protonation dramatically alters the reactivity of a molecule. As such, Brønsted acid (proton donor) catalysts have long provided a potent strategy for the acceleration of a diverse array of chemical transformations (*1*, *2*). In recent years, the invention of effective chiral Brønsted acid catalysts has enabled the development of numerous asymmetric reactions that furnish valuable chemicals in enantioenriched form (*3*–*6*). By and large, this area of enantioselective Brønsted acid catalysis has been dominated by the binaphthol (BINOL) phosphoric acid class of catalysts originally developed by Akiyama (*7*) and Terada (*8*). Although the utility of these catalysts is unquestionable, the major drawback to substituted BINOL-based catalysts is the lengthy, laborious, and expensive protocol required for their synthesis (*9*), which complicates catalyst optimization and limits their application on scale. Although alternative catalysts have been developed (*10*–*16*), the majority of these still rely on binaphthyl or other unnatural frameworks [e.g., VAPOL (*17*) or SPINOL (*18*)] as the basis of their chirality. This monocultural reliance on a single chiral scaffold is thus a major limiting factor for this important area of catalysis, and the identification of more readily accessible architectures is an important goal. Here, we describe a carbon acid platform for enantioselective Brønsted acid catalysis that uses aromaticity as its central acidifying element.

Although carbon acids typically manifest relatively high pK_a values (where K_a is the acid dissociation constant), several structural modifications can substantially increase the propensity of C–H bonds to undergo ionization by stabilizing the anionic charge of the conjugate bases (*19*, *20*) (Fig. 1A). The most common of these modifications involve σ-delocalization (induction) by electronegative elements or groups and π-delocalization (resonance) by conjugated functionality. A third mode of carbanion stabilization involves a special form of resonance known as aromaticity, epitomized by the dramatic increase (10^{17}) in acidity of cyclopentadiene versus its acyclic analog (*21*) due to the aromatic nature of the cyclopentadienyl anion. In the case of a 1,2,3,4,5-pentacarboxycyclopentadiene (PCCP) **1** (Fig. 1B), the three elements of induction-, resonance-, and aromaticity-induced acidification conspire to produce extremely strong carbon acids that rival the acidity of the mineral acids (*22*–*24*). In fact, the extended conjugation of such substituted cyclopentadienes is such that their acidic protons reside not on carbon but rather on oxygen as hydroxyfulvenes (compare **3**) (*25*). With such strong acidity, we reasoned that PCCPs could serve as potent Brønsted acid catalysts and that ester or amide derivatives incorporating simple chiral alcohols or amines could offer synthetically accessible and effective enantioselective variants. Herein, we demonstrate the realization of this vision with the use of chiral PCCPs as highly efficient enantioselective Brønsted acid catalysts.

1,2,3,4,5-Pentacarbomethoxycyclopentadiene is readily available via the reaction of dimethyl malonate (**4**) and dimethylacetylene dicarboxylate (**5**) in pyridine-acetic acid, followed by treatment with potassium acetate (KOAc) to yield, after acidic workup, the acid **6** (*26*) (Fig. 2A). Compound **6** is a stable crystalline solid, and we have scaled this procedure to produce more than 50 g of this material. To access chiral derivatives, we found that refluxing **6** with excess (–)-menthol in the presence of *N*-methylimidazole in toluene furnished the pentamenthyl ester **7** in 95% yield. Because (–)-menthol is a naturally occurring commodity chemical, we calculate that catalyst **7** can be prepared for about US$4/g (<$5.50/g for the unnatural enantiomer). As an alternative means to introduce chirality, we have also found that treatment of **6** with 1.0 equivalent of a primary amine (e.g., *sec*-naphthethylamine) in refluxing toluene resulted in production of the corresponding monoamide product **8** in good yield. Because in the area of Brønsted acid catalysis, reaction rate has been shown to have a linear correlation with catalyst acidity (*27*), at least to a first approximation, we determined the pK_a (CH_3CN) of both pentaester **6** (8.85 ± 0.05) and monoamide **9** (11.7 ± 0.1) and found that they compared quite favorably with known BINOL-phosphoric acids **10** (*12*–*14*) and other derivatives (Fig. 2B).

To evaluate the effectiveness of chiral PCCPs as enantioselective catalysts, we examined their performance in a Mukaiyama-Mannich reaction, which was known to be amenable to this type of asymmetric promotion (*7*) (Fig. 3A). We observed that 1 mole percent (mol %) of menthol-derived acid **7** catalyzed the addition of silyl ketene acetal **12** to imine **11** in ethyl acetate at –78°C in 1 hour to furnish the adduct **13** in 97% yield and 97% enantiomeric excess (ee). This result compares quite favorably to BINOL-phosphoric acid catalyst **14**, which at 10 mol % loading was reported to catalyze the same reaction (in toluene) over 24 hours to furnish **13** in 98% yield and 89% ee. The loading of cyclopentadienyl catalyst **7** could be reduced to 0.01 mol % without compromising enantioselectivity. In terms of further catalyst screening, monoamides **8** and **15** were also found to induce appreciable enantioselectivity in this reaction, suggesting such catalysts may also be worthy of further development. Nevertheless, pentaester catalysts have thus far proven optimal

Department of Chemistry, Columbia University, New York, NY 10027, USA.
*Corresponding author. E-mail: tl2240@columbia.edu

Downloaded from on February 25, 2016

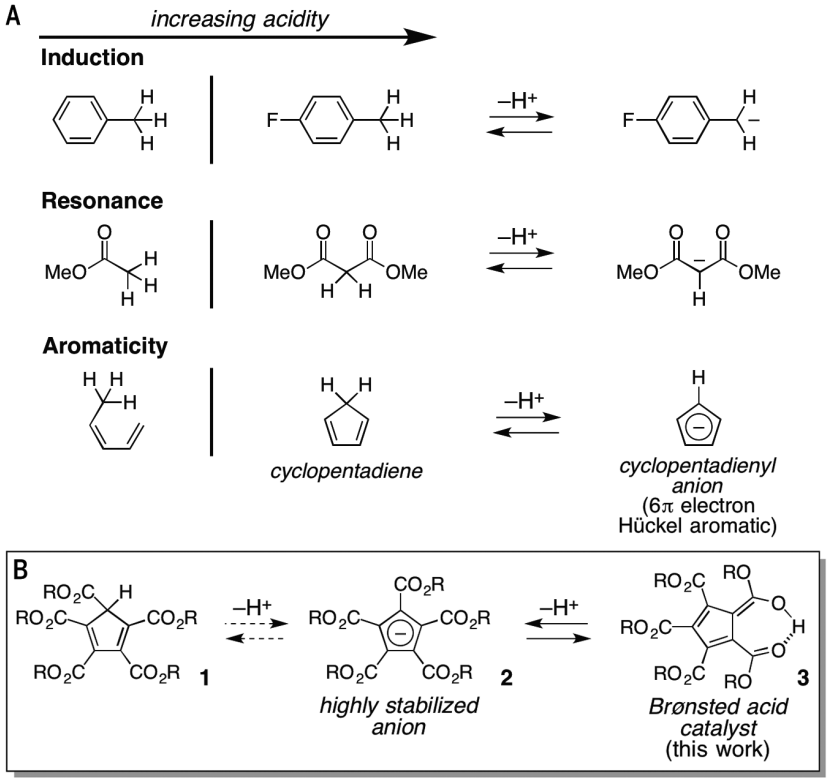

Fig. 1. Tuning carbon acids for catalysis. (**A**) Common strategies for increasing C–H acidity, including induction, resonance, and aromaticity, the latter epitomized by the relatively high acidity of cyclopentadiene. (**B**) PCCPs combine all three acidifying elements to produce powerful Brønsted acid catalysts. Me, methyl; R, generic substituent.

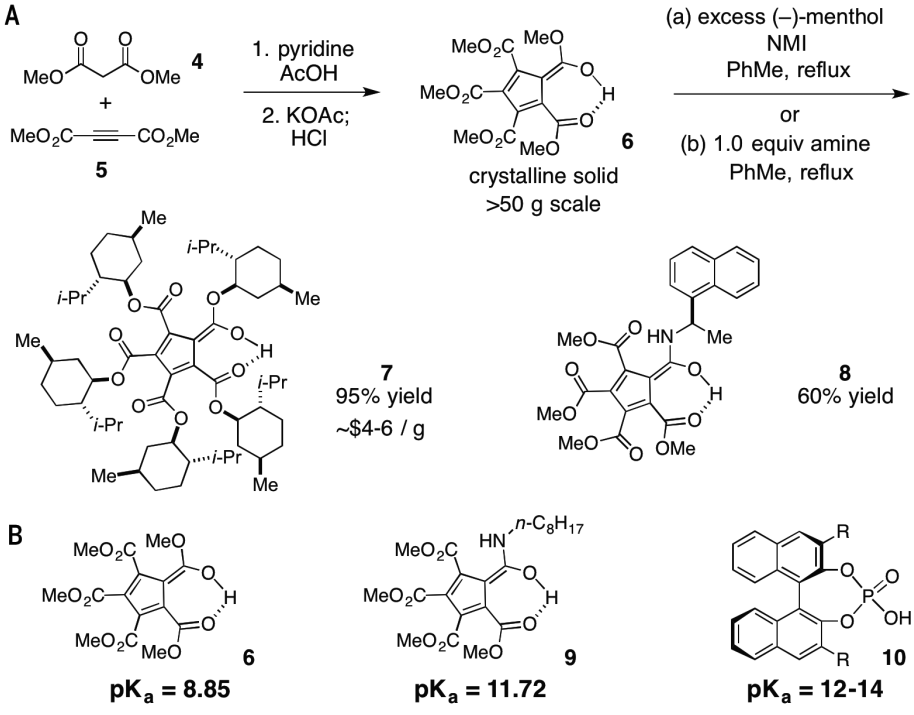

Fig. 2. Catalyst preparation and characterization. (**A**) Synthesis of 1,2,3,4,5-pentacarbomethoxycyclopentadiene **6** and chiral derivatives **7** and **8**. (**B**) pK_a values measured in acetonitrile. i-Pr, isopropyl; Ph, phenyl; NMI, *N*-methylimidazole.

both in terms of reactivity and enantioselectivity, as further exemplified by the performance of the 2-phenylcyclohexanol-derived catalyst **16**.

To investigate the preparative utility of **7**, we conducted a Mannich reaction on scale to produce 25 g of product **13** using 0.1 mol % of the acid catalyst (Fig. 2B, entry 1), which resulted in yield and enantioselectivity comparable to the smaller-scale reactions. In terms of additional substrate scope, we found that a variety of aryl or vinyl imines could be engaged efficiently and with high selectivities (entries 2 to 7). In addition, an aliphatic imine substrate, which is typically challenging for this type of chemistry, could also be productively engaged (entry 8). An alternative silyl ketene acetal bearing a cyclohexyl ring was found to react in high yield and with high selectivity (entry 9). Thus far, reactions that lead to diastereomeric mixtures have exhibited only modest selectivities with catalyst **7** (see the supplementary materials, p. S15).

To demonstrate the potential of PCCPs to move beyond established capabilities, we investigated the enantioselective addition to oxocarbenium ions. In comparison to iminium ion additions, enantioselective reactions with oxocarbenium ions are notoriously difficult to achieve because they typically lack the traditional organizational elements (e.g., hydrogen bonding groups) employed by many asymmetric catalysts. Indeed, only recently have successful approaches to enantioselective oxocarbenium ion chemistry begun to appear [see, e.g., (*28*–*38*)]. We probed the capacity of catalyst **7** to catalyze the addition of silyl ketene acetal **12** to oxocarbenium ion intermediates **29** generated from salicylaldehyde acetals **27**, a so-called Mukaiyama oxocarbenium aldol (Fig. 2C) (*35*). First, we attempted the reaction of benzaldehyde dimethyl acetal, which in fact led to product **30** in high yield but, as expected, with essentially no enantioselectivity (entry 1). On the other hand, the dimethyl acetal of salicylaldehyde led to the production of adduct **31** with an encouraging 71% ee (entry 2). Modification to the diethyl acetal resulted in an appreciable improvement in selectivity to 85% ee for adduct **32** (entry 3), whereas further increasing the steric demand of the acetal substituent to *n*-butyl or *i*-propyl (entries 4 and 5) led to comparable enantioselectivities for products **33** and **34**. An alternative ketone product **35** could also be obtained in 80% ee with the use of a silyl enol ether nucleophile (entry 6). These results demonstrate that chiral PCCPs have the ability to address one of the more notable challenges in asymmetric catalysis, and it is a reasonable expectation that optimization of catalyst structure will enable further improvements in this area.

The mechanistic rationale for the operation of catalyst **7** is shown in Fig. 4A, in which initial protonation of acetal **36** produces intermediate salt **37**. Addition of the silyl ketene acetal **12** to the highly electrophilic oxocarbenium ion (compare **38**) then leads to intermediate **39**. Silyl transfer to the alcohol produced in the initial ionization step would then furnish the ether product **32** and return the acid **7** to the catalytic cycle.

To investigate whether proton catalysis was indeed the operative mode for catalyst **7**, we ran the Mannich reaction of **11** and **12** using deprotonated **7** as its sodium salt (Fig. 4B). As expected, no reaction was observed at −78°C, lending credence to the notion that the catalyst operates as a Brønsted acid (entry 1). Interestingly, however, when the reaction was performed at higher temperatures, product formation was observed, with appreciable enantioenrichment (entry 2). As there was no acidic catalyst proton in this case, this result suggests that perhaps a silylium-catalyzed process was operative, with the cyclopentadienyl group serving as a chiral anion. This notion is supported by the fact that the reaction worked with comparable efficiency and enantioselectivity even in the presence of 2,6-di-*tert*-butyl-4-methylpyridine (entry 3). It is worth noting that chiral anion catalysis has also proven to be an effective strategy for asymmetric synthesis (*36*–*38*), and so the current

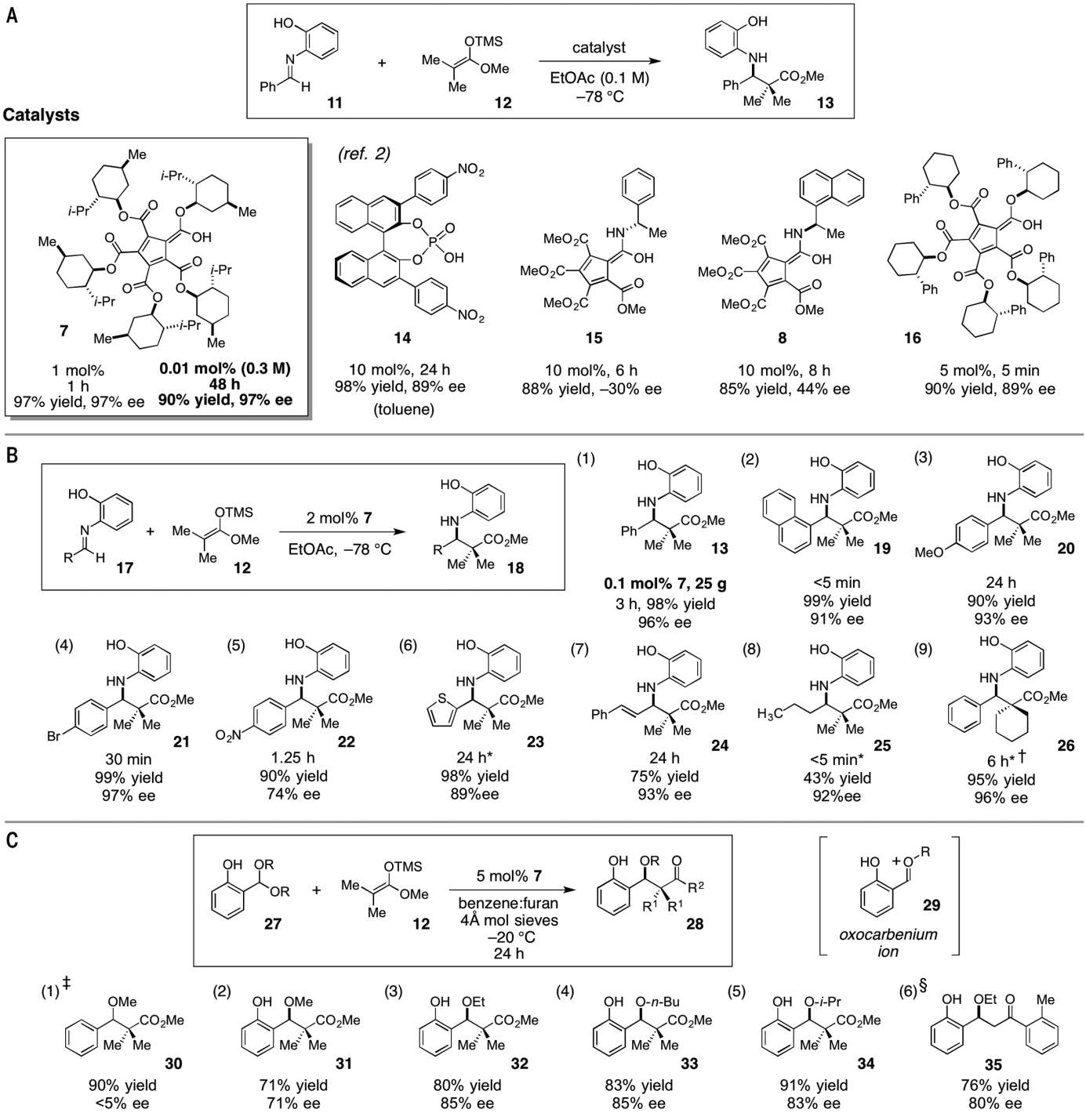

Fig. 3. Exploration of substrate scope. (**A**) Catalyst screen for enantioselective Mukaiyama-Mannich reaction. (**B**) Substrate scope for acid-catalyzed Mannich reaction. (**C**) Enantioselective catalytic Mukaiyama oxocarbenium aldol. *5 mol % **7** was used. †Reaction was performed with the trimethylsilyl ketene acetal derived from methyl cyclohexanecarboxylate. ‡Reaction was performed in ethyl acetate at room temperature for 72 hours. §Reaction was performed with 1-*o*-tolyl-1-trimethylsiloxy ethylene as the nucleophile. R, R^1, and R^2, generic substituent; TMS, trimethylsilyl; EtOAc, ethyl acetate.

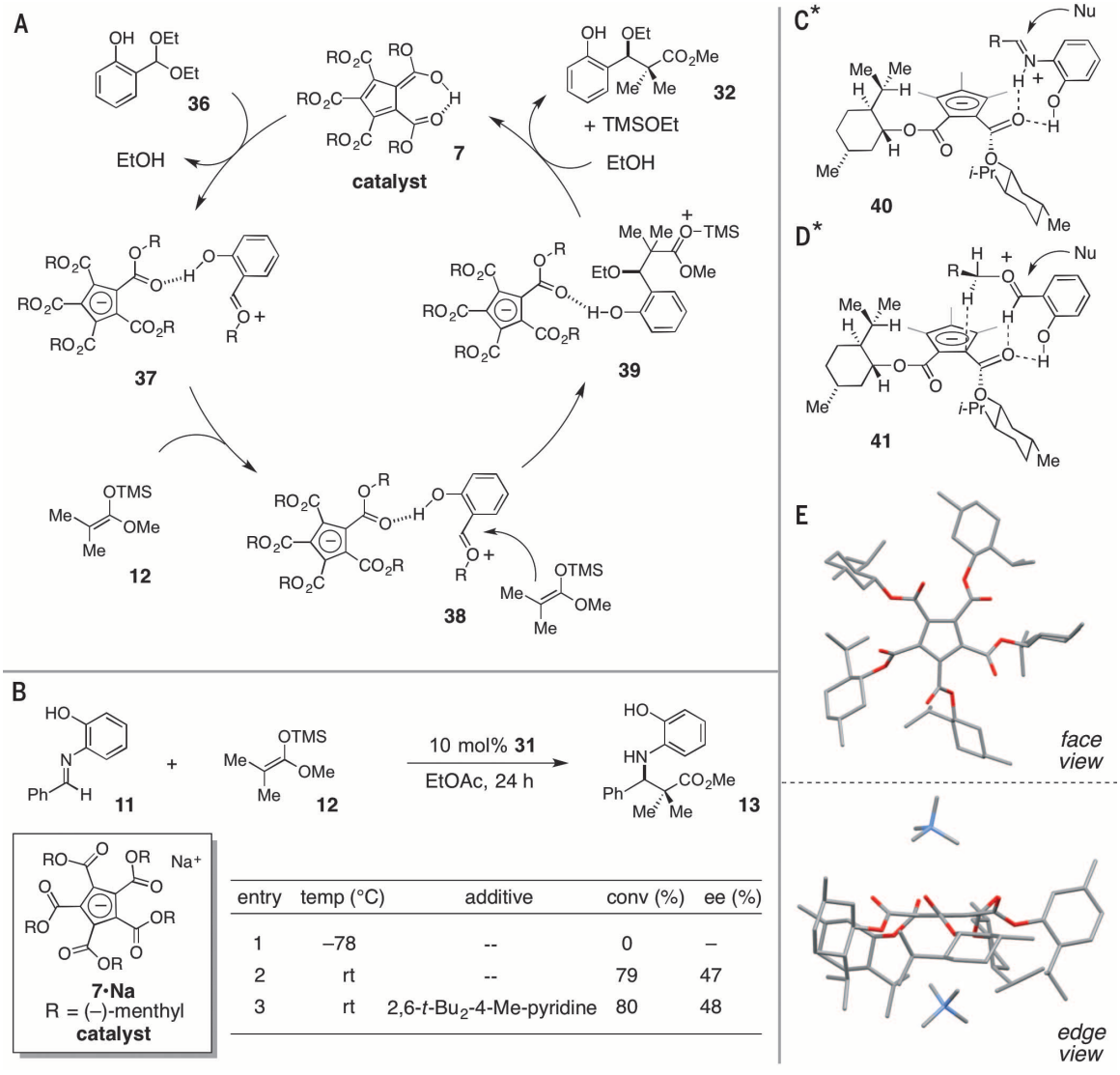

entry	temp (°C)	additive	conv (%)	ee (%)
1	–78	--	0	–
2	rt	--	79	47
3	rt	2,6-*t*-Bu_2-4-Me-pyridine	80	48

Fig. 4. Mechanistic considerations. (**A**) Mechanistic rationale for Mukaiyama oxocarbenium addition reaction. (**B**) Demonstration of an alternative chiral anion catalysis pathway. (**C** and **D**) Stereochemical rationale for (C) the Mannich reaction catalyzed by acid **7** and (D) the oxocarbenium aldol catalyzed by acid **7**. *Three of the carboxylates (at the end of gray bonds) are not shown for clarity. (**E**) Molecular structure of **7•NMe$_4$**. In the face view, the cation is not shown. In the edge view, two adjacent cations are shown.

platform may have utility in this burgeoning area as well.

A stereochemical rationale for this chemistry is shown in Fig. 4C. The presence of multiple rotatable bonds in catalyst **7** renders a number of transition-state organizations plausible. For the Mannich reaction, one possible scenario involves association of the protonated imine and one of the carbonyl oxygens of the catalyst via two hydrogen bonds (Fig. 4C). To accommodate this interaction would require substantial torquing of the carboxyl substituent, thereby placing the iminium in close proximity to an adjacent carboxymenthyl substituent. Blocking of the *re* prochiral face of the iminium would then rationalize the observed stereochemistry.

A similar model can be invoked for the oxocarbenium addition; however, in this case only a single hydrogen bonding substituent is present (Fig. 4D). We speculate that there may be additional organizing interactions between the C–H bonds adjacent to the oxygen of the oxocarbenium ion and the catalyst carbonyl and/or the cyclopentadienyl ring. In this case, π-facial blocking as described above would lead to reaction via the *si* prochiral face, which corresponds to the observed stereoselectivity for the *R*-enantiomer.

We have obtained a single-crystal x-ray structure of catalyst **7** as its tetramethylammonium salt (Fig. 4E). The face view (cation removed) shows a gearing of the carboxyl substituents all in the same direction, presumably to minimize steric repulsion of the menthyl substituents. The alternative edge view shows the substantial dihedral angle between each carbonyl and the cyclopentadienyl ring ranging from 30.6° to 52.1°, with an average of 43.8°, and the orientation of each of the carbonyl oxygens to the same side of the ring. In this view, two adjacent (and equivalent) cations are included, which shows that one half of each ammonium is embedded in a hydrophobic pocket formed by the menthyl groups, whereas the other half is associated with the opposite ring face toward which the carbonyls are oriented. The extent to which this structure is related to the catalytic operation of **7** is not currently known and will be the subject of further study.

The ability to synthesize asymmetric catalysts rapidly, inexpensively, and on scale is an important goal for the field of organic chemistry. The current platform offers a useful advance in this regard by allowing preparation of an effective chiral Brønsted acid catalyst in a single step from a readily available acid core and simple chiral alcohols or amines. The central feature of this platform, the cyclopentadienyl anion, enables the cooperation of multiple acidifying elements to produce powerful acid catalysts.

REFERENCES AND NOTES

1. J. N. Brønsted, *Rec. Trav. Chim.* **42**, 718–728 (1923).
2. T. M. Lowry, *Chem. Ind.* **42**, 43–47 (1923).
3. D. Parmar, E. Sugiono, S. Raja, M. Rueping, *Chem. Rev.* **114**, 9047–9153 (2014).
4. T. Akiyama, J. Itoh, K. Fuchibe, *Adv. Synth. Catal.* **348**, 999–1010 (2006).
5. T. Akiyama, in *Acid Catalysis in Modern Organic Synthesis*, H. Yamamoto, K. Ishihara, Eds. (Wiley-VCH, Weinheim, 2008), pp. 62–107.

6. T. Hashimoto, in *Asymmetric Organocatalysis 2: Brønsted Base and Acid Catalysts, and Additional Topics*, K. Maruoka, Ed. (Georg Thieme Verlag, Stuttgart, New York, 2012), pp. 279–296.
7. T. Akiyama, J. Itoh, K. Yokota, K. Fuchibe, *Angew. Chem. Int. Ed.* **43**, 1566–1568 (2004).
8. D. Uraguchi, M. Terada, *J. Am. Chem. Soc.* **126**, 5356–5357 (2004).
9. I. Ahmed, D. A. Clark, *Org. Lett.* **16**, 4332–4335 (2014).
10. D. Kampen, C. M. Reisinger, B. List, *Top. Curr. Chem.* **291**, 395–456 (2010).
11. T. James, M. van Gemmeren, B. List, *Chem. Rev.* **115**, 9388–9409 (2015).
12. T. Akiyama, *Chem. Rev.* **107**, 5744–5758 (2007).
13. T. Akiyama, K. Mori, *Chem. Rev.* **115**, 9277–9306 (2015).
14. A. Berkessel, P. Christ, N. Leconte, J.-M. Neudörfl, M. Schäfer, *Eur. J. Org. Chem.* **2010**, 5165–5170 (2010).
15. D. Nakashima, H. Yamamoto, *J. Am. Chem. Soc.* **128**, 9626–9627 (2006).
16. M. Treskow, J. Neudörfl, R. Giemoth, *Eur. J. Org. Chem.* **2009**, 3693–3697 (2009).
17. G. B. Rowland *et al.*, *J. Am. Chem. Soc.* **127**, 15696–15697 (2005).
18. F. Xu *et al.*, *J. Org. Chem.* **75**, 8677–8680 (2010).
19. H. Yanai, T. Taguchi, *J. Fluor. Chem.* **174**, 108–119 (2015).
20. H. Yamamoto, D. Nakashima, in *Acid Catalysis in Modern Organic Synthesis*, vol. 1, H. Yamamoto, K. Ishihara, Eds. (Wiley-VCH, Weinheim, 2008), pp. 35–62.
21. F. G. Bordwell, G. E. Drucker, H. E. Fried, *J. Org. Chem.* **46**, 632–635 (1981).
22. M. I. Bruce, A. H. White, *Aust. J. Chem.* **43**, 949–995 (1990).
23. O. Diels, *Ber. Dtsch. Chem. Ges.* **75**, 1452–1467 (1942).
24. O. Diels, U. Kock, *Liebigs Ann. Chem.* **556**, 38–50 (1944).
25. I. E. Mikhailov, G. A. Dushenko, V. I. Minkin, L. P. Olekhnovich, *J. Org. Chem. USSR* **20**, 1509–1514 (1984).
26. E. Le Goff, R. LaCount, *J. Org. Chem.* **29**, 423–427 (1964).
27. K. Kaupmees, N. Tolstoluzhsky, S. Raja, M. Rueping, I. Leito, *Angew. Chem. Int. Ed.* **52**, 11569–11572 (2013).
28. S. E. Reisman, A. G. Doyle, E. N. Jacobsen, *J. Am. Chem. Soc.* **130**, 7198–7199 (2008).
29. N. Z. Burns, M. R. Witten, E. N. Jacobsen, *J. Am. Chem. Soc.* **133**, 14578–14581 (2011).
30. M. R. Witten, E. N. Jacobsen, *Angew. Chem. Int. Ed.* **53**, 5912–5916 (2014).
31. G. C. Tsui, L. Liu, B. List, *Angew. Chem. Int. Ed.* **54**, 7703–7706 (2015).
32. J. H. Kim, I. Čorić, S. Vellalath, B. List, *Angew. Chem. Int. Ed.* **52**, 4474–4477 (2013).
33. I. Čorić, B. List, *Nature* **483**, 315–319 (2012).
34. A. Borokiva, P.-I. Tang, S. Klapman, P. Nagorny, *Angew. Chem. Int. Ed.* **52**, 13424–13428 (2013).
35. L. Ratjen, P. García-García, F. Lay, M. E. Beck, B. List, *Angew. Chem. Int. Ed.* **50**, 754–758 (2011).
36. G. L. Hamilton, E. J. Kang, M. Mba, F. D. Toste, *Science* **317**, 496–499 (2007).
37. K. Brak, E. N. Jacobsen, *Angew. Chem. Int. Ed.* **52**, 534–561 (2013).
38. M. Mahlau, B. List, *Angew. Chem. Int. Ed.* **52**, 518–533 (2013).

ACKNOWLEDGMENTS

Funding for this work was provided by the National Science Foundation under CHE-0953259. C.D.G. is grateful for a National Science Foundation Graduate Fellowship. We thank P. Quinlivan and the Parkin group, as well as D. Paley, for x-ray structure determination and the National Science Foundation (CHE-0619638) for acquisition of an x-ray diffractometer. We are grateful to M. Vetticatt (State University of New York, Binghamton) and V. Roytman for assistance with the stereochemical models. Metrical parameters for the structures of 7•NMe_4 and the oxocarbenium Aldol product are available free of charge from the Cambridge Crystallographic Data Centre under CCDC 1450055 and 1450056, respectively.

SUPPLEMENTARY MATERIALS

www.sciencemag.org/content/351/6276/961/suppl/DC1
Materials and Methods
Figs. S1 to S4
Tables S1 to S4
References (*39*–*57*)

20 July 2015; accepted 27 January 2016
10.1126/science.aad0591

CATALYSIS

Palladium-tin catalysts for the direct synthesis of H_2O_2 with high selectivity

Simon J. Freakley,[1]*† Qian He,[2,3]† Jonathan H. Harrhy,[1] Li Lu,[2] David A. Crole,[1] David J. Morgan,[1] Edwin N. Ntainjua,[1] Jennifer K. Edwards,[1] Albert F. Carley,[1] Albina Y. Borisevich,[3,4] Christopher J. Kiely,[2] Graham J. Hutchings[1]*

The direct synthesis of hydrogen peroxide (H_2O_2) from H_2 and O_2 represents a potentially atom-efficient alternative to the current industrial indirect process. We show that the addition of tin to palladium catalysts coupled with an appropriate heat treatment cycle switches off the sequential hydrogenation and decomposition reactions, enabling selectivities of >95% toward H_2O_2. This effect arises from a tin oxide surface layer that encapsulates small Pd-rich particles while leaving larger Pd-Sn alloy particles exposed. We show that this effect is a general feature for oxide-supported Pd catalysts containing an appropriate second metal oxide component, and we set out the design principles for producing high-selectivity Pd-based catalysts for direct H_2O_2 production that do not contain gold.

Currently, the demand for H_2O_2 is met by an indirect process, which produces H_2O_2 through the sequential hydrogenation and oxidation of a substituted anthraquinone (*1*). For economic reasons, the process is operated at large scale and produces concentrated H_2O_2. In reality, many applications, such as disinfection and water purification, require only dilute H_2O_2, which means that concentrated H_2O_2 must be diluted at the point of use. Research into the direct synthesis of H_2O_2 from H_2 and O_2 as a more suitable solution to small-scale, on-site H_2O_2 production has focused on palladium (Pd)–based catalysts (*2*–*4*). However, H_2O_2 is itself highly reactive, and the presence of H_2 favors hydrogenation and decomposition reactions that form water. The addition of strong acids and halides to the reaction medium can suppress the sequential hydrogenation and degradation in supported Pd catalysts (*5*) but can also promote metal leaching and requires further purification of the H_2O_2 before use.

Bimetallic Au-Pd alloy catalysts have been extensively studied as catalysts for the direct H_2O_2 synthesis reaction on a number of support materials, including TiO_2, SiO_2, and activated carbon (*6*–*9*). Yields comparable to monometallic Pd catalysts can be achieved without the need for acid and halide additives in the reaction mixture, and 95% selectivity to H_2O_2 can be achieved with Au-Pd alloy nanoparticles (NPs) dispersed on an acid-pretreated activated carbon support material (*10*). Hydrogen peroxide hydrogenation could be decoupled from H_2O_2 synthesis with an acid pretreatment that blocked sites on the carbon support material responsible for H_2O_2 degradation (*10*). Although this approach was very successful on an activated carbon support material, the same blocking effect could not be fully achieved on other commercial support materials such as SiO_2 and TiO_2.

Because O_2 dissociation is undesirable in the direct synthesis of H_2O_2, the reaction can be treated as a selective hydrogenation of O_2. We explored other Pd-metal combinations that are used for selective hydrogenation reactions as potential catalysts for H_2O_2 synthesis, focusing on nonprecious metals to lower costs. Tin (Sn) has been used to modify hydrogenation catalysts in reactions such as the selective hydrogenation of 1,3-butadiene (*11*). Further examples have been reported for the liquid-phase hydrogenation of hexa-1,3-diene and hexa-1,5-diene (*12*) as well as the hydrogenation of unsaturated alcohols (*13*). The addition of Sn to Pd or Pt can alter the behavior of the catalyst during hydrogenation reactions and, in particular, may have an effect on subsequent reactions of the products with the catalyst.

We report the development of Sn-containing Pd catalysts on commercially available TiO_2 and SiO_2 supports that can achieve >95% selectivity toward direct H_2O_2 synthesis. These catalysts, after being subjected to an appropriate heat treatment regimen, obviate the need for pretreating the support with acids and contain far less precious metal than Au-Pd catalysts. We also present the general principles whereby high-selectivity catalysts can be obtained with other Pd-metal combinations.

Simple impregnation of Au and Pd metal salts onto many catalyst supports has been shown to generate highly active catalysts for direct H_2O_2 synthesis. In addition, high-temperature calcination or reduction treatments are known to be crucial to improve the stability of the catalyst. As a starting point, we used this simple catalyst preparation methodology to prepare a 2.5 weight percent (wt%) Pd–2.5 wt % Sn/TiO_2 catalyst as well as its monometallic analogs (*8*, *10*). A synergistic effect toward higher H_2O_2 productivity was observed when both metals were present

[1]Cardiff Catalysis Institute and School of Chemistry, Cardiff University, Cardiff CF10 3AT, UK. [2]Department of Materials Science and Engineering, Lehigh University, Bethlehem, PA 18015, USA. [3]Materials Science and Technology Division, Oak Ridge National Laboratory, Oak Ridge, TN 37831, USA. [4]Center for Nanophase Materials Sciences, Oak Ridge National Laboratory, Oak Ridge, TN 37831, USA.
***Corresponding author. E-mail: hutch@cf.ac.uk (G.J.H.); freakleys@cf.ac.uk (S.J.F.)** †These authors contributed equally to this work.

Downloaded from on February 25, 2016

Table 1. Direct H_2O_2 synthesis and degradation testing. Catalytic testing results of the optimized 3 wt % Pd–2 wt % Sn/TiO_2, 1 wt % Pd–4 wt % Sn/SiO_2, and 2.5 wt% Pd–2.5 wt % Au/TiO_2 catalysts after being subjected to various heat treatment regimens. H_2O_2 productivity was determined under the following reaction conditions: 5% H_2/CO_2 (2.9 MPa) and 25% O_2/CO_2 (1.1 MPa), 8.5 g solvent (2.9 g HPLC water, 5.6 g MeOH), 0.01 g catalyst, 2°C, 1200 rpm, 30 min. Second-use values are in parentheses. H_2O_2 degradation was calculated from the loss of H_2O_2 using standard reaction conditions: 5% H_2/CO_2 (2.9 MPa), 8.5 g solvent (5.6 g MeOH, 2.22 g H_2O, and 0.68 g 50% H_2O_2), 0.01 g catalyst, 2°C, 1200 rpm, 30 min. n.d., not determined.

Entry	Catalyst	H_2O_2 productivity (mol kg_{cat}^{-1} $hour^{-1}$)	H_2O_2 degradation (mol kg_{cat}^{-1} $hour^{-1}$)	H_2 conversion (%)	H_2O_2 selectivity (%)
	3 wt % Pd–2 wt % Sn/TiO_2				
1	500°C, 3 hours, air	68 (14)	65	n.d.	n.d.
2	+ Reduced 200°C, 2 hours	60 (60)	300	20	46
3	+ 400°C, 4 hours, air	61 (60)	0	9	96
	2.5 wt % Pd–2.5 wt % Au/TiO_2				
4	400°C, 3 hours, air	64 (64)	235	22	66
5	+ Reduced 200°C, 2 hours	135	396	n.d.	n.d.
6	+ 400°C, 4 hours, air	82	277	n.d.	n.d.
	1 wt % Pd–4 wt % Sn/SiO_2				
7	400°C, 3 hours, air	66 (22)	62	n.d.	n.d.
8	+ Reduced 200°C, 2 hours	76 (76)	340	13	70
9	+ 400°C, 3 hours, air	50 (50)	0	8	95

after calcination in static air at 500°C for 3 hours (table S1). The measured activity of this 2.5 wt % Pd–2.5 wt % Sn/TiO_2 catalyst (62 mol kg^{-1} $hour^{-1}$) is similar to that of a 2.5 wt % Pd–2.5 wt % Au/TiO_2 catalyst (*8*) (i.e., 64 mol kg^{-1} $hour^{-1}$). We then optimized the Sn/Pd ratio while maintaining a total metal content of 5 wt% (table S2) and found an optimum nominal composition, 3 wt % Pd–2 wt % Sn/TiO_2, that exhibited an H_2O_2 productivity of 68 mol kg^{-1} $hour^{-1}$ (Table 1, entry 1). By comparison, the H_2O_2 degradation activity of the optimized Sn-Pd catalyst was very low relative to that reported for Au-Pd systems (65 mol kg^{-1} $hour^{-1}$ for 3 wt% Pd–2 wt% Sn/TiO_2 versus 235 mol kg^{-1} $hour^{-1}$ for 2.5 wt % Pd–2.5 wt % Au/TiO_2); this result indicates that Sn is also playing a beneficial role in preventing the overhydrogenation and decomposition of H_2O_2. However, the Sn-Pd catalysts calcined at 500°C for 3 hours under static air were unstable to multiple reaction cycles (Table 1, entry 1).

The nature of the catalyst surface, in particular the oxidation state of the active metal, is crucial to obtaining high selectivity. Therefore, we characterized this 3 wt % Pd–2 wt % Sn/TiO_2 catalyst after calcination by x-ray photoelectron spectroscopy (XPS). This showed that the majority of the surface Pd was present as Pd^{2+}, whereas the Sn Auger parameter showed that SnO_2 was present in the calcined catalyst (fig. S1 and table S3). Analysis of the nanostructure of this catalyst using high-angle annular dark-field scanning transmission electron microscopy (HAADF-STEM) and electron energy loss spectroscopy (EELS) revealed that the SnO_x was present as a thin amorphous film (thickness <2 nm) coating the TiO_2 support particles (Fig. 1, A to D, and fig. S2). A population of 5- to 10-nm NPs was also present in the sample that contained a homogeneous mixture of both Pd and Sn (Fig. 1, A to D, and fig. S3). Lattice fringe fitting of these particles strongly suggests a metallic Pd-Sn alloy structure rather than segregated metal/metal oxides or mixed oxides, which would mean that only the surface of the particles is oxidized. Many sub–2-nm Pd-rich NPs were also observed and were often associated with the SnO_x thin films, and because these species were much less numerous in a 5 wt% Sn-only/TiO_2 sample (fig. S4), they were primarily associated with the PdO_x component in the bimetallic catalyst.

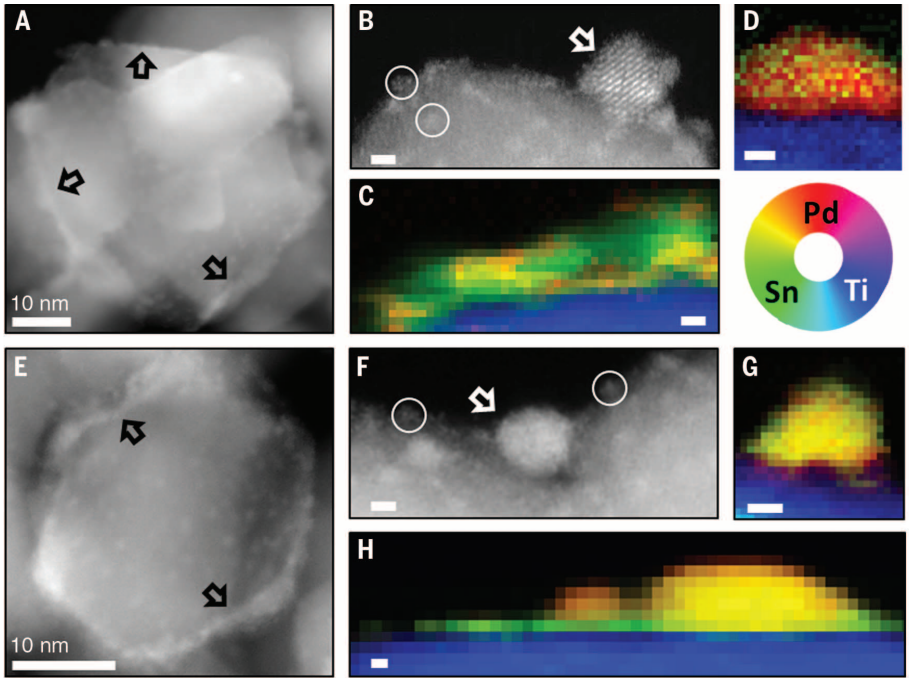

Fig. 1. Microstructural analysis of 3 wt % Pd–2 wt % Sn/TiO_2. (**A** to **D**) Representative STEM-HAADF grayscale images and STEM-EELS (RGB) maps of 3 wt % Pd–2 wt % Sn/TiO_2 catalysts at the oxidized stage. (**E** to **H**) Images and maps as in (A) to (D) for the same catalyst at the oxidized-reduced-oxidized (O-R-O) stage. From the STEM-HAADF images, three distinct supported species are found in both these catalysts: (i) relatively large (i.e., 3 to 10 nm) nanoparticles (white arrows), (ii) smaller clusters on the nanometer or subnanometer scale (white circles), and (iii) continuous film covering the TiO_2 support surface. The qualitative elemental distribution of Pd, Sn, and Ti is represented by red, green, and blue, respectively, in the STEM-EELS maps. As shown in (C) and (H), the continuous film mainly contains Sn, which either supports or embeds the smaller Pd-rich species; (D) and (G) show that the larger particles are Pd-Sn alloys. Scale bars in the images and maps represent 1 nm unless noted otherwise.

A limiting factor in achieving high selectivity toward H_2O_2 with Au-Pd/TiO_2 catalysts prepared

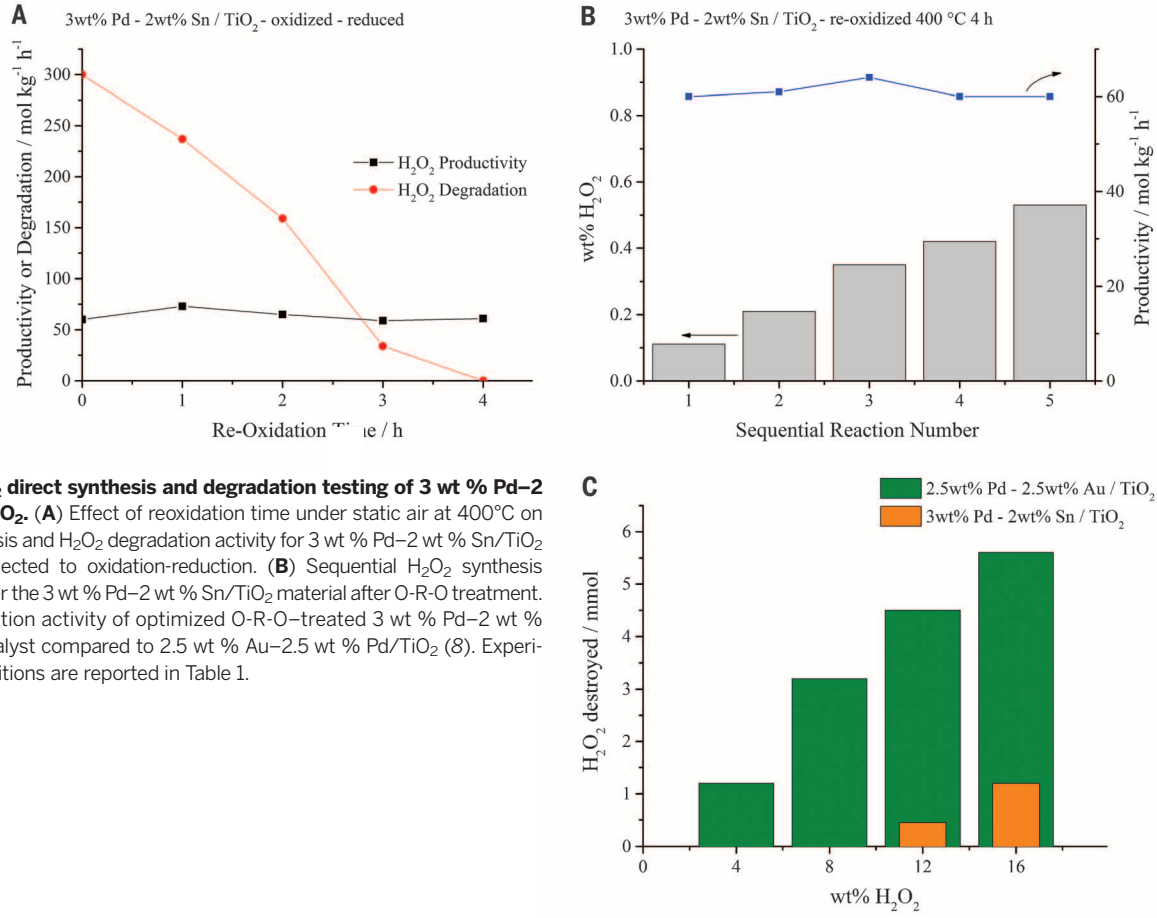

Fig. 2. H_2O_2 direct synthesis and degradation testing of 3 wt % Pd–2 wt % Sn/TiO_2. (**A**) Effect of reoxidation time under static air at 400°C on H_2O_2 synthesis and H_2O_2 degradation activity for 3 wt % Pd–2 wt % Sn/TiO_2 catalyst subjected to oxidation-reduction. (**B**) Sequential H_2O_2 synthesis reactions over the 3 wt % Pd–2 wt % Sn/TiO_2 material after O-R-O treatment. (**C**) Degradation activity of optimized O-R-O–treated 3 wt % Pd–2 wt % Sn/TiO_2 catalyst compared to 2.5 wt % Au–2.5 wt % Pd/TiO_2 (*8*). Experimental conditions are reported in Table 1.

by the wet impregnation method is that the catalyst nanoparticles exhibit a variation in composition with particle size, with the smallest particles being Pd-rich (*9*). These small Pd-rich NPs are likely to be highly active for H_2O_2 synthesis and also for its subsequent hydrogenation and decomposition, as has been shown when Au-Pd catalysts are prepared by colloidal techniques with particle sizes typically 2 to 4 nm (*14*). In the case of the Sn-Pd system, the small Pd-rich NPs are often associated with the amorphous SnO_x films. We postulated that it might be possible to further decrease the H_2O_2 degradation activity of the catalyst by inducing encapsulation of the ultrasmall Pd-rich NPs by this SnO_x film. We therefore used subsequent thermal treatments in an attempt to induce a strong metal-support interaction (SMSI) between the Pd and SnO_x layer (*15*–*20*). We first added a low-temperature reduction step (200°C, 2 hours, 5% H_2 in Ar), which made the catalysts stable to multiple reaction cycles (Table 1, entry 2). However, the H_2O_2 degradation activity increased markedly, from 65 mol kg^{-1} $hour^{-1}$ to 300 mol kg^{-1} $hour^{-1}$; this rate increase was associated with the reduction of Pd^{2+} to metallic Pd, as shown by XPS (table S3 and fig. S1). Metallic Pd is known to be a more effective H_2O_2 hydrogenation catalyst (*7*).

Detailed STEM analysis of this reduced sample was carried out to investigate any structural changes in the sample on reduction (figs. S5 and S6). Analysis identified the presence of thin SnO_x films, sub–2-nm Pd NPs, and 5- to 10-nm NPs whose lattice fringe spacings and angles were consistent with Pd-Sn metallic alloy phases. We then reoxidized this reduced catalyst to restore Pd^{2+} as the predominant surface species (as confirmed by XPS; fig. S1 and table S3), thereby completing an oxidation-reduction-oxidation (O-R-O) cycle, with the aim of encapsulating the small Pd species and regenerating the oxidized Pd-Sn surface on the larger NPs. Reoxidizing the reduced catalyst for various time periods at 400°C under static air had little effect on the H_2O_2 synthesis productivity but markedly decreased the H_2O_2 degradation activity (Fig. 2A). After 4 hours of reoxidation treatment, the catalyst showed no activity toward H_2O_2 degradation and could produce H_2O_2 with a H_2 selectivity of >95% (Table 1, entry 3). This catalyst was stable to multiple reaction cycles and showed negligible leaching of Sn (0 ppb) or Pd (2 ppb) during a 30-min reaction, as measured by inductively coupled plasma mass spectrometry. This reoxidized 3 wt % Pd–2 wt % Sn/TiO_2 catalyst was subjected to further H_2O_2 testing, including multiple sequential H_2O_2 synthesis tests (Fig. 2B). After running the reaction five times consecutively, the H_2O_2 concentration increased linearly to 0.53 wt %, retaining both the high H_2O_2 synthesis and zero H_2O_2 degradation rates. This result implies that no subsequent decomposition or hydrogenation reactions of H_2O_2 took place with this catalyst. The reoxidized 3 wt % Pd–2 wt % Sn/TiO_2 catalyst was also tested for H_2O_2 degradation with varying concentrations of H_2O_2 under a pressure of 5% H_2/CO_2 (Fig. 2C) and showed no degradation of H_2O_2 in solutions of up to 8 wt%, whereas the corresponding Au-Pd/TiO_2 catalyst showed substantially higher H_2O_2 degradation activity at all concentrations studied.

The nanostructure of the catalyst after the O-R-O treatment was characterized to identify any structural changes that could be responsible for the observed high selectivity. Three structures were again revealed to be present in the catalyst: amorphous SnO_x films on the TiO_2 particles, small Pd species associated with these films, and larger Pd-Sn NPs (Fig. 1, E to H, and figs. S7 and S8).

Detailed EELS analysis of the thin film regions (fig. S9) after various heat treatments indicated the presence of SnO_x films, which can be either reduced or oxidized depending on the final heat treatment stage, as indicated by the absence or presence of the O K edge in the EELS spectrum. In contrast to the thin films, EELS analysis of Sn-Pd nanoparticles (fig. S10) at different stages of the heat treatment cycle showed no clear O K edge. This confirms these nanoparticles to be metallic Pd-Sn alloys, at least in the bulk, which

is also consistent with the lattice fringe fitting. Some slight oxidation of the surface of these particles is possible, as detected by our XPS measurements, but at such a level that it is below the detectability limit of the EELS measurements. The 3 wt % Pd–2 wt % Sn/TiO_2 catalyst after the O-R-O cycle shows evidence that the small Pd-rich NPs responsible for high hydrogenation activity often appear to be encapsulated in the amorphous SnO_x layer (fig. S11). We suggest that by generating SMSIs that can effectively "bury" the population of smaller Pd-rich NPs, the H_2O_2 degradation activity of the catalyst is limited (Fig. 3A). The larger uncovered Pd-Sn alloy NPs are then mainly responsible for the H_2O_2 production and are inherently less prone than Pd-Au NPs to cause subsequent H_2O_2 degradation. The monometallic Pd/TiO_2 catalyst that was subjected to the optimized O-R-O cycle (table S4, entries 1 and 2) did not induce this effect, confirming that the amorphous layer responsible for SMSI is not TiO_2-based.

To investigate whether this effect was unique to the 2 wt % Sn–3 wt % Pd/TiO_2 catalyst, we applied similar heat treatment protocols to the analogous 2.5 wt % Au–2.5 wt % Pd/TiO_2 system. The catalytic results (Table 1, entries 4 to 6) show that the same suppression of H_2O_2 degradation was also not observed for a corresponding O-R-O Au-Pd/TiO_2 catalyst. Results obtained for monometallic Pd and bimetallic Sn-Pd catalysts (table S4, entries 3 to 5) also indicate that the reduction step is crucial, as three oxidative treatments failed to induce the effect. Note that the 200°C reduction temperature used in this study is much lower than that typically reported to induce SMSI effects in TiO_2-only supported catalyst systems (*21*). To demonstrate the proposed SMSI effect with SnO_2, we also prepared a "model" 5 wt % Pd/SnO_2 catalyst and studied it by electron microscopy. In the oxidized state, EELS mapping showed that the PdO_x particles appear to be clean (Fig. 3B and figs. S12 and S13), whereas after the O-R-O treatment, the Pd particles showed clear evidence of an SnO_x overlayer (Fig. 3C and figs. S14 and S15).

Further evidence that the suppression of the H_2O_2 degradation does not originate from encapsulation of small Pd particles by TiO_2 but is an SMSI effect arising from the secondary SnO_x component was obtained by using a nonreducible SiO_2 support in place of the TiO_2. When the Sn/Pd ratio on SiO_2 was optimized (table S5) and the same O-R-O heat treatment regimen was applied (Table 1, entries 7 to 9), the resulting 1 wt % Pd–4 wt % Sn/SiO_2 catalyst produced H_2O_2 at a rate of 50 mol kg^{-1} $hour^{-1}$ (Table 1, entry 9) and showed no activity toward subsequent H_2O_2 degradation. This 1 wt % Pd–4 wt % Sn/SiO_2 catalyst showed no propensity to decompose or hydrogenate H_2O_2 even in solutions containing up to 12 wt % H_2O_2 (fig. S16). Furthermore, the catalytic performance of the 1 wt% Pd–4 wt % Sn/SiO_2 material was stable through multiple uses (table S5). XPS analysis (fig. S1 and table S4) and electron microscopy characterization (figs. S17 and S18) of the 1 wt % Pd–4 wt % Sn/SiO_2 catalyst showed compositional and structural features (i.e., amorphous SnO_x films and associated ultrasmall Pd-rich NPs, as well as larger Pd-Sn alloy particles) analogous to its 3 wt % Pd–2 wt % Sn/TiO_2 counterpart.

Our approach of encapsulating small Pd-rich species generated by wet impregnation preparations with secondary oxides can be generalized if the second metal oxide added to the Pd/primary oxide (e.g., TiO_2/SiO_2) support system (i) shows no decomposition activity toward H_2O_2 when in oxide form, (ii) forms an alloy or mixed oxide phase with Pd, and (iii) can encapsulate small Pd-rich particles by SMSI. Following these design rules with the use of a nominal composition of 0.5 wt % Pd–4.5 wt % M/TiO_2 that had been subjected to the optimized O-R-O treatment, we synthesized a series of bimetallic catalysts where M = Ni, Zn, Ga, In, and Co. All of these catalysts showed activity for H_2O_2 synthesis (30 to 64% of that displayed by the Sn-Pd catalyst) and no activity for H_2O_2 degradation (table S6). Thus, our approach opens up the possibility of designing reusable catalysts with greatly reduced precious metal content while still retaining high selectivity to H_2O_2.

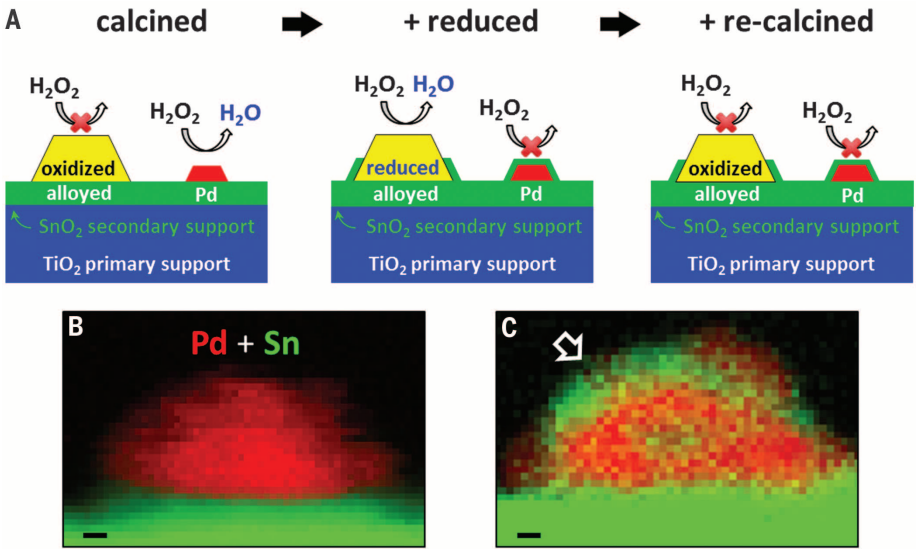

Fig. 3. Evolution of catalyst through oxidation-reduction-oxidation cycle. (**A**) Proposed mechanism for switching off H_2O_2 hydrogenation by small Pd-rich NPs through a strong metal-support interaction (SMSI). The secondary metal must both form an alloy with Pd and oxidize to form a secondary support (i.e., SnO_x) that can encapsulate the relatively small, poorly alloyed, Pd-rich NPs after an O-R-O cycle. This step prevents these NPs from decomposing and hydrogenating the H_2O_2 product. (**B** and **C**) STEM-EELS mapping of a 5 wt % Pd/SnO_2 model catalyst at the oxidized (B) and O-R-O (C) stages, showing partial encapsulation of the Pd NP (red) by SnO_x (green) after the O-R-O heat treatment cycle. The Sn intensities in the SnO_2 support area were deliberately saturated to reveal any relatively weak signals in the particle region. Scale bars, 1 nm.

REFERENCES AND NOTES

1. J. K. Edwards, G. J. Hutchings, *Angew. Chem. Int. Ed.* **47**, 9192–9198 (2008).
2. H. Henkel, W. Weber, U.S. Patent 1,108,752 (1914).
3. J. H. Lunsford, *J. Catal.* **216**, 455–460 (2003).
4. D. P. Dissanayake, J. H. Lunsford, *J. Catal.* **206**, 173–176 (2002).
5. V. R. Choudhary, C. Samanta, P. Jana, *Appl. Catal. A* **317**, 234–243 (2007).
6. J. K. Edwards *et al.*, *Catal. Sci. Technol* **3**, 812–818 (2013).
7. J. K. Edwards *et al.*, *J. Catal.* **292**, 227–238 (2012).
8. J. K. Edwards *et al.*, *J. Catal.* **236**, 69–79 (2005).
9. J. K. Edwards, S. J. Freakley, A. F. Carley, C. J. Kiely, G. J. Hutchings, *Acc. Chem. Res.* **47**, 845–854 (2014).
10. J. K. Edwards *et al.*, *Science* **323**, 1037–1041 (2009).
11. K. Pattamakomsan *et al.*, *Catal. Today* **164**, 28–33 (2011).
12. E. A. Sales, J. Jove, M. de Jesus Mendes, F. Bozon-Verduraz, *J. Catal.* **195**, 88–95 (2000).
13. J. P. Stassi, P. D. Zgolicz, S. R. de Miguel, O. A. Scelza, *J. Catal.* **306**, 11 (2013).
14. J. Pritchard *et al.*, *Langmuir* **26**, 16568–16577 (2010).
15. S. J. Tauster, S. C. Fung, R. L. Garten, *J. Am. Chem. Soc.* **100**, 170–175 (1978).
16. G. L. Haller, D. E. Resasco, *Adv. Catal.* **36**, 173–235 (1989).
17. Q. Fu, T. Wagner, *Surf. Sci. Rep.* **62**, 431–498 (2007).
18. D. W. Goodman, *Catal. Lett.* **99**, 1–4 (2005).
19. S. J. Tauster, *Acc. Chem. Res.* **20**, 389–394 (1987).
20. J. Liu, *Chem. Cat. Chem* **3**, 934 (2011).
21. Q. Fu, T. Wagner, S. Olliges, H. D. Carstanjen, *J. Phys. Chem. B* **109**, 944–951 (2005).

ACKNOWLEDGMENTS

Supported by NSF Major Research Instrumentation Program grant MRI/DMR-1040229 (C.J.K.); the U.S. Department of Energy, Office of Science, Basic Energy Sciences, Materials Sciences and Engineering Division (Q.H. and A.Y.B.); a user project supported by Oak Ridge National Laboratory's Center for Nanophase Materials Sciences, sponsored by the Scientific User Facilities Division, Office of Science, Basic Energy Sciences, U.S. Department of Energy; and European Research Council grant ERC-2011-ADG, grant agreement no. 291319, acronym "AFTERTHEGOLDRUSH" (G.J.H.). The data contained in this paper are archived at DOI: 10.17035/d.2016.0008119507.

SUPPLEMENTARY MATERIALS

www.sciencemag.org/content/351/6276/965/suppl/DC1
Materials and Methods
Figs. S1 to S18
Tables S1 to S6
References (*22*–*24*)

2 October 2015; accepted 25 January 2016
10.1126/science.aad5705

CELL NUCLEUS

Visualizing the molecular sociology at the HeLa cell nuclear periphery

Julia Mahamid,[1]* Stefan Pfeffer,[1] Miroslava Schaffer,[1] Elizabeth Villa,[1,2] Radostin Danev,[1] Luis Kuhn Cuellar,[1] Friedrich Förster,[1] Anthony A. Hyman,[3] Jürgen M. Plitzko,[1] Wolfgang Baumeister[1]*

The molecular organization of eukaryotic nuclear volumes remains largely unexplored. Here we combined recent developments in cryo–electron tomography (cryo-ET) to produce three-dimensional snapshots of the HeLa cell nuclear periphery. Subtomogram averaging and classification of ribosomes revealed the native structure and organization of the cytoplasmic translation machinery. Analysis of a large dynamic structure—the nuclear pore complex—revealed variations detectable at the level of individual complexes. Cryo-ET was used to visualize previously elusive structures, such as nucleosome chains and the filaments of the nuclear lamina, in situ. Elucidation of the lamina structure provides insight into its contribution to metazoan nuclear stiffness.

Cellular functions arise from an intricate network of macromolecular interactions. Hence it is of fundamental importance to decipher this "molecular sociology" of cells, ideally by direct visualization (*1*). Cryo–electron tomography (cryo-ET) provides three-dimensional (3D) images of cellular landscapes at increasingly higher resolutions; with cellular fractionations, subnanometer resolutions have been attained (*2*, *3*). Structural investigations in situ sensu stricto are more challenging owing to a number of limitations, which can now be overcome; (i) cryo–focused ion beam (FIB) micromachining has opened windows into frozen-hydrated cells and tissues, otherwise too thick to be examined directly by transmission electron microscopy (TEM) (*4*–*7*). However, freestanding lamellas produced by cryo-FIB have little contact with the conductive support film, increasing the likelihood of beam-induced specimen charging in the TEM (*8*, *9*). We resolved this by sputtering a fine metal coating onto the FIB-lamellas, as routinely applied for biological cryo–scanning electron microscopy (SEM) imaging (*10*). (ii) Direct detectors improve the quality of cryo-TEM images substantially (*11*), and (iii) the recently developed Volta phase plate (VPP) enhances (phase) contrast especially for lower spatial frequencies without the need of defocusing, rendering the tomograms directly interpretable (*9*, *12*, *13*). Here, we combined these developments to produce in situ high-resolution 3D snapshots of the HeLa cell nuclear periphery.

HeLa cells expressing β-tubulin:green fluorescent protein and histone2B:mCherry were cultured on TEM grids, vitrified by plunge freezing, and subsequently observed by cryo–fluorescence microscopy (*14*). Interphase cells were thinned by FIB milling (fig. S1, A and B). A central slice through a cell is generated by removing the biological material above and below an area of interest, resulting in a 200-nm-thick lamella traversing the whole cell (figs. S1, C and D, and S2). Data acquired with the VPP on nonconductive (uncoated) lamellas resulted in distorted images (fig. S3). The

[1]Max Planck Institute of Biochemistry, Department of Molecular Structural Biology, Am Klopferspitz 18, 82152 Martinsried, Germany. [2]Department of Chemistry and Biochemistry, University of California, San Diego, CA, USA. [3]Max Planck Institute of Molecular Cell Biology and Genetics, Pfotenhauerstrasse 108, 01307 Dresden, Germany
*Corresponding author. E-mail: mahamid@biochem.mpg.de (J.M.); baumeis@biochem.mpg.de (W.B.)

Downloaded from on February 25, 2016

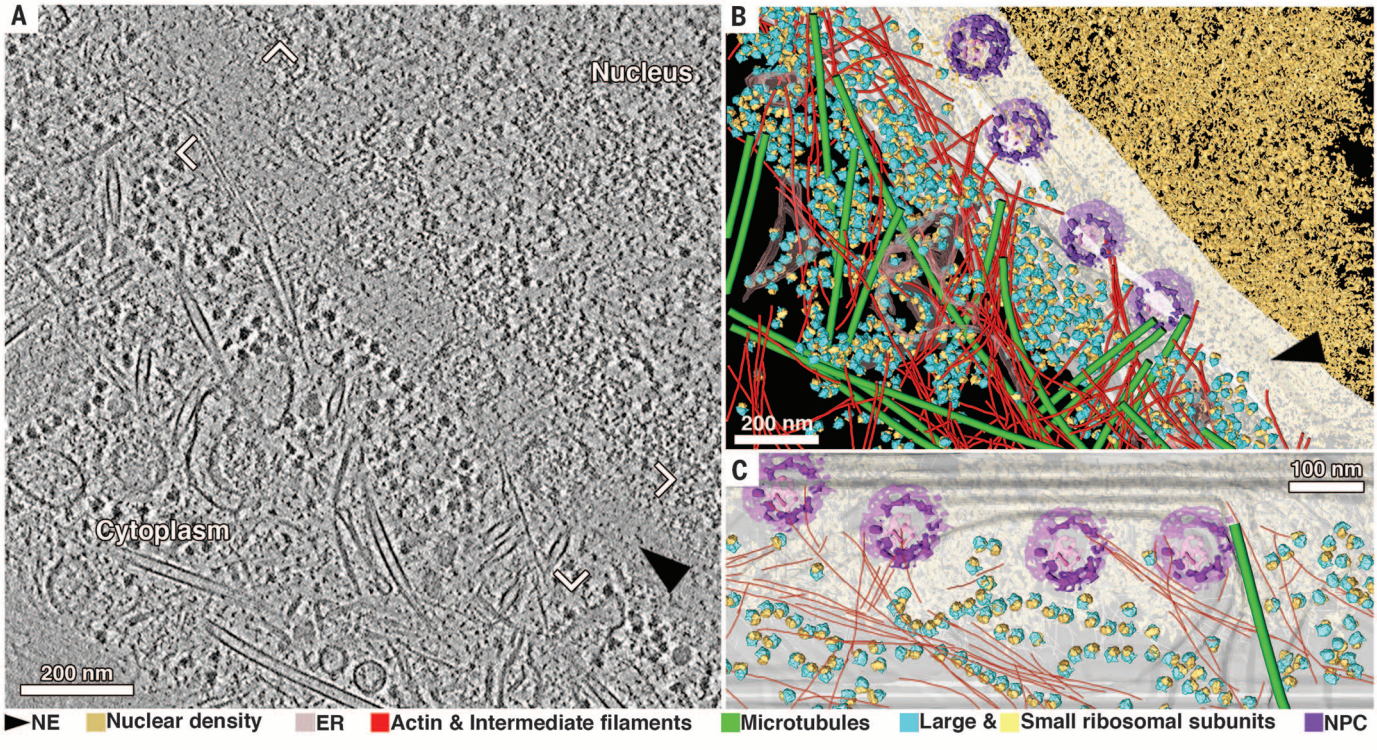

Fig. 1. The nuclear periphery of a HeLa cell revealed by cryo-ET. (**A**) Tomographic slice with 8.4-nm thickness of an interphase HeLa cell thinned by cryo-FIB. (**B**) Annotated view of the tomographic data. Color labels are defined for each structure in (B) and (C). (**C**) Cross-section view of the segmentation in the vicinity of the nuclear envelope [frame in (A)]. NE: nuclear envelope; ER: endoplasmic reticulum; NPC: nuclear pore complex.

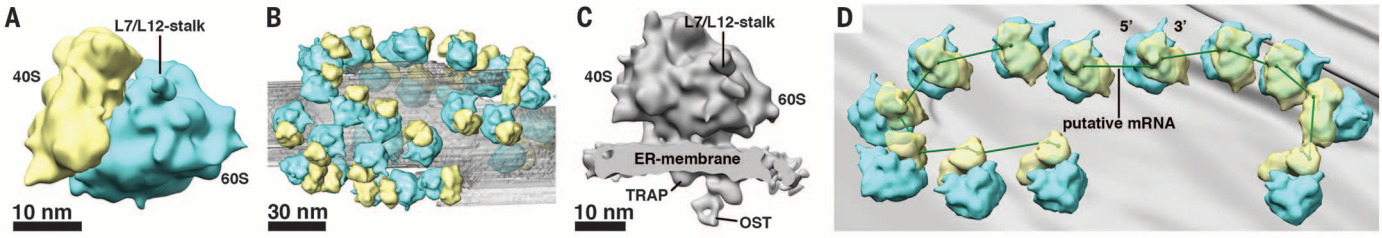

Fig. 2. Subvolume averages of ribosomes and 3D analysis of polysomes. (**A**) Average of cytoplasmic ribosomes. (**B**) ER-associated ribosomes were selected on the basis of their proximity to segmented ER-membranes and averaged independently in (**C**)**:** Side view shows ER-luminal densities of the translocation machinery; TRAP: translocon-associated protein complex; OST: oligosaccharyltransferase. (**D**) Representative polysomes on the NE membrane traced by an automatic approach.

Fig. 3. The molecular organization at the nuclear envelope. Consecutive tomographic slices (8.4 nm) along the nucleocytoplasmic axis. Dashed lines indicate the center positions of three NPCs. (**A**) Density inside the nucleus. Inset: chains of nucleosomes (arrowheads). (**B**) Nuclear lamina. Inset: segmentation of putative lamina filaments. (**C**) NPCs within the NE. Inset: magnified central NPC. Arrowhead: ring density in the luminal space with radial connections to the protomer density. (**D**) The outer NE. Inset: magnified central NPC. (**E**) Polysomes and cytoskeletal filaments at the NE. IF: intermediate filaments. MT: microtubules.

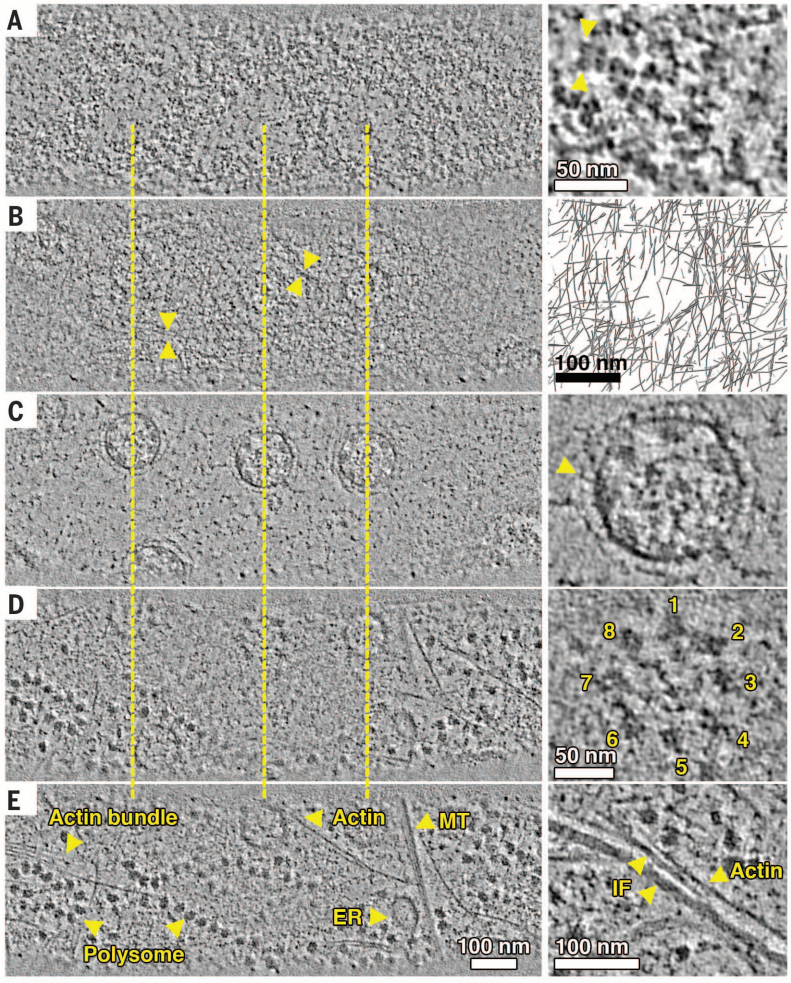

charges building up on the sample produced a field similar to that of an electrostatic lens and led to detrimental beam deformations at the phase plate plane. Thus, a thin platinum layer (<5 nm) was sputtered after lamella preparation to improve conductivity (fig. S2). Our reconstructed volumes acquired with the VPP exhibit high contrast, which allowed for direct visualization and identification of molecular complexes inhabiting the nucleus and the nuclear envelope (NE) (Fig. 1 and movie S1).

To provide a quantitative measure for the attained resolution, we subjected 80*S* ribosomes to subvolume averaging. Cytoplasmic ribosomes from a single tomogram (900 particles) yielded an average with a resolution of 28 Å (Fig. 2A and fig. S4A). Subsequently, ribosomes were sorted according to their spatial association to either the endoplasmic reticulum (ER) or the NE outer membrane (Fig. 2, B and D). An average of the ER-bound fraction (143 particles) yielded a resolution of 35 Å (Fig. 2C and fig. S4A). ER-luminal densities of the translocon-associated protein (TRAP) complex and the oligosaccharyltransferase (OST) complex (*15*) were clearly rendered in ER- and NE-bound particles (Fig. 2C and fig. S4, B to D). Further classification revealed that OST is found on 33% of ER-translocon complexes, in agreement with the stoichiometry of OST observed with isolated rough-ER vesicles (*15*).

Subtomogram averaging of individual ribosomes yielded additional densities in close proximity, indicating arrangement into polysomes with a topology dictated by membrane association (fig. S4E) (*16*). Clustering of the angles describing relative neighbor positions and orientations (fig. S5A) revealed two highly populated classes

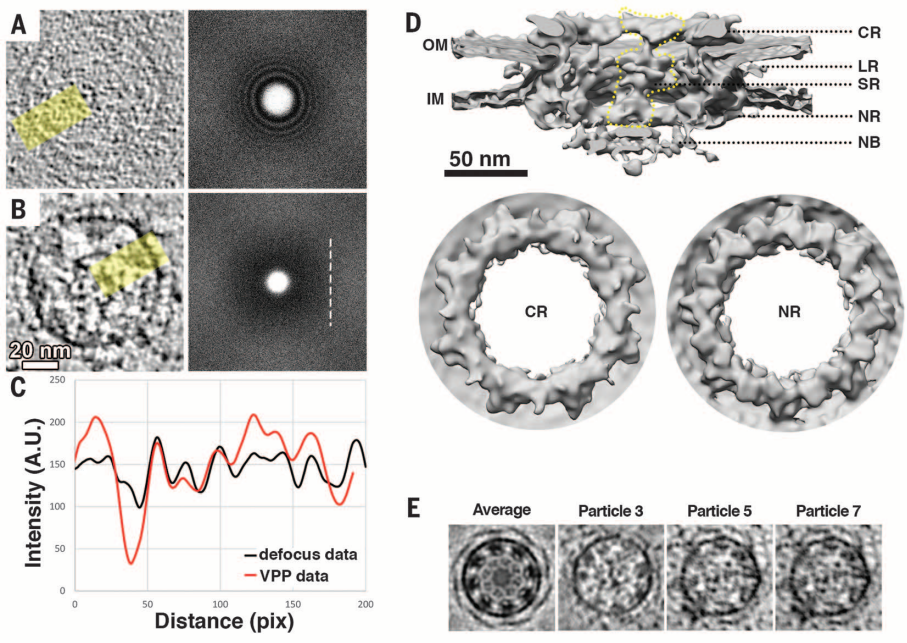

Fig. 4. Tomographic reconstruction and average of the nuclear pore complex. (**A**) Tomographic slices (8.4 nm) obtained at 6-μm defocus (right: FFT at zero tilt) and (**B**) with VPP at 700-nm defocus (right: FFT at zero tilt; dashed line indicates first zero). (**C**) Intensity profiles within yellow boxes in (A) and (B). (**D**) Average of NPCs perpendicular to (top: a protomer is delineated by dashed yellow line) and along the nucleo-cytoplasmic axis (bottom, higher threshold). CR: cytoplasmic ring; OM: outer membrane; LR: luminal ring. SR: spoke ring; IM: inner membrane; NR: nuclear ring. NB: nuclear basket. (**E**) Filtered 2D central slices of the average and representative particles.

representing the left and right neighbors within the same polysome (fig. S5B), in which mRNA entry and exit sites of adjacent ribosomes allow threading of an interconnecting mRNA molecule on a smooth path (fig. S5C). We then performed automatic tracing of polysomes to quantify ribosome organization at the level of individual polysomes (Fig. 2D and table S1) (*14*). A large fraction of membrane-bound ribosomes were associated into polysomes comprising up to 10 particles and exhibiting a close-packed arrangement with a mean distance of 28 nm. This analysis provided a detailed description of the native structure and organization of the cytoplasmic translation machinery in human cells, recapitulating information obtained from microsomes (*15*, *16*) in a single in situ data set.

Large complexes tend not to be strictly deterministic and are often subject to functional and structural variations, which are obscured by averaging. We therefore set to investigate whether the quality of our data would allow characterization of individual complexes. A cross-sectional view of the NE (Figs. 1C and 3) shows four nuclear pore complexes (NPCs), in which we visually identified the eight protomers at the level of the spoke (Fig. 3C) and the cytoplasmic rings (Fig. 3D). An additional ring density surrounding the membrane is distinguished within the NE lumen at the level of the spoke ring (Fig. 3C, inset: arrowhead). Structures at these positions were previously described as discrete luminal densities (*17*, *18*). Here, these densities formed a complete flexible ring with radial connections to the protomers.

The superior contrast provided by the VPP is demonstrated in comparison to data acquired at 6-μm defocus (fig. S6). Density profiles of the NPC obtained from data acquired with and without the VPP show similar variation in the intensities (Fig. 4, A to C). However, the contrast is improved by almost 60% with the VPP despite a lower electron dose (60 e/Å^2 with VPP versus 100 e/Å^2 with defocus). This allowed us to examine previously reported variations in NPC diameter (*17*, *18*). We extracted subvolumes of eight complete NPCs from three interphase cells and performed alignment and averaging. The average reproduced the densities for the cytoplasmic and nuclear rings previously described for the human NPC obtained both in situ and from purified nuclei (Fig. 4D and fig. S7) (*18*, *19*). Deviations from previous structures were evident for the pore diameter in the spoke ring (fig. S7C). We determined the membrane circumference at the spoke ring level for each of the eight particles and our average and found up to 13% difference in the mean particle diameter between the individual pores (Fig. 4E, fig. S8, and table S2). Within the same particle, we observed radial variations of up to 18%. Complexes from the same cells were more homogeneous among themselves, a phenomenon recapitulated in the averages (fig. S8 and table S2), pointing to the intriguing possibility that variations in pore dimensions are related to specific physiological states. This confirmed previous observations of NPC plasticity and illustrates the problem of analyzing large flexible structures by averaging methods. At the same time, it emphasizes the importance of obtaining high-quality primary data allowing analysis of individual complexes.

A network of intermediate filaments, forming the nuclear lamina underlying the NE, is thought to provide mechanical support to the nucleus (*20*). TEM images of the lamina are rare (*21*, *22*), and 10-nm-diameter filaments arranged on an orthogonal lattice have been described in preparations of Triton-extracted and metal-shadowed oocyte NEs (*20*). Here, a volume of 30 nm in thickness underlying the NE is dominated by entangled, 4-nm-diameter filaments (Fig. 3B and fig. S9, B and C). The filaments' diameter in the somatic HeLa cells is in agreement with molecular models proposed for the structure of lamins; namely, dimers of coiled-coils assembled head-to-tail (*23*).

Segmentation of such thin structures is challenging; nevertheless, careful inspection of traced filaments allowed us to obtain an estimate of their flexibility. We measured a persistence length of ~560 nm (fig. S10 and table S3), well within the range described for intermediate filaments and lamins obtained ex situ (*22*–*25*). However, the small filament diameter determined herein resulted in a radically higher elastic modulus for the putative lamina fibrils than what could previously be derived based on a diameter of 10 nm (*14*). An elastic modulus of 190 MPa calculated for the individual filaments recapitulates measurements on whole nuclei, primarily attributed to lamin A (*26*), suggesting that the fine isotropic matrix is the key player in conferring high stiffness to metazoan nuclei.

The complex molecular organization at the NE is demonstrated in Fig. 3. Nuclear volumes exhibit regions of dense material, wherein chains of 10-nm-diameter toroid densities are observed (Fig. 3A and fig. S9A). The morphology of the abundant nuclear complexes is reminiscent of nucleosome core particles (*27*) arranged in a staggered conformation of nucleosome chains (*28*). The clarity with which the individual complexes are discerned should allow unambiguous localization of single nucleosomes by template matching (*29*) and determining their connectivity. Variations in chromatin density correlate with the appearance of the lamina filaments, and they are both diminished in the vicinity of NPCs (Fig. 3, A and B). Extensive polysomes reside on the outer

NE membrane (Fig. 3, D and E). The cytoplasm contains filaments of the cell's cytoskeleton, distinguishable according to size and morphology: actin fibers with a helical pitch, smooth intermediate filaments of variable diameters, and 13-protofilament microtubules (Fig. 3E and fig. S10). Occasionally, actin filaments formed direct physical connections to NPCs (Fig. 3E). With the NPCs embedded within the stiff lamina on one side and directly connected to the cytoskeleton on the other, it becomes feasible to comprehend how NPC diameter may differ considerably upon the action of mechanical forces.

In conclusion, the volumes reconstructed from these data reveal that many macromolecular complexes can be visually recognized without the need for computational averaging approaches and provide insight into structural variations at the level of individual complexes. Assisted by the synergistic application of recent technical developments, cryo-ET holds promise for revealing the molecular organization giving rise to cellular function in unperturbed environments.

REFERENCES AND NOTES

1. C. V. Robinson, A. Sali, W. Baumeister, *Nature* **450**, 973–982 (2007).
2. S. Pfeffer *et al.*, *Nat. Commun.* **6**, 8403 (2015).
3. F. K. Schur *et al.*, *Nature* **517**, 505–508 (2015).
4. M. Marko, C. Hsieh, R. Schalek, J. Frank, C. Mannella, *Nat. Methods* **4**, 215–217 (2007).
5. A. Rigort *et al.*, *J. Struct. Biol.* **172**, 169–179 (2010).
6. C. Hsieh, T. Schmelzer, G. Kishchenko, T. Wagenknecht, M. Marko, *J. Struct. Biol.* **185**, 32–41 (2014).
7. J. Mahamid *et al.*, *J. Struct. Biol.* **192**, 262–269 (2015).
8. R. Danev, S. Kanamaru, M. Marko, K. Nagayama, *J. Struct. Biol.* **171**, 174–181 (2010).
9. Y. Fukuda, U. Laugks, V. Lučić, W. Baumeister, R. Danev, *J. Struct. Biol.* **190**, 143–154 (2015).
10. P. Walther, Y. Chen, L. L. Pech, J. B. Pawley, *J. Microsc.* **168**, 169–180 (1992).
11. G. McMullan, A. R. Faruqi, D. Clare, R. Henderson, *Ultramicroscopy* **147**, 156–163 (2014).
12. S. Asano *et al.*, *Science* **347**, 439–442 (2015).
13. R. Danev, B. Buijsse, M. Khoshouei, J. M. Plitzko, W. Baumeister, *Proc. Natl. Acad. Sci. U.S.A.* **111**, 15635–15640 (2014).
14. Materials and methods and supplementary text are available as supplementary materials on *Science* Online.
15. S. Pfeffer *et al.*, *Nat. Commun.* **5**, 3072 (2014).
16. S. Pfeffer *et al.*, *Structure* **20**, 1508–1518 (2012).
17. K. H. Bui *et al.*, *Cell* **155**, 1233–1243 (2013).
18. T. Maimon, N. Elad, I. Dahan, O. Medalia, *Structure* **20**, 998–1006 (2012).
19. A. von Appen *et al.*, *Nature* **526**, 140–143 (2015).
20. U. Aebi, J. Cohn, L. Buhle, L. Gerace, *Nature* **323**, 560–564 (1986).
21. C. W. Akey, *J. Cell Biol.* **109**, 955–970 (1989).
22. E. Grossman *et al.*, *J. Struct. Biol.* **177**, 113–118 (2012).
23. K. Ben-Harush *et al.*, *J. Mol. Biol.* **386**, 1392–1402 (2009).
24. D. S. Fudge, K. H. Gardner, V. T. Forsyth, C. Riekel, J. M. Gosline, *Biophys. J.* **85**, 2015–2027 (2003).
25. N. Mücke *et al.*, *J. Mol. Biol.* **335**, 1241–1250 (2004).
26. J. Schäpe, S. Prausse, M. Radmacher, R. Stick, *Biophys. J.* **96**, 4319–4325 (2009).
27. K. Luger, A. W. Mäder, R. K. Richmond, D. F. Sargent, T. J. Richmond, *Nature* **389**, 251–260 (1997).
28. C. L. Woodcock, L. L. Frado, J. B. Rattner, *J. Cell Biol.* **99**, 42–52 (1984).
29. A. S. Frangakis *et al.*, *Proc. Natl. Acad. Sci. U.S.A.* **99**, 14153–14158 (2002).

ACKNOWLEDGMENTS

We are grateful to I. Poser for providing the HeLa cells; Y. Fukuda for advice on plunging; the local workshop for the design and production of tools; F. Beck and F. Bäuerlein for advice in data processing; P. Fratzl for advice on biomechanics; and D. Mastronarde for continuous developments in SerialEM and 3dmod. J.M. was supported by postdoctoral fellowships from the European Molecular Biology Organization and Human Frontier Science Program, and by the Weizmann Institute Women in Science Program. F.F. was supported by Deutsche Forschungsgemeinschaft grant FO 716/4. W.B. was supported by Center for Integrated Protein Science Munich. R.D. is a coinventor on a patent US 9129774 B2, "Method of using a phase plate in a transmission electron microscope," concerning the Volta phase plate. A.A.H. and W.B. are on the scientific advisory board of FEI Company. The supplementary materials contain additional data. EM densities have been deposited in the EMDataBank with the following accession numbers: EMD-8057, EMD-8056, EMD-8055, and EMD-8054.

SUPPLEMENTARY MATERIALS

www.sciencemag.org/content/351/6276/969/suppl/DC1
Materials and Methods
Supplementary Text
Figs. S1 to S10
Tables S1 to S3
References (*30*–*43*)
Movie S1

16 November 2015; accepted 22 January 2016
10.1126/science.aad8857

FOREST ECOLOGY

Leaf development and demography explain photosynthetic seasonality in Amazon evergreen forests

Jin Wu,[1]* Loren P. Albert,[1] Aline P. Lopes,[2] Natalia Restrepo-Coupe,[1,3] Matthew Hayek,[4] Kenia T. Wiedemann,[1,4] Kaiyu Guan,[5,6] Scott C. Stark,[7] Bradley Christoffersen,[1,8] Neill Prohaska,[1] Julia V. Tavares,[2] Suelen Marostica,[2] Hideki Kobayashi,[9] Mauricio L. Ferreira,[10,11] Kleber Silva Campos,[12] Rodrigo da Silva,[12] Paulo M. Brando,[13,14] Dennis G. Dye,[15] Travis E. Huxman,[16] Alfredo R. Huete,[3] Bruce W. Nelson,[2] Scott R. Saleska[1]*

In evergreen tropical forests, the extent, magnitude, and controls on photosynthetic seasonality are poorly resolved and inadequately represented in Earth system models. Combining camera observations with ecosystem carbon dioxide fluxes at forests across rainfall gradients in Amazônia, we show that aggregate canopy phenology, not seasonality of climate drivers, is the primary cause of photosynthetic seasonality in these forests. Specifically, synchronization of new leaf growth with dry season litterfall shifts canopy composition toward younger, more light-use efficient leaves, explaining large seasonal increases (~27%) in ecosystem photosynthesis. Coordinated leaf development and demography thus reconcile seemingly disparate observations at different scales and indicate that accounting for leaf-level phenology is critical for accurately simulating ecosystem-scale responses to climate change.

The seasonal rhythm of ecosystem metabolism—the aggregated photosynthesis, transpiration, or respiration of all organisms in a landscape—emerges from interactions among climate, ecology of individuals and communities, and biosphere-atmosphere exchange (*1*). In temperate zones, seasonality of terrestrial production drives annual oscillations in atmospheric carbon dioxide (*2*). In the tropics, plant transpiration seasonality mediates tropical convection and the timing of dry-to-wet season transitions—a potentially important climate feedback (*3*).

Seasonality in temperate zones is tightly linked to plant phenology (*4*) (the timing of periodic life-cycle events, including leaf development and senescence), which in turn is synchronized by cold-season dormancy (*4*). However, the extent, magnitude, and controls on seasonality of ecosystem metabolism in year-round warm tropical evergreen forest systems are less clear (*5*–*7*). For example, most current Earth system models represent little or no phenology in evergreen tropical biomes, so any seasonality in photosynthetic flux that emerges is due to seasonality in climatic drivers (*8*–*10*). However, remote-sensing observations (*5*–*7*, *11*–*13*) suggest that central Amazon forests seasonally increase their photosynthetic capacity ("green-up") during dry seasons, whereas southern Amazon and African tropical forests show declines (*13*). There is extensive debate over the mechanisms driving these patterns (including whether they might be remote-sensing artifacts) (*5*–*7*) and how they might be modeled (*8*–*10*, *14*).

To determine the extent of seasonality in tropical ecosystem photosynthesis (or gross ecosystem productivity, GEP), and to develop a more mechanistic understanding of how it emerges from climatic and biological processes, we address two key questions: (i) What is the relative importance of climatic drivers versus plant phenology in controlling GEP seasonality? (ii) What are the mechanisms by which these factors exert control? These questions conceptualize GEP as potentially driven by climate variability (e.g., temperature, light, or water) interacting with fixed photosynthetic infrastructure (e.g., leaf surface area, leaf photosynthetic capacity), or alternatively, by variability in that photosynthetic infrastructure, or some combination of the two.

To evaluate the first question, we compared GEP seasonality (derived from eddy covariance

Downloaded from on February 25, 2016

measurements of ecosystem CO_2 exchange) to candidate explanatory variables at four Amazon sites distributed across gradients in rainfall and taxonomic composition. These variables include (i) five key climatic variables (*15*) and (ii) a metric of aggregate forest canopy phenology. The phenology metric—ecosystem-scale photosynthetic capacity (PC)—is an estimate of photosynthetic infrastructure independent of environment, derived by averaging the amount of photosynthesis per unit of incoming light, under fixed reference climatic conditions (*15*).

We found that GEP was strongly seasonal at all sites, but was not consistently driven by climate variability (Fig. 1 and table S4). Instead, GEP consistently tracked PC seasonality across all four sites (coefficient of determination R^2 = 0.82 – 0.92; Fig. 1), notably including both water-sufficient sites (Fig. 1, A to C), which increase photosynthesis (i.e., "green-up") in the dry season, and a water-limited site (Fig. 1D), which decreases photosynthesis in the dry season. PC phenology thus appears to be the primary driver of GEP seasonality in these forests. This contrasts with most ecosystem models, which represent tropical evergreen forests' GEP seasonality as arising primarily from climate variability interacting with aseasonal photosynthetic infrastructure (*8*, *10*). It also contrasts with observations at shorter diel time scales, during which large GEP changes closely track light levels (photosynthetically active radiation, PAR), whereas PC remains fixed (fig. S11).

We then evaluated the second question: What are the mechanisms driving seasonal changes in PC? We first used tower-mounted cameras—widely used in temperate zones (*16*), but not previously in the tropics (*15*)—to observe dynamics of leaf quantity metrics in three forests (the drier k67 site near Santarém, the wetter k34 site near Manaus, and ATTO in between Santarém and Manaus; fig. S1).

We found that seasonality in camera-derived leaf area index (LAI) (15) (figs. S5 and S8) and in the fraction of PAR absorbed by leaves (FAPAR)—common biotic drivers in photosynthesis models—were insufficient to account for PC seasonality at the two sites with long-term eddy flux measurements (Fig. 2, A to D). Though LAI and FAPAR significantly increased during dry seasons at both sites, their increases preceded PC by at least 1 month, and their relative amplitudes were much smaller than that of PC, which increased proportionally twice as much as LAI and 10 times more than FAPAR. Thus, typical photosynthesis models, which predict that changes in GEP are driven by proportional changes either in PAR (climate) or in FAPAR (biology), would not be able to represent observed photosynthetic seasonality of these forests.

In addition, remotely sensed vegetation activity—as observed by the Enhanced Vegetation Index from Moderate-Resolution Imaging Spectroradiometer (MODIS) [MAIAC EVI, rigorously corrected for clouds, aerosols, and Sun-angle artifacts (*17*)]—closely tracked the magnitude and timing of LAI seasonality (Fig. 2, A to D). In sum, though phenological metrics of leaf quantity from multiple platforms (ground, tower, and satellite) all showed consistent dry-season increases in the central Amazon, these increases were systematically too small to explain the variation in PC that we found is responsible for GEP dynamics in these forests (Fig. 2, C and D).

Next, investigating effects of leaf quality (photosynthetic capacity per leaf area) (*9*, *11*, *18*), we found that increasing leaf losses (litterfall) during dry seasons are more than compensated by simultaneous increases in new leaf production (Fig. 2, E and F). This dynamic drives net increases in

[1]Department of Ecology and Evolutionary Biology, University of Arizona, Tucson, AZ 85721, USA. [2]Brazil's National Institute for Amazon Research (INPA), Manaus, Amazonas, Brazil. [3]Plant Functional Biology and Climate Change Cluster, University of Technology Sydney, Sydney, NSW, Australia. [4]John A. Paulson School of Engineering and Applied Sciences, Harvard University, Cambridge, MA 02138, USA. [5]Department of Natural Resources and Environmental Science, University of Illinois at Urbana Champaign, Urbana, IL 61081, USA. [6]Department of Earth System Science, Stanford University, Stanford, CA 94025, USA. [7]Department of Forestry, Michigan State University, East Lansing, MI 48824, USA. [8]Earth and Environmental Sciences Division, Los Alamos National Lab, Los Alamos, NM 87545, USA. [9]Department of Environmental Geochemical Cycle Research, Japan Agency for Marine-Earth Science and Technology, Yokohama, Japan. [10]Centro de Energia Nuclear na Agricultura, University of Sao Paulo, Piracicaba, SP, Brazil. [11]Smart and Intelligent Cities Programme, University Nove de Julho, São Paulo, SP, Brazil. [12]Department of Environmental Physics, University of Western Para (UFOPA), Santarem, Para, Brazil. [13]Instituto de Pesquisa Ambiental da Amazônia (IPAM), Belem, Para, Brazil. [14]Woods Hole Research Center, Falmouth, MA 02450, USA. [15]Western Geographic Science Center, U.S. Geological Survey, Flagstaff, AZ 86001, USA. [16]Ecology and Evolutionary Biology and Center for Environmental Biology, University of California, Irvine, CA 92629, USA.
***Corresponding author. E-mail: jinwu@email.arizona.edu (J.W.); saleska@email.arizona.edu (S.R.S)**

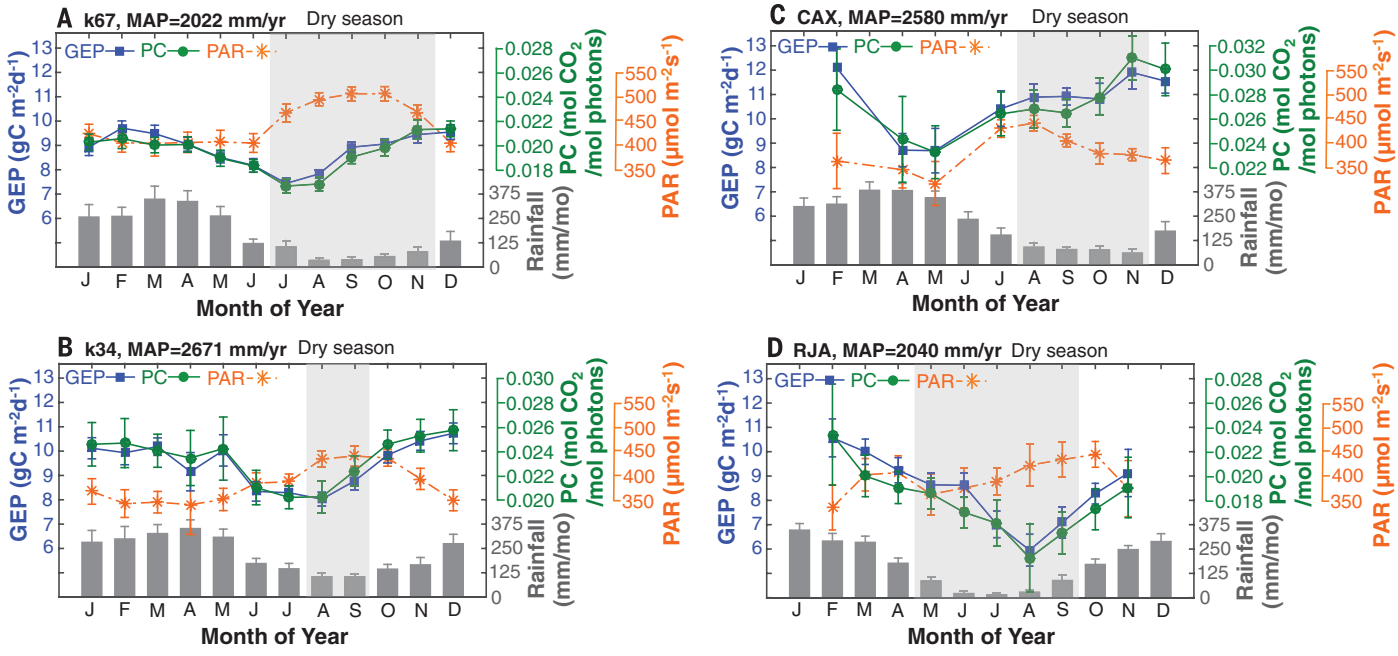

Fig. 1. Gross ecosystem productivity (GEP) seasonality at four Amazon forests is highly correlated with seasonality in intrinsic canopy photosynthetic capacity (PC), but not with seasonality in climatic driving variables (rainfall and photosynthetically active radiation, PAR). Flux tower sites are in three equatorial forests: (**A**) Tapajós National Forest (k67 site near Santarém); (**B**) Cuieiras Reserve (k34 site near Manaus); (**C**) Caxiuana National Forest (CAX near Belem); and in one southern (10°S) forest, (**D**) the Jaru Reserve (RJA) (*15*). Monthly values of GEP, PC, and PAR are averages from 2002–2005 and 2009–2011 at k67 (n = 7 years), 1999–2006 at k34 (n = 8), 1999–2003 at CAX (n = 4), and 1999–2002 at RJA (n = 3). Error bars are ± 1 SEM. MAP, mean annual precipitation. Shading indicates dry seasons.

LAI, but also significantly shifts the age composition of these canopies toward younger leaves, which should have higher average "quality" than the older leaves they replace (*11*, *19*).

To test whether simultaneous changes in leaf quantity and quality could account for the large variations in PC and thus GEP, we represented their dynamics in a "leaf demography-ontogeny model" (*15*) (fig. S10). In this model, demography partitions leaf quantity (LAI) into separate age classes, and ontogeny (leaf development) assigns a different "leaf quality" (photosynthetic capacity) to each age class, and these jointly determine ecosystem PC. Driven by new leaf production (assumed to contribute only to young LAI) and by ground-observed litterfall (assumed to come only from old LAI), and constrained to match the mean seasonality of camera-observed total LAI, the model is fit by adjusting parameters of leaf aging and leaf quality (*15*) (fig. S10) to optimize the match between simulated and observed PC at the k67 site (Fig. 3A).

Optimized PC simulations closely tracked observed PC at k67 (R^2 = 0.91; Fig. 3A, upper panel), which rose and fell with the simulated abundance of the mature (3 to 5 months old) age class (Fig. 3A, lower panel). This correspondence indicates that the mature leaves have the highest photosynthetic capacity and explains the time lag between PC and total LAI (Fig. 2, A and B) as a consequence of leaf maturation time [the time to transition from young (LAI_Y) to mature (LAI_M), fig. S10]. A sensitivity analysis showed that varying leaf quality alone could explain about twice as much seasonal variation in ecosystem PC as leaf quantity alone, consistent with a previous simpler analysis at a single site near k67 (*11*). The same leaf demography-ontogeny model [using the same parameters fit for k67, but driven by local k34 LAI and litterfall and scaled so that their mean values match (*15*)] well predicted seasonality of ecosystem PC (R^2 = 0.89; Fig. 3B, upper panel) at k34 near Manaus, 600 km away, with a shorter dry season and more rainfall. That it does this without reparameterization strongly supports leaf demography and ontogeny as general mechanisms of photosynthetic seasonality in central Amazonian forests.

For validation, we found that simulated seasonality of young leaves matches ground-based observations of leaf flushing rates (*12*) (Fig. 4A, R^2 = 0.95) and that differences with age among model-fitted leaf-level photosynthetic parameters were consistent with field-measured maximum

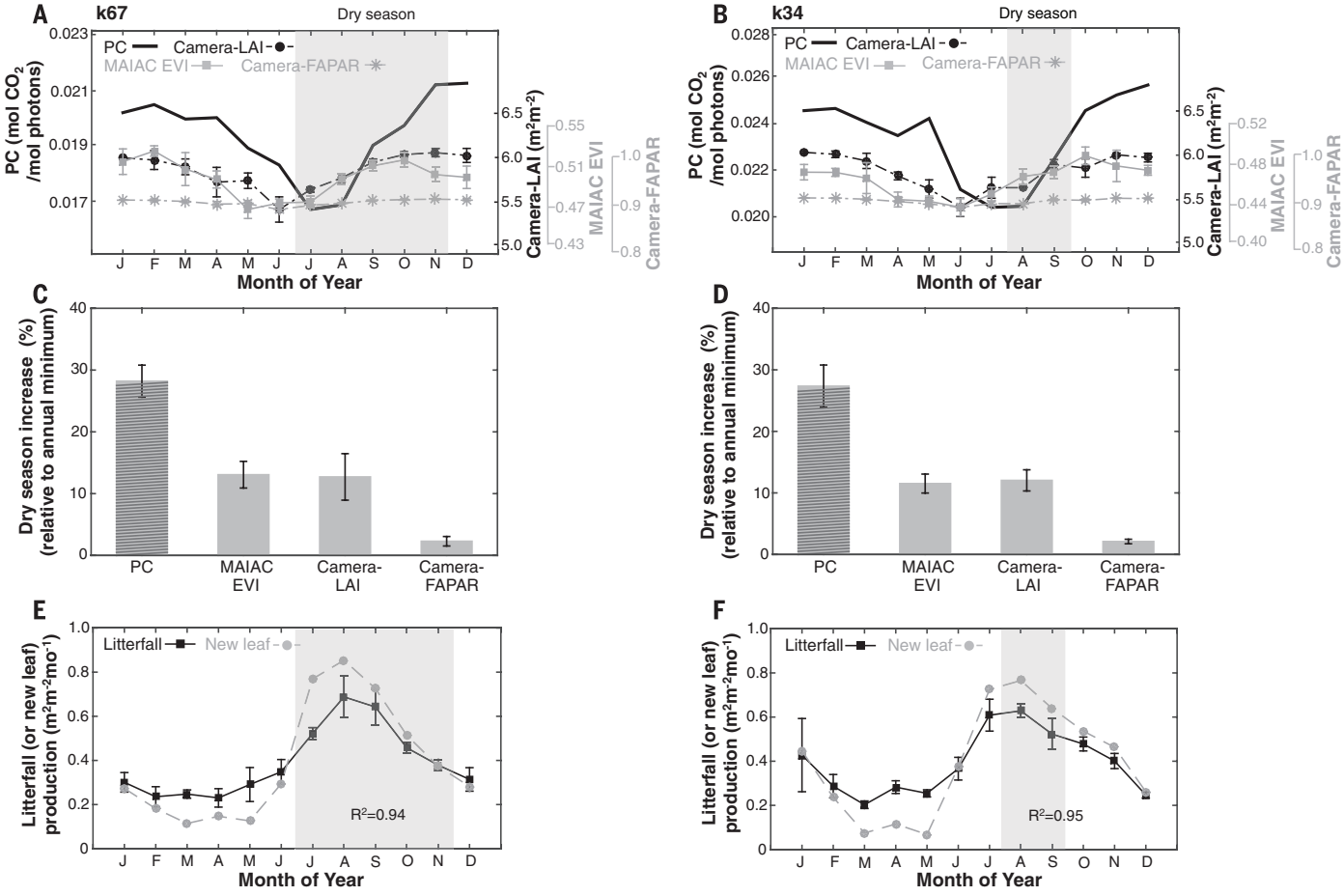

Fig. 2. Leaf quantity alone cannot explain PC seasonality, highlighting the importance of leaf quality. (**A** and **B**) Average annual cycle of photosynthetic capacity (PC) (thick black lines, from Fig. 1) has higher amplitude [at both (A) k67, a long dry-season forest near Santarem, and (B) k34, a short dry-season forest near Manaus] than three key phenological metrics used to drive photosynthesis models: leaf area index (LAI, black circles), fractional absorption of incoming sunlight (FAPAR, gray stars), and the satellite-derived enhanced vegetation index (MAIAC EVI, gray squares). Metrics are scaled so that a given fractional increase is the same magnitude across metrics, relative to the annual minimum. (**C** and **D**) Average dry-season increase (relative to annual minimum) in eddy flux–derived PC (in hatched bars) and its candidate explanatory variables (in gray bars)—satellite-derived MAIAC EVI, camera-derived LAI, and FAPAR at (C) k67 and (D) k34. (**E** and **F**) Average annual cycle of litterfall (black squares) and new leaf production (gray circles) at the same two sites [(E) k67 and (F) k34] shows that modest dry-season increases in LAI [in (A) and (B)] are associated with rapid leaf turnover due to coordinated leaf loss and new leaf production. Grayed months are local dry season (<100 mm of monthly precipitation). Observations from k67 tower (flux-derived data, 2002–2005 and 2009–2011, n = 7; camera-derived data 2010–2011, n = 2), from a nearby biometric plot (*12*) (litterfall, 2001–2005, n = 5), and from MODIS satellite (2003–2012, n = 10); observations from k34 tower (flux-derived data, 1999–2006, n = 8; camera-derived data 2012–2013, n = 2), from a nearby biometric plot (litterfall, 2004–2008, n = 5), and from MODIS satellite (2003–2012, n = 10). Error bars are ± 1 SEM. Shading indicates dry seasons.

carboxylation rates (V_{cmax}) across these age classes (Fig. 4B). These results substantially advance previous work (*11*) by showing that a common phenological mechanism operates across the central Amazonian rainfall gradient, and by demonstrating this mechanism with a model that could be used to represent leaf demography in larger ecosystem models.

Our study provides evidence that despite enormous biodiversity (*20*), synchronization of leaf phenology patterns among leaf flushing species and at different sites (hundreds of kilometers distant) is sufficient to drive convergent ecosystem-scale seasonal patterns of forest productivity. Such dynamics are not easily captured by standard phenology metrics (LAI, FAPAR, or satellite vegetation indices like EVI), but are evidently critical for understanding mechanisms underlying evergreen tropical forest functional dynamics.

This work has two implications for understanding controls on tropical forest photosynthesis. First, it reconciles much-debated discrepancies between different spatial scales of observation.

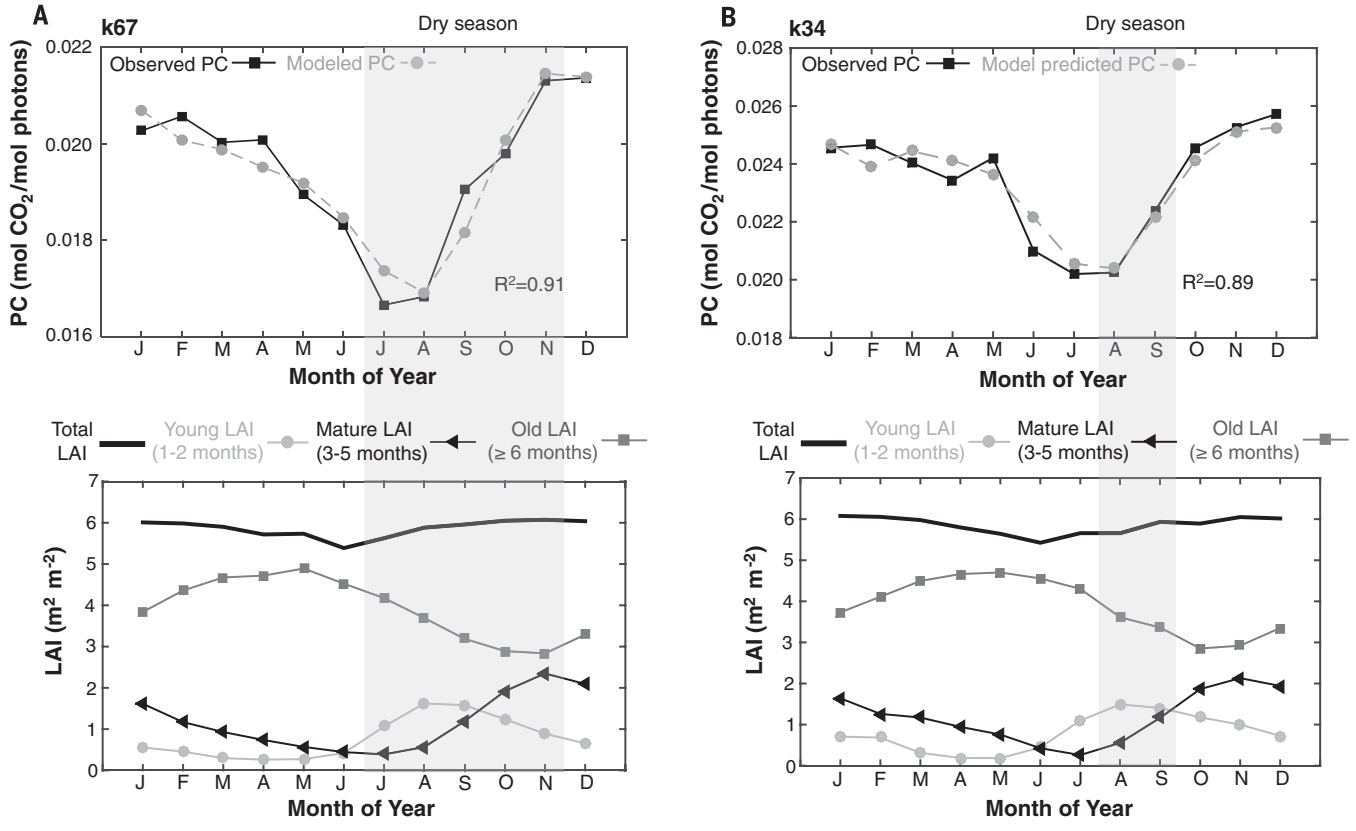

Fig. 3. Leaf demography-ontogeny model simulations. (**A**) Observed and simulated PC seasonality at k67 (upper panel), and associated simulations of LAI in three leaf age classes (three different shades of gray), constrained to sum to total camera-observed LAI (thick black line), with optimal residence times for each age class shown in the legend (lower panel). (**B**) Observed and model-predicted PC seasonality at the wetter k34 site, with parameters optimized for k67 and then scaled to adjust for intersite PC differences (upper panel); associated k34 modeled LAI in three leaf age classes (three different shades of gray); and total camera-observed LAI (black line) (lower panel). Shading indicates dry seasons.

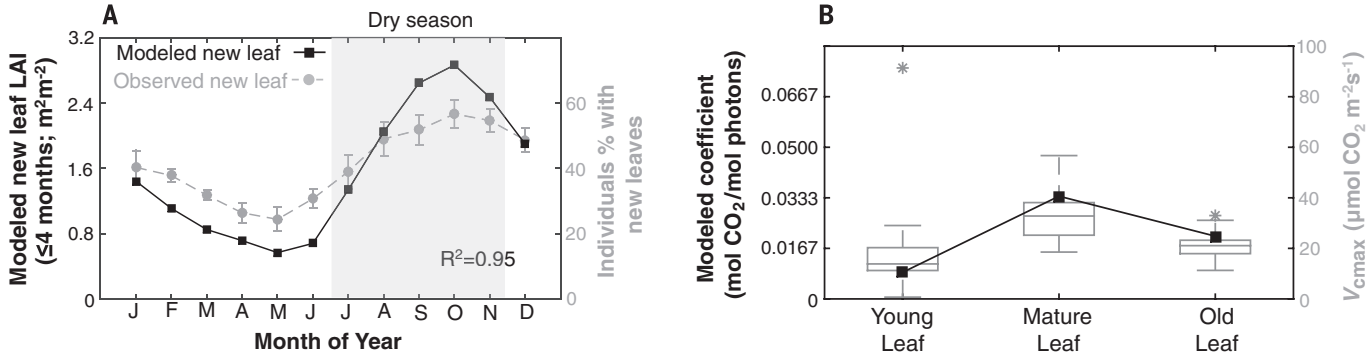

Fig. 4. Validation of leaf demography-ontogeny model. (**A**) Simulations of new leaf age composition (quantity of LAI with age ≤4 months; black squares) along with ground observations of percentage of individuals with new leaves ≤4 months of age (averaged over 1999–2004; $n = 5$) at k67 (gray circles). Shading indicates dry seasons. (**B**) Optimal age-specific photosynthetic efficiency parameters (a_Y, a_M, and a_O; in black squares), compared with age-specific V_{cmax} derived from leaf gas-exchange measurements in 2012 at the k67 site (box plots, in gray, $n = 5$ species × 2 light environments = 10) (*15*). Box plots show median (center line), middle 50% of the distribution (box edges), 1.5 times the interquartile range (whiskers), and outliers (points).

For example, previous work at k67 (*21*) reported little seasonality in leaf-scale photosynthetic parameters, concluding that leaf-level productivity did not explain seasonality of ecosystem productivity. However, that analysis focused on mature leaves only, neglecting the demography and ontogeny here shown to be critical for scaling leaf-level photosynthesis to ecosystems.

At larger scales, this study supports the hypothesis that leaf-demographic mechanisms underlie seasonal increases in tropical vegetation productivity seen from satellites (*6*, *7*, *13*). And, because leaf stomates link evapotranspiration to photosynthesis, these mechanisms may also facilitate the dry-season maxima in water fluxes (fig. S4). By moistening the dry-season atmospheric boundary layer, these fluxes hasten transition to the wet season ahead of the southward migration of the intertropical convergence zone (*3*). Further, because dry-season water fluxes in South America may influence the timing of the North American Monsoon demise (*22*), tropical leaf phenology may contribute to important ecologically mediated teleconnections (*23*) in the climate system.

The second implication is that leaf phenology is needed to correctly detect, attribute, and model climate sensitivity of tropical forests. Empirical studies that analyze climatic sensitivity of carbon and water fluxes without accounting for phenology (*24*, *25*) will misattribute phenological changes to climatic causes. Models that are tuned to match current observations while assuming that LAI or FAPAR are aseasonal risk making erroneous predictions of forest response to future climate changes.

This work highlights the importance of leaf level phenology—especially coordination of leaf growth with senescence—in regulating land surface fluxes of carbon and water, and of associated feedbacks to climate. The causes of phenological patterns may arise from adaptive strategies for avoiding herbivores or pathogens (*26*) or for optimizing plant physiology for carbon gain under seasonal resource availability (*13*, *27*–*29*). Ultimately, understanding the evolutionary and physiological basis for phenological mechanisms may be critical to predicting the long-term response and resiliency of tropical forests to changing climate.

REFERENCES AND NOTES

1. L. Gu *et al.*, in *Phenology: An Integrative Environmental Science*, M.D. Schwartz, Ed. (Kluwer, Netherlands, 2003), pp. 467–485.
2. C. D. Keeling, T. P. Whorf, M. Wahlen, J. van der Plichtt, *Nature* **375**, 666–670 (1995).
3. R. Fu, W. Li, *Theor. Appl. Climatol.* **78**, 97–110 (2004).
4. E. E. Cleland, I. Chuine, A. Menzel, H. A. Mooney, M. D. Schwartz, *Trends Ecol. Evol.* **22**, 357–365 (2007).
5. D. C. Morton *et al.*, *Nature* **506**, 221–224 (2014).
6. J. Bi *et al.*, *Environ. Res. Lett.* **10**, 064014 (2015).
7. A. R. Huete *et al.*, *Geophys. Res. Lett.* **33**, L06405 (2006).
8. I. T. Baker *et al.*, *J. Geophys. Res.* **114**, G00B01 (2008).
9. Y. Kim *et al.*, *Glob. Change Biol.* **18**, 1322–1334 (2012).
10. V. Y. Ivanov *et al.*, *Water Resour. Res.* **48**, W12507 (2012).
11. C. E. Doughty, M. L. Goulden, *J. Geophys. Res.* **113**, G00B06 (2008).
12. P. M. Brando *et al.*, *Proc. Natl. Acad. Sci. U.S.A.* **107**, 14685–14690 (2010).
13. K. Guan *et al.*, *Nat. Geosci.* **8**, 284–289 (2015).
14. B. O. Christoffersen *et al.*, *Agric. For. Meteorol.* **191**, 33–50 (2014).
15. Materials and methods are available as supporting material on *Science* Online.
16. A. D. Richardson, B. H. Braswell, D. Y. Hollinger, J. P. Jenkins, S. V. Ollinger, *Ecol. Appl.* **19**, 1417–1428 (2009).
17. A. I. Lyapustin *et al.*, *Remote Sens. Environ.* **127**, 385–393 (2012).
18. N. Restrepo-Coupe *et al.*, *Agric. For. Meteorol.* **182-183**, 128–144 (2013).
19. K. Kitajima, S. Mulkey, S. Wright, *Am. J. Bot.* **84**, 702–708 (1997).
20. S. Fauset *et al.*, *Nat. Commun.* **6**, 6857 (2015).
21. T. F. Domingues, L. A. Martinelli, J. R. Ehleringer, *Plant Ecol. Divers.* **7**, 189–203 (2014).
22. R. Fu, P. A. Arias, H. Wang, in *The Monsoons and Climate Change*, L.M.V. de Carvalho, C. Jones, Eds. (Springer, 2015), pp. 187–206.
23. S. C. Stark *et al.*, *Landsc. Ecol.* **31**, 181–194 (2016).
24. C. E. Doughty, M. L. Goulden, *J. Geophys. Res.* **114**, G00B07 (2008).
25. J. E. Lee *et al.*, *Proc. Biol. Sci.* **280**, 20130171 (2013).
26. R. Lieberei, *Ann. Bot. (London)* **100**, 1125–1142 (2007).
27. S. Elliott, P. J. Baker, R. Borchert, *Glob. Ecol. Biogeogr.* **15**, 248–257 (2006).
28. S. J. Wright, C. P. van Schaik, *Am. Nat.* **143**, 192–199 (1994).
29. K. Kikuzawa, *Can. J. Bot.* **73**, 158–163 (1995).

ACKNOWLEDGMENTS

Funding was provided by NSF PIRE (no. 0730305), NASA Terra-Aqua Science program (NNX11AH24G), the Agnese Nelms Haury Program in Environment and Social Justice, and the GoAmazon project, funded jointly by U.S. Department of Energy (DOE) (no. DE-SC0008383) and the Brazilian state science foundations in Sao Paulo state (FAPESP), and Amazônas state (FAPEAM). J.W. was supported by a NASA Earth and Space Science fellowship. B.C. was supported in part by DOE (BER) NGEE-Tropics projects at Los Alamos National Laboratory. We thank our GoAmazon co–principal investigators V. Ivanov, M. Ferreira, R. Oliveira, and L. Aragão for discussions, the Brazilian Large Scale Biosphere-Atmosphere experiment in Amazônia (LBA) project and A. Araujo for data from the Brazilian flux tower network, and the LBA office in Santarem for logistical support at the k67 tower site. We thank F. Luizão for sharing the litterfall data at Manaus k34 site, funded by Brazilian Long-term Ecological Research Program (PELD-Brazil). We thank the Max Planck Society, INPA, Amazonas State University, Amazonas State Government, the German Federal Ministry of Education and Research, and the Brazilian Ministry of Science Technology and Innovation for support at the ATTO tower site. Eddy flux data at k67 site are available at http://ameriflux-data.lbl.gov:8080/SitePages/siteInfo.aspx?BR-Sa1. All other data published here are available at http://dx.doi.org/10.5061/dryad.8fb47. J.W., L.P.A., and S.R.S. designed the phenology experiment and analysis. J.W.,N.R.C, K.T.W., M.H., K.S.C., B. C., R.d.S., and S.R.S. contributed to the installation, maintenance, or analysis of data of the k67 eddy flux system. J.W., N.P., M.L.F., and P.M.B. contributed to or analyzed ground-based phenology data, and J.W. and S.R.S. developed the leaf demography-ontogeny model. N.R.C. and S.RS. engineered and installed the k67 camera system, and J.W., B.W.N., A.P.L, S.M., and J.V.T. analyzed the camera-based phenology data. L.P.A. collected and analyzed leaf-level gas exchange data with advice from T.E.H. K.G. analyzed MAIAC EVI data. J.W. drafted the manuscript, and S.R.S, L.P.A, T.E.H, S.C.S, B.W.N, N.R.C, K.G., A.R.H., H.K., and D.G.D. contributed to writing the final version. The authors declare no competing financial interests.

SUPPLEMENTARY MATERIALS

www.sciencemag.org/content/351/6276/972/suppl/DC1
Materials and Methods
Supplementary Text
Figs. S1 to S11
Tables S1 to S5
References (*30*–*66*)

24 September 2015; accepted 25 January 2016
10.1126/science.aad5068

Downloaded from on February 25, 2016

CIRCADIAN RHYTHMS

Synchronous *Drosophila* circadian pacemakers display nonsynchronous Ca^{2+} rhythms in vivo

Xitong Liang, Timothy E. Holy, Paul H. Taghert*

In *Drosophila*, molecular clocks control circadian rhythmic behavior through a network of ~150 pacemaker neurons. To explain how the network's neuronal properties encode time, we performed brainwide calcium imaging of groups of pacemaker neurons in vivo for 24 hours. Pacemakers exhibited daily rhythmic changes in intracellular Ca^{2+} that were entrained by environmental cues and timed by molecular clocks. However, these rhythms were not synchronous, as each group exhibited its own phase of activation. Ca^{2+} rhythms displayed by pacemaker groups that were associated with the morning or evening locomotor activities occurred ~4 hours before their respective behaviors. Loss of the receptor for the neuropeptide PDF promoted synchrony of Ca^{2+} waves. Thus, neuropeptide modulation is required to sequentially time outputs from a network of synchronous molecular pacemakers.

Circadian clocks help animals adapt their physiology and behavior to local time. The clocks require a highly conserved set of genes and proteins (*1*) operating through molecular feedback loops to generate robust rhythms that produce a 24-hour timing signal (*2*). These clocks are expressed by pacemaker neurons, which themselves are assembled into an interactive network (*3*). Through network encoding and cellular interactions, pacemaker neurons in the suprachiasmatic nucleus (SCN) of the mammalian brain coordinate many circadian rhythmic outputs (*4*–*7*). To study how molecular clocks couple to network encoding and how network encoding relates to specific behavioral outputs, we conducted an in vivo brainwide analysis of the circadian

Department of Neuroscience, Washington University School of Medicine, St. Louis, MO 63110, USA.
***Corresponding author. E-mail: taghertp@pcg.wustl.edu**

pacemaker network in *Drosophila* across an entire 24-hour day.

This network contains ~150 synchronized pacemaker neurons (*8*, *9*) (fig. S1), yet it produces biphasic behavioral outputs—the morning and evening peaks of locomotor activity (Fig. 1A). The molecular clocks are entrained by environmental cues and by network interactions, for example, by release of the neuropeptide PDF (pigment-dispersing factor) (*10*). Genetic mosaic studies indicate that morning and evening peaks of locomotor activity are controlled by distinct pacemaker groups (*11*–*14*) (Fig. 1B). We reasoned that (i) synchronous signals from the pacemaker network might diverge in downstream circuits or (ii) the pacemaker network might itself generate different timing signals to downstream circuits. To explore this, we developed an in vivo imaging assay to monitor the intracellular Ca^{2+} concentration ($[Ca^{2+}]_i$) in pacemaker cell bodies over a ~24-hour period (Fig. 1C and supplementary materials). Intracellular Ca^{2+} dynamics directly reflect amounts of neuronal activity, and Ca^{2+} imaging allows monitoring activity across neuronal ensembles (*15*).

We used objective-coupled planar illumination (OCPI) microscopy (*16*), which illuminates an

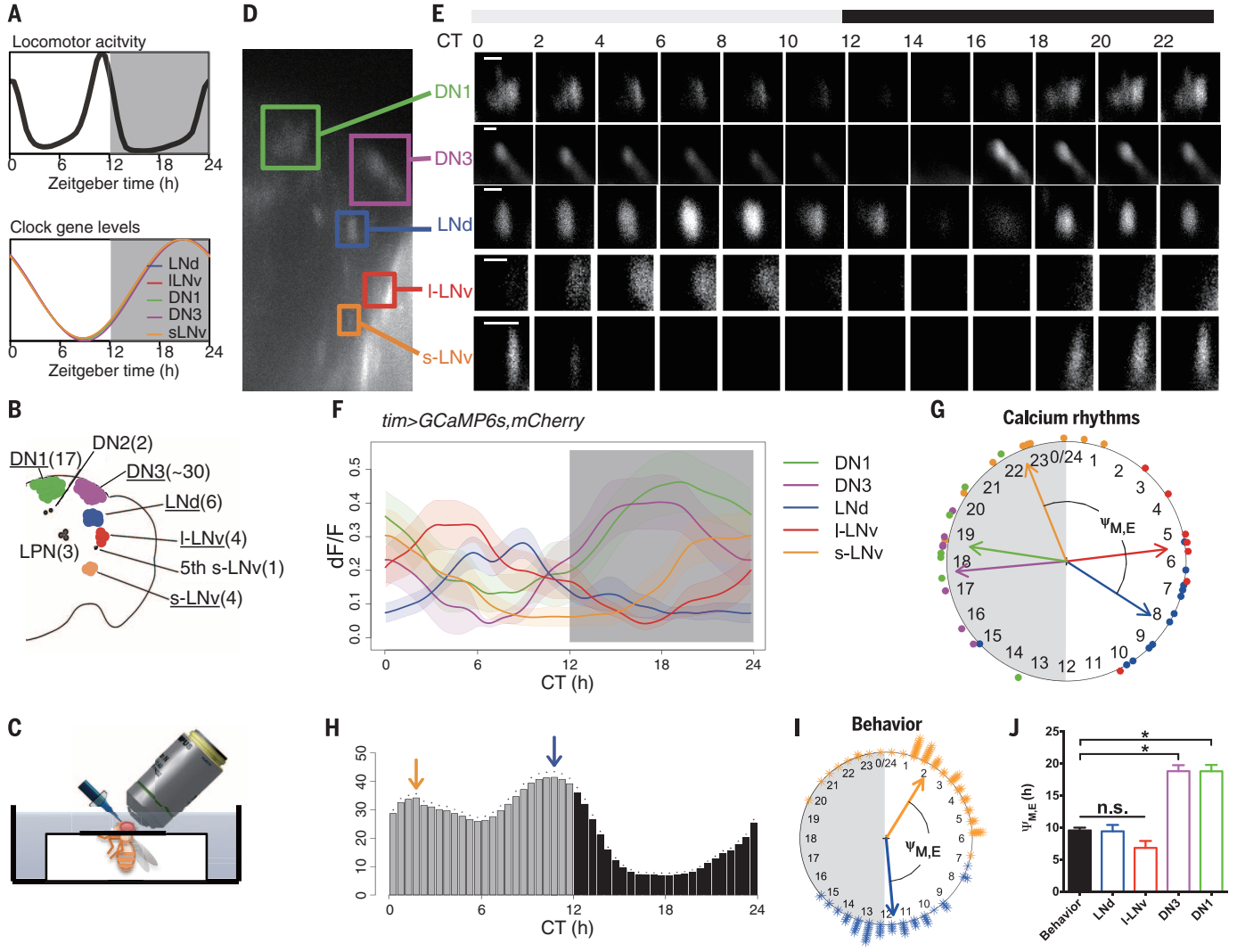

Fig. 1. Ca^{2+} activity patterns in circadian pacemaker neurons in vivo. (**A**) Schematic representations of bimodal behavioral rhythms (top) that are driven by a pacemaker network that displays synchronous, unimodal molecular clocks. (**B**) Map of the eight major clock pacemaker groups in the fly brain; those imaged for GCaMP6s signals are underlined. Numbers in parentheses indicate the cell number per group. (**C**) Illustration of method for long-term in vivo imaging; the head is immersed in saline while the body remains in an air-filled enclosure (see supplementary materials for details). (**D**) A representative image of *tim>GCaMP6s* signals showing the locations of five identifiable pacemaker groups. (**E**) Representative images showing 24-hour Ca^{2+} activity patterns of five identifiable groups. Scale bars, 20 μm. (**F**) Average Ca^{2+} transients in the five pacemaker groups as a function of circadian time (n = 13 flies). Gray aspect indicates the period of lights-off during the preceding 6 days of 12:12 photoentrainment. (**G**) Phase distributions of 24-hour Ca^{2+} transients in different pacemaker groups [data from (F)]. Each colored dot outside of the clock face represents the calculated peak phase of one group in one fly, as described in the supplement. Colored arrows are mean vectors for the different clock neuron groups. The arrow magnitude describes the phase coherence of Ca^{2+} transients in a specific pacemaker group among different flies (n = 13; not all five groups were visible in each fly because of the size of the cranial windows; see table S1). $\Psi_{M,E}$ is the phase difference between M cells (s-LNv) and E cells (LNd). (**H**) The average activity histogram of *tim>GCaMP6s,mCherry.NLS* flies in the first day under constant darkness (DD1). Arrows indicate behavioral peak phases (orange, morning; blue, evening). Dots indicate SEM (n = 47 flies). (**I**) Phase distributions of behavioral peaks indicated by arrows in (H) (asterisks, peak phases of individual flies; orange, morning; blue, evening). $\Psi_{M,E}$ is the phase difference between morning and evening behavioral peaks. (**J**) Comparing phase differences between M cells (s-LNv) and other pacemaker groups (potential E cells); the difference between s-LNv and LNd ($\Psi_{M,LNd}$) best compares to the behavioral $\Psi_{M,E}$. n.s., not significant; asterisk denotes significantly different groups (P < 0.05) by analysis of variance (ANOVA) followed by post hoc Tukey tests. $\Psi_{M,LNd}$ matched behavioral $\Psi_{M,E}$ (t test, P = 0.91; f test, P = 0.65). Error bars denote SEM.

entire focal plane simultaneously; this method accelerates volumetric imaging and reduces phototoxicity caused by repeated illumination. To permit imaging, we made cranial holes in the heads of living *tim* > *GCaMP6s* flies, which express the Ca^{2+} sensor GCaMP6s in all pacemaker neurons (*15*) (Fig. 1C), and monitored $[Ca^{2+}]_i$ in five of the eight major pacemaker groups: small lateral neuron ventral (s-LNv), large lateral neuron ventral (l-LNv), lateral neuron dorsal (LNd), dorsal neuron 1 (DN1), and dorsal neuron 3 (DN3) (Fig. 1D). Each of the five groups displayed a prominent peak of $[Ca^{2+}]_i$ during the 24-hour recording sessions, and each peak had distinct timing (Fig. 1E). To test whether these Ca^{2+} dynamics reflected intrinsic circadian patterning, we began 24-hour recording sessions at different zeitgeber times (ZT). In all such recordings, the peaks of Ca^{2+} activity reflected the pacemaker group identity, not the time at which recordings began (fig. S2). Thus, Ca^{2+} varies in pacemaker neurons systematically as a function of the time of day according to biologically defined rules of entrainment (Fig. 1F).

Three *Drosophila* pacemaker groups (l-LNv, s-LNv, and DN1p) show morning peaks of electrical activity when measured in acutely dissected brains (*17*–*19*). Thus, the phases of Ca^{2+} rhythms we observed are roughly coincident with, or slightly anticipate, their peak electrical activity. Ca^{2+} rhythms produced by different pacemaker groups were similar in amplitude (Fig. 1F) but different in waveform (fig. S3) and phase (Fig. 1G). We confirmed our results using the fluorescence resonance energy transfer (FRET)–based cameleon2.1 imaging method (*20*), for which the ratio of fluorescence between yellow and cyan fluorescent proteins reflects $[Ca^{2+}]_i$ independent of the abundance of the sensor. $[Ca^{2+}]_i$ estimated by this assay exhibited a factor of ~2 circadian variation, with temporal patterns consistent with those obtained with GCaMP6s (fig. S4). In addition, the $[Ca^{2+}]_i$ rhythms did not result from experimental activation of CRYPTOCHROME (fig. S5). These observations demonstrate that the *Drosophila* pacemaker network exhibits stereotyped and diverse spatiotemporal patterns of Ca^{2+} activity during the course of the 24-hour day.

We compared this diversity of Ca^{2+} activity patterns with the diversity of pacemaker functions. Pacemaker functions have been revealed by genetic mosaic experiments, as exemplified by the categorization of M (morning) and E (evening) cells (*11*–*14*). These autonomous oscillators primarily drive the morning and evening peaks of locomotor activity, respectively. The phase relationships ($\Psi_{M,E}$) between the peaks of Ca^{2+} rhythms in canonical M (s-LNv) and E (LNd) cells and the two daily peaks of locomotor activity were highly correlated (Fig. 1, H to J). In M cells, the Ca^{2+} rhythm peaked toward the end of the subjective night, whereas in E cells it peaked toward the end of the subjective day (Fig. 1F). The ~10-hour phase difference between Ca^{2+} rhythms in M and E pacemakers is similar to the ~10-hour phase difference between the morning and evening behavioral peaks (Fig. 1J). Thus, M and E pacemaker Ca^{2+} activations precede by ~4 hours the behavioral outputs they control. The distinct phases of Ca^{2+} rhythms in the other three pacemaker groups (l-LNv, DN1, and DN3) may also involve the morning and evening behavioral peaks, or may regulate other, distinct circadian-gated outputs.

The E category of pacemakers includes the LNd as well as the fifth s-LNv (*11*–*14*). However, the LNd is a heterogeneous group of neurons that exhibits diverse entrainment properties (*21*); likewise, the critical fifth s-LNv could not be unambiguously identified with *tim*-GAL4. To better understand the function of these subsets of E pacemakers, we used a PDF receptor [*pdfr(B)*] GAL4 driver (*22*); this driver restricts GCaMP6s expression to s-LNv, to three of six LNds, and to the single fifth s-LNv (Fig. 2A). The three PDFR-expressing LNds and the fifth s-LNv displayed the same basic E cell pattern of Ca^{2+} activity—a peak in late subjective day—which suggests that they both function as circadian pacemakers (Fig. 2B). Thus, the phase difference between Ca^{2+} rhythms in these PDFR-expressing M and E cell groups again matched that between the morning and evening behavioral activity peaks (Fig. 2, C to F).

M and E cell categorization supports a classic model of seasonal adaptation (*23*) wherein a two-oscillator system responds differentially to light and so can track dawn and dusk independently. For example, under long-day conditions, light accelerates a "morning" clock and decelerates an "evening" clock. If these Ca^{2+} rhythms are critical output features of M and E cells, their properties may also reflect differences in photoperiodic entrainment. We entrained flies under either long-day (16 hours light, 8 hours dark) or short-day (8 hours light, 16 hours dark) conditions. In these flies, the phase difference between the morning and evening behavioral activity peaks tracked dawn and dusk (fig. S6). Likewise, the phases of pacemaker Ca^{2+} rhythms also tracked dawn and dusk (Fig. 3, A, B, E, and F, and fig. S7). Regardless of the photoperiodic schedule, the s-LNv (M cells) always peaked around dawn, whereas the LNd (E cells) always peaked before dusk (Fig. 3, B to D and F to H). Thus, Ca^{2+} activity patterns within the pacemaker network correspond to the circadian temporal landmarks of dawn and dusk.

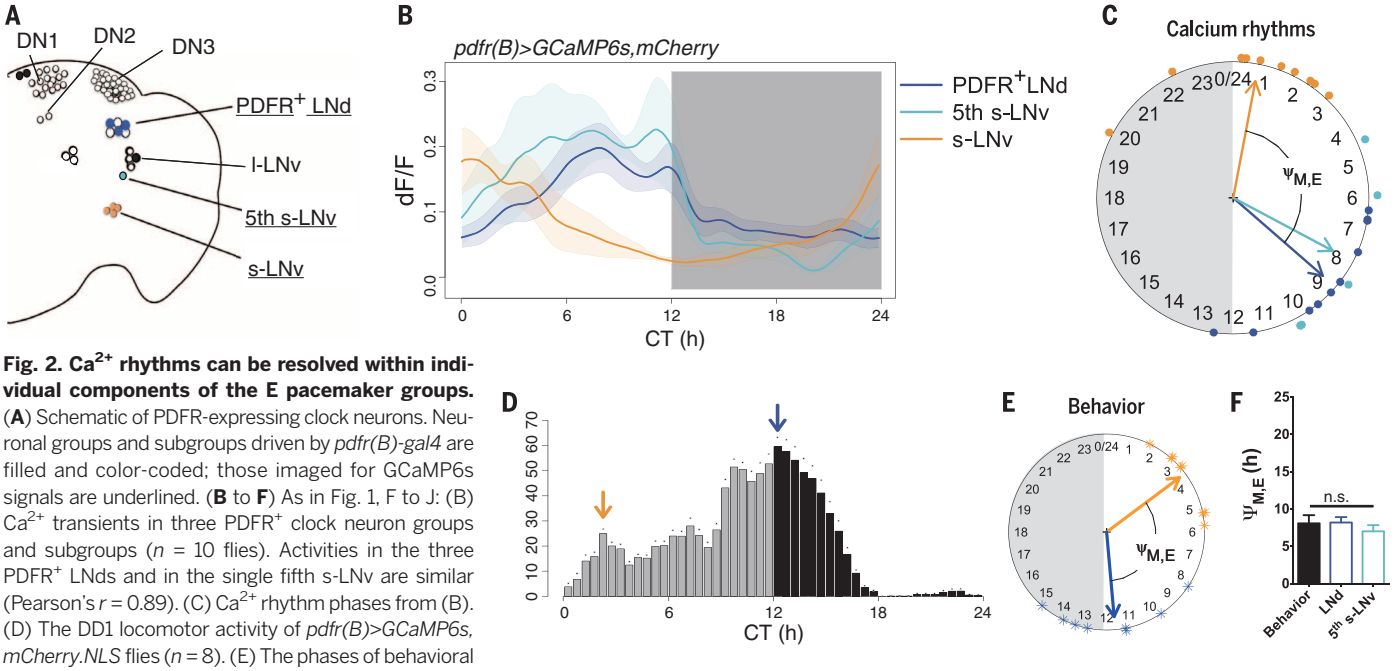

Fig. 2. Ca^{2+} rhythms can be resolved within individual components of the E pacemaker groups. (**A**) Schematic of PDFR-expressing clock neurons. Neuronal groups and subgroups driven by *pdfr(B)-gal4* are filled and color-coded; those imaged for GCaMP6s signals are underlined. (**B** to **F**) As in Fig. 1, F to J: (B) Ca^{2+} transients in three $PDFR^+$ clock neuron groups and subgroups (n = 10 flies). Activities in the three $PDFR^+$ LNds and in the single fifth s-LNv are similar (Pearson's r = 0.89). (C) Ca^{2+} rhythm phases from (B). (D) The DD1 locomotor activity of *pdfr(B)>GCaMP6s, mCherry.NLS* flies (n = 8). (E) The phases of behavioral peaks from (D). (F) Phase differences from M cells (s-LNv) to both LNd and the fifth s-LNv matched behavioral $\Psi_{M,E}$ (ANOVA, P = 0.7239).

We tested whether changes in the molecular oscillator would alter the patterns of $[Ca^{2+}]_i$. We used different alleles of the gene *period*, which encodes a state variable of the *Drosophila* circadian clock. In per^{01} (null) mutant flies, which lack inherent rhythmicity in their molecular oscillators and in free-running behavior (*24*, *25*) (fig. S8), all clock neurons showed reduced rhythmicity in $[Ca^{2+}]_i$. The amplitudes of Ca^{2+} fluctuations were reduced

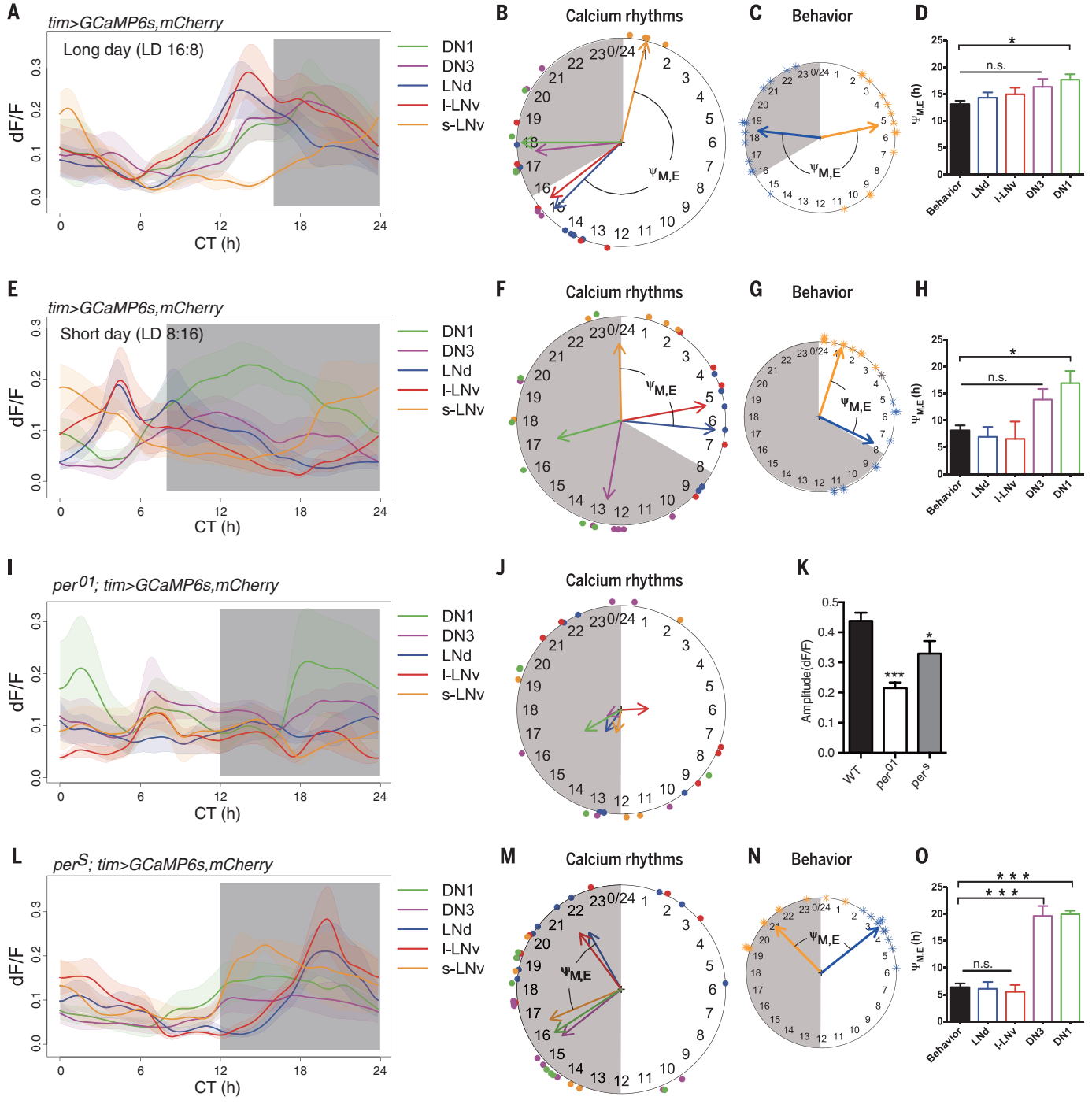

Fig. 3. Effects of environmental information and molecular clocks on the spatiotemporal patterns of Ca^{2+} activity in the pacemaker network. (**A** and **E**) Ca^{2+} transients: (A) under long (16:8 LD) photoperiod (n = 6 flies) and (E) under short (8:16 LD) photoperiod (n = 6 flies). (**B** and **F**) Ca^{2+} rhythm phases under long photoperiod (B) and under short photoperiod (F). The shaded circular sectors indicate lights-out periods of 8 hours (B) and 16 hours (F). Note that M cells (s-LNv, orange) peaked around lights-on and E cells (LNd, blue) peaked before lights-off, regardless of photoperiod. (**C** and **G**) The phases of behavioral peaks in DD1 after 6 days of photoperiodic entrainment: (C) long photoperiod (n = 13 flies) and (G) short photoperiod (n = 12 flies). See fig. S5 for details. (**D** and **H**) $\Psi_{M,LNd}$ matches behavioral $\Psi_{M,E}$ under long photoperiod (t test, P = 0.32; f test, P = 0.88) and under short photoperiod (t test, P = 0.30; f test, P = 0.16). (**I**) Arrhythmic Ca^{2+} transients in per^{01} mutants (n = 5 flies). (**J**) Phase coherence of Ca^{2+} transients was poor among per^{01} flies (Rayleigh test, $P > 0.5$). (**K**) Amplitude of Ca^{2+} transients (maximum dF/F) was significantly smaller in per^{01} and in per^{S} mutants (versus control flies; Mann-Whitney test, $^*P < 0.1$, $^{***}P < 0.001$). (**L**) Ca^{2+} transients in per^{S} mutants (n = 6 flies). (**M**) Ca^{2+} rhythm phases of per^{S} mutants. (**N**) Phases of behavioral peaks corresponding to Ca^{2+} rhythm phases in (M) (n = 16 flies). (**O**) $\Psi_{M,LNd}$ matched behavioral $\Psi_{M,E}$ (t test, P = 0.83; f test, P = 0.13).

by half (Fig. 3, I and K) and coherence was lost within groups (Rayleigh test, $P > 0.5$; Fig. 3J and table S1). In fast-running per^S mutant flies, which have a free-running period of ~19 hours (*24*, *25*) (fig. S9), the Ca^{2+} rhythms were phase-shifted (Fig. 3, L and M, and fig. S10), consonant with the direction of behavioral phase shifts (Fig. 3N and fig. S9). The phase difference between Ca^{2+} rhythm peaks in per^S M and E pacemakers still matched the phase difference between M and E behavioral peaks (Fig. 3, N and O). Thus, molecular clocks determine the pace of Ca^{2+} rhythms in the pacemaker network.

To explore how synchronous molecular clocks can have phases of Ca^{2+} activation that are staggered by many hours, we tested whether PDF, which mediates interactions between pacemakers, was required. Flies bearing the severely hypomorphic han^{5304} mutation of the PDF receptor show

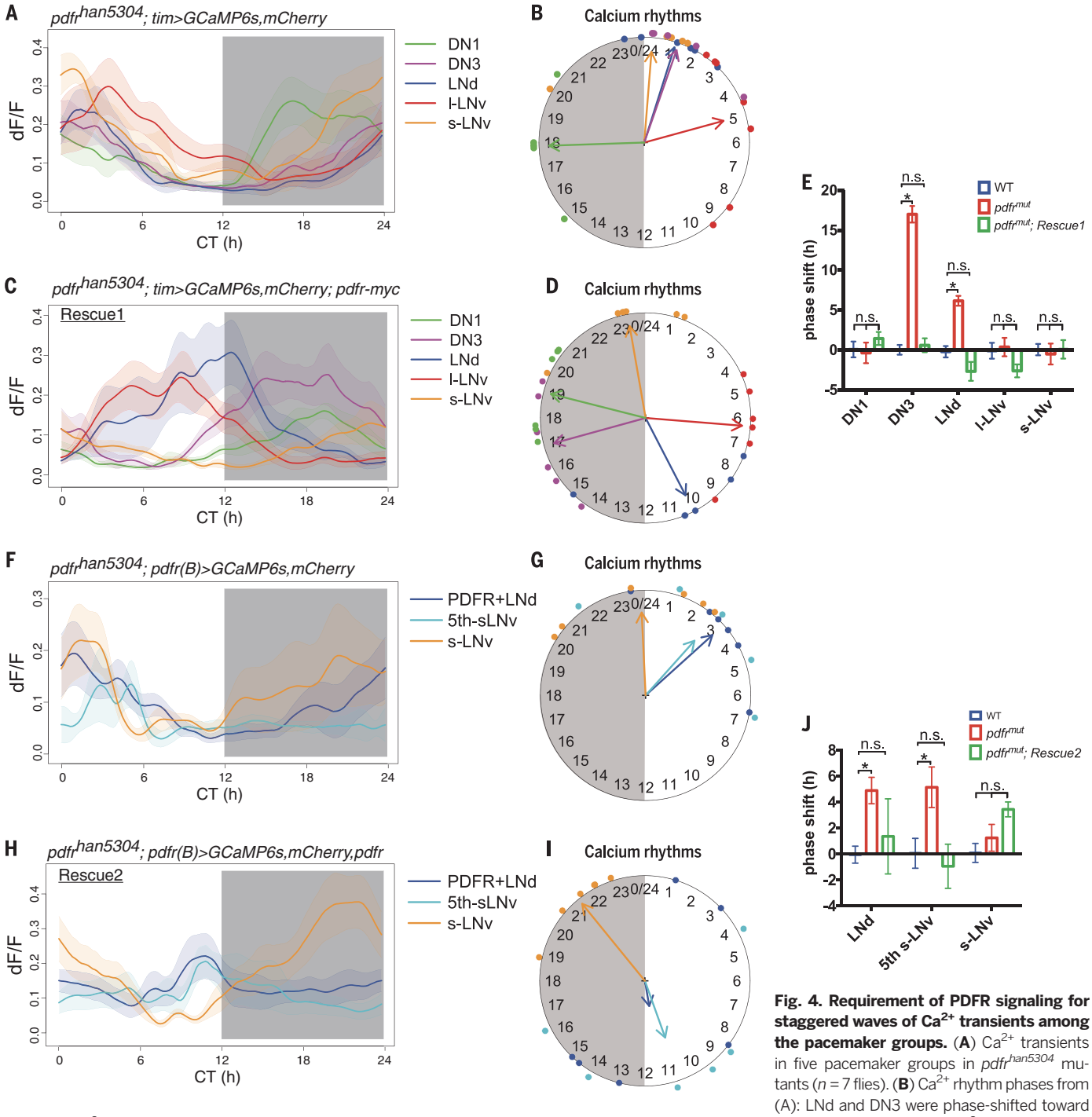

Fig. 4. Requirement of PDFR signaling for staggered waves of Ca^{2+} transients among the pacemaker groups. (**A**) Ca^{2+} transients in five pacemaker groups in $pdfr^{han5304}$ mutants ($n = 7$ flies). (**B**) Ca^{2+} rhythm phases from (A): LNd and DN3 were phase-shifted toward s-LNv. (**C**) Ca^{2+} transients in *pdfr* mutant flies that are restored by a large BAC-recombineered *pdfr-myc* transgene (rescue 1, $n = 6$ flies). (**D**) Ca^{2+} rhythm phases from (C). (**E**) The phase shifts in mutants were fully rescued by restoring PDFR (two-way ANOVA followed by Bonferroni post hoc test, $^*P < 0.001$). Colors indicate genotype. (**F**) Ca^{2+} transients in three pacemaker groups targeted by *pdfr(B)-gal4* in $pdfr^{han5304}$ mutants ($n = 6$ flies). (**G**) Ca^{2+} rhythm phases from (F). (**H**) Ca^{2+} transients in *pdfr* mutant flies that are restored by *pdfr(B)-gal4>pdfr* (rescue 2, $n = 6$ flies). (**I**) Ca^{2+} rhythm phases from (H): The $PDFR^+$ LNd and the single fifth s-LNv display restored phases but lack strong phase coherence (Rayleigh test, $P > 0.1$) (see also fig. S12). (**J**) Phase shifts in mutant flies were partially restored by restoring *pdfr* in subsets of $PDFR^+$ cells (two-way ANOVA followed by Bonferroni post hoc test, $^*P < 0.001$). Colors indicate genotype.

unimodal or arrhythmic behavior patterns under constant darkness (*26*) (fig. S11 and table S2). In these flies, we found that the Ca^{2+} rhythms in M cells (s-LNv and DN1) were unaffected, but they were phase-shifted in LNd and DN3, such that these two groups now produced Ca^{2+} rhythms around dawn, roughly in synchrony with M cells (Fig. 4, A and B). The phase of l-LNv did not change, consistent with the absence of PDF sensitivity by this pacemaker group (*27*). The phase shifts in LNd and DN3 were fully restored by the expression of complete *pdfr* from a bacterial artificial chromosome (BAC) transgene (Fig. 4, C to E, "rescue 1," and fig. S11). Thus, PDF, which promotes synchronization of molecular clocks under constant conditions (*10*, *28*), is also needed to properly stagger their Ca^{2+} activity phases across the day. Whether the phases of the l-LNv and DN1 are set by other intercellular signals remains to be determined.

We further examined the *pdfr* mutant phenotype at higher cellular resolution [*pdfr(B)> GCaMP6s*; Fig. 2A]. The PDFR-expressing E cell groups (the three PDFR-expressing LNd and the fifth s-LNv) displayed phase shifts similar to those of the entire LNd group (Fig. 4, F and G). When *pdfr* expression was restored just in these subsets of pacemaker neurons (with GAL4-UAS), both behavior and Ca^{2+} rhythms were partially restored (Fig. 4, H to J, "rescue 2," and fig. S11 and table S2). The phase of the fifth s-LNv was fully restored, which suggests that PDFR signaling is required for cell-autonomous setting of Ca^{2+} phase in this pacemaker group. However, in rescue 2, a single LNd typically remained active around dawn, whereas two LNds were active around dusk (fig. S12), which we interpret as a partial restoration or a nonautonomous phase-setting mechanism for LNd.

Our results show that molecular clocks drive circadian rhythms in the neural activity of pacemakers. Temporally patterned neural activity encodes different temporal landmarks of the day in a manner that reflects the different functions of the pacemaker groups. The homogeneous molecular clock produces sequential activity peaks by a mechanism dependent on PDFR signaling. By generating diverse phases of neural activity in different pacemaker groups, the circadian clock greatly expands its functional output.

REFERENCES AND NOTES

1. C. Lim, R. Allada, *Nat. Neurosci.* **16**, 1544–1550 (2013).
2. C. L. Partch, C. B. Green, J. S. Takahashi, *Trends Cell Biol.* **24**, 90–99 (2014).
3. D. K. Welsh, J. S. Takahashi, S. A. Kay, *Annu. Rev. Physiol.* **72**, 551–577 (2010).
4. G. M. Freeman Jr., R. M. Krock, S. J. Aton, P. Thaben, E. D. Herzog, *Neuron* **78**, 799–806 (2013).
5. N. Inagaki, S. Honma, D. Ono, Y. Tanahashi, K. Honma, *Proc. Natl. Acad. Sci. U.S.A.* **104**, 7664–7669 (2007).
6. J. A. Evans, T. L. Leise, O. Castanon-Cervantes, A. J. Davidson, *Neuron* **80**, 973–983 (2013).
7. M. Brancaccio, E. S. Maywood, J. E. Chesham, A. S. Loudon, M. H. Hastings, *Neuron* **78**, 714–728 (2013).
8. T. Yoshii, S. Vanin, R. Costa, C. Helfrich-Förster, *J. Biol. Rhythms* **24**, 452–464 (2009).
9. L. Roberts *et al.*, *Curr. Biol.* **25**, 858–867 (2015).
10. Y. Lin, G. D. Stormo, P. H. Taghert, *J. Neurosci.* **24**, 7951–7957 (2004).
11. D. Stoleru, Y. Peng, J. Agosto, M. Rosbash, *Nature* **431**, 862–868 (2004).
12. B. Grima, E. Chélot, R. Xia, F. Rouyer, *Nature* **431**, 869–873 (2004).
13. T. Yoshii *et al.*, *J. Insect Physiol.* **50**, 479–488 (2004).
14. Y. Zhang, Y. Liu, D. Bilodeau-Wentworth, P. E. Hardin, P. Emery, *Curr. Biol.* **20**, 600–605 (2010).
15. T. W. Chen *et al.*, *Nature* **499**, 295–300 (2013).
16. T. F. Holekamp, D. Turaga, T. E. Holy, *Neuron* **57**, 661–672 (2008).
17. G. Cao, M. N. Nitabach, *J. Neurosci.* **28**, 6493–6501 (2008).
18. G. Cao *et al.*, *Cell* **154**, 904–913 (2013).
19. M. Flourakis *et al.*, *Cell* **162**, 836–848 (2015).
20. A. Miyawaki, O. Griesbeck, R. Heim, R. Y. Tsien, *Proc. Natl. Acad. Sci. U.S.A.* **96**, 2135–2140 (1999).
21. Z. Yao, O. T. Shafer, *Science* **343**, 1516–1520 (2014).
22. S. H. Im, P. H. Taghert, *J. Comp. Neurol.* **518**, 1925–1945 (2010).
23. C. S. Pittendrigh, S. Daan, *J. Comp. Physiol. A Neuroethol. Sens. Neural Behav. Physiol.* **106**, 223–252 (1976).
24. R. J. Konopka, S. Benzer, *Proc. Natl. Acad. Sci. U.S.A.* **68**, 2112–2116 (1971).
25. P. E. Hardin, J. C. Hall, M. Rosbash, *Nature* **343**, 536–540 (1990).
26. S. Hyun *et al.*, *Neuron* **48**, 267–278 (2005).
27. O. T. Shafer *et al.*, *Neuron* **58**, 223–237 (2008).
28. T. Yoshii *et al.*, *J. Neurosci.* **29**, 2597–2610 (2009).

ACKNOWLEDGMENTS

We thank W. Li and D. Oakley for technical assistance; D. Dolezel for technical advice; the Holy and Taghert laboratories for advice; E. Herzog for comments on the manuscript; the Bloomington Stock Center, Janelia Research Center, J. Kim, and M. Affolter for sharing fly stocks; and M. Rosbash for antibodies to PER. Supported by the Washington University McDonnell Center for Cellular and Molecular Neurobiology and by NIH grants R01 NS068409 and R01 DP1 DA035081 (T.E.H.) and NIMH 2 R01 MH067122-11 (P.H.T.). Author contributions: X.L., T.E.H., and P.H.T. conceived the experiments; X.L. performed and analyzed all experiments; and X.L., T.E.H., and P.H.T. wrote the manuscript. T.E.H. has a patent on OCPI microscopy. Materials are available upon request.

SUPPLEMENTARY MATERIALS

www.sciencemag.org/content/351/6276/976/suppl/DC1
Materials and Methods
Supplementary Text
Figs. S1 to S12
Tables S1 and S2
References (*29*–*44*)

8 September 2015; accepted 26 January 2016
10.1126/science.aad3997

SYNAPTIC VESICLES

Single-vesicle imaging reveals different transport mechanisms between glutamatergic and GABAergic vesicles

Zohreh Farsi,[1] Julia Preobraschenski,[1] Geert van den Bogaart,[2] Dietmar Riedel,[3] Reinhard Jahn,[1]* Andrew Woehler[4,5]

Synaptic transmission is mediated by the release of neurotransmitters, which involves exo-endocytotic cycling of synaptic vesicles. To maintain synaptic function, synaptic vesicles are refilled with thousands of neurotransmitter molecules within seconds after endocytosis, using the energy provided by an electrochemical proton gradient. However, it is unclear how transmitter molecules carrying different net charges can be efficiently sequestered while maintaining charge neutrality and osmotic balance. We used single-vesicle imaging to monitor pH and electrical gradients and directly showed different uptake mechanisms for glutamate and γ-aminobutyric acid (GABA) operating in parallel. In contrast to glutamate, GABA was exchanged for protons, with no other ions participating in the transport cycle. Thus, only a few components are needed to guarantee reliable vesicle filling with different neurotransmitters.

All synaptic vesicles (SVs) are energized by vacuolar H^+-dependent adenosine triphosphatases (V-ATPases) that pump protons into the vesicle lumen (*1*) independently of the neurotransmitter phenotype that they contain. As a result, the vesicle interior acidifies, resulting in a pH gradient (ΔpH) and an inside positive membrane potential (Δψ) that both contribute to the free energy of the gradient ($\Delta\mu_{H+}$) across the vesicle membrane. Shifting the balance between Δψ and ΔpH has profound influence on the uptake kinetics of different neurotransmitters; in vitro, uptake of negatively charged glutamate is maximal when Δψ dominates. In contrast, uptake of positively charged monoamines requires mainly ΔpH, whereas neutral γ-amino butyric acid (GABA) uses both components of $\Delta\mu_{H+}$ (*2*). Because only a few hundred protons need to be translocated to saturate $\Delta\mu_{H+}$, other ions must compensate for the transport of the estimated 2000 to 5000 transmitter molecules (*3*, *4*). However, it has been surprisingly difficult to unravel such compensating ion fluxes and the responsible channels and/or transporters. In particular, the transport mechanism for GABA has remained enigmatic, with both $GABA/H^+$ exchange and $GABA/Cl^-$ cotransport having been proposed (*5*).

Mechanistic studies on vesicular transporters are generally carried out by using highly purified

[1]Department of Neurobiology, Max Planck Institute for Biophysical Chemistry, 37077 Göttingen, Germany. [2]Department of Tumor Immunology, Radboud University Medical Center, 6525GA Nijmegen, Netherlands. [3]Laboratory of Electron Microscopy, Max Planck Institute for Biophysical Chemistry, 37077 Göttingen, Germany. [4]Department of Membrane Biophysics, Max Planck Institute for Biophysical Chemistry, 37077 Göttingen, Germany. [5]Deutsche Forschungsgemeinschaft (DFG) Research Center for Nanoscale Microscopy and Molecular Physiology of the Brain (CNMPB), Göttingen, 37073, Germany.
*Corresponding author. E-mail: rjahn@gwdg.de

Downloaded from on February 25, 2016

SVs or, more recently, purified transporters that are reconstituted in artificial vesicles (*6*–*8*). Although our present knowledge of transport mechanisms is largely based on such approaches, only average properties can be studied. In contrast, almost no information is available about the properties of single SVs such as kinetics, heterogeneity, or properties specific for different neurotransmitter phenotypes. To overcome these limitations, we developed an approach to measure both ΔpH and Δψ in single SVs whose neurotransmitter phenotype is subsequently identified. SVs purified from transgenic mice expressing super-ecliptic pHluorin in the vesicular lumen (spH-SVs) (*9*) were imaged by using total internal reflection fluorescence microscopy in order to accurately measure luminal pH changes above pH 6, as described previously (Fig. 1, A and B, and fig. S5A) (*10*). We combined this approach with a potentiometric assay by labeling SVs with the voltage-sensitive dye VF2.1.Cl (*11*) to quantitatively measure Δψ across the lipid bilayer of single SVs (Fig. 1, C and D, and fig. S5C). After measuring ΔpH or Δψ, we performed onstage labeling with antibodies against vesicular GABA (VGAT) or vesicular glutamate transporter 1 (VGLUT1) to distinguish between GABA-containing (GABAergic) and glutamatergic SVs unequivocally (Fig. 1, E and F, and fig. S4).

At all tested adenosine 5′-triphosphate (ATP) concentrations (0.6 to 3 mM), significant differences in $\Delta\mu_{H+}$ were observed between glutamatergic and GABAergic SVs in the same population (significance in all experiments was determined with Student's two-tailed *t* test). In the absence of monovalent ions, $\Delta\mu_{H+}$ generated by the V-ATPase across the membrane of glutamatergic SVs was on average greater by 17.79 ± 6.9 (SD) mV [11.99 ± 5.2 mV larger Δψ and 0.1 ± 0.03 larger ΔpH (*12*)] than that of GABAergic SVs (Fig. 2, A and B). Three parameters may account for these differences in $\Delta\mu_{H+}$: the rate of proton pumping; the amount of free protons in the lumen, which depends on the luminal buffering capacity (β); and the rate of proton efflux (*13*). We excluded the first parameter because the rate of proton pumping was not different between glutamatergic and GABAergic SVs (fig. S6A). Next, we measured β using a modified ammonium pulse technique (fig. S7) (*14*). Although β increased as the lumen of vesicles acidified, there was no significant difference in β between both SV populations (fig. S8B). Last, we measured the proton efflux rate in these vesicles as described previously (fig. S9) (*10*, *12*). Significantly faster proton efflux was measured in GABAergic as compared with glutamatergic SVs (Fig. 2C). This indicates higher proton permeability (P_{H+}) in these SVs ($P_{H+} = 15.2 \times 10^{-3}$ and 13.5×10^{-3} cm sec^{-1} in GABAergic and glutamatergic SVs, respectively), thus accounting for the reduced $\Delta\mu_{H+}$ in GABAergic SVs. To exclude that the higher proton efflux rate is simply caused by nonspecific leakage owing to an increased surface area, we measured the diameter of SVs with electron microscopy, using immunogold labeling to distinguish between vesicle types (fig. S10), and observed no difference between these vesicle

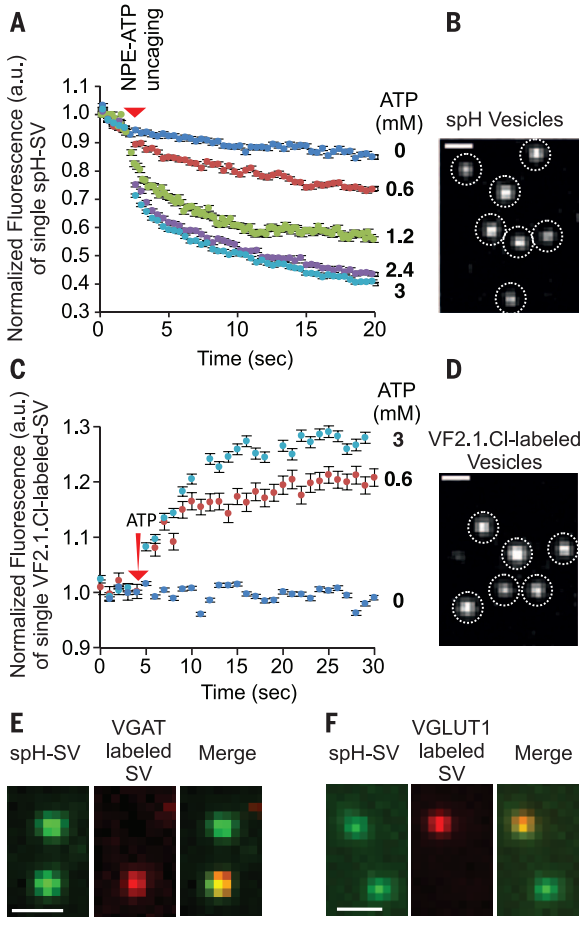

Fig. 1. $\Delta\mu_{H+}$ measured at the single-vesicle level. (**A**) Averaged spH time-trace in response to 5-(N-Ethyl-N-isopropyl)amiloride (NPE)–ATP uncaging by an ultraviolet flash (*12*). (**B**) Representative image of spH-SVs. (**C**) Averaged VF2.1.Cl time-trace in response to ATP addition. (**D**) Representative image of VF2.1.Cl–labeled SVs. (**E** and **F**) Representative spH-SVs immunolabeled for (E) VGAT and (F) VGLUT1. Dashed circles in (B) and (D) indicate detected SVs. Scale bars, 1 μm. In (A) and (C), the traces in the absence of ATP show the photobleaching of the probes, and error bars represent SEM from more than 500 single SVs.

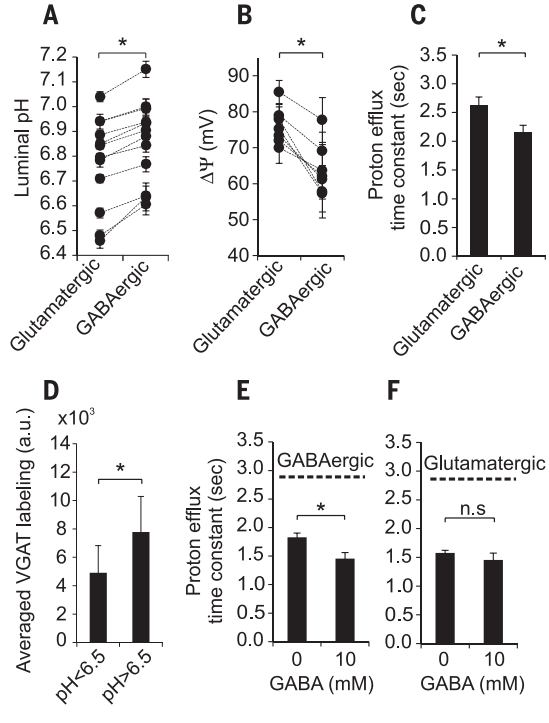

Fig. 2. VGAT functions as a GABA/H$^+$ antiporter. (**A**) Luminal pH and (**B**) Δψ of acidified glutamatergic and GABAergic SVs ($P = 2.7 \times 10^{-5}$ and 0.03, respectively). The variations in luminal pH are partially due to different ATP concentrations in some of the experiments (0.6 to 3 mM). Two circles connected via a dashed line represent one experiment. (**C**) Proton efflux time constant of glutamatergic versus GABAergic SVs ($P = 0.03$). (**D**) Correlation between luminal pH of acidified GABAergic SVs with intensity of antibody against VGAT ($P = 0.011$). (**E** and **F**) Proton efflux time constant of (E) GABAergic and (F) glutamatergic SVs in the presence and absence of GABA [$P = 7.7 \times 10^{-3}$ in (E)]. Data in (A) and (B) represent mean ± SEM from on average 450 glutamatergic and 160 GABAergic SVs per experiment; in (C), (E), and (F), data represent mean ± SEM from on average 50 single SVs compiled from independent experimental replicates with a coefficient of determination (R^2) > 0.7; and in (D), data represent mean ± SD of seven independent experiments. n.s., not significant ($P > 0.05$).

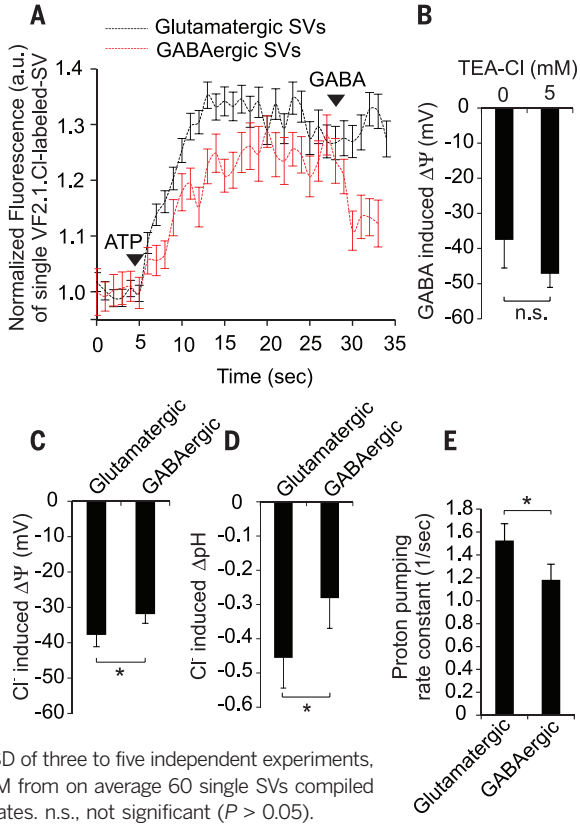

Fig. 3. VGAT is not a GABA/Cl⁻ cotransporter. (**A**) Averaged VF2.1.Cl time-trace in response to addition of 3 mM ATP and 10 mM GABA, indicating changes in Δψ associated with GABA uptake in GABAergic (red trace) but not in glutamatergic (black trace) SVs. Error bars represent SEM of 50 and 392 SVs in red and black traces, respectively. (**B**) Changes in Δψ induced by addition of GABA to acidified SVs in the absence and presence of 5 mM tetra-ethylammonium chloride (TEA-Cl) in the bath solution. (**C**) Δψ induced by addition of 20 mM TEA-Cl to acidified glutamatergic and GABAergic SVs (P = 0.006). (**D**) ΔpH induced by including TEA-Cl in the bath solution in glutamatergic and GABAergic SVs (P = 0.01). (**E**) Proton pumping rate constant of glutamatergic [1.52 ± 0.15 (SEM) s^{-1}] and GABAergic [1.18 ± 0.14 (SEM) s^{-1}] SVs with 2.4 mM ATP in the presence of Cl^- (P = 0.045). Data in (B), (C), and (D) represent mean ± SD of three to five independent experiments, and in (E), data represent mean ± SEM from on average 60 single SVs compiled from independent experimental replicates. n.s., not significant (P > 0.05).

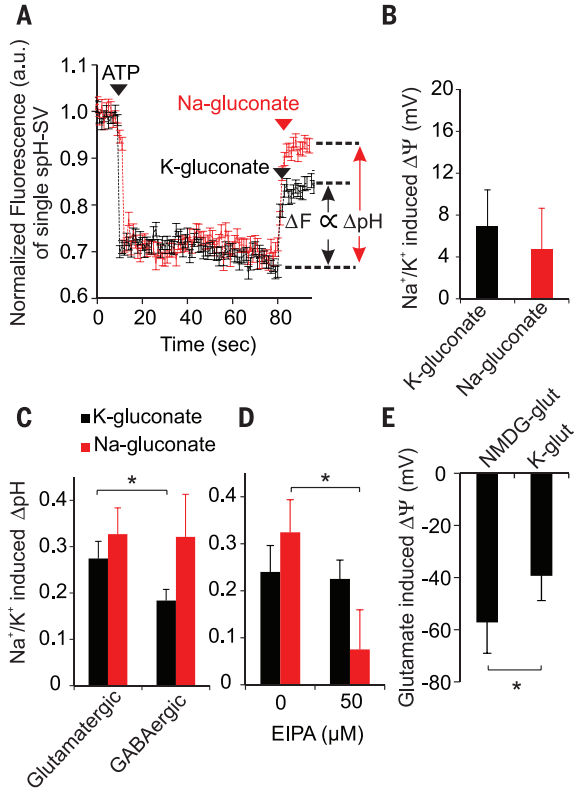

Fig. 4. Cation/H⁺ exchange is more pronounced in glutamatergic SVs. (**A**) Averaged fluorescence trace of SVs in response to 1 mM ATP and 30 mM K-gluconate (black trace) or 10 mM Na-gluconate (red trace). (**B**) Δψ induced by addition of 30 mM K-gluconate or 10 mM Na-gluconate to acidified SVs. (**C**) ΔpH induced by K-gluconate or Na-gluconate in glutamatergic and GABAergic SVs (P = 0.009 for K^+ effect). (**D**) Inhibition of Na^+ but not K^+ induced ΔpH by EIPA (P = 0.002 for Na^+ effect). (**E**) Changes in Δψ induced by addition of 10 mM *N*-methyl-D-glucamine (NMDG)–glutamate and K-glutamate to acidified SVs (P = 0.02). Data in (A) represent mean ± SEM from on average 600 single SVs, and in (B) to (E), data are mean ± SDs of three to five independent experiments.

populations. These data strongly suggest that a protein specific for GABAergic SV is responsible for the increased proton efflux rate. Because only the vesicular transporters are exclusively present in each vesicle population (*15*), we hypothesized that VGAT contributes to proton efflux in GABAergic SVs. Indeed, in each acidification measurement the luminal pH of acidified GABAergic SVs correlated with the immunolabeling intensity for VGAT, indicating that SVs with greater VGAT copy numbers had greater proton permeability (Fig. 2D).

As discussed above, the transport mechanism of VGAT is controversial, with both GABA/H^+ antiport (*16*–*19*) and GABA/Cl^- cotransport (*8*) having been proposed. In the former case, proton efflux of GABAergic SVs should be enhanced when GABA is added. Indeed, we observed significantly accelerated proton efflux from GABAergic vesicles (Fig. 2E) in the presence of 10 mM GABA, whereas that of glutamatergic SVs remained unchanged (Fig. 2F), clearly indicating that VGAT does in fact function as a GABA/H^+ exchanger. The same result was obtained with 20 mM glycine, which is another substrate of VGAT (fig. S11, A and B). However, glutamate had no significant effect on proton efflux rate in any of the vesicle populations (fig. S12).

The experiments described above were carried out in the absence of Cl^-. To test whether Cl^- contributes to GABA transport, we characterized the effects of GABA and Cl^- on Δψ. When vesicles were allowed to acidify, addition of GABA partially dissipated Δψ exclusively in GABAergic SVs (Fig. 3A), confirming that GABA (no net charge at neutral pH) is exchanged for protons. When Cl^- was included, only a slightly higher reduction of Δψ was observed (Fig. 3B), ruling out any prominent GABA-coupled transport of Cl^- by VGAT (*8*). Thus, the stimulatory effect of Cl^- on GABA uptake observed previously (*5*, *18*, *19*) is probably due to a shift from Δψ to ΔpH. Indeed, addition of 20 mM Cl^- to acidified vesicles caused a shift in the $\Delta\mu_{H+}$ balance, dissipating the membrane potential while enhancing luminal acidification (Fig. 3, C and D, and fig. S14). Cl^- influx, presumably through the vesicular Cl^-/H^+ exchanger 3 (ClC3) (*20*) or VGLUT2 (*21*), effectively shunts the membrane potential, allowing the V-ATPase to drive more protons into the lumen, which in turn are exchanged for GABA by VGAT. Addition of Cl^- resulted in significantly larger dissipation of Δψ and greater acidification in glutamatergic rather than in GABAergic SVs (Fig. 3, C and D). Moreover, Cl^- selectively enhanced the rate of proton pumping in glutamatergic SVs (Fig. 3E). Because ClC3 is present in both vesicle types in comparable quantities (*15*), our data indicate that VGLUT directly contributes to Cl^- transport, which is in agreement with previous reports (*6*, *7*).

Last, we examined whether Na^+ and K^+ exert different effects on the two vesicle populations. Both ions convert ΔpH to Δψ via cation/H^+ exchange mechanisms (*22*) but involve different pathways: Na^+/H^+ exchange is mediated by the Na^+/H^+ exchanger NHE6, whereas K^+/H^+ exchange is proposed to be mediated by VGLUT (*6*). Our single-vesicle assay allowed for discriminating these two exchange activities in single vesicles. Indeed, addition of each cation to acidified vesicles significantly alkalinized the luminal pH (Fig. 4A and fig. S14A) and slightly increased the

membrane potential (Fig. 4B), but with notable differences between the two vesicle populations: Less K^+-induced alkalinization was observed in GABAergic SVs, whereas Na^+ induced similar alkalinization levels in both vesicle populations (Fig. 4C). When the experiments were repeated in the presence of the NHE inhibitor ethyl-isopropyl amiloride (EIPA), Na^+-induced alkalinization was significantly blocked, whereas K^+-induced alkalinization remained unchanged (Fig. 4D). The greater effect of K^+ in glutamatergic SVs as well as its resistance to EIPA confirms that VGLUT is mainly responsible for K^+ transport into the lumen of SVs. The smaller but still substantial effect of K^+ in GABAergic SVs may be due to the presence of VGLUT2 that is known to be expressed in subsets of GABAergic neurons (*21*). It is also possible that VGAT contributes to the measured K^+/H^+ exchange but with a different stoichiometry than that of VGLUT. Both the NHE-mediated Na^+/H^+ and VGLUT-mediated K^+/H^+ exchange convert ΔpH to $\Delta\psi$, counteracting the effect of Cl^- on $\Delta\mu_{H+}$. Moreover, we observed that dissipation of $\Delta\psi$ by glutamate uptake (fig. S15) was significantly mitigated by the presence of K^+ (Fig. 4E). This further emphasizes the crucial role of VGLUT-mediated K^+/H^+ exchange as a charge-compensating mechanism that helps to sustain $\Delta\psi$ and enhances glutamate uptake (*6*).

Through the quantitative characterization of $\Delta\mu_{H+}$ in single vesicles, we report here that not only the pH gradient of $\Delta\mu_{H+}$ (*10*) but also $\Delta\psi$ is generated across the membrane of SVs within 1 to 2 s. Moreover, our data clearly demonstrate that VGAT is not a GABA/Cl^- cotransporter (*8*) but functions as a GABA/H^+ antiporter. Surprisingly, our data suggest that VGAT is leaky to protons in the absence of substrate, raising the question of whether the presence of GABA prevents nonspecific proton leakage, replacing it with a strict GABA/H^+ antiport. In addition, ion fluxes through VGLUT can shift the balance of the components of $\Delta\mu_{H+}$ toward greater $\Delta\psi$ and ensure charge and osmolarity compensation during neurotransmitter loading. Thus, neurotransmitter transporters are critical regulators of $\Delta\mu_{H+}$, which adds another level of complexity to their contribution to maintenance of fidelity in synaptic transmission.

REFERENCES AND NOTES

1. M. Nakanishi-Matsui, M. Sekiya, R. K. Nakamoto, M. Futai, *Biochim. Biophys. Acta* **1797**, 1343–1352 (2010).
2. R. D. Blakely, R. H. Edwards, *Cold Spring Harb. Perspect. Biol.* **4**, a005595 (2012).
3. N. Riveros, J. Fiedler, N. Lagos, C. Muñoz, F. Orrego, *Brain Res.* **386**, 405–408 (1986).
4. P. M. Burger *et al*., *Neuron* **3**, 715–720 (1989).
5. G. Ahnert-Hilger, R. Jahn, *Nat. Neurosci.* **14**, 405–407 (2011).
6. J. Preobraschenski, J. F. Zander, T. Suzuki, G. Ahnert-Hilger, R. Jahn, *Neuron* **84**, 1287–1301 (2014).
7. S. Schenck, S. M. Wojcik, N. Brose, S. Takamori, *Nat. Neurosci.* **12**, 156–162 (2009).
8. N. Juge, A. Muroyama, M. Hiasa, H. Omote, Y. Moriyama, *J. Biol. Chem.* **284**, 35073–35078 (2009).
9. Z. Li *et al*., *Proc. Natl. Acad. Sci. U.S.A.* **102**, 6131–6136 (2005).
10. K. L. Budzinski, M. Zeigler, B. S. Fujimoto, S. M. Bajjalieh, D. T. Chiu, *Biophys. J.* **101**, 1580–1589 (2011).
11. E. W. Miller *et al*., *Proc. Natl. Acad. Sci. U.S.A.* **109**, 2114–2119 (2012).
12. Materials and methods are available as supplementary materials on *Science* Online.
13. M. Grabe, G. Oster, *J. Gen. Physiol.* **117**, 329–344 (2001).
14. L. Maresová, B. Hosková, E. Urbánková, R. Chaloupka, H. Sychrová, *Yeast* **27**, 317–325 (2010).
15. M. Grønborg *et al*., *J. Neurosci.* **30**, 2–12 (2010).
16. S. L. McIntire, R. J. Reimer, K. Schuske, R. H. Edwards, E. M. Jorgensen, *Nature* **389**, 870–876 (1997).
17. P. M. Burger *et al*., *Neuron* **7**, 287–293 (1991).
18. V. Riazanski *et al*., *Nat. Neurosci.* **14**, 487–494 (2011).
19. J. W. Hell, P. R. Maycox, R. Jahn, *J. Biol. Chem.* **265**, 2111–2117 (1990).
20. S. M. Stobrawa *et al*., *Neuron* **29**, 185–196 (2001).
21. J. F. Zander *et al*., *J. Neurosci.* **30**, 7634–7645 (2010).
22. G. Y. Goh *et al*., *Nat. Neurosci.* **14**, 1285–1292 (2011).

ACKNOWLEDGMENTS

The authors thank V. N. Murthy (Cambridge, MA) and W. Tyler (Roanoke, VA) for providing transgenic mice, U. Teichmann (Göttingen) for arranging animal delivery and husbandry, M. Kohansal-Nodehi (Göttingen) for mass spectrometry, L. Kastrup (Göttingen) for assistance in setting up total internal reflection fluorescence microscopy, S. Ahmed (Göttingen) for help in subcellular fractionation, and E. Neher (Göttingen) for scientific discussions. We thank V. N. Belov, J. Schimpfhauser, and J. Bienert (Facility for the Synthetic Chemistry of Max Planck Institute for Biophysical Chemistry) for the synthesis of VF2.1.Cl. G.v.d.B. is funded by a Hypatia fellowship from the Radboud University Medical Center and is the recipient of a Starting Grant from the European Research Council (ERC) under the European Union's Seventh Framework Programme (grant agreement 336479). A.W. is funded by the Cluster of Excellence and the DFG Research Center for Nanoscale Microscopy and Molecular Physiology of the Brain. Additional data described in the manuscript are presented in the supplementary materials.

SUPPLEMENTARY MATERIALS

www.sciencemag.org/content/351/6276/981/suppl/DC1
Materials and Methods
Supplementary Text
Figs. S1 to S15
References (*23*–*36*)

5 November 2015; accepted 14 January 2016
Published online 11 February 2016
10.1126/science.aad8142

WHO WILL BE THE NEXT PRIZEWINNER?

We are now calling for recommendations for the 2016 International Cosmos Prize!

› International Cosmos Prize is awarded for excellent research and work that contributes to the development of the concept of Expo '90, ***"The Harmonious Coexistence between Nature and Mankind"***.

› The Prize is an annual academic prize presented by the Expo '90 Foundation in Osaka, Japan. The monetary prize is 40 million yen.

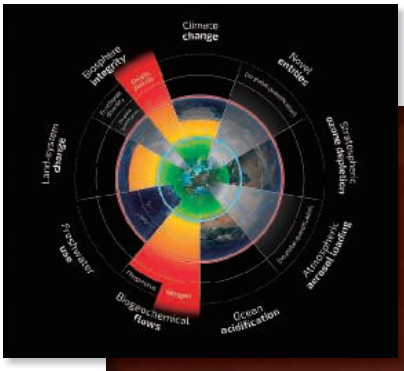

Dr. Rockström cautioned that we have reached a saturation point in terms of human pressures on the Earth System, and that if we let these anthropogenic pressures continue increasing to cross the thresholds or tipping points defined as "planetary boundaries," there is a risk of irreversible and abrupt environmental change.

2015 Prizewinner

Dr. Johan Rockström

Nationality : Sweden
Specialty : environmental science

Prizewinner

2014 Prizewinner

Dr. Philippe Descola

Nationality : France
Specialty : Anthropology

2013 Prizewinner

Dr. Robert Treat Paine

Nationality : U.S.A.
Specialty : Conservation Ecology

2012 Prizewinner

Dr. Edward Osborne Wilson

Nationality : U.S.A.
Specialty : Biology

2011 Prizewinner

Scientific Steering Committee of the Census of Marine Life

Nationality : U.S.A.
Specialty : Compiling the Ocean Biogeographic Information System

2010 Prizewinner

Dr. Estella Bergere Leopold

Nationality : U.S.A.
Specialty : Paleontology

2009 Prizewinner

Dr. Gretchen Cara Daily

Nationality : U.S.A.
Specialty : Environmental Science

2008 Prizewinner

Dr. Phan Nguyen Hong

Nationality : Vietnam
Specialty : Conservation Ecology

2007 Prizewinner

Dr. Georgina Mary Mace

Nationality : London, U.K.
Specialty : Conservation Ecology

2006 Prizewinner

Dr. Raman Sukumar

Nationality : India
Specialty : Conservation Ecology

2005 Prizewinner

Dr. Daniel Pauly

Nationality : Canada
Specialty : Marine Biology

2004 Prizewinner

Prof. Julia Carabias Lillo

Nationality : Mexico
Specialty : Environmental Science

2003 Prizewinner

Dr. Peter Hamilton Raven

Nationality : U.S.A.
Specialty : Botany

2002 Prizewinner

The Charles Darwin Research Station

Nationality : Ecuador
Specialty : Diverse activities in the Galapagos Islands

2001 Prizewinner

Prof. Anne Whiston Spirn

Nationality : U.S.A.
Specialty : Landscape Architecture

2000 Prizewinner

Sir David Attenborough

Nationality : U.K.
Specialty : Zoology, Film producer

1999 Prizewinner

Dr. Wu Zheng-Yi

Nationality : China
Specialty : Botany

1998 Prizewinner

Dr. Jared Mason Diamond

Nationality : U.S.A.
Specialty : Geographic History

1997 Prizewinner

Dr. Richard Dawkins

Nationality : U.K.
Specialty : Evolutionary Biology

1996 Prizewinner

Dr. George Beals Schaller

Nationality : U.S.A.
Specialty : Biology

1995 Prizewinner

Dr. Tatuo Kira

Nationality : Japan
Specialty : Plant Ecology

1994 Prizewinner

Dr. Jacques François Barrau

Nationality : France
Specialty : Ethnobiology

1993 Prizewinner

Sir Ghillean Prance

Nationality : U.K.
Specialty : Botany

If you have a candidate whom you would like to recommend, please e-mail us at the address below.
We will send you a recommendation form (in Microsoft Word). The deadline for recommendations is April 15.

EXPO '90 FOUNDATION **E-mail: rec-cosmos@expo-cosmos.or.jp**

BOYALIFE & Science Science Translational Medicine Award in Stem Cells and Regenerative Medicine

Stem cells and regenerative medicine is the new frontier in life sciences. Boyalife, Science and Science Translational Medicine jointly establish a global award to recognize significant contributions in advancing basic science to clinical applications in this field.

The award is to recognize and reward scientists in the fields of stem cells and/or regenerative medicine with a focus on developing cell-based treatments for cancer, degenerative disorders, immunotherapy and stem cells transplantation.

You could be next to win this prize and to receive

- ★ A Grand Prize of **$25,000** and a Runner-Up Prize of **$5,000** will be awarded.
- ★ The Grand Prize Winning Essay will be published in Science; a brief abstract of the Runner-Up Essay will be published in Science.

The 2016 Award is now open. The deadline for submissions is March 1, 2016
For more information, please visit : *http://www.sciencemag.org/prizes/boyalife*

BOYALIFE® For Better Health

Science AAAS

Science Translational Medicine AAAS

eppendorf & Science

PRIZE FOR NEURO BIOLOGY

2015 Winner
Shigeki Watanabe, Ph.D.
Johns Hopkins University
For research on synaptic vesicle endocytosis

Application Deadline
June 15, 2016

Call for Entries

Eppendorf & Science Prize for Neurobiology
The annual Eppendorf & Science Prize for Neurobiology is an international award which honors young scientists for their outstanding contributions to neurobiological research based on methods of molecular and cell biology. The winner and finalists are selected by a committee of independent scientists, chaired by Science's Senior Editor, Dr. Peter Stern. Researchers who are not older than 35 years are invited to apply.

You could be next to win this prize and to receive
> Prize money of US$25,000
> Publication of your work in Science
> Full support to attend the Prize Ceremony held in conjunction with the Annual Meeting of the Society for Neuroscience in the USA
> An invitation to visit Eppendorf in Hamburg, Germany

It's easy to apply!
Learn more about the Prize and its past winners at:

www.eppendorf.com/prize

eppendorf Science AAAS

AAAS® and Science® are registered trademarks of the American Association for the Advancement of Science, USA. Eppendorf® and the Eppendorf logo are registered trademarks of Eppendorf AG, Germany. U.S. Design Patents are listed on www.eppendorf.com/ip. All rights reserved, including graphics and images. Copyright © 2016 by Eppendorf AG. Kurstin Roe Photography.

HLA Analysis Software

The Axiom HLA Analysis software is designed for automated, high-resolution human leukocyte antigen (HLA) typing from any genotyping dataset containing coverage of the extended major histocompatibility complex (MHC) region. The software's unique imputation algorithm enables four-digit HLA typing from genome-wide association studies (GWAS), combining genotyping and high-resolution HLA typing into a single assay. Prior to the availability of Axiom HLA Analysis, researchers conducted separate HLA molecular testing of their samples or used complex analysis workflows to generate HLA types from genotype data. The algorithms incorporated into the software provide simple, "push-button" analysis to dramatically decrease researchers' cost and workload. The Axiom HLA Analysis software can be used with data from a number of Affymetrix array products, including the new Axiom Transplant Genotyping Array and UK Biobank Axiom Array, as well as the Genome-Wide Human SNP Array 6.0. Genotyping data produced by other manufacturers' systems can be economically HLA-typed by Affymetrix Research Service Laboratory using the new software.

Affymetrix
For info: 888-362-2447
www.affymetrix.com

Tissue Analysis Software

Tissue Studio 4.1 features powerful machine learning and the ability to automate routine image analysis tasks, enabling researchers to develop a customized image analysis solution in as little as 20 minutes, and to reduce preclinical safety and toxicity study lengths from weeks to just days. It offers scientists an out-of-the-box solution that provides comprehensive and consistent data from any tissue-based assay, and can handle complex tasks such as biological heterogeneity and staining variation. Tissue Studio 4.1's image analysis allows researchers to automate tedious manual analysis, produces quantitative readouts that can be mined and correlated, and simplifies analysis tasks and workflows. Adding to these standard benefits, Tissue Studio uniquely overcomes inherent biological and staining variability to accurately detect regions of interest and distinguish cell types and subtypes within target regions across any number of tissue slides. Tissue Studio 4.1 brings powerful speed and efficiency improvements to the solution of choice for image analysis.

Definiens
For info: +49-(0)-89-231180-0
www.definiens.com

Microscope Tools

Taking well-plate imaging to the next level, Olympus presents two innovative tools for the customizable IX3 inverted microscopes. The new IX3-ZDC2 module offers cutting-edge focal drift compensation technology, enabling accurate focus stability during long time-lapse experiments. Complementing this is the latest cellSens version 1.14 software, which features an improved Well Navigator tool for smart and flexible multiwell experimental setup. Combined, these updates form a highly accurate, reliable, and easy-to-use well-plate imaging system for live-cell imaging. Compensating for changes such as thermal drift, Z-drift compensation (ZDC) technology employs an infrared laser diode to measure focus distance. The new IX3-ZDC2 is able to focus up to four times faster than the previous model, and includes a fully motorized dichroic mirror movement. The Well Navigator makes it possible to move to a specific well with one click and simplifies management of different imaging parameters in individual wells or groups of wells.

Olympus
For info: +49-(0)-40-23773-5913
www.olympus-lifescience.com

Imaging Software

The ZEN 2 core imaging software is easy to use and simply designed. It allows users to achieve the highest quality results together with established ZEISS hardware. ZEN 2 core gives users the benefit of an adaptive user interface suited specifically to industrial and research applications. The easy graphical user interface (GUI) configuration fits tasks of all kinds and of any complexity. Users can adapt the GUI to their workflows to simplify their work. ZEISS ZEN 2 core also offers configurable user management, adjusting the software to different users and user levels. Given the ZEN 2 core's straightforward workflows, users can count on fast, reproducible analysis and measurement results. Its ability to create job templates ensures users get comparable results every time. ZEISS ZEN 2 core offers an interface to many other software platforms and hardware accessories.

ZEISS
For info: +49-3641-64-3949
www.zeiss.com

Gene Editing Software

Developed in collaboration with Desktop Genetics, gUIDEbook bioinformatics software has been designed to support researchers working with clustered regularly interspaced short palindromic repeats (CRISPR) genome editing. Successful CRISPR genome editing relies on the quality of the guide RNA (gRNA) design, determined by bioinformatics software. The gUIDEbook software has been developed to provide the most complete solution available for designing CRISPR genome editing experiments. The platform enables researchers to generate knockouts, knockins, mutations, or tags through powerful, laboratory-validated DNA search algorithms behind a simple and intuitive user interface. Utilizing state-of-the-art scoring functions, gUIDEbook allows an entire gene to be quickly reviewed for the best guide or guides for both wild-type and CRISPR-associated 9 protein (Cas9) "nickase" experiments. The current version of gUIDEbook supports human and mouse genomes with additional genomes to be added later, and offers two levels of use depending on experimental requirements and the level of user experience. Once researchers have selected the best guides for an experiment, they can then easily order their chosen guides.

Horizon Discovery
For info: 844-655-7800
www.horizondiscovery.com

Electronically submit your new product description or product literature information! Go to www.sciencemag.org/about/new-products-section for more information.

Newly offered instrumentation, apparatus, and laboratory materials of interest to researchers in all disciplines in academic, industrial, and governmental organizations are featured in this space. Emphasis is given to purpose, chief characteristics, and availability of products and materials. Endorsement by *Science* or AAAS of any products or materials mentioned is not implied. Additional information may be obtained from the manufacturer or supplier.

want new technologies?

antibodies
apoptosis
biomarkers
cancer
cytometry
data
diseases
DNA
epigenetics
genomics
immunotherapies
medicine
microbiomics
microfluidics
microscopy
neuroscience
proteomics
sequencing
toxicology
transcriptomics

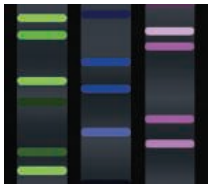

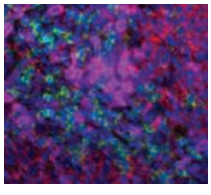

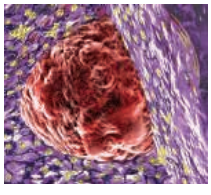

watch our webinars

Learn about the latest breakthroughs, new technologies, and ground-breaking research in a variety of fields. Our expert speakers explain their quality research to you and answer questions submitted by live viewers.

VIEW NOW!
webinar.sciencemag.org

Science
AAAS

Brought to you by the *Science*/AAAS Custom Publishing Office

@SciMagWebinars

The American Association for the Advancement of Science (AAAS) is the world's most trusted resource for science across disciplines and a leader in empowering scientific information in the public sphere.

By joining, you are bridging a gap between science and society. You are strengthening an organization that develops evidence-based policy making, enhances science education, and communicates unbiased science to the public. Your member benefits include:

- 51 weekly issues of *Science*, the leading journal of original science research
- Career resources and networking opportunities
- Member-only webinars, videos, blogs, online courses, podcasts, and more
- Advocacy, community outreach, and volunteer opportunities
- Timely science and technology news
- Access to research dating back to 1880
- Discounts on journals, meetings, products, and services

AAAS

Visit www.aaas.org/join. Together, we can make a difference.

Science Careers Advertising

For full advertising details, go to ScienceCareers.org and click For Employers, or call one of our representatives.

Tracy Holmes
Worldwide Associate Director
Science Careers
Phone: +44 (0) 1223 326525

THE AMERICAS

E-mail: advertise@sciencecareers.org

Fax: +1 (202) 289 6742

Tina Burks
Phone: +1 (202) 326 6577

Nancy Toema
Phone: +1 (202) 326 6578

Online Job Posting Questions
Phone: +1 (202) 312 6375

EUROPE / INDIA / AUSTRALIA / NEW ZEALAND / REST OF WORLD

E-mail: ads@science-int.co.uk

Fax: +44 (0) 1223 326532

Sarah Lelarge
Phone: +44 (0) 1223 326527

Kelly Grace
Phone: +44 (0) 1223 326528

Online Job Posting Questions
Phone: +44 (0) 1223 326528

JAPAN

Katsuyoshi Fukamizu (Tokyo)
E-mail: kfukamizu@aaas.org
Phone: +81 3 3219 5777

Hiroyuki Mashiki (Kyoto)
E-mail: hmashiki@aaas.org
Phone: +81 75 823 1109

CHINA / KOREA / SINGAPORE / TAIWAN / THAILAND

Ruolei Wu
Phone: +86 186 0082 9345
E-mail: rwu@aaas.org

All ads submitted for publication must comply with applicable U.S. and non-U.S. laws. *Science* reserves the right to refuse any advertisement at its sole discretion for any reason, including without limitation for offensive language or inappropriate content, and all advertising is subject to publisher approval. *Science* encourages our readers to alert us to any ads that they feel may be discriminatory or offensive.

ScienceCareers
FROM THE JOURNAL SCIENCE AAAS

ScienceCareers.org

Fantastic Recruiting Opportunity!

POSTDOC CAREERS | March 25, 2016

Be sure to promote your openings to the thousands of scientists who will be reading *Science* to find out about the latest postdoc opportunities.

Reserve ads by March 8 to guarantee space.

Produced by the *Science*/AAAS Custom Publishing Office.

SCIENCECAREERS.ORG

Science Careers AAAS

To book your ad: **advertise@sciencecareers.org**

The Americas
+202 326 6582

Japan
+81 3 3219 5777

Europe/RoW
+44(0)1223 326500

China/Korea/Singapore/Taiwan
+86 186 0082 9345

Memorial Sloan-Kettering Cancer Center

Postdoctoral Research Fellow

A post doctoral research position is available immediately to join the newly established laboratory of Dr. Anas Younes, within the Lymphoma Service at Memorial Sloan Kettering Cancer Center (MSKCC).

The major focus of the laboratory is the development of novel targeted therapy and mechanism-based novel combination regimens for the treatment of lymphoma. The lab is actively investigating genetic and molecular biomarkers for predicting treatment response, and identifying negative feedback loops that may facilitate the design of combination strategies. Highly motivated individuals (Ph.D. or M.D.) with outstanding training in cell biology, cell signaling, cancer genetics, or related areas, are encouraged to apply.

Interested candidates should email CV and contact information for three references to:

Anas Younes, M.D.
Chief, Lymphoma Service, MSKCC
email: younesa@mskcc.org

Assistant Professor

Departments of Cancer Biology Dana-Farber Cancer Institute *and* Cell Biology Harvard Medical School

The Departments of Cancer Biology at the Dana-Farber Cancer Institute and Cell Biology at Harvard Medical School invite applicants for a tenure-track faculty position at the rank of Assistant Professor or Associate Professor who will be appointed from October 1st 2016. We are seeking individuals with a demonstrated potential for imaginative research who propose to work on exciting problems in Molecular Metabolism and who directly utilize Mass Spectrometry methods. This may include metabolomics, proteomics or both to uncover novel metabolic pathways in health and diseased states. The successful candidate will be expected to direct innovative and independent research and participate in the teaching of graduate and/or medical students. Our highly interactive environment provides the opportunity to engage and collaborate with other dedicated researchers both within the Division of Metabolism and Chronic Disease of the Cancer Biology Department (chaired by Bruce Spiegelman) and throughout the diverse Harvard research community. Significant scholarly and scientific resources will be made available for this appointment. For further information about our Department, please see our web page: http://www.dana-farber.org/Research/Departments-and-Centers/Department-of-Cancer-Biology.aspx

Applicants should submit electronic copies of their curriculum vitae, a description of research accomplishments and future research interests (three pages maximum), and ask at least three references to provide letters of recommendation. These materials should be submitted using the following link: https://academicpositions.harvard.edu/postings/6703.
Please contact Kim Wilkinson (Kim_Wilkinson@dfci.harvard.edu) with any questions regarding submission of documents.
Applications must be received by: 4-29-2016.

Dana-Farber Cancer Institute and Harvard Medical School are Equal Opportunity/Affirmative Action employers.
We are actively committed to increasing the diversity of our faculty. People with disabilities, veterans, women and members of underrepresented minority groups are therefore strongly encouraged to apply.

DANA-FARBER CANCER INSTITUTE
HARVARD MEDICAL SCHOOL

NIMS ICYS

Research Position at ICYS, NIMS, Japan

The International Center for Young Scientists (ICYS) of the National Institute for Materials Science (NIMS) is now seeking a few researchers. Successful applicants are expected to pursue innovative research on broad aspects of materials science using most advanced facilities in NIMS (http://www.nims.go.jp/eng/index.html)

In the ICYS, we offer a special environment that enables young scientists to work independently based on their own idea and initiatives. All management and scientific discussions will be conducted in English. An annual salary approximately 5.35 million yen (level of 2015) will be offered depending on qualification and experience. Additional research grant of 2 million yen per year will be supplied to each ICYS researcher. The initial contract term is two years and may be extended by one more year depending on the person's performance.

All applicants must have obtained a PhD degree within the last ten years. Applicants should submit an **application form** including a research proposal to be conducted during the ICYS tenure, **CV Header**, CV with list of publications and patents (Be sure to attach the header), list of DOI of journal publications following our instruction, reprints of three significant publications to ICYS Recruitment Desk by **MARCH 31, 2016 JST**. The **application form** and **CV header** can be downloaded from **our website**. Please visit our website for more details.

ICYS Recruitment Desk,
National Institute for Materials Science
http://www.nims.go.jp/icys/recruitment/index.html

ASHG THE AMERICAN SOCIETY OF HUMAN GENETICS
AJHG The American Journal of Human Genetics

Editor
The American Journal of Human Genetics

The American Society of Human Genetics is seeking an Editor for *The American Journal of Human Genetics*. The Editor of *The American Journal of Human Genetics* provides leadership and vision for one of the oldest and most prestigious human genetics journals in the world that publishes primary research in human genetics.

Among the Editor's responsibilities are: determining the scope and direction of the scientific content of *The Journal*, overseeing manuscripts submitted for review and their publication, selecting and supervising an editorial staff, and directing and managing interactions with the publisher (currently Cell Press). The Editor serves as a member of the Board of Directors of the American Society of Human Genetics (ASHG), as well as the ASHG Finance Committee, and reports to the Board of Directors. All Associate Editors of *The Journal* are appointed by the Editor, who also determines their duties. At the ASHG Annual Meeting, the Editor presides over a meeting of the Associate Editors and presents an annual report to the ASHG membership.

The term of the appointment is five years and includes a yearly stipend. The new Editor will be selected by the end of 2016 and will begin receiving manuscripts about September 2017, with partial overlap with the current editorial office, in Houston. Applicants should be accomplished scientists in human genetics and should have a broad knowledge and appreciation of the field. Nominations, as well as applications consisting of a letter of interest and curriculum vitae, should be sent to address below prior to **April 1, 2016**.

AJHG Editorial Search Committee
American Society of Human Genetics
9650 Rockville Pike
Bethesda, MD 20814
Joseph D. McInerney, Executive Vice President, ASHG
jmcinerney@ashg.org

ScienceCareers online @sciencecareers.org

Cancer Feature:

Cancer Research

Issue date: April 8

Reserve space by March 22

Ads accepted until April 1 if space allows

For recruitment in science, there's only one *Science*.

Looking to hire a cancer researcher? Reach them through the pages of *Science*. Our upcoming cancer feature explores how major institutions are planning to prepare for the challenges involved in precision medicine. This hot research area is sure to draw the readers you need to reach.

What makes *Science* the best choice for recruiting?

- Read and respected by 400,000 readers around the globe
- Your ad dollars support AAAS and its programs, which strengthens the global scientific community.

Why choose this feature for your advertisement?

- Relevant ads lead off the career section with a special cancer research banner
- Bonus distributions:

  American Association for Cancer Research, April 16–20, New Orleans, LA

  AACR Career Fair, April 16, New Orleans, LA.

Expand your exposure by posting your print ad online:

- Link on the job board homepage to a landing page for cancer research positions.

Produced by the *Science*/AAAS Custom Publishing Office.

Deliver your message to a global audience of targeted, qualified scientists.

129,574
subscribers in print every week

352,966
monthly unique browsers on ScienceCareers.org

65%
of our weekly readers are Ph.D.s

SCIENCECAREERS.ORG

ScienceCareers
FROM THE JOURNAL SCIENCE AAAS

To book your ad: **advertise@sciencecareers.org**

The Americas
+202 326 6582

Japan
+81 3 3219 5777

Europe/RoW
+44 (0) 1223 326500

China/Korea/Singapore/Taiwan
+86 186 0082 9345

RESEARCH ASSISTANT PROFESSOR

THE UNIVERSITY OF ARIZONA CANCER CENTER

An outstanding position is available working in the laboratory of Dr. Andrew S. Kraft, Director of the University of Arizona Cancer Center in Tucson, Arizona. The research project will focus on the role of the Pim protein kinase in malignant disease with experiments aimed at discovering how this kinase drives cell growth in tumors, e.g. prostate cancer and leukemia, including understanding the substrates and signaling pathways driven by the Pim protein kinase. Investigators will have the opportunity to submit grant applications, and will be appointed in a basic or clinical science department.

To apply, please complete the on-line application at: www.uacareers.com and seek job #F20390 or #F20392.

Andrew S. Kraft, M.D.
Director, University of Arizona Cancer Center
tsaeed@uacc.arizona.edu / hrsim@email.arizona.edu

Outstanding UA benefits include health, dental, and vision insurance plans; life insurance and disability programs; paid vacation, sick leave, and holidays; UA/ASU/NAU tuition reduction for the employee and qualified family members; state and optional retirement plans; access to UA recreation and cultural activities; and more!

The University of Arizona is an EEO/AA employer-M/W/D/V.

Medizinische Fakultät Heidelberg

An der **Medizinischen Fakultät** der Universität Heidelberg ist ab 1. Oktober 2017 eine

W3-Professur für Geschichte und Ethik der Medizin (Nachfolge Prof. Dr. Eckart)

zu besetzen. Die Stelleninhaberin/Der Stelleninhaber vertritt den Querschnittsbereich „Geschichte, Theorie und Ethik der Medizin“ in Forschung und Lehre und unterstützt die Medizinische Fakultät und das Universitätsklinikum in Fragen der Medizinethik. Mit der Professur ist die Leitung des Instituts für „Geschichte und Ethik der Medizin“ der Universität Heidelberg verbunden.

Es wird erwartet, dass die Bewerberin/der Bewerber auf der Grundlage langjähriger Erfahrung die Fächer Geschichte, Theorie und Ethik der Medizin in Forschung und Lehre in ihrer ganzen Breite vertritt. Erfahrungen in der Einwerbung von Drittmittelprojekten werden ebenso vorausgesetzt wie einschlägige Publikationen zur Geschichte und Ethik der Medizin. Darüber hinaus wird erwartet, dass die Bewerberin/der Bewerber an der ethischen Profilbildung der Heidelberger Universitätsmedizin (Ethikbeirat, klinische Ethikberatung) aktiv mitwirkt und zugleich den Brückenschlag zu den übrigen Fakultäten, vorzugsweise zur Theologie, zur Philosophie, den Geschichts- und Sprachwissenschaften mitgestaltet.

Gesucht wird eine in Forschung und Lehre ausgewiesene Persönlichkeit.

Einstellungsvoraussetzungen sind ein mit der Promotion abgeschlossenes Studium der Medizin und/oder eines geisteswissenschaftlichen Faches, dann vorzugsweise der Geschichtswissenschaften oder der Philosophie. Weiterhin werden die Habilitation in Geschichte der Medizin oder im Querschnittsbereich Geschichte, Theorie, Ethik der Medizin oder gleichwertige wissenschaftliche Leistungen auf diesen Gebieten erwartet.

Auf die weiteren in § 47 und § 48, Abs. 2, Satz 3 des baden-württembergischen Landeshochschulgesetzes genannten Einstellungsvoraussetzungen wird hingewiesen.

Die Universität Heidelberg strebt eine Erhöhung des Anteils der Frauen im wissenschaftlichen Personal an und fordert qualifizierte Frauen nachdrücklich auf, sich zu bewerben. Schwerbehinderte werden bei gleicher Qualifikation bevorzugt berücksichtigt.

Bitte richten Sie Ihre Bewerbung in Papierform mit den notwendigen Unterlagen bis zum **24. März 2016** an **Prof. Dr. W. Herzog, Dekan der Medizinischen Fakultät Heidelberg, Im Neuenheimer Feld 672, 69120 Heidelberg.** Ihre Bewerbungsunterlagen sollten den Kriterien entsprechen, welche Sie auf der Webseite der Fakultätsgeschäftsstelle unter www.medizinische-fakultaet-hd.uni-heidelberg.de/professur einsehen können.

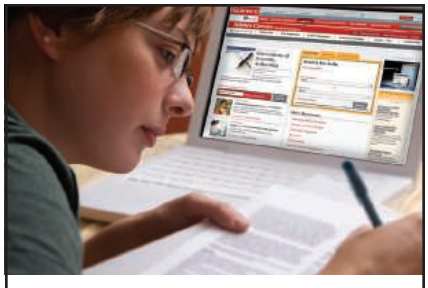

AAAS is here –
helping scientists achieve career sucess.

Every month, over 400,000 students and scientists visit ScienceCareers.org in search of the information, advice, and opportunities they need to take the next step in their careers.

A complete career resource, free to the public, *Science* Careers offers hundreds of career development articles, webinars and downloadable booklets filled with practical advice, a community forum providing answers to career questions, and thousands of job listings in academia, government, and industry. As a AAAS member, your dues help AAAS make this service available to the scientific community. If you're not a member, join us. Together we can make a difference.

To learn more, visit
aaas.org/plusyou/sciencecareers

AAAS + U = Δ

APS physics™

EDITOR IN CHIEF

The American Physical Society invites nominations and applications for the position of Editor in Chief.

The American Physical Society (APS), a nonprofit membership organization with over 50,000 members working in academia, national laboratories, and industry, is the world's leading publisher of physics journals serving the global physics community. APS publishes a suite of 12 outstanding journals covering a wide scope of physics-related science, including the flagship journal *Physical Review Letters*.

APS seeks a highly respected member of the physics community to serve as Editor in Chief (EiC) for all APS journals. Key responsibilities include: ensuring the excellence and integrity of APS journal content; effectively communicating and representing APS journals to a broad range of constituencies; and partnering with APS senior leaders, particularly the Publisher, to articulate and drive a strategic vision for the APS publishing enterprise. The ideal candidate will have a demonstrated record of intellectual leadership and exceptional communication and interpersonal skills. For the detailed job description go to:

http://storbeckpimentel.com/resources/uploads/institution/APSEiCPD.pdf

Evaluation of candidate materials will begin immediately and continue until a new Editor in Chief is selected. For best consideration, nominations, together with a brief supporting statement, and applications from potential candidates should be sent to:

storbeck / pimentel
executive search consultants

Shelly Storbeck, Managing Partner
Ethan Dubow, Associate
Storbeck/Pimentel & Associates
APSEditorinChief@storbeckpimentel.com

Competitive salary and benefits to be negotiated. The APS Editorial Office is located in Ridge, Long Island, NY, and the EiC, if not based at Ridge, would be expected to travel there frequently.

APS is an Equal Opportunity/Affirmative Action employer. All qualified applicants will receive consideration for employment without regard to race, color, religion, sex, national origin, disability, or protected veteran status. EOE M/F/D/V

ScienceCareers online @sciencecareers.org

myIDP: A career plan customized for you, by you.

For your career in science, there's only one Science

my IDP
ScienceCareers

Recommended by leading professional societies and the NIH

Features in myIDP include:

- Exercises to help you examine your skills, interests, and values.
- A list of 20 scientific career paths with a prediction of which ones best fit your skills and interests.
- A tool for setting strategic goals for the coming year, with optional reminders to keep you on track.
- Articles and resources to guide you through the process.
- Options to save materials online and print them for further review and discussion.
- Ability to select which portion of your IDP you wish to share with advisors, mentors, or others.
- A certificate of completion for users that finish myIDP.

Visit the website and start planning today!
myIDP.sciencecareers.org

ScienceCareers In partnership with:

advancing the life sciences 1912-2012 FASEB Federation of American Societies for Experimental Biology

UCSF University of California San Francisco

Medical College of Wisconsin

Burroughs Wellcome Fund

UNM SCHOOL of MEDICINE

TENURE-TRACK ASSISTANT PROFESSOR

THE DEPARTMENT OF ANESTHESIOLOGY & CRITICAL CARE MEDICINE

The Department of Anesthesiology & Critical Care Medicine invites applications to fill a tenure-track faculty position at the Assistant Professor level. The appointment would be a primary appointment in the Department of Anesthesiology and Critical Care Medicine within the newly developed Anesthesiology Research Laboratory with a secondary appointment in the Department of Neurosciences.

Minimum Requirements: Applicants must have a Ph.D. and/or M.D. degree, or the equivalent, with postdoctoral experience.

Preferences: Applicants with an independent research program, or strong potential for obtaining extramural funding, as evidenced by funding history, high quality publications and their research plan; Neuroscientists with primary research interests that build upon department collaborative research strengths in molecular, cellular and behavioral models of mammalian neurodevelopmental, neurodegenerative diseases involving neuroinflammation and/or pain mechanisms, and techniques involving a variety of neuroimaging modalities as evidenced by CV, references and research plan; Teaching experience or interest in participating in graduate and medical education programs as evidenced by CV and references.

For more details on current research activities in the Department of Anesthesiology & Critical Care Medicine, see **http://anesthesiology.unm.edu**, and in Neurosciences, see **http://neurosciences.unm.edu/**, and in the College of Pharmacy, see **http://hsc.unm.edu/pharmacy/graduateradio.shtml**.

Numerous opportunities exist for research collaborations with faculty in other departments within the Health Sciences Center, our Centers on Biomedical Research Excellence on CNS Pathology and on Neuropsychiatric Disorders, the New Mexico Alcohol Research Center, the Brain & Behavioral Health Institute, and the Clinical & Translational Science Center, along with the College of Pharmacy, the MIND Research Network, and Sandia and Los Alamos National Laboratories.

The position includes a competitive salary, research start-up funds and access to staffed research facilities. Electronic applications should include a cover letter, curriculum vitae, list of references, research plans, and history of grant awards.

For best consideration, applications must be received by December 20, 2015; however, the position will remain open until filled.

For complete details of this position and to apply, access Faculty Postings at: **https://unmjobs.unm.edu/**. Reference Posting **#0832516**.

UNM's confidentiality policy ("Disclosure of Information about Candidates for Employment," UNM Board of Regents' Policy Manual 6.7), which includes information about public disclosure of documents submitted by applicants, is located at **http://www.unm.edu/~brpm/r67.htm**.

The University of New Mexico is an Equal Opportunity/ Affirmative Action employer and educator.

UNM SCHOOL of MEDICINE

VICE CHAIR OF RESEARCH

THE DEPARTMENT OF ANESTHESIOLOGY & CRITICAL CARE MEDICINE

The Department of Anesthesiology & Critical Care Medicine invites applications to fill a tenure-track faculty position at the Assistant, Associate Professor or Professor level as Vice Chair of Research. The appointment would be a primary appointment in the Department of Anesthesiology which is developing the Anesthesiology Research Laboratory, with possible secondary appointments in other departments as indicated. The position includes opportunities to lead and expand the Department research endeavors together with the Department of Neurosciences in the School of Medicine and also with the College of Pharmacy.

Minimum Requirements: Applicants must have a Ph.D. and/or M.D. degree, or the equivalent, with postdoctoral experience. If the candidate has a M.D. or M.D., Ph.D. degree, then the preferred field of expertise would be Anesthesiology.

Preferences: 1. Applicants with an independent research program, or strong potential for obtaining extramural funding, as evidenced by funding history, high quality publications and their research plan; 2. Neuroscientists and/or Neuropharmacology and/or Pharmacologists and/or Molecular Imaging Scientists with primary research interests that build upon department collaborative research strengths in molecular, cellular and behavioral models of mammalian neurodevelopmental, neurodegenerative diseases involving neuroinflammation and/or pain mechanisms, and techniques involving a variety of neuroimaging modalities, as evidenced by CV, references and research plan; 3. Teaching experience or interest in participating in graduate and medical education programs as evidenced by CV and references.

For more details on current research activities in the Department of Anesthesiology & Critical Care Medicine, see **http://anesthesiology.unm.edu,** in Neurosciences, see **http://neurosciences.unm.edu/,** and in the College of Pharmacy, see **http://hsc.unm.edu/pharmacy/graduateradio.shtml**.

Numerous opportunities exist for research collaborations with faculty in other departments within the Health Sciences Center, our Centers on Biomedical Research Excellence on CNS Pathology and the New Mexico Alcohol Research Center, the Brain & Behavioral Health Institute, and the Clinical & Translational Science Center, along with the MIND Research Network, and Sandia and Los Alamos National Laboratories.

The position includes a competitive salary based on degree, rank, and, if pertinent, the level of clinical activity, research start-up funds and staffed research facilities. Electronic applications should include a cover letter, curriculum vitae, list of references, research plans, and history of grant awards.

For best consideration, applications must be received by May 20, 2016; however, the position will remain open until filled.

For complete details of this position and to apply, go to: **unmjobs.unm.edu/applicants/Central?quickFind=86065** or access Faculty Postings at: **https://unmjobs.unm.edu/**. Reference Posting #**0833300**.

UNM's confidentiality policy ("Disclosure of Information about Candidates for Employment," UNM Board of Regents' Policy Manual 6.7), which includes information about public disclosure of documents submitted by applicants, is located at **http://www.unm.edu/~brpm/r67.htm**.

The University of New Mexico is an Equal Opportunity/ Affirmative Action employer and educator.

Science Careers online @sciencecareers.org

POSITIONS OPEN

Perelman School of Medicine
University of Pennsylvania

The Center of Excellence in Environmental Toxicology (CEET) at the University of Pennsylvania Perelman School of Medicine announces the availability of a postdoctoral position on its Translational Research Training Program in Environmental Health Sciences. The focus of the Center includes research in Lung and Airway Disease, Oxidative Stress/Oxidative Stress Injury; Reproduction, Endocrinology, and Development; and Gene-Environment Interactions. To learn more about the CEET visit website: **http://ceet.upenn.edu/**.

Postdoctoral applicants must conduct full time research in translational environmental health sciences. Applicants must be a United States Citizen or Permanent Resident and would be supported for up to two years. Salary and benefits are commensurate with National Research Service Award approved levels. For further information, application procedure, and list of faculty mentors, please go to the Center Excellence Environmental Toxicology website at **ceet.upenn.edu** or email **webster@upenn.edu**. The deadline to apply for an appointment beginning July 01, 2016 is **April 01, 2016**.

FULL TIME PROFESSOR

The University of Minnesota Medical School, Duluth campus invites applications for a full-time **PROFESSOR (TENURED)** to develop a team-based science initiative in American Indian/Rural Health Equity research. While the precise area of disease focus and disciplinary background is open, we seek candidates with a M.D., Ph.D., or equivalent, and a national reputation and proven track record of grant activity, publication, and scholarship in rural and/or American Indian health disparities and health equity research. Current NIH funding is a requirement for this position. In addition, the successful candidate must also have the vision and leadership capacity to develop a team science model for a discovery team of interprofessional collaborative research capable of constructing a successful NIH P series or equivalent application within the first five years of the inception of the discovery team program. This involves the capability to recruit, nurture, and direct a diverse and transdisciplinary team of four scientists. We seek a person with leadership ideas who wants to develop a team that meshes with the array of strengths currently on the ground at the Duluth campus as well as more broadly, across the two Medical School campuses and the Academic Health Center of the University of Minnesota. The team will be housed in the newly re-organized Center for Rural Health Studies, an existing Center of the University of Minnesota system, which the successful candidate will direct. Preference will be given to candidates with research interest in rural and/or Indigenous health, a strong history of externally funded research, and experience teaching in a university setting. To be considered for this position, please send a cover letter, a curriculum vitae and NIH biosketch, and four recent publications via the online process at website: **http://www1.umn.edu/ohr/employment/index.html (Job ID 306593)**.

Post Your Jobs

1.4 million candidates*
235,000 job applications*

Reach Scientists.
Fill Positions.

*Jan–Dec 2015

ScienceCareers
employers.sciencecareers.org

Learn more and conduct your job search the easy way.

- Search thousands of job postings
- Create job alerts based on your criteria
- Get career advice from our Career Forum experts
- Download career advice articles and webinars
- Complete an individual development plan at "myIDP"

Target your job search using relevant resources on **ScienceCareers.org**.

ScienceCareers
FROM THE JOURNAL SCIENCE AAAS

COLUMBIA UNIVERSITY MEDICAL CENTER

Assistant/Associate/Full Professor

The Department of Pathology and Cell Biology at Columbia University seeks highly qualified individuals for two tenure-track or tenured faculty positions in research in Cell Biology. Appointments can be at the Assistant, Associate or Professor level depending on experience and qualifications. All positions require outstanding academic credentials and a record of scholarly productivity.

Candidates with a Ph.D. and/or M.D. and an interest in any aspect of basic cell biology will be considered. Individuals conducting research in the following areas are of particular interest:

- membrane trafficking
- organelle biology
- cell motility
- imaging approaches to probe and/or manipulate cellular or intracellular function

Significant start-up packages will be available to successful candidates who we expect will develop dynamic research programs and participate in graduate teaching. Women and minorities are strongly encouraged to apply.

All applications must be submitted through Columbia University's online Recruitment of Academic Personnel System (RAPS). Please submit a CV, a 2-page statement of research interests and the names of three referees. Review of applications will begin on **May 1, 2016** and continue until positions are filled.

To apply, please visit RAPS: **https://academicjobs.columbia.edu/applicants/Central?quickFind=62248**

AIMR 原子分子材料科学高等研究機構

Advanced Institute for Materials Research, Tohoku University, Japan

The Advanced Institute for Materials Research, Tohoku University (AIMR), is a research institute that conducts interdisciplinary research that fuses together the fields of materials science and mathematics. There is no other research institute of its kind in the world.

AIMR is one of nine institutes established by World Premier International Research Center Initiative (WPI) Program launched by the Government of Japan. Many outstanding materials science scholars, chemists, physicists, and mathematicians are gathered here. Half of its members are of non-Japanese nationalities, and the official language used in the research institute is English. There is also a thorough support system for foreign researchers. It can be described as a truly international research institute.

In AIMR's world-class research environment, a diverse group of researchers are vigorously engaging themselves in the creation of predictive materials science through mathematics-materials science collaboration. AIMR has also established four joint laboratories in Europe, the United States and China as part of their efforts to bring AIMR's new materials science, including spin-centered materials science, to a global level. AIMR is enabling interdisciplinary integration that easily transcends the barriers of national borders and academic disciplines.

AIMR is located in Sendai, the "City of Trees," which has a population exceeding 1 million. It is a city in the northern part of Japan with lush and beautiful greenery. Freely engaging in research here in Sendai, which offers a rich cultural environment and beautiful nature, will certainly help you produce wonderful research output.

AIMR is an attractive research institute that always welcomes outstanding researchers.

The Advanced Institute for Materials Research, Tohoku University (AIMR) is recruiting tenure-track researchers in FY2016.

Advanced Institute for Materials Research, Tohoku University (AIMR)
2-1-1 Katahira, Aoba-ku, Sendai 980-8577
http://www.wpi-aimr.tohoku.ac.jp

Download the *Science* Careers jobs app from Science

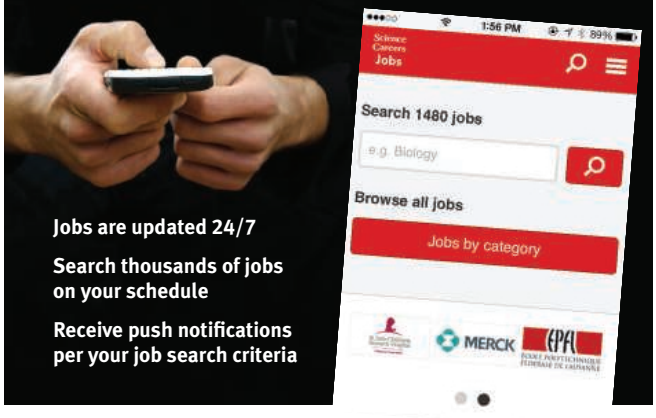

Jobs are updated 24/7

Search thousands of jobs on your schedule

Receive push notifications per your job search criteria

Get a job on the go.

Search worldwide for thousands of scientific jobs in academia, industry, and government. The application process is seamless, linking you directly to job postings from your customized push notifications.

Scan this code to download app or visit **apps.sciencemag.org** for information.

ScienceCareers | AAAS
FROM THE JOURNAL SCIENCE

ScienceCareers.org

UNIVERSITY OF CAMBRIDGE

www.jobs.cam.ac.uk

Charles Darwin Professorship of Animal Embryology

School of Biological Sciences

The Board of Electors to the Charles Darwin Professorship of Animal Embryology invite applications for this Professorship from persons whose work falls within the general field of the Professorship to take up appointment on 1 October 2016 or as soon as possible thereafter.

Candidates will have an outstanding research record of international stature in some area of animal embryology and the vision, leadership, experience and enthusiasm to build on current strengths in maintaining and developing a leading research presence. They will hold a PhD or equivalent postgraduate qualification.

Standard professorial duties include teaching and research, contribution to clinical service delivery, examining, supervision and administration. The Professor will be based in Cambridge. A competitive salary will be offered.

To apply online for this vacancy and to view further information about the role, please visit: http://www.jobs.cam.ac.uk/job/9519.

Further information is available at: www.admin.cam.ac.uk/offices/academic/secretary/professorships/ or contact the Academic Secretary, University Offices, The Old Schools, Cambridge, CB2 1TT, (email: ibise@admin.cam.ac.uk).

Applications, consisting of a letter of application, a statement of current and future research plans, a curriculum vitae and a publications list, along with details of three referees should be made online no later than 17 March 2016.

Informal enquiries may be directed to Professor Michael Akam, Head, Department of Zoology, tel: +44 (0)1223 336601, e-mail: hod@zoo.cam.ac.uk

Please quote reference PF08362 on your application and in any correspondence about this vacancy.

The University values diversity and is committed to equality of opportunity.

The University has a responsibility to ensure that all employees are eligible to live and work in the UK.

By **France A. Córdova**

Embrace uncertainty

I am often asked, "What advice can you give to graduate students?" When this happens I have to pause a moment, as I was an unusual case: an English-major undergraduate who went on to graduate study in physics. The first thing that comes to mind is to explore as much as possible, because eureka moments do happen. And when they do, don't be afraid of the decisions that may arise. My own came when, as a college graduate, I was watching a television show about neutron stars. As I listened to researchers discuss their observations and theories, a long-dormant light switched on, and I knew I had to realize my childhood dream of becoming a physicist. It would be a challenge, but I was confident in my passion, and it was a risk I was willing to take.

I am also asked, "What prepared you for being a graduate student?" Perhaps surprisingly, the single thing that most prepared me to persevere with the trials of graduate school was rock climbing. I'm not advocating that all graduate students become climbers, but for me it was both an engaging passion and a metaphor for my professional progress. Climbing requires trust in one's partners, patience, practice, and more practice. The moments of expansiveness when you are at rest—perched on a crag hundreds of feet above a valley floor with your mind roaming freely—can lead to epiphanies. Making room for passions outside your research, and time for friends and family, enables you to be a more whole person, and a more whole scientist.

"The moments of expansiveness when you are at rest ... can lead to epiphanies."

Here are a few more pieces of advice I would like to share:

If you haven't chosen a research topic, talk to top faculty members about their ideas on the most interesting problems in their fields. I knew I wanted to take on something big—to be the first person on the planet to see something—and found the sense of discovery pure euphoria; I promise you will, too.

Don't spend more time than you need to in graduate school. It may seem fun to be a student, or scary to figure out next steps, but you will have greater responsibility and freedom (and get paid more) after you graduate, so get a postgraduation plan together.

If you are about to receive your Ph.D. and find yourself faced with multiple options for what to do after graduation, don't fret—rejoice! Examine the options, but don't let the decision burden you. You can't go wrong if you choose the one that resonates with you the most. And if you don't have job offers, your world is wide open. Choose where you want to work, go there, and find a way to get an informational interview. This can put you first in line when jobs open up. You may have to start at a low level, but with hard work and good humor, you will "graduate" quickly to a position with more responsibility. People are willing to help if you apply yourself.

Try not to make decisions based solely on money, especially early in your career, when salaries tend to be at their lowest. As a young researcher married to a high school science teacher, we had to pay for child care—a hefty expense for many young families. But we decided to pay for the best care we could afford because it gave us peace of mind: I knew our children were in good care, and I could focus on my work and raising my family. I also knew that, in time, I would make more money. Financial decisions are personal and often difficult, but remember that money should help you, not define you.

Speaking of children, don't fret about when or whether to have them. You will know. I've seen scientists have children when they were still graduate students, and others (like me) when they were full professors and department chairs. You will survive no matter what, and so will your children.

In summary, don't fear decisions; embrace them. They allow you to explore new ideas and places. They mark the pathways that make your journey unique. Your choices will define you, so my last piece of advice is simple: Be yourself. You can't make a bad choice if you remain true to yourself. ■

France A. Córdova is director of the National Science Foundation. Send your story to SciCareerEditor@aaas.org.

ILLUSTRATION: ROBERT NEUBECKER

Downloaded from on February 25, 2016

Published by AAAS